

2020

**ANNUAL REPORT**  
JAHRESBERICHT



**Paul-Drude-Institut  
für Festkörperelektronik**

Leibniz-Institut im Forschungsverbund Berlin e. V.



# Table of Contents

## Inhaltsverzeichnis

Preface	
<a href="#">Vorwort</a> .....	5
Scientific Advisory Board	
<a href="#">Wissenschaftlicher Beirat</a> .....	8
Research Highlights	
<a href="#">Forschungshighlights</a> .....	11
Core Research Areas	
<a href="#">Forschungsschwerpunkte</a> .....	36
Brief Reports	
<a href="#">Kurzberichte</a> .....	64
Departments	
<a href="#">Abteilungen</a> .....	131
Facts & Figures	
<a href="#">Zahlen &amp; Fakten</a> .....	155
Contact	
<a href="#">Kontakt</a> .....	171
Imprint	
<a href="#">Impressum</a> .....	175



# Preface

## Vorwort

Dear Readers,

The year 2020 brought several special challenges for the Paul-Drude-Institut (PDI), Leibniz-Institut im Forschungsverbund Berlin e.V.. First and foremost is the COVID-19 pandemic, which caused unprecedented restrictions around the world. At the PDI, we massively reduced work at the institute premises for an extended period of time, learned to work instead on a mobile basis from home to a large extent, and implemented a comprehensive hygiene concept to be able to perform again the experiments that are indispensable for our research. Nevertheless, essential aspects of scientific work such as attending meetings or hosting visiting scientists were completely missed, and delays in research projects were unavoidable.

In addition, the PDI found itself in the special situation that the outgoing director, Prof. Dr. Henning Riechert, retired at the end of the previous year and that there were delays in the procedure to reappoint the director position. At the end of 2020,

Sehr geehrte Leserinnen und Leser,

das Jahr 2020 brachte für das Paul-Drude-Institut (PDI), Leibniz-Institut im Forschungsverbund Berlin e.V. mehrere besondere Herausforderungen. Zuvorderst ist hier die COVID-19-Pandemie zu nennen, die auf der ganzen Welt zu beispiellosen Einschränkungen führte. Am PDI reduzierten wir für einen längeren Zeitraum massiv die Arbeit in den Institutsräumlichkeiten, lernten, stattdessen in großem Umfang mobil von zu Hause aus zu arbeiten, und führten ein umfangreiches Hygienekonzept ein, um die für unsere Forschung unabdingbaren Experimente wieder durchführen zu können. Nichtsdestotrotz fielen wesentliche Aspekte wissenschaftlicher Arbeit wie die Teilnahme an Tagungen oder der Besuch von Gastwissenschaftlern komplett weg, und Verzögerungen in Forschungsprojekten waren unumgänglich.

Zusätzlich fand sich das PDI in der speziellen Situation, dass der vorherige Direktor, Prof. Dr. Henning Riechert, zum Ende des Vorjahres in den Ruhestand ging und es im



this procedure had not yet been completed. Thus, without a full-time director, the PDI prepared the extensive documentation for the evaluation of the institute by the Leibniz Association, which was scheduled for February 2021. The preparation for this evaluation shaped the work at the institute in 2020 to a significant degree.

The colleagues at the PDI met these special challenges with strong team spirit and great commitment. This year, we again achieved exciting research results, published a considerable number of articles in prestigious journals, and acquired funding for new projects. We present selected results in this annual report, based on our research between the annual meetings of our Scientific Advisory Board in September 2019 and 2020.

We feature three research studies of which we are particularly proud as highlights. In each case, the contributions in English are preceded by a short summary in German. We then describe in German and English the five core research areas in which we organize our scientific work. This is followed by 17 short reports highlighting recent progress in these core research areas. Subsequently, we introduce the four departments of the institute, which are defined by our various fields of expertise and the associated facilities. In general, we work at the PDI in a matrix structure of departments and core research areas. In addition to the aforementioned texts, we present various lists and tables with facts and figures from the calendar year 2020.

I would like to thank all colleagues at the institute for their dedication, creativity, and understanding of the special working conditions this year. Even under the constraints of a pandemic, research thrives on international exchange, and I am grateful to our academic and industrial partners for the fruitful collaborations. I sincerely thank the members of our Scientific Advisory Board for their constructive critical feedback on

Verfahren zur Wiederbesetzung des Direktorenposten zu Verzögerungen kam. Zum Jahresende 2020 war dieses Verfahren noch nicht abgeschlossen. Somit erstellte das PDI ohne hauptamtlichen Direktor die umfangreichen Unterlagen für die Evaluierung des Institutes durch die Leibniz-Gemeinschaft, die turnusgemäß für Februar 2021 angesetzt worden war. Die Vorbereitung auf diese Evaluierung prägte die Arbeit am Institut im Jahr 2020 ganz wesentlich.

Diesen besonderen Herausforderungen stellten sich die Kolleginnen und Kollegen am PDI mit starkem Zusammenhalt und großem Engagement. Auch dieses Jahr erzielten wir spannende Forschungsergebnisse, veröffentlichten eine beachtliche Anzahl von Artikeln in angesehenen Fachzeitschriften und warben Fördermittel für neue Projekte ein. Ausgewählte Ergebnisse stellen wir Ihnen im vorliegenden Jahresbericht vor, der auf unserer Forschung zwischen den jährlichen Treffen unseres wissenschaftlichen Beirates im September 2019 und 2020 basiert.

Drei Forschungsergebnisse, auf die wir besonders stolz sind, präsentieren wir als Highlights. Den Beiträgen auf Englisch ist dabei jeweils eine kurze Zusammenfassung auf Deutsch vorangestellt. Anschließend beschreiben wir auf Deutsch und Englisch die fünf Forschungsschwerpunkte, in denen wir unsere wissenschaftliche Arbeit organisieren. Danach folgen 17 Kurzberichte, in denen aktuelle Fortschritte in diesen Forschungsschwerpunkten hervorgehoben werden. Daraufhin stellen wir die vier Abteilungen des Instituts vor, die durch unsere verschiedenen Kompetenzfelder und dazugehörigen Anlagen definiert sind. Generell arbeiten wir am PDI in einer Matrixstruktur aus Abteilungen und Forschungsschwerpunkten. Zusätzlich zu den genannten Textbeiträgen legen wir verschiedene Listen und Tabellen mit Zahlen und Fakten aus dem Kalenderjahr 2020 vor. Allen Kolleginnen und Kollegen des Insti-

our work and the strong support we received, including at the first-ever online Advisory Board meeting. Finally, I would like to express my gratitude to our funders at the Federal Government and the State of Berlin.

I hope you enjoy reading this annual report. You can additionally find the latest news about our institute and highlights from our research on our website [www.pdi-berlin.de](http://www.pdi-berlin.de).

tuts danke ich für ihren Einsatz, ihre Kreativität und ihr Verständnis für die besonderen Arbeitsumstände in diesem Jahr. Auch unter den Randbedingungen einer Pandemie lebt Forschung von internationalem Austausch, und ich bin unseren akademischen und industriellen Partnern für die fruchtbaren Zusammenarbeiten dankbar. Den Mitgliedern unseres wissenschaftlichen Beirats danke ich herzlich für die konstruktiv-kritische Begleitung unserer Arbeit und die starke Unterstützung, die wir auch bei dem erstmals online veranstalteten Beiratstreffen erfahren. Schließlich spreche ich meinen Dank unseren Fördergebern beim Bund und beim Land Berlin aus.

Ich wünsche Ihnen viel Freude bei der Lektüre dieses Jahresberichts. Aktuelle Neuigkeiten zu unserem Institut und Highlights aus unserer Forschung finden Sie zusätzlich auf unserer Website [www.pdi-berlin.de](http://www.pdi-berlin.de).



Dr. Lutz Geelhaar  
Acting director  
Kommissarischer Direktor

**Prof. Dr. Manfred Bayer**

Fakultät Physik, Experimentelle Physik 2,  
Technische Universität Dortmund  
Deutschland

**Dr. Martin Behringer**

OSRAM Opto Semiconductors GmbH,  
OS CTO TLED R  
Regensburg, Deutschland

**Prof. Oscar Dubon Jr.**

University of California  
Berkeley, CA, USA

**Prof. Nicolas Grandjean**

Ecole Polytechnique Federale de Lausanne  
Schweiz

**Prof. Dr. Dagmar Gerthsen**

Karlsruher Institut für Technologie (KIT)  
Karlsruhe, Deutschland

**Dr. Michelle D. Johannes**

Center for Computational Materials Science,  
Naval Research Laboratory  
Washington DC, USA

**Prof. Dr. Jochen Mannhart**

Max-Planck-Institut für Festkörperforschung  
Stuttgart, Deutschland

**Dr. Heike E. Riel**

IBM Research – Zürich  
Rüschlikon, Schweiz

**Prof. Dr. Werner Wegscheider**

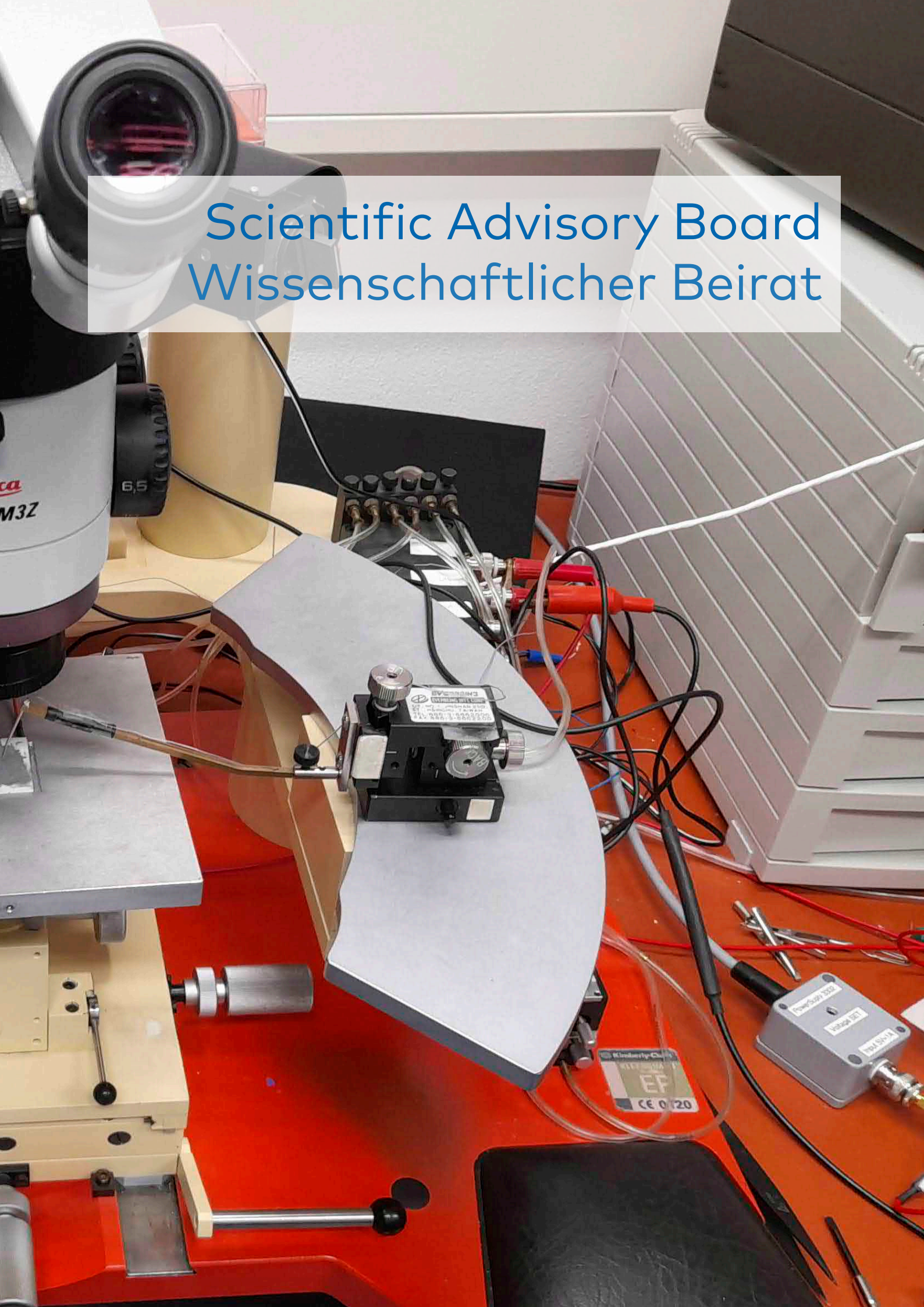
Advanced Semiconductor Quantum Materials  
Laboratory for Solid State Physics, ETH Zürich,  
Schweiz

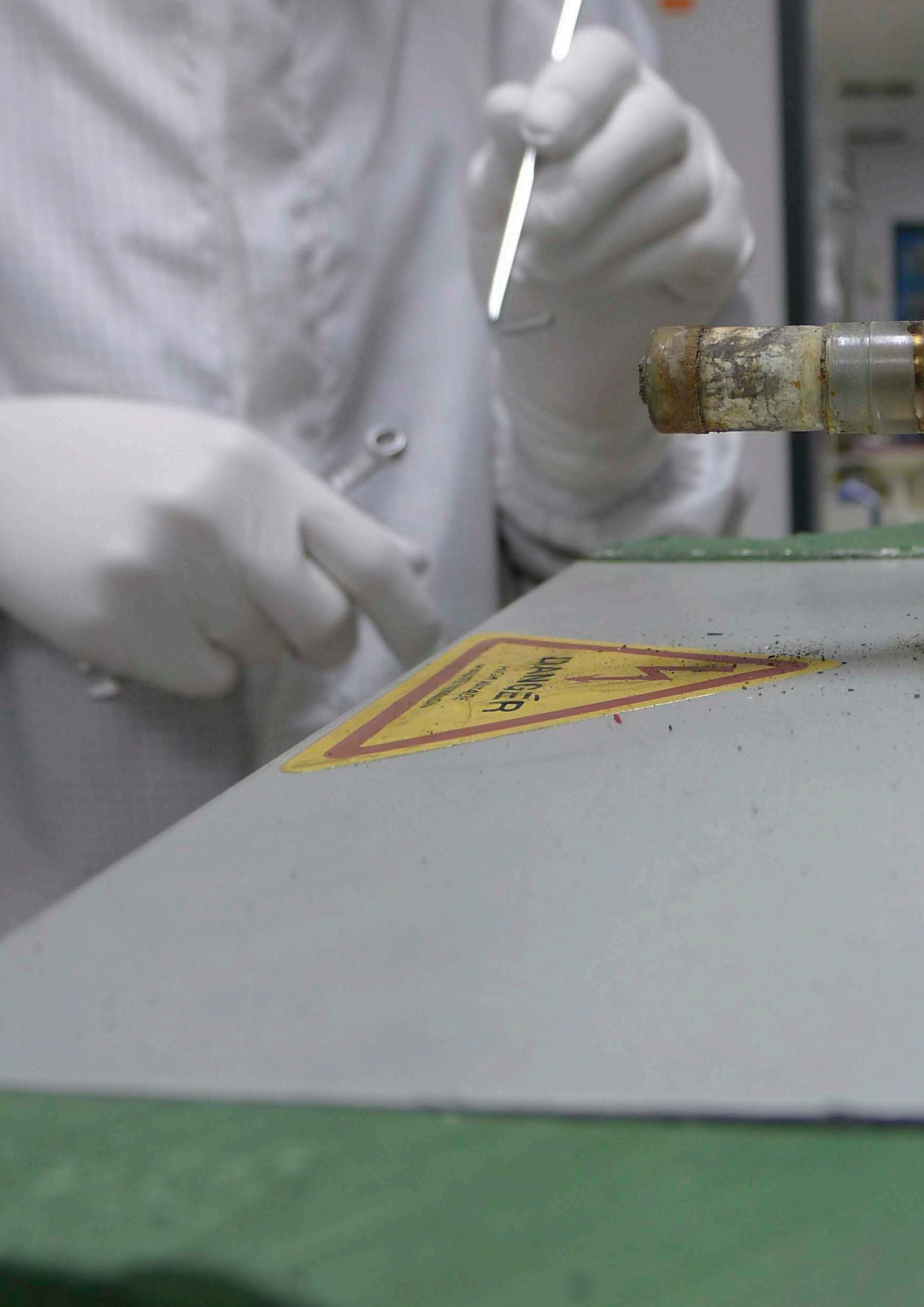
**Prof. Dr. Matthias Wuttig**

Rheinisch-Westfälische Technische Hochschule Aachen,  
Physikalisches Institut  
Aachen, Deutschland



# Scientific Advisory Board Wissenschaftlicher Beirat







# Research Highlights Forschungs-Highlights

Selektive van-der-Waals-Epitaxie von h-BN/Graphen-Heterostrukturen mittels He <sup>+</sup> -bestrahlungsinduziertem Defekt-Engineering in zweidimensionalen Substraten . . .	12
Selective-area van der Waals epitaxy of h-BN/graphene heterostructures via He <sup>+</sup> -irradiation-induced defect engineering in two-dimensional substrates . . . . .	13
Anwendung der Elektronentomographie zur umfassenden Bestimmung von III-V-Grenzflächeneigenschaften . . . . .	20
Application of electron tomography for comprehensive determination of III-V interface properties . . . . .	21
Nicht-reziproke Propagation von akustischen Oberflächenwellen entlang epitaktischer Fe <sub>3</sub> Si/GaAs-Hybridstrukturen . . . . .	28
Non-reciprocal transmission of surface acoustic waves along epitaxial Fe <sub>3</sub> Si/GaAs hybrid structures . . . . .	29

# Selektive van-der-Waals-Epitaxie von h-BN/Graphen-Heterostrukturen mittels He<sup>+</sup>-bestrahlungsinduziertem Defekt-Engineering in zweidimensionalen Substraten

Durch die Stapelung verschiedener zweidimensionaler (2D) Materialien können neuartige 2D-Heterostrukturen mit maßgeschneiderten Eigenschaften für die Anwendung in atomar dünnen optoelektronischen, elektronischen und Sensorvorrichtungen hergestellt werden. Innerhalb der Familie der 2D Materialien spielt das hexagonale Bornitrid (h-BN) in zweierlei Hinsicht eine zentrale Rolle: Elektronisch ermöglicht seine große Bandlücke eine effiziente Einschränkung von Elektronen, wie er in ultradünnen Schichten erforderlich ist. Andererseits machen es seine chemische Inaktivität (das heißt das Fehlen freier Bindungen) und seine hohe mechanische Beständigkeit in Kombination mit seinen isolierenden Eigenschaften zu einem idealen Material als Substrat oder Umhüllung für andere 2D-Materialien.

Die derzeit gebräuchlichste Herstellungstechnik für 2D-Heterostrukturen basiert auf dem mechanischen Abschälen und Stapeln von 2D-Kristallen, ein Prozess, der nur schwer skalierbar und nicht leicht reproduzierbar ist. In dieser Hinsicht erscheint das Wachstum von 2D-Schichten übereinander mittels Van-der-Waals-Epitaxie (vdWE) als attraktive Alternative für eine skalierbare Synthese. Aufgrund der schwachen Bindung zwischen 2D-Materialien ist die vdWE jedoch empfindlich gegenüber Oberflächendefekten und morphologischen Merkmalen wie etwa Stufenkanten, die die Nukleation stark beeinflussen und dadurch zu einem ungleichmäßigen Wachstum von polykristallinem Material führen. Daher wird die Kontrolle des Ortes der Nukleation als eine der wichtigsten Herausforderungen für eine skalierbare Herstellung von 2D-Heterostrukturen mittels vdWE angesehen.

In dieser Arbeit verwendeten wir einen fokussierten Ionenstrahl in einem He-Ionenmikroskop als neuartiges Werkzeug, um vorsätzlich atomare Defekte in epitaktischem Graphen auf SiC(0001) zu erzeugen, welche als bevorzugte Position für die Nukleation von atomar dünnem h-BN agieren, das über Molekularstrahlepitaxie gewachsen wurde. Dadurch konnten wir eine maskenlose, selektive vdWE aufzeigen, die eine beispiellose Kontrolle über die Bildung von 2D-Heterostrukturen mittels Bottom-up-Ansatz ermöglicht. Dies eröffnet eine neue Perspektive nicht nur für die skalierbare Herstellung von h-BN / Graphen-Heterostrukturen, sondern auch von 2D-Heterostrukturen anderer 2D Materialien, welche mittels vdWE hergestellt werden können, zum Beispiel 2D-Halbleiter wie die Übergangsmetalldichalkogenide.

# Selective-area van der Waals epitaxy of h-BN/graphene heterostructures via He<sup>+</sup>-irradiation-induced defect engineering in two-dimensional substrates

M. Heilmann, V. Deinhart<sup>1</sup>, A. Tahraoui, K. Höflich<sup>1</sup>, J. M. J. Lopes

The stacking of different two-dimensional (2D) materials allows to fabricate novel 2D heterostructures with tailored properties for application in atomically thin optoelectronic, electronic, and sensing devices. Within the family of 2D materials, hexagonal boron nitride (h-BN) plays a central role in two ways: Electronically, its large band-gap enables efficient electronic confinement as required in ultra-thin layers. On the other hand, its chemical inertness (i.e. the lack of dangling bonds) and high mechanical strength, in combination with its insulating nature, make it an ideal substrate or encapsulation layer for other 2D materials.

State-of-the-art preparation techniques for 2D heterostructures rely on mechanical exfoliation and stacking of 2D crystals, processes which are hardly scalable and lack reproducibility. Thus, the growth of 2D layers on top of each other via van der Waals epitaxy (vdWE) appears as an attractive alternative for a scalable synthesis. However, due to the weak bonding between 2D materials, vdWE is sensitive to surface defects and morphological features such as step edges, which strongly influence the nucleation, thereby giving rise to non-uniform growth of polycrystalline material. Hence, the control over nucleation location is considered as one of the key challenges to achieve scalable fabrication of 2D heterostructures via vdWE.

In this work, we utilized a focused ion beam (FIB) within a He ion microscope as a nov-

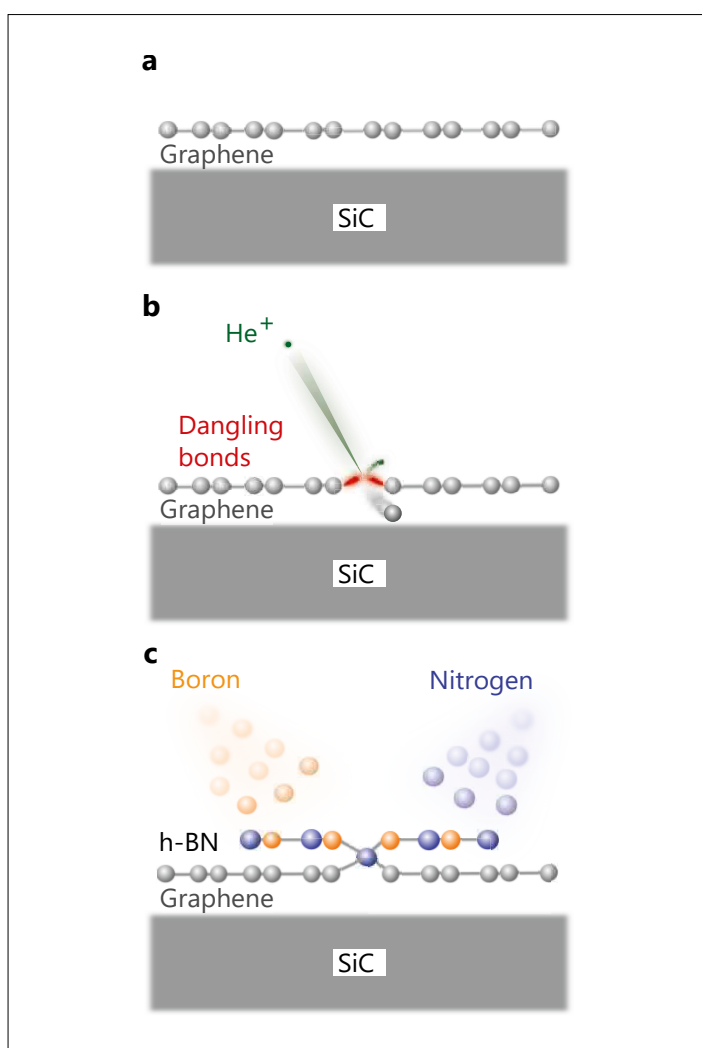


**Fig. 1.** Schematic representation of the SAvdWE process.

(a) Pristine EG on SiC substrate fabricated via surface graphitization. (b) Deterministic placement of defects in EG via He FIB. (c) Growth of h-BN via MBE, where the dangling bonds at the defects act as preferential nucleation sites. For simplicity the C-rich interface layer to the SiC was neglected in these images.

<sup>1</sup> Ferdinand-Braun-Institut, Leibniz-Institut für Höchstfrequenztechnik, Berlin, and Helmholtz-Zentrum Berlin für Materialien und Energie GmbH, Berlin

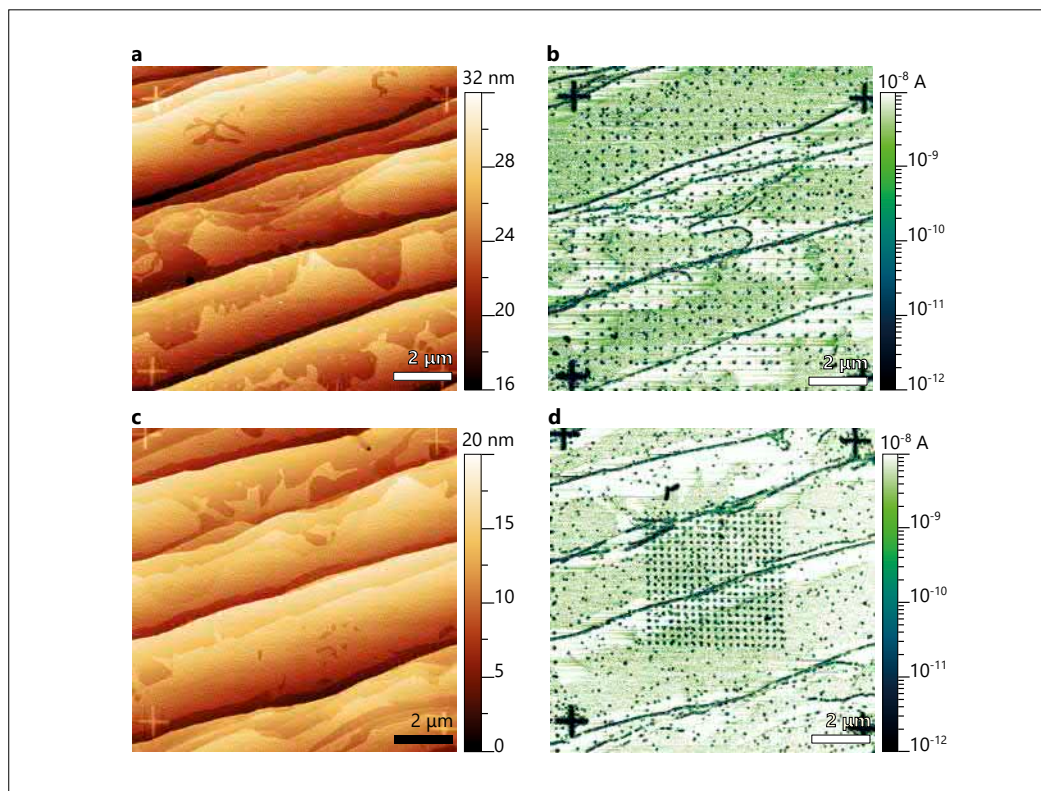


**Fig. 2.** AFM images of an area of  $19 \times 19$  defects written in between the cross-shaped markers with 20000 ions per IID in a distance of (a) 500 nm and (c) 250 nm to each other. The corresponding cAFM images showing the position of the insulating h-BN islands are seen in (b) and (d). During cAFM, a bias of 100 mV was applied to the graphene.

el tool to deliberately create atomic-scale defects in epitaxial graphene (EG) on SiC(0001), which act as preferential nucleation sites for atomically thin hexagonal boron nitride (h-BN) grown via molecular beam epitaxy (MBE). By  $\text{He}^+$  irradiation, chemically active defects in graphene could be deterministically placed and engineered (see Fig. 1). This mask-free selective-area vdWE (SAvdWE) is superior to the typically performed processing of a mask on the substrates via photo- and electron beam lithography (EBL), as no residues from a mask threaten to contaminate the surface of the 2D template. Ideally, only a single C atom needs to be removed from pristine graphene, which in itself serves as a mask through its chemically inert nature. Furthermore, our approach is significant-

ly faster than EBL, as only small ion doses are required for inducing point defects in 2D materials.

Irradiation with ions of noble gases with energies in the keV range is promising for the formation of defects in graphene with control down to single vacancies [O. Lehtinen *et al.*, Phys. Rev. B **81**, 153401 (2010)]. To systematically investigate h-BN nucleation at such irradiation-induced defects (IIDs), we grew h-BN islands for 300 min at 850 °C on EG templates (synthesized via surface graphitization of SiC), where IID patterns were written via a 30 keV He FIB with different ion numbers per intended defect location. The MBE growth of h-BN was performed by utilizing  $\text{N}_2$  plasma and B evaporated from an effusion cell. Figures

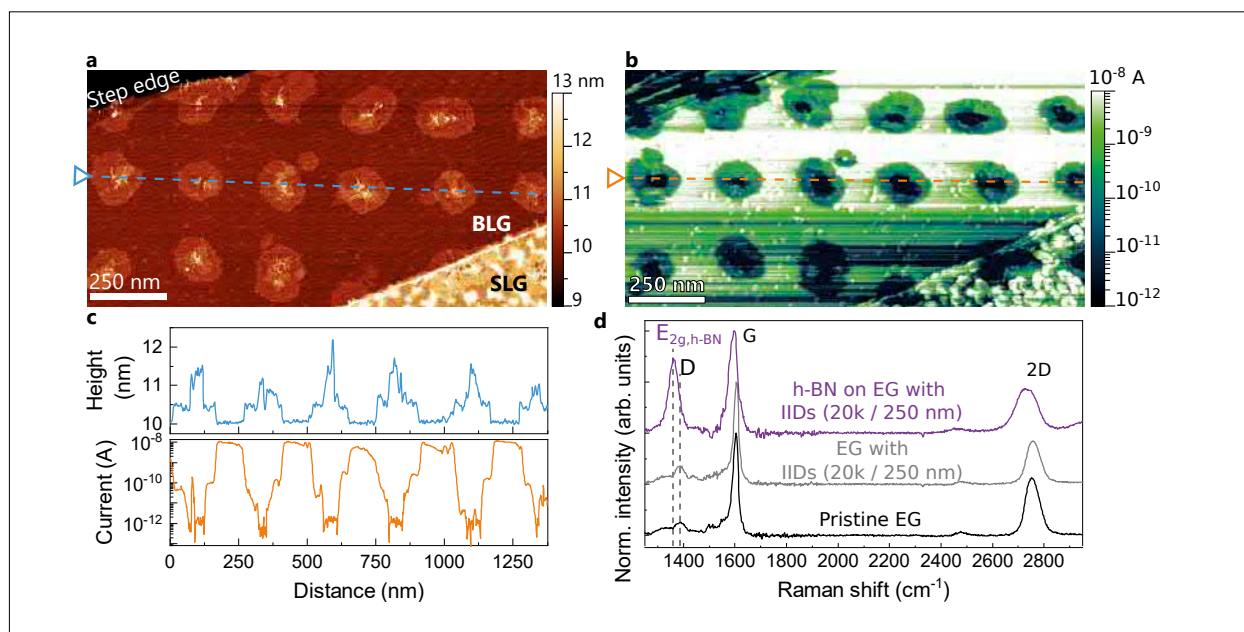


**Fig. 3.** (a) AFM image of h-BN islands forming close to a step edge on BLG following the IID pattern. (b) Corresponding cAFM image measured with a bias of 200 mV applied to graphene. (c) Linescans of the height (upper graph) and current maps (lower graph) from the blue and orange dotted lines in (a) and (b), respectively. (d) Comparison of mean Raman spectra obtained from pristine EG, and from EG with IIDs patterned with a 250 nm spacing and 20000 He ions per defect, before and after SAvdWE of h-BN islands.

2(a) and 2(c) show atomic force microscopy (AFM) images of an area of  $19 \times 19$  IIDs written in between the cross-shaped markers with 20000 ions per IID, in a distance of 500 nm and 250 nm to each other, respectively. Corresponding conductive AFM (cAFM) images, which show the position of the insulating h-BN islands (darker points in the images), are presented in Fig. 2(b) and 2(d). CAFM allows a clear contrast between graphene and h-BN given their semi-metallic and insulating nature, respectively.

The IID patterns were written across terraces and step edges on the surface, which is covered in single-layer graphene (SLG) and bi-layer graphene (BLG). A detailed AFM image of h-BN islands forming close to a step edge on BLG is depicted in Fig. 3(a). They exhibit a similar lateral size as observed during vdWE on pristine EG [M. Heilmann *et al.*, 2D Mater. **5**, 025004 (2018)], but closely follow the IIDs located 250 nm away from each other. This reveals

an unprecedented control of the nucleation placement and thus the feasibility of our approach to realize SAvdWE of h-BN/graphene heterostructures. An area with a rough surface can be distinguished from the smoother area close to the step edges with h-BN islands on top. The rough area is attributed to SLG overgrown by h-BN. The different morphology in this region is attributed to the higher reactivity of SLG, a product of its closer proximity to the C-rich and partially  $sp^3$ -bonded interface layer to SiC in EG. A direct consequence of this effect is the formation of multiple, disordered h-BN layers on SLG [M. Heilmann *et al.*, ACS Appl. Mater. Interfaces **12**, 8897 (2020)]. Here, we will concentrate the discussion on the overgrowth of IIDs on BLG, where the influence of the corrugated interface layer (which is specific for EG on SiC) is negligible.

Figure 3(c) shows a linescan which crosses several islands, revealing that they are

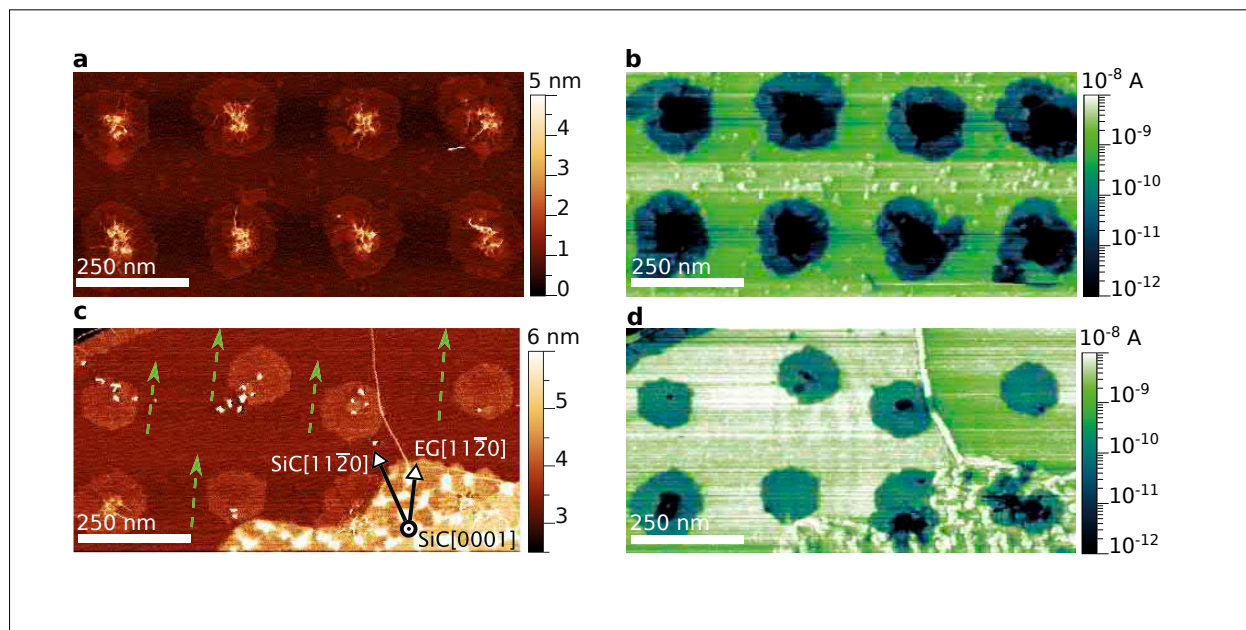


**Fig. 4.** AFM images of h-BN islands forming close to a step edge on BLG patterned with (a) 40000 and (c) 10000 He ions per IID with corresponding cAFM image in (b) and (d), respectively. During cAFM a bias of 200 mV was applied to graphene. The green dotted arrows in (c) are intended as a guide to the eye, indicating the common orientation among the h-BN islands, which shows an epitaxial alignment with the EG (directions marked with black arrows as derived from the step edge directions).

mainly composed of an extended h-BN monolayer (height of 0.35 nm). Additional h-BN layers can be observed around the island center, close to where the IID is located. The existence of thicker h-BN is confirmed by the corresponding cAFM image [(see Fig. 3(b))] and a linescan across it [(see Fig. 3(c)], where much lower current values were detected.

The creation of IIDs in EG as well as the SA-vdWE of h-BN were also probed by Raman spectroscopy. As shown in Fig. 3(d), the creation of defect patterns via He FIB leads to an increase in the intensity of the D peak, which results from disorder in graphene. The appearance of the  $E_{2g}$  peak around  $1361\text{ cm}^{-1}$  confirms the formation of h-BN after SA-vdWE. Moreover, a broadening of the graphene-related G and 2D peaks is observed. We attribute this to strain and doping fluctuations in the h-BN/graphene heterostructures [M. Heilmann 2020, *op. cit.*].

Single crystalline h-BN islands are expected to exhibit either a triangular or a hexagonal shape [Y. Liu *et al.*, *Nano Lett.* **12**, 3113 (2011)]. Thus, the shape of the h-BN islands depicted in Fig. 3(a) indicates they are polycrystalline. This is probably due to the nucleation of multiple h-BN islands at each IID. According to molecular dynamics simulations, the sputtering rate of C atoms from graphene upon  $\text{He}^+$  irradiation with an energy of 30 keV is expected to be relatively low. However, the defect formation is not only determined by the ion mass and its energy, but it is also affected by the interactions with the substrate, e.g. by atoms sputtered from the substrate [S. Kretschmer *et al.*, *ACS Appl. Mater. Interfaces* **10**, 30827 (2018)]. Therefore, unlike the simplified representation in Figure 1, the He FIB may have removed more than only one C atom per intended defect location, which would offer multiple nucleation points within a single IID, resulting in h-BN



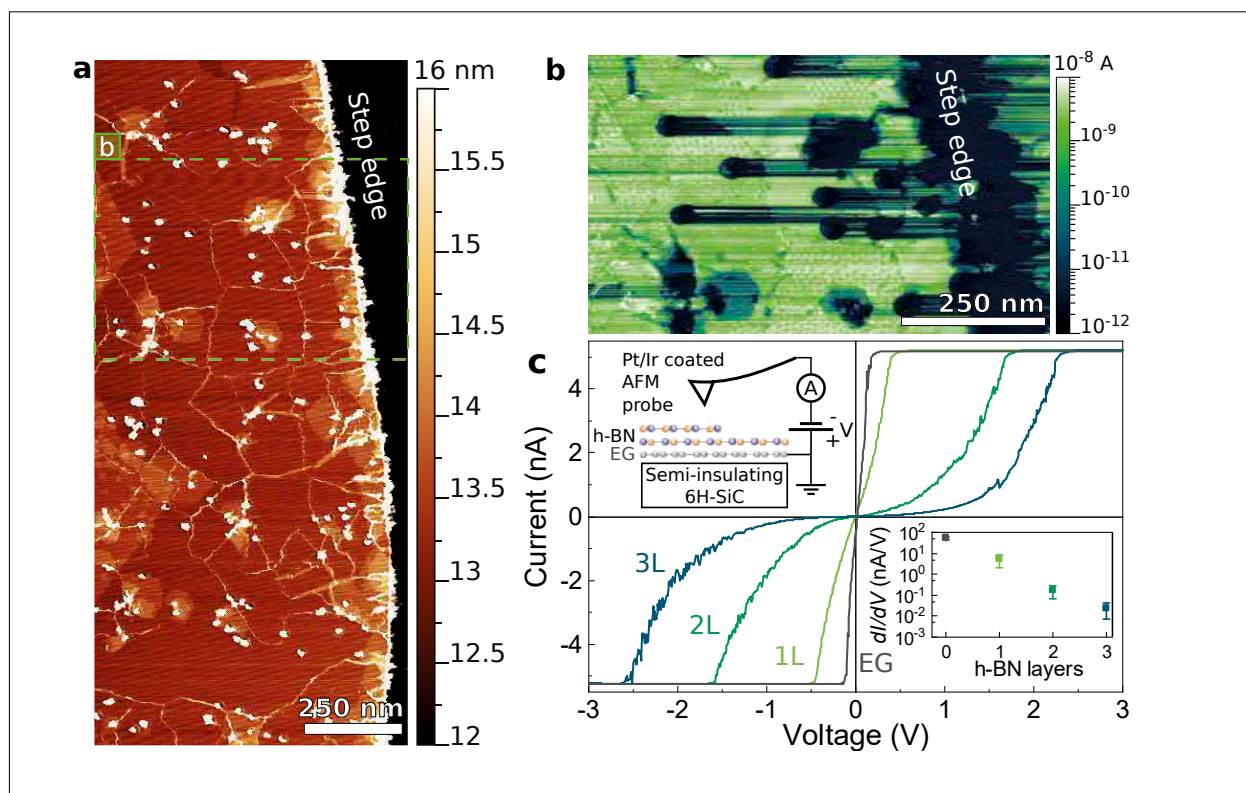


**Fig. 5.** (a) AFM image of an area close to a step edge with 3x7 IIDs in a distance of 250 nm to each other and written with 20000 He ions per IID, overgrown with h-BN for 480 min. (b) cAFM image of the green framed region in (a), where multiple h-BN layers can be observed close to nucleation centers at IIDs. During cAFM a bias of 100 mV was applied to graphene. (c) Vertical transport measurements of h-BN tunnel barriers, with I-V curves shown for single, bi- and tri-layer h-BN with the inset on the upper left showing the measurement configuration, and the inset to the lower right the tunnel conductance extracted from the linear regime of the I-V curves. The latter is attributed to direct tunneling of electrons through the h-BN layers.

with different in-plane rotation, forming polycrystalline islands.

Based on this assumption, fewer He ions per IID at the same ion energies should result in fewer C atoms being knocked out, resulting at best in a single vacancy, which in turn may allow only one h-BN domain to nucleate as a single crystal. Figure 4 shows a comparison of AFM and corresponding cAFM images obtained for h-BN islands formed at IIDs created with 40000 and 10000 ions. Indeed, a drastic change in the morphology of the h-BN can be observed when the number of He ions per IID is lowered to 10000. Several of the h-BN islands

present well-defined edges with a hexagonal shape and without wrinkles, which is taken as an indication that a single h-BN domain is forming at each IID. The mean diameter of the h-BN islands amounts to 165 nm and 135 nm for IIDs created with 40000 and 10000 ions, respectively. For the latter, the smaller growth rate may be attributed to a longer incubation time for the nucleation of h-BN at the smaller defects. The most significant morphological feature is the common alignment among the hexagonally shaped islands, as indicated by green arrows in Figure 4(c). Based on the well-known orientation of the step edges as well as the epitaxial relationship

between EG and SiC, with their hexagonal lattices relatively rotated by  $30^\circ$  (e.g., EG[10 $\bar{1}$ 0] || SiC[11 $\bar{2}$ 0]), one can see that the edges of the h-BN islands follow EG[11 $\bar{2}$ 0], revealing the alignment between the two materials.

We also explored the growth of closed h-BN layers by attaining the coalescence of islands formed via SAvdWE. For this purpose, an increased deposition rate of B and a longer growth time was employed. Figure 5(a) shows an AFM image of a BLG area in EG, where a closed h-BN monolayer formed. The pattern was written with 20000 ions per IID with a 250 nm spacing. Interestingly, the cAFM image in Fig. 5(b) reveals that the grain boundaries between differently oriented h-BN monolayer domains exhibit lower tunneling currents, exactly where the morphology image [Fig. 5(a)] shows the presence of wrinkles. This result suggests that overlapping of h-BN monolayers takes place upon coalescence of neighboring domains, similar to observations in h-BN grown via chemical vapor deposition on metals. Note that using 10000 ions per IID should reduce grain boundary formation, as it allows to obtain h-BN islands with a common orientation [see Fig. 4(c)]. However, for the h-BN growth rates utilized in the present study, the lower nucleation yield at IIDs written with 10000 ions impeded complete coalescence. This aspect will be investigated in the future by employing suitable h-BN growth conditions. Regardless, no increased tunneling current could be detected at grain boundaries, which is a key aspect if such h-BN layers are to be employed as tunneling barriers. In comparison to standard growth, another advantage of SAvdWE is the potential of controlling grain boundary location by IID pattern design.

Despite their low occurrence,  $\approx 8$  nm high BN nanoparticles as well as additional h-BN monolayers also formed at the surface. Further refinement of the growth protocols for h-BN is anticipated to mitigate their formation. Nevertheless, for the specific

case of the additional h-BN monolayers, it is worth noticing that they preferentially grew in the vicinity of the IIDs. This suggests that the artificially created defects can also provide preferential nucleation points for the formation of additional h-BN layers on top of the first coalesced one. Thereby, also other 2D materials could be connected to the IIDs upon completion of the first 2D layer, allowing more complex 2D heterostructures to form via SAvdWE.

Figure 5(c) shows representative current-voltage (I-V) curves from different locations with varying numbers of h-BN layers, with the measurement configuration depicted in the inset to the upper left. The tunnel conductance shown in the inset (lower right) was extracted from the linear regime of the IV curves. The observed exponential decay with increasing layer number is expected for direct tunneling of electrons, similar to measurements performed in high-quality exfoliated h-BN flakes [L. Britnell *et al.*, *Nano Lett.* **12**, 1707 (2012)].

In conclusion, we have demonstrated a mask-less SAvdWE process which is based on the deterministic placement of defects in EG by He FIB, followed by MBE of h-BN. This approach allowed an unprecedented control over the formation of 2D heterostructures via bottom-up epitaxy. It opens up a new perspective for the scalable fabrication of not only h-BN/graphene heterostructures, but also other 2D heterostructure systems combining any layered material that can be synthesized via vdWE, such as 2D semiconductors like transition metal dichalcogenides.



01.02.23

DIERVMBR

KZ H-052-67 RT-012

MSYK udipnd -01

M60770 --044-81

MSYK udipnd

M60770

1.000000

# Anwendung der Elektronentomographie zur umfassenden Bestimmung von III-V-Grenzflächeneigenschaften

Wir präsentieren eine neue Analysemethode zur umfassenden Charakterisierung von vergrabenen III-V-Halbleitergrenzflächen auf der Basis der Elektronentomographie. Die Elektronentomographie nutzt eine Vielzahl von zweidimensionalen Aufnahmen der Probe aus verschiedenen Richtungen – eine sogenannte Kippserie – aus, um eine dreidimensionale Rekonstruktion des Schichtsystems zu erzeugen. Die Aufnahmen basieren auf dem Einsatz eines ringförmigen Dunkelfelddetektors im Rastertransmissionselektronenmikroskop, welcher ein chemisch sensitives Signal liefert. Der damit erhaltene Bildkontrast der einzelnen Projektionen erfüllt die notwendige Rekonstruktionsbedingung. Als Fallbeispiel ist das technologisch relevante (Al,Ga)As/GaAs-Mehrschichtsystem verwendet worden, das mit Hilfe der Molekularstrahlepitaxie hergestellt wurde. Dieses besteht aus einer Vielzahl von kohärenten Grenzflächen zwischen Schichten mit unterschiedlicher chemischer Zusammensetzung und ist daher für diese Art der Tomographieuntersuchung ideal geeignet.

Isokonzentrationsflächen, welche auf den Daten des Tomograms basieren und die Lagen der mittleren Konzentrationen der aneinandergrenzenden (Al,Ga)As-Schichten beschreiben, werden ausgenutzt, um topographische Höhenkarten von 120 nm x 120 nm Fläche zu erhalten, die die Grenzflächenmorphologie offenbaren. Die Höhenkarten erlauben die Bestimmung der quadratischen Rauheit der Grenzflächen und durch die Anwendung der Höhen-Höhen-Korrelationsfunktion sind wir in der Lage, wichtige Grenzflächeneigenschaften wie die laterale Korrelationslänge verschiedener Grenzflächen des (Al,Ga)As/GaAs-Systems quantitativ zu bestimmen. Außerdem wurden mit Hilfe von Höhendifferenzkarten, welche auf Isoflächen basieren, die 30% und 70% der gesamten Konzentrationsdifferenz an den Grenzflächen entsprechen, topographische Karten der Grenzflächenbreite erstellt, aus denen sich wiederum eine durchschnittliche Breite des chemischen Grenzflächenübergangs berechnen lässt.

Die Grenzflächentomographie quantifiziert Unterschiede in den Eigenschaften von direkter und invertierter Grenzfläche und ermöglicht die Beobachtung von Grenzflächenanisotropien. Die wesentliche Stärke der Methodik liegt darin, mit dem kompletten dreidimensionalen Datensatz alle chemisch-strukturellen Parameter vergrabener Grenzflächen mit einer Messung bestimmen zu können.

# Application of electron tomography for comprehensive determination of III-V interface properties

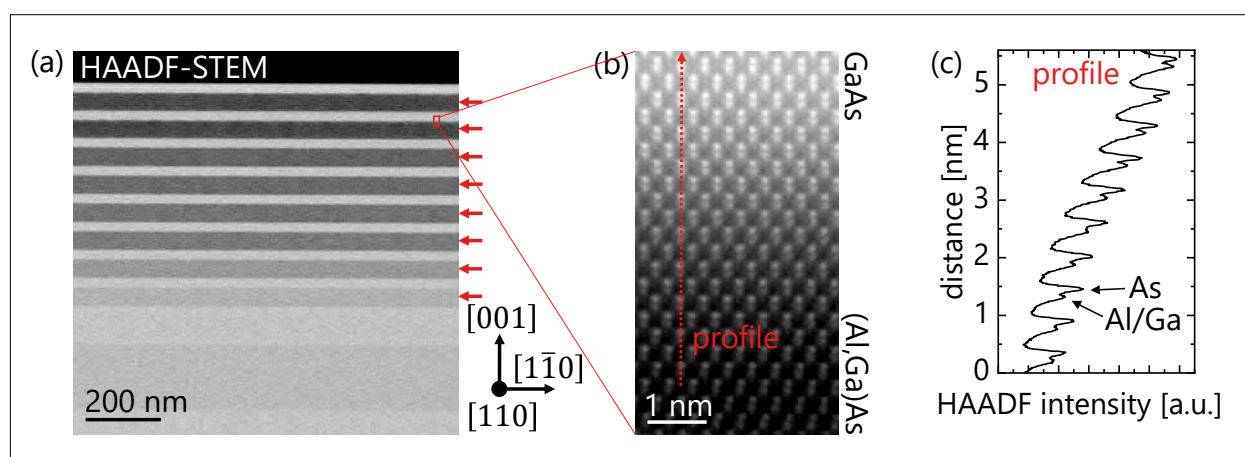
L. Nicolai, K. Biermann, A. Trampert

Most modern III-V heterostructure devices require a high level of control over the quality of their interface structures due to their large impact on many physical properties like, for example, the electron mobility in quantum wells or the tunneling behavior of sophisticated heterostructures like quantum cascade lasers. Therefore, a comprehensive interface characterization is necessary to allow the development of novel III-V compound semiconductor devices. In general, heterostructure interfaces are characterized by two fundamental properties: the physical roughness and the chemical intermixing. These properties are typically described by the root mean square (RMS) value of the interface roughness and the lateral and vertical correlation lengths as well as the chemical width of the interface. Unfortunately, experimental tools to measure these quantities in the case of buried

interfaces are fairly limited. X-ray scattering methods are able to deliver detailed information about surfaces and interfaces on large scales, and, complementary, spatially resolved methods like scanning probe microscopy are used to observe local variations providing, however, two-dimensional (2D) images. Conventional transmission electron microscopy (TEM) in combination with the site-specific focused ion-beam (FIB) sample preparation allows to investigate interfaces in cross-sectional samples down to the atomic level. TEM micrographs are projections of samples with a thickness of up to several nanometers that make it typically difficult to distinguish between the physical roughness and the chemical width without further information.

In this contribution, a novel method is proposed to obtain a comprehensive, quantita-

**Fig. 1.** HAADF STEM micrographs of multi-layered (Al,Ga)As sample. (a) Overview of the layered structure. The red arrows mark the (Al,Ga)As layers which are separated by a GaAs barrier. The Al-concentration is increasing from bottom to the top. (b) Fourier-filtered atomic-resolution HAADF image at the third interface from top. (c) Corresponding line profile indicating a broad transition between (Al,Ga)As and GaAs [position marked by arrow in (b)].



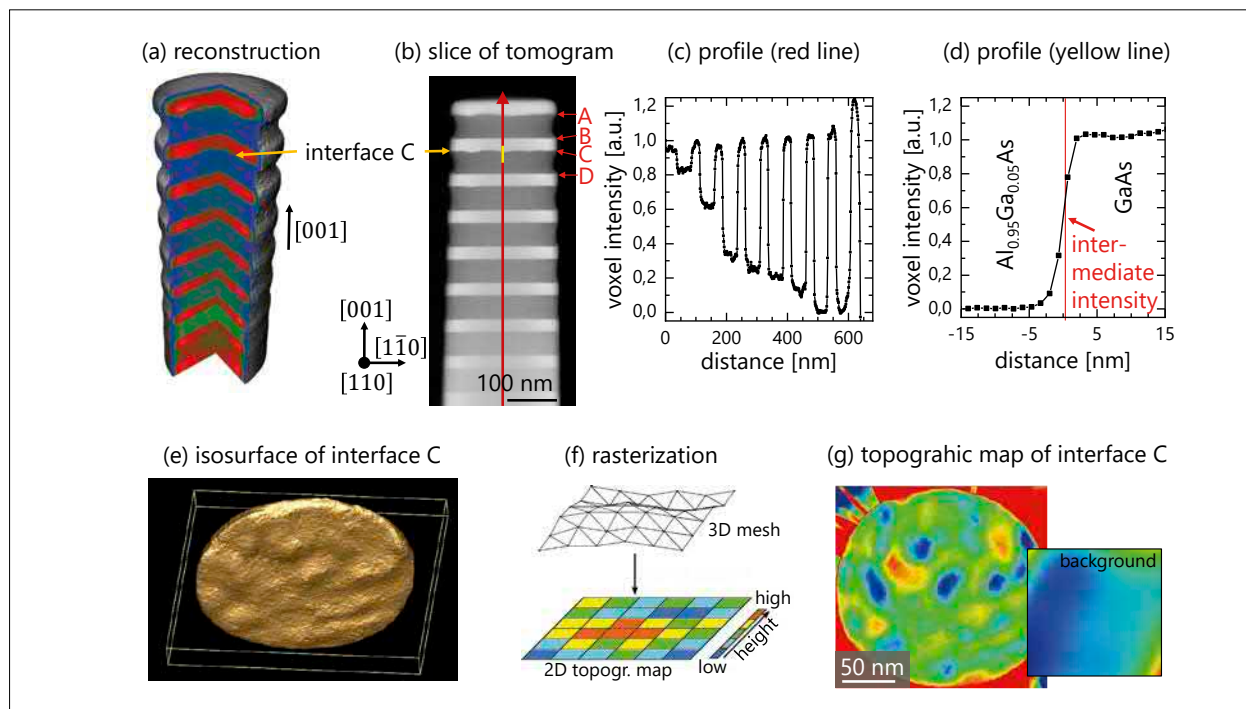


**Fig. 2.** Electron tomography of interfaces. (a) 3D representation of the reconstruction of the multi-layered (Al,Ga)As sample. (b) Single slice extracted from the tomogram. Higher intensities (brighter pixels) correspond to higher mean atomic number. (c) Intensity profile across all interfaces [position marked by red line in (b)]. (d) Intensity profile across interface C [position marked by yellow line in (b)]. (e) Isosurface of interface C at the intensity corresponding to the intermediate composition of GaAs and  $\text{Al}_{0.95}\text{Ga}_{0.05}\text{As}$ . (f) Scheme showing the transformation of an isosurface to a topographic map. (g) Final topographic map of interface C. A background was subtracted which is shown as inset.

tive three-dimensional (3D) analysis of III-V heterostructure interfaces. This method is based on electron tomography using the chemical sensitive high-angle annular dark-field (HAADF) imaging mode in scanning transmission electron microscopy (STEM).

The complete 3D interface characterization was performed on an (Al,Ga)As/GaAs multi-heterostructure. Figure 1(a) shows a HAADF STEM micrograph of a FIB lamella giving an overview of this sample. The structure is a multi-layered (Al,Ga)As sample with pure GaAs barriers (bright contrast) between each (Al,Ga)As layer (dark contrast). The composition  $x$  of the consecutive  $\text{Al}_x\text{Ga}_{1-x}\text{As}$  layers is 25%, 50%, 75%, 80%, 85%, 90%, 95% and 100%, respectively [layers marked by red arrows in

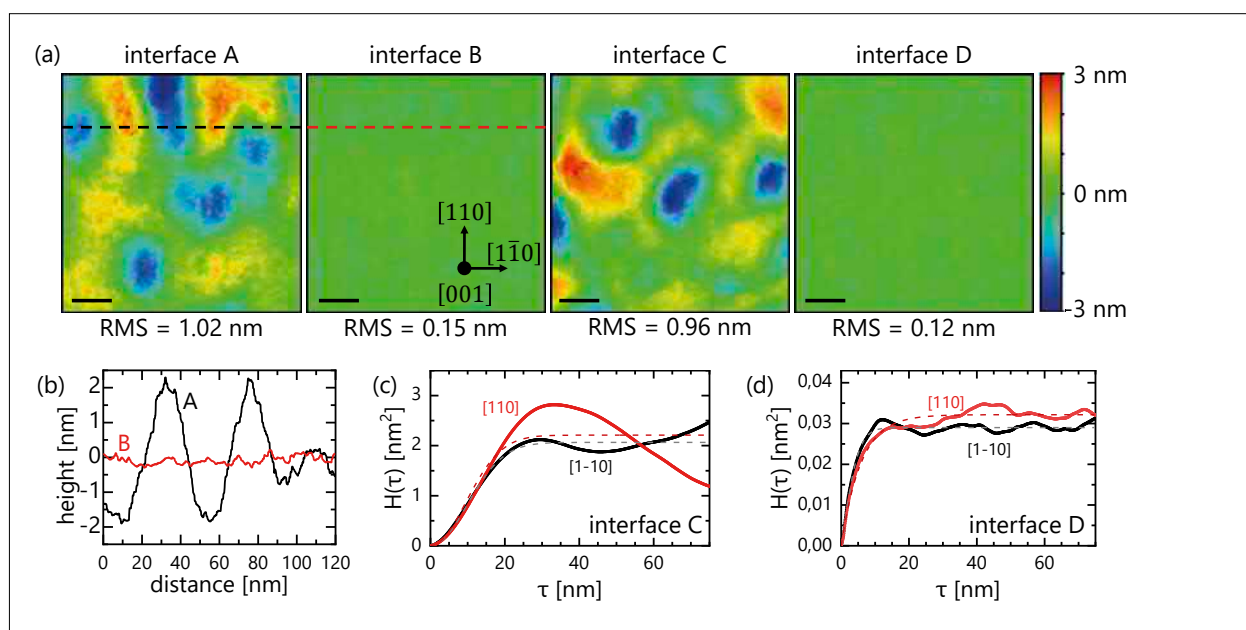
Fig. 1(a)]. An atomically resolved HAADF STEM micrograph of one interface is depicted in Fig. 1(b) identifying each column position of Ga, mixed Al/Ga and As atoms. The corresponding intensity profile is shown in Fig. 1(c) indicating a broad transition between (Al,Ga)As and GaAs, i.e. the intensity gradient extends over the entire length of the micrograph. Due to the signal averaging along the projection direction of conventional TEM micrographs it is not possible to make a robust statement about the origin of this broad transition.

For the following tomography measurement, a needle-shaped specimen was fabricated from a lamella using a specialized FIB preparation technique. A series of HAADF STEM images of the needle was recorded

with  $2^\circ$  tilt steps between each micrograph using an aberration-corrected JEOL ARM-200F microscope in combination with a double-tilt tomography holder. An iterative reconstruction algorithm was applied to obtain the 3D reconstruction of the tomography needle. Figure 2 summarizes the results of the tomography measurement including the procedure of creating topographic maps of buried interfaces. A 3D representation of the reconstructed tomogram is depicted in Fig. 2(a) revealing the complete multi-layered structure. The reconstructed voxel intensities are reflecting the local material density because the HAADF image intensity is primarily dependent on the thickness  $t$  and mean atomic number  $Z$  ( $I_{\text{HAADF}} = t \cdot Z^\alpha$ , with  $1 < \alpha < 2$ , so-called Z-contrast). Therefore, the thin slice cut out from the center of the 3D tomogram, cf. Fig. 2(b), emphasizes the internal structure visualizing the different material components. The voxel intensity profile in Fig. 2(c),

which is taken perpendicular to the interfaces (marked by red arrow), measures the changes in composition of the various (Al,-Ga)As layers following the nominal increase in Al-concentration. In Fig. 2(d), the voxel intensity profile of one interface labeled C is used to determine the intermediate intensity between the  $\text{Al}_{0.95}\text{Ga}_{0.05}\text{As}$  and the GaAs layer. This intermediate intensity was used to create an isosurface, i.e. a surface following the same voxel intensity, reflecting the central position of the interface. Due to the direct correspondence between voxel intensity and chemical composition, this isosurface can be seen as an iso-concentration surface, which qualitatively and quantitatively reveals the physical roughness of this interface. Figure 2(e) presents such an isosurface for interface C. To allow a quantitative analysis, the isosurface needs to be transformed into a topographic map. For this purpose, the 3D mesh of the isosurface is projected into a 2D array. Each

**Fig. 3.** Interface roughness characterization using electron tomography. (a) Topographic maps of interface A, B, C and D. Scale bar corresponds to 20 nm. (b) Height-profile of interface A and B extracted at the positions labeled as dashed line in (a). Height-height correlation functions along the  $[110]$  and  $[\bar{1}\bar{1}0]$  directions for (c) interface C and (d) interface D. The dashed lines are fits [cf. equation (3)] of the corresponding experimental data.



pixel of this array is thereby reproducing the average height of the mesh points above the pixel. In this way, a topographic map of the interface is generated. This procedure – called rasterization – is schematically illustrated in Fig. 2(f) and the final topographic map of interface C is exemplary given in Fig. 2(g). A background intensity, which is shown as inset, was subtracted to counteract tilts of the surfaces with regard to the projection plane avoiding systematic errors during the analysis.

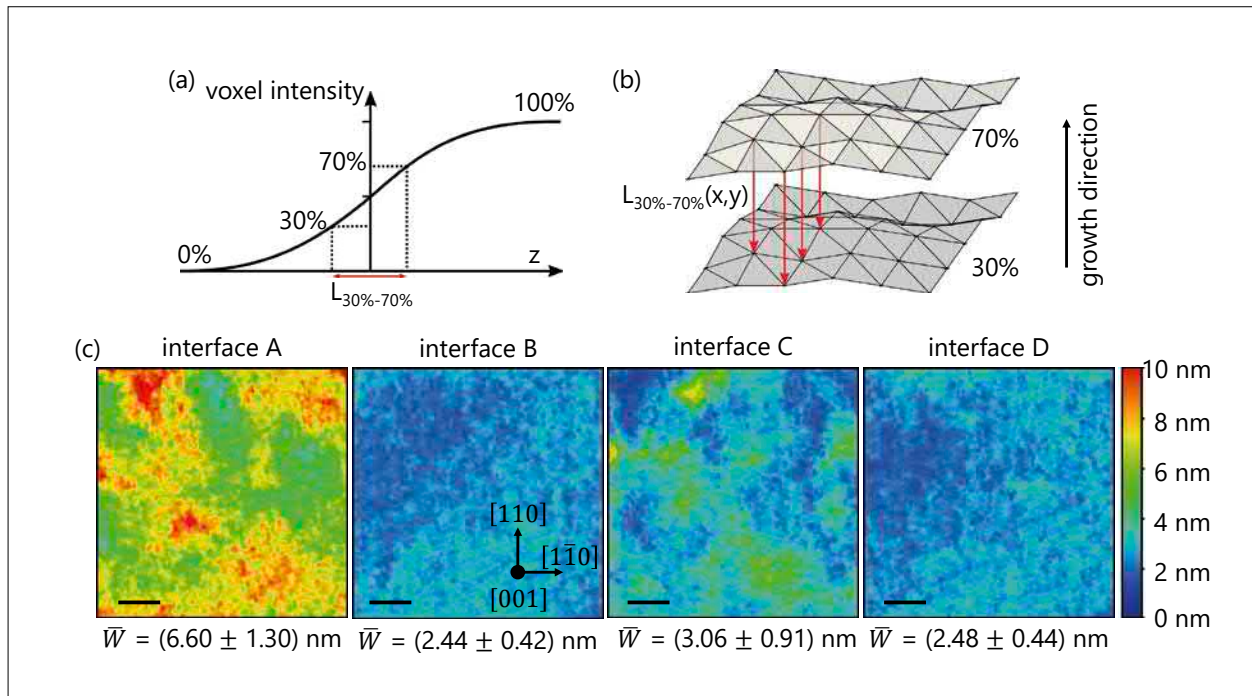
Figure 3(a) represents the results of the topographic mapping of the top four interfaces between AlAs and GaAs (labeled A, B) as well as between  $\text{Al}_{0.95}\text{Ga}_{0.05}\text{As}$  and GaAs [labeled C, D, see also Fig. 2(b)] visualizing the spatial distribution of the physical roughness. Strong differences in the magnitude of the physical roughnesses are visible between normal (Al,Ga)As-on-GaAs

and inverted GaAs-on-(Al,Ga)As interfaces, cf. line profile of interface A and B shown in Fig. 3(b). Smooth interface structures with height variations in the order of a few Ångstrom are detected for the normal interfaces, whereas the height variations of inverted interfaces are more than an order of magnitude higher. For more precise quantification of the roughness the RMS value  $\sigma_{\text{RMS}}$  is calculated as follows:

$$\sigma_{\text{RMS}} = \sqrt{\frac{1}{N} \sum_{n=1}^N (z_n - \bar{z})^2} \quad (1)$$

$N$  is the number of pixels,  $z_n$  the height value of the  $n$ -th pixel and  $\bar{z}$  the average height. RMS values have been determined for each interface over the whole (120 nm x 120 nm) area of the topographic maps with the result of 1.02 nm and 0.96 nm for the inverted and 0.15 nm and 0.12 nm for the normal interfaces, respectively. In agreement with the topographic maps, the RMS values are

**Fig. 4.** Interface width characterization using electron tomography. (a) Scheme of the sigmoidal shape of the concentration gradient at the interface. (b) Scheme explaining the interface width determination using isosurfaces. (c) Interface width maps of interface A, B, C and D. The average interface width  $\bar{W}$  and standard deviation of the width within each map was calculated. The scale bar corresponds to 20 nm.





significantly higher for the inverted compared to the normal interfaces. On the other hand, the RMS value is not sufficiently meaningful to describe the characteristic lateral length scale defining the average spacings between interfacial steps. The height-height correlation function (HHCF) is used to extract this characteristic length by evaluating the in-plane correlation length. The one-dimensional HHCF for discrete pixels is defined as:

$$H_x(\tau) = \frac{1}{N(M-m)} \sum_{l=1}^N \sum_{n=1}^{M-m} (z_{n+m} - z_n)^2 \quad (2)$$

where  $m = \frac{\tau}{\Delta x}$ ,  $\Delta x$  is the discrete sampling interval (pixel distance),  $M$  and  $N$  are the number of pixels in x-direction and the perpendicular direction, respectively. The HHCF can be phenomenologically described by:

$$H_x(\tau) = 2\sigma_x^2 \left[ 1 - \exp\left(-\left(\frac{\tau}{\Lambda_x}\right)^{2h_x}\right) \right] \quad (3)$$

where  $\sigma_x$  is the one-dimensional RMS value,  $\Lambda_x$  the correlation length and  $h_x$  the Hurst parameter. The HHCF function is plotted for the interfaces C and D along the two crystallographic directions  $[110]$  and  $[\bar{1}\bar{1}0]$  in Fig. 3(c) and (d), respectively. After fitting the curve according to equation (3), the fit parameters reveal a lateral correlation length of 14 nm for interface C along both, the  $[\bar{1}\bar{1}0]$  and  $[110]$  direction, and 3.6 nm and 5.8 nm for interface D along the  $[\bar{1}\bar{1}0]$  and  $[110]$  direction, respectively. The results show that the one-dimensional roughness values  $\sigma_x$  obtained by the HHCF fit agree with the previously determined RMS value  $\sigma_{\text{RMS}}$ . It can also be deduced from the results that measurements of the interface width by conventional TEM will give accurate values if the sample thickness is in the same range or smaller than the in-plane correlation length. In the case of the inverted interface B this would require a sample thickness below 14 nm.

In a final step, electron tomography was used to determine the chemical intermixing at each interface position in order to obtain a comprehensive picture of the 3D


structural interface property. As schematically shown in Fig. 4(a), any III-V interface has a gradient in composition and hence several iso-concentration surfaces at different voxel intensities can be created. Accordingly, the height difference of isosurfaces of the same interface corresponding to different concentration values are used to evaluate changes in the interface width. Here, isosurfaces corresponding to 30% and 70% of the total compositional difference were generated and then rasterized as shown schematically in Fig. 4(b). Subsequently, the topographic height maps of the 30%-isosurfaces were subtracted from the height maps of the 70%-isosurfaces. As a result, height-difference-maps are obtained which spatially measure the interface distance  $L_{30\%-70\%}$ . On the other hand, the interface width  $W$  is typically defined in the literature by the distance at which the concentration changes from 10% to 90% of the total difference. These specific isosurfaces were not created due to the larger influence of noise on isosurfaces corresponding to these compositions. Instead, a sigmoidal profile of the concentration change across the interface was assumed so that the width  $L_{30\%-70\%}$  can be extrapolated to the interface width  $W$  by using the factor 2.6. The spatially resolved interface width maps of interface A, B, C and D are depicted in Fig. 4(c) showing a random distribution of the spatial change of the interface width. The maps reveal higher average interface widths  $\bar{W}$  for the inverted interfaces A and C (i.e. 6.60 nm and 3.06 nm) compared to the normal interfaces (i.e. 2.44 nm and 2.48 nm). The magnitude of the variations measured by the standard deviation of the width within the full area of the maps is significantly larger for the inverted (1.3 nm and 0.91 nm) compared to the normal interfaces (0.42 nm and 0.44 nm). These results also emphasize very clearly the strength of the electron tomography interface characterization in comparison to conventional TEM, in particular for interfaces with large variations in the physical and/or chemical width.

In summary, it was demonstrated that a comprehensive determination of interface properties can be achieved by using electron tomography. For this purpose, a method was developed to extract topographic height maps and interface width maps out of the reconstruction of a III-V heterostructure specimen. This method allows the quantitative 3D characterization of interfaces. The strength of this method is that all important interface characteristics can be extracted at once. In addition, the analysis is site-specific due to the FIB prepara-

tion technique and therefore allows the investigation on specific regions of a sample. Anisotropic features can be revealed due to the spatially resolved maps and the difficulties caused by the signal averaging in conventional TEM can be circumvented.

This work was partially supported by the European Union and the State of Berlin within the frame of the European Regional Development Fund (ERDF) project "Applikationslabor Elektronentomographie", project number 2016011843.



12  AI



# Nicht-reziproke Propagation von akustischen Oberflächenwellen entlang epitaktischer $\text{Fe}_3\text{Si}/\text{GaAs}$ -Hybridstrukturen

In den letzten Jahren hat das Interesse an der Realisierung nicht reziproker Systeme zur effizienten Manipulation von Schall zugenommen. Von besonderer Bedeutung für Anwendungen sind akustische Geräte, die auf Oberflächenwellen (surface acoustic waves, SAWs) basieren. SAWs sind elastische Schwingungen, die auf die Oberfläche eines Festkörpers beschränkt sind und seismischen Wellen ähneln, die während eines Erdbebens erzeugt werden. Aufgrund ihrer effizienten piezoelektrischen Erzeugung und Detektion sowie ihrer geringen Ausbreitungsgeschwindigkeiten werden SAWs erfolgreich als On-Chip-Signalverarbeitungsgeräte wie Hochfrequenzfilter eingesetzt. Darüber hinaus liegen die Wellenlängen von hochfrequenten SAWs (einige GHz) in der Größenordnung eines Mikrometers, wodurch die dynamische Dehnung und das piezoelektrische Feld von SAWs ideal für die Manipulation von Elementaranregungen in Festkörpern geeignet sind. Daher wäre die Steuerung der SAW-Ausbreitungsrichtung durch nicht reziproke Bauelemente ein wichtiger Schritt in Richtung einer effizienten Verbindung von Festkörperquantensystemen unter Verwendung von SAWs.

Ein möglicher Weg, eine nicht reziproke SAW-Transmission zu erhalten, besteht darin, das Dehnungsfeld der SAW an Spinwellen in einem Ferromagneten durch die magnetoelastische Wechselwirkung zu koppeln. Da die Magnetisierungspräzession der Spinwelle eine genau definierte Helizität aufweist, hängt die Energieübertragung vom akustischen zum magnetischen System von der Helizität des effektiven Magnetfelds ab, das durch die Längs- und Scherdehnungen der SAW induziert wird. Dies hängt wiederum von der relativen Phasenverzögerung zwischen beiden Dehnungskomponenten ab, die das Vorzeichen ändert, wenn die SAW-Ausbreitungsrichtung umgekehrt wird.

In diesem Beitrag zeigen wir die nicht-reziproke Propagation von hochfrequenten SAWs (3,45 GHz) entlang einer Hybridstruktur, die aus einem  $\text{Fe}_3\text{Si}$ -Dünnsfilm besteht, der epitaktisch auf einem GaAs-Substrat gewachsen ist.  $\text{Fe}_3\text{Si}$  ist ein binäres Heusler-ähnliches ferromagnetisches Metall, das als möglichen Baustein in spintronischen Geräten angesehen wird. Da seine Kristallstruktur fast gitterangepasst an das GaAs-Substrat ist, ist es möglich, epitaktische  $\text{Fe}_3\text{Si}$ -Filme mit hoher Grenzflächenperfektion und Strukturqualität zu züchten, was zu niedrigen magnetischen Dämpfungskoeffizienten führt. In unserem Experiment zeigen wir, dass die magnetoelastische Wechselwirkung für bestimmte Magnetisierungsrichtungen im  $\text{Fe}_3\text{Si}$ -Film Energie vom akustischen zum magnetischen System überträgt, so dass SAW-Dämpfung induziert wird. Die Stärke der Dämpfung hängt vom relativen Winkel zwischen Magnetisierung und SAW-Wellenvektor ab und kann über die Größe und Ausrichtung eines externen Magnetfelds oder durch Umkehren der SAW-Ausbreitungsrichtung gesteuert werden. Die resultierende Nicht-Reziprozität der SAW-Transmission, definiert als die Differenz zwischen der übertragenen Schallleistung für die SAW-Ausbreitung vorwärts und rückwärts, erreicht unter magnetoelastischer Resonanz Werte von bis zu 20%. Diese Werte sind unseres Wissens die größte Nicht-Reziprozität, die für SAWs gemeldet wurde, die sich in einem halbleitenden Substrat ausbreiten, das von einem epitaktischen ferromagnetischen Film bedeckt ist.

Die experimentellen Ergebnisse werden durch ein theoretisches Modell für die zeitliche Reaktion der Magnetisierung im  $\text{Fe}_3\text{Si}$ -Film unter der SAW gut unterstützt. Die Simulationen zeigen auch, dass die geringe magnetische Dämpfung des  $\text{Fe}_3\text{Si}$ -Films entscheidend ist, um große nicht reziproke Effekte zu erzeugen. Aufgrund der Kombination aus großer Magnetostriktion, geringer magnetischer Dämpfung und der Möglichkeit des Wachstums von Mehrschichten sind epitaktische  $\text{Fe}_3\text{Si}/\text{GaAs}$ -Hybride vielversprechende Systeme für die Realisierung nicht reziproker akustischer Bauelemente in Halbleiter-Heterostrukturen auf GaAs-Basis.

# Non-reciprocal transmission of surface acoustic waves along epitaxial Fe<sub>3</sub>Si/GaAs hybrid structures

A. Hernández-Mínguez, F. Macià<sup>1</sup>, J. M. Hernández<sup>1</sup>, J. Herfort, P. V. Santos

In the last years, there has been an increasing interest in the realization of non-reciprocal acoustic systems for the efficient manipulation of sound. Of special importance for applications are acoustic devices based on surface acoustic waves (SAWs). SAWs are elastic vibrations confined to the surface of a solid that resemble seismic waves created during an earthquake. Because of their low propagation velocities, the dynamic strain and piezoelectric fields produced by high-frequency SAWs are on the order of a micrometer, thus making SAWs ideally suited for the manipulation of elementary excitations in solids. Therefore, the on-demand control of the SAW propagation direction by means of non-reciprocal devices would represent an important step toward the efficient interfacing of solid-state quantum systems using SAWs.

As acoustic propagation is reciprocal in linear systems preserving time reversibility, one possible way of obtaining non-reciprocal SAW transmission is to break time-inversion symmetry. This can be achieved by for example coupling the strain field of the SAW to the magnetization dynamics of a ferromagnet through the magneto-elastic (ME) interaction. Here, we demonstrate the non-reciprocal transmission of high-frequency SAWs traveling along a hybrid structure consisting of an Fe<sub>3</sub>Si thin film grown epitaxially on a GaAs substrate. Fe<sub>3</sub>Si is a binary Heusler-like ferromagnetic metal, which has attracted interest as a possible component in spintronic devices. As its cubic crystal structure is almost lattice-matched to GaAs, it is possible to grow epitaxial Fe<sub>3</sub>Si films with high interfacial

perfection and structural quality as well as very low magnetic damping coefficients (i.e., as low as  $\alpha \approx 3 \times 10^{-4}$ ). Moreover, the estimated ME coefficients for Fe<sub>3</sub>Si are of the same order of magnitude as other crystalline ferromagnetic metals such as Fe and Ni, thus making Fe<sub>3</sub>Si a promising material for ME applications. Finally, the high Curie temperature (above 800 K) of Fe<sub>3</sub>Si makes this material suitable for room temperature devices.

We fabricated the magneto-acoustic device sketched in Fig. 1(a) as follows. First, a clean  $c(4 \times 4)$ -reconstructed GaAs surface was prepared by growing a 500-nm-thick GaAs buffer layer in a dedicated chamber for the growth of III-V semiconductors by molecular beam epitaxy (MBE). The substrate was then transferred in ultra-high vacuum into an As-free chamber, where the Fe<sub>3</sub>Si film with a thickness  $d=50$  nm was grown by co-deposition of Si and Fe from high-temperature effusion cells onto the GaAs substrate, which was held at 200 °C. Next, we etched the Fe<sub>3</sub>Si film into octagonal mesas with a distance  $L=1.2$  mm between opposite sides. In the final fabrication step, we patterned pairs of interdigital transducers (IDTs) by e-beam lithography, metal evaporation, and lift-off at the opposite sides of the Fe<sub>3</sub>Si mesas for the generation and detection of SAWs. The finger periodicity of the IDTs determines the SAW wavelength, which was set to  $\lambda_{\text{SAW}}=800$  nm.

The ME experiments were performed at room temperature by placing the magneto-acoustic device between the poles of an electromagnet for the application of a

<sup>1</sup> Dept. of Condensed Matter Physics, University of Barcelona, Barcelona, Spain

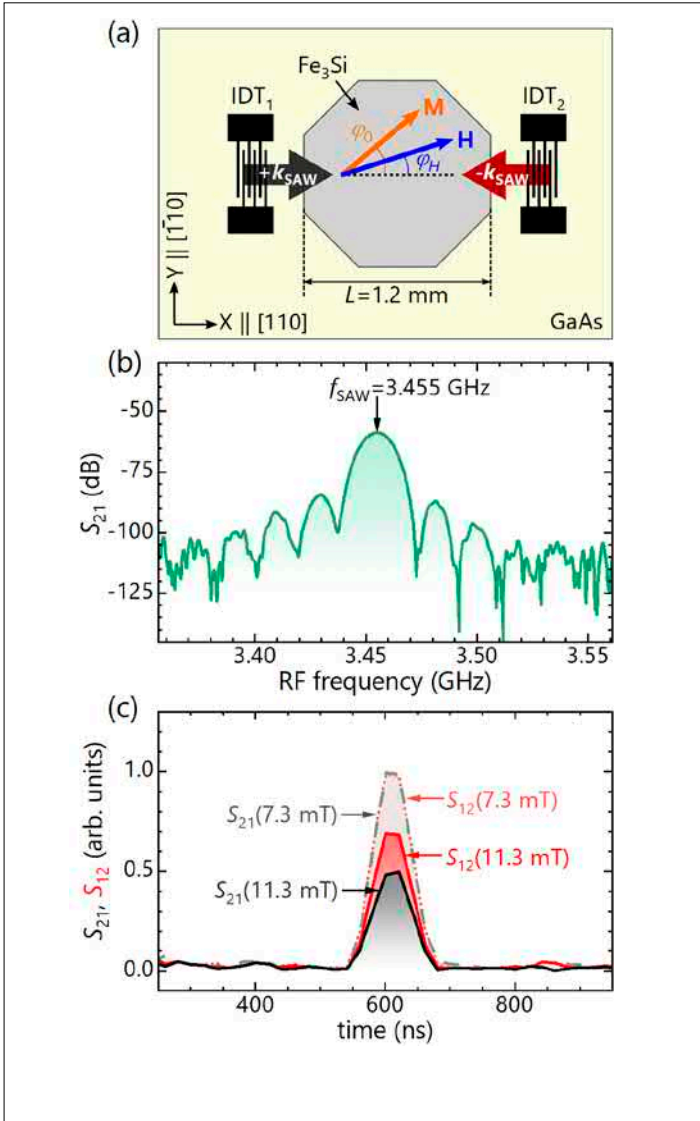


**Fig. 1.** (a) Schematic illustration of the magneto-acoustic device. (b) Frequency spectrum of the power transmission coefficient  $S_{21}$ . (c) Time-resolved coefficients  $S_{21}$  and  $S_{12}$  measured for  $\varphi_H = -0.6^\circ$  at two different magnetic field strengths, normalized to the magnitude of the  $S_{21}$  transmission peak for  $\mu_0 H = 7.3$  mT.

static in-plane magnetic field  $\mathbf{H}$ . The sample was mounted on an electrically controlled rotation stage that settles the angle  $\varphi_H$  between  $\mathbf{H}$  and the SAW propagation direction. The angle  $\varphi_0$  defines the equilibrium direction of the magnetization  $\mathbf{M}$ . Radio-frequency (RF) signals applied to the IDTs excite SAWs propagating with wave

vector  $k_{SAW} = 2\pi/\lambda_{SAW}$  parallel (+ $k_{SAW}$ ) or anti-parallel ( $-k_{SAW}$ ) to the [110] direction of the Fe<sub>3</sub>Si/GaAs hybrid structure, see Fig. 1(a). As the SAW is a Rayleigh mode, the strain tensor consists of three non-zero  $\epsilon_{xx}$ ,  $\epsilon_{zz}$  and  $\epsilon_{xz}$  components when expressed with respect to a rotated reference frame with the  $x$ ,  $y$ , and  $z$  axes pointing along the [110],  $[\bar{1}10]$ , and [001] directions, respectively.

The magneto-acoustic interaction was studied by measuring, for each values of  $\varphi_H$  and  $H$ , the amplitude of the forward ( $S_{21}$ , corresponding to + $k_{SAW}$ ) and the backward ( $S_{12}$ , corresponding to  $-k_{SAW}$ ) power transmission coefficients between the two IDTs using a vector network analyzer. Figure 1(b) displays the dependence of  $S_{21}$  on the RF frequency applied to IDT<sub>1</sub>. The transmission spectrum shows a maximum at the resonant frequency  $f_{SAW} = v_{SAW}/\lambda_{SAW} = 3.455$  GHz, where  $v_{SAW}$  is the SAW propagation velocity. Then, we Fourier transformed the results of the frequency-dependent measurements into the time domain to eliminate the electro-magnetic cross-talk and analyze the amplitude of the SAW-related transmission peak. Figure 1(c) compares the time-resolved  $S_{21}$  and  $S_{12}$  coefficients for two magnetic field strengths applied at an angle  $\varphi_H = -0.6^\circ$ . The peak at the time delay  $\Delta t \approx 610$  ns is attributed to the arrival of the SAW after traveling from the exciting to the detecting IDT. For  $\mu_0 H = 7.3$  mT, the intensities of the  $S_{21}$  (dashed line) and  $S_{12}$  (dotted line) transmission peaks are exactly the same, thus confirming the reciprocal behavior of the SAW delay line. When the magnetic field increases to  $\mu_0 H = 11.3$  mT, the acoustic and magnetic systems enter into resonance. Under these conditions, the ME coupling converts acoustic waves propagating along the Fe<sub>3</sub>Si/GaAs hybrid structure into spin waves in the Fe<sub>3</sub>Si film, thus leading to a decrease of both  $S_{21}$  and  $S_{12}$  transmission peaks. Most important, the SAW transmission under ME resonance is clearly different for SAWs propagating with wave vec-

tors  $+k_{\text{SAW}}$  and  $-k_{\text{SAW}}$ . For  $S_{21}$  (black line), the ME coupling reduces the transmitted SAW power to 50% of the corresponding out-of-resonance value, while for  $S_{12}$  (red line) the transmission of the SAW peak is still 70% of the out-of-resonance one.

To get further insight into the non-reciprocal behavior, we display in Fig. 2 the dependence of the SAW attenuation,  $A = 1 - T$ , on the magnetic field strength, measured at four angles  $\varphi_H$ . Here,  $T$  represents the area of the SAW transmission peak in the time domain spectrum normalized to the corresponding area for  $H$  away from the ME resonance. Each trace shows two ME resonances at two field values. For the resonance at low magnetic fields,  $\mathbf{M}$  is still rotating towards  $\mathbf{H}$ , while  $\mathbf{M}$  and  $\mathbf{H}$  are fully aligned for the resonance at high magnetic fields. The difference between the magnetic fields of the two ME resonances reaches a maximum for  $\varphi_H \approx 0$ . As  $\varphi_H$  rotates away from  $[110]$ , the two ME resonances move towards each other, until they merge at  $|\varphi_H| \approx 4^\circ$ . For larger values of  $\varphi_H$ , the spin wave frequency lies above the SAW frequency for all applied magnetic fields, and no ME resonance can be excited. For all four  $\varphi_H$  values in Fig. 2,  $A(+k_{\text{SAW}})$  (squares) is clearly different from  $A(-k_{\text{SAW}})$  (circles) at the ME resonance. Moreover, for  $\varphi_H < 0$ ,  $A(+k_{\text{SAW}}) > A(-k_{\text{SAW}})$ , while for  $\varphi_H > 0$  the situation reverses and  $A(+k_{\text{SAW}}) < A(-k_{\text{SAW}})$ .

The two-dimensional color plots of Figs. 3(a) and 3(b) summarize the dependence of the SAW attenuation ( $A$ ) on the strength  $H$  and angular direction  $\varphi_H$  of the magnetic field. For both  $+k_{\text{SAW}}$  and  $-k_{\text{SAW}}$  configurations, the resonant ME interaction (and, consequently, SAW attenuation) takes place only on a  $\varphi_H \times H$  lobe defined by a very narrow range of angles  $\varphi_H$  around  $0^\circ$ . For the quasi-parallel configuration, the magnitude of the attenuation is strongly angular dependent with clearly different values on the upper and lower side of the  $\varphi_H \times H$  lobe, see Fig. 3(a). In contrast, in the quasi-antiparallel case, the angular depen-

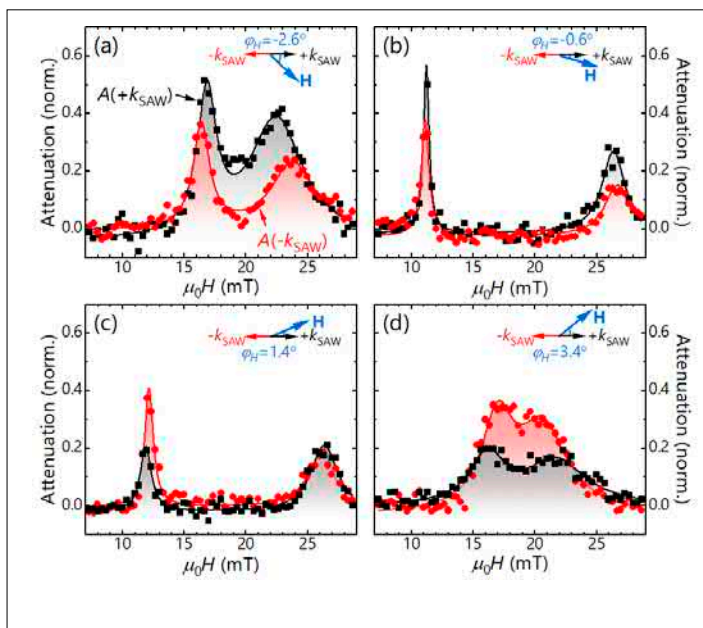


**Fig. 2.** Dependence of the ME-induced SAW attenuation,  $A$ , on the magnetic field strength,  $H$ , for SAWs with  $+k_{\text{SAW}}$  (squares) and  $-k_{\text{SAW}}$  (circles). The panels show measurements taken for magnetic field angles: (a)  $\varphi_H = -2.6^\circ$ , (b)  $\varphi_H = -0.6^\circ$ , (c)  $\varphi_H = 1.4^\circ$ , and (d)  $\varphi_H = 3.4^\circ$ . The lines are Lorentzian fits to the ME resonances.

dence is less pronounced, see Fig. 3(b). As will be discussed below, this weaker dependence arises from a small deviation of the SAW wave vector from the  $[110]$  axis.

Figure 3(c) shows the non-reciprocal attenuation efficiency,  $\Delta A = A(+k_{\text{SAW}}) - A(-k_{\text{SAW}})$ , determined from the difference between the data in panels Figs. 3(a) and 3(b).  $\Delta A$  has different signs on the upper and lower sides of the  $\varphi_H \times H$  lobe, where it reaches values as large as  $\pm 20\%$ . By taking into account the length  $L$  of the  $\text{Fe}_3\text{Si}$  film, we estimate a non-reciprocal attenuation rate,  $\eta \approx \Delta A/L \approx 16\%/\text{mm}$ . For comparison, we have also estimated  $\eta$  from the attenuation reported for SAWs of 2.24 GHz frequency propagating along hybrid structures consisting of a polycrystalline Ni film on a  $\text{LiNbO}_3$  substrate [M. Weiler *et al.*, Phys. Rev. Lett. **106**, 117601 (2011); R. Sasaki *et al.*, Phys. Rev. B **95**, 020407(R) (2017)]. In that case, the

values obtained are  $\eta \approx (1.6 \pm 0.9)\%/mm$ . That is one order of magnitude lower than the ones obtained in the  $Fe_3Si/GaAs$  structures reported here. We attribute this difference to the fact that the high structural quality of the epitaxial  $Fe_3Si$  film leads to a magnetization response with lower magnetic damping than for polycrystalline Ni (typically  $\alpha \approx 0.05$ ) and therefore to narrow ME resonances with strong non-reciprocal effects.

The experimental results were analyzed using a theoretical model for the temporal response of the magnetization of the  $Fe_3Si$  film under the SAW strain field. For small

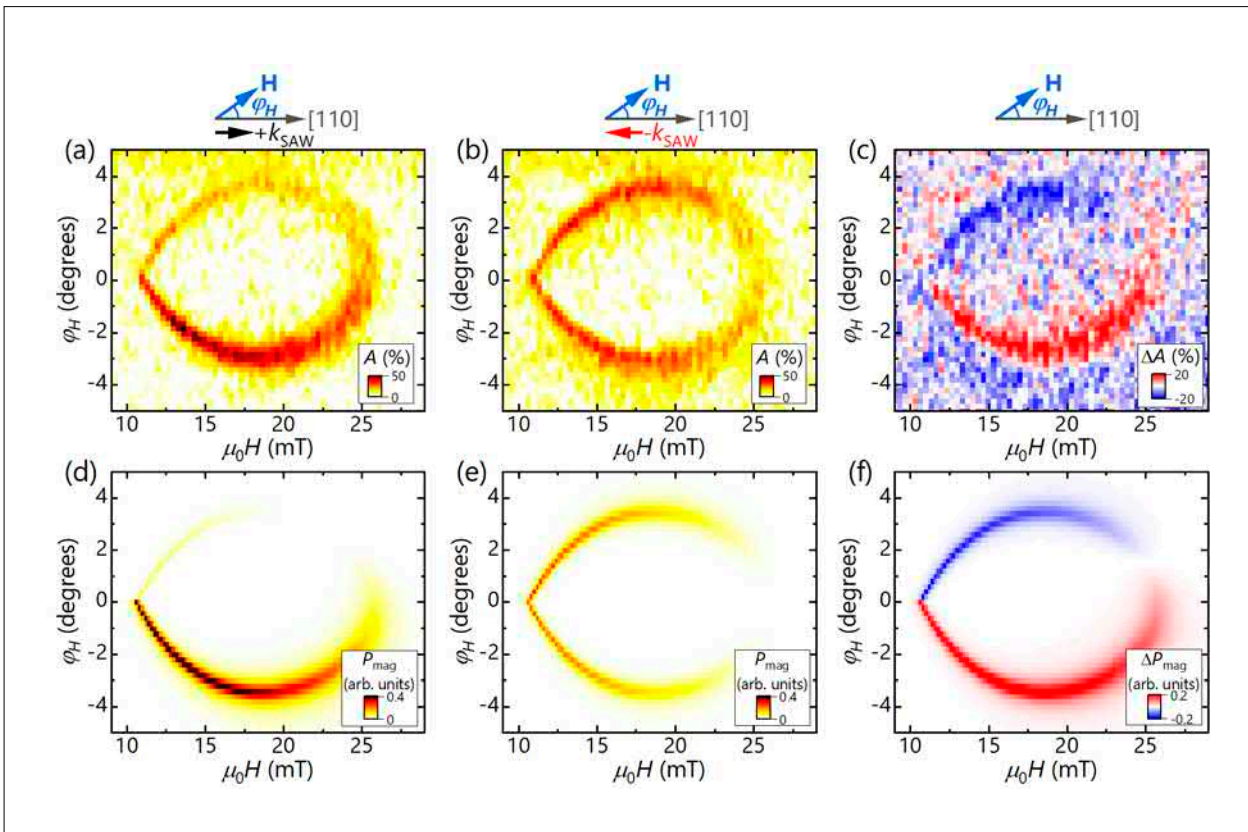
angular deviations of  $\mathbf{M}$  with respect to its equilibrium direction, the effective ME field driving the magnetization precession consists of an in-plane ( $h_\varphi$ ) and out-of-plane component ( $h_\theta$ ) perpendicular to  $\mathbf{M}$  given by:

$$\mu_0 h_\varphi = 2b_2 \sin(\varphi_0) \cos(\varphi_0) \varepsilon_{xx}, \quad (1)$$

$$\mu_0 h_\theta = 2b_2 \cos(\varphi_0) \varepsilon_{xz}, \quad (2)$$

where  $\mu_0$  is the vacuum permeability and  $b_2$  represents the shear ME coefficient of the  $Fe_3Si$  film. Both components depend on the in-plane equilibrium direction of  $\mathbf{M}$  through  $\varphi_0$ . However, the in-plane component  $h_\varphi$  is proportional to the longitudinal strain of

**Fig. 3.** ME-induced attenuation maps as a function of magnetic field strength,  $H$ , and angle,  $\varphi_H$ , for SAWs propagating with wave vectors (a)  $+k_{SAW}$  and (b)  $-k_{SAW}$ . (c) SAW attenuation difference,  $\Delta A$ , calculated from the data in (a) and (b). (d) Simulation of the magnetic power dissipated by the  $Fe_3Si$  film,  $P_{mag}$ , as a function of  $H$  and  $\varphi_H$  for SAW with wave vector  $+k_{SAW}$ . (e) Same as (d), but for SAW with wave vector  $-k_{SAW}$ . (f) Difference  $\Delta P_{mag}$  between (d) and (e).





the SAW,  $\varepsilon_{xx}$ , while the out-of-plane component  $h_\theta$  is proportional to the shear strain,  $\varepsilon_{xz}$ . As  $\varepsilon_{xz}$  vanishes at a free surface,  $h_\theta$  is usually very small for thin ferromagnetic films and/or large SAW wavelengths and can normally be neglected. For thicker films and/or shorter SAW wavelengths, however,  $\varepsilon_{xz}$  becomes relevant, and the contribution of  $h_\theta$  to the magnetization dynamics must be taken into account.

The observed non-reciprocal SAW attenuation can be understood as an interplay between the  $h_\varphi$  and  $h_\theta$  components. Due to the  $\pi/2$  time phase shift between  $\varepsilon_{xx}$  and  $\varepsilon_{xz}$ , the ME driving field  $\mathbf{h} = h_\varphi \hat{\varphi} + h_\theta \hat{\theta}$  is, in general, elliptically polarized. As the magnetization precession described by the Landau-Lifshitz-Gilbert (LLG) equation has a well-defined helicity, the strength of the ME coupling will depend on the helicity of  $\mathbf{h}$ . For example, for an SAW propagating with  $+k_{\text{SAW}}$ ,  $\varepsilon_{xx} \propto \cos(\omega t)$  and  $\varepsilon_{xz} \propto \sin(\omega t)$ . In the absence of an external magnetic field,  $\mathbf{M}$  points along one of the  $\langle 100 \rangle$  easy axes (i.e.,  $\varphi_0 = \pm 45^\circ$ ) of the  $\text{Fe}_3\text{Si}$  film. If  $\mathbf{H}$  rotates the magnetization towards  $0 < \varphi_0 < 45^\circ$ , then  $\mathbf{h}$  and  $\mathbf{M}$  will precess with opposite helicities under ME resonance, and the coupling of the SAW to the magnetization dynamics will be weak, as on the upper side of the  $\varphi_H \times H$  lobe in Fig. 3(a). If, in contrast,  $\mathbf{H}$  orients  $\mathbf{M}$  towards  $-45^\circ < \varphi_0 < 0$ , the sign of  $h_\varphi$  will reverse, and now both  $\mathbf{h}$  and  $\mathbf{M}$  will precess with the same helicity. Under these conditions, the ME coupling will be strong, thus inducing a larger SAW attenuation [lower side of the  $\varphi_H \times H$  lobe in Fig. 3(a)]. When  $\mathbf{H}$  reverses and the magnetization points against the SAW wave vector,  $h_\theta$  changes sign and inverts the helicity dependence of  $\mathbf{h}$  on  $\varphi_0$ . The same happens if the magnetization stays along  $[110]$ , but the SAW propagates with  $-k_{\text{SAW}}$ , causing  $\varepsilon_{xz} \propto \sin(\omega t)$  to be replaced by  $\varepsilon_{xz} \propto -\sin(\omega t)$ .

According to the previous discussion, the SAW attenuation profiles for quasi-parallel and quasi-antiparallel configurations of  $\mathbf{H}$  and SAW wave vector in Figs. 3(a) and

3(b) should be mirror images of each other. However, as already mentioned above, this is not exactly the case for the experimental data. We attribute this discrepancy to a small, unintentional misalignment angle  $\beta$  between the SAW wave vector and the  $[110]$  direction, probably caused during the patterning of the sample. This misalignment makes  $h_\varphi$  and  $h_\theta$  dependent on  $\beta$  and on the longitudinal ME coefficient,  $b_1$ , and also modifies their simple dependence on  $\varphi_0$  expressed by Eqs. (1) and (2). As a consequence, the non-reciprocity with respect to  $\varphi_0$  is enhanced in the quasi-parallel configuration, but partially compensated in the quasi-antiparallel configuration. To confirm this assumption, we have calculated the dependence of the attenuated SAW power on  $H$  and  $\varphi_H$  by taking into account that, according to energy conservation, the attenuated SAW power must equal the magnetic power,  $P_{\text{mag}}$ , dissipated by the spin waves in the  $\text{Fe}_3\text{Si}$  film. The latter can be determined using the following expression:

$$P_{\text{mag}} \propto -\text{Im} \left[ \mu_0 \int_V (\mathbf{h}^* \bar{\chi} \mathbf{h}) dV \right] \quad (3)$$

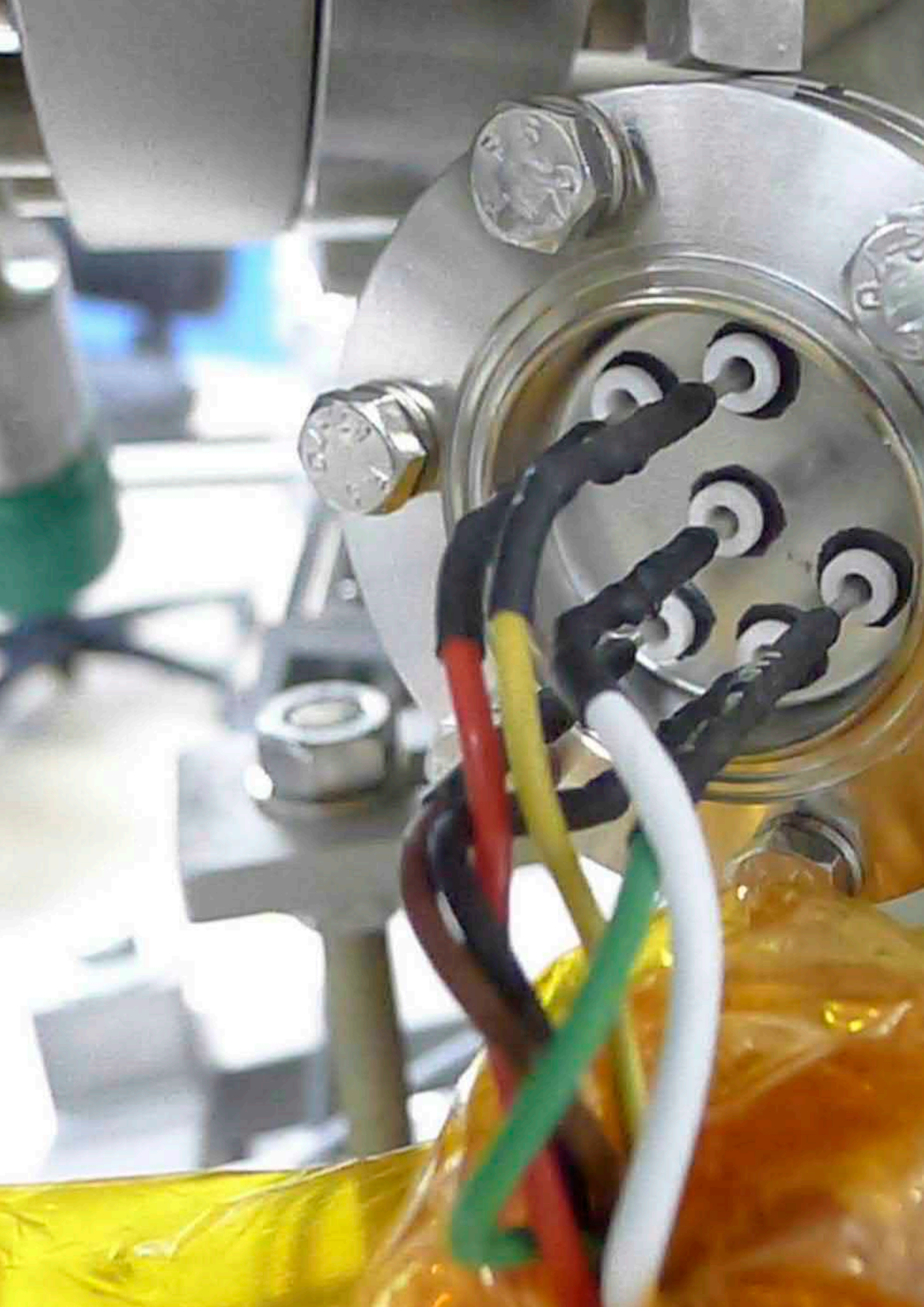
where  $V$  is the volume of the ferromagnetic film traversed by the SAW and  $\bar{\chi}$  is the Polder susceptibility tensor describing the response of the magnetization to  $\mathbf{h}$ . To obtain  $\bar{\chi}$ , we have solved the linearized LLG equation supposing harmonic solutions for  $\varepsilon_{xx}$ ,  $\varepsilon_{xz}$ , and the angular deviations of the magnetization. In the simulation, we have used the values for the gyromagnetic ratio and magnetic anisotropy coefficients of the  $\text{Fe}_3\text{Si}$  film obtained from ferromagnetic resonance experiments, and we have set  $b_1 = 6$  T,  $b_2 = 2$  T,  $\varepsilon_{xx} = 10^{-4}$ ,  $\varepsilon_{xz} = 0.5 \times 10^{-4}$ , and  $\beta = 1^\circ$ . The width of the ME resonance depends on the damping coefficient, which was set to  $\alpha = 8 \times 10^{-3}$ . Figures 3(d) and 3(e) display  $P_{\text{mag}}$  for  $\mathbf{H}$  and SAW wave vector in the quasi-parallel and quasi-antiparallel configurations, respectively, while the difference  $\Delta P_{\text{mag}}$  between both configurations is shown in Fig. 3(f). The theoretical model reflects qualitatively well the position of the ME resonances, their amplitude depen-

dence on  $H$  and  $\varphi_H$ , and the non-reciprocal behavior.

In conclusion, we have demonstrated the non-reciprocal propagation of SAWs along a GaAs substrate covered with an epitaxial  $\text{Fe}_3\text{Si}$  film. The strength of the SAW attenuation depends on the relative orientations of the magnetization and SAW wave vector and leads to attenuation differences of up to 20% for SAWs propagating along opposite directions. We attribute the non-reciprocal behavior to the dependence of the

magnetization dynamics on the helicity of the elliptically polarized ME field associated with the SAW. Our simulations confirm these results and show that non-zero longitudinal and shear strain at the ferromagnetic film, together with low magnetic damping, are critical to achieve large non-reciprocal effects. The large magnetostriction and low magnetic damping makes epitaxial  $\text{Fe}_3\text{Si}/\text{GaAs}$  hybrid structures promising for the realization of non-reciprocal acoustic devices in GaAs-based semiconductor heterostructures.







# Core Research Areas Forschungsschwerpunkte

Nanofabrication Nanofabrikation .....	39
Nanoanalytics Nanoanalytik .....	44
Control of Elementary Excitations by Acoustic Fields Die Kontrolle von elektrischen Anregungen in Halbleiter-Nanostrukturen .....	50
III-V Nanowires for Optoelectronics III-V-Nanodrähte und deren Anwendung in der Optoelektronik .....	54
Intersubband Emitters: GaAs-based Quantum-Cascade Lasers Intersubbandemitter: GaAs-basierte Quantenkaskadenlaser .....	58



# Nanofabrication / Nanofabrikation

Dr. Lutz Geelhaar

Dr. Klaus Biermann – Group-III arsenides

Dr. Oliver Bierwagen – Oxides

Dr. Stefano Cecchi – GeTe-Sb<sub>2</sub>Te<sub>3</sub> phase-change materials

Dr. Jens Herfort – Ferromagnet semiconductor hybrid structures

Dr. Joao Marcelo J. Lopes – Two-dimensional materials

The subject of this core research area is the fabrication of novel types of crystalline thin films and nanostructures and the investigation of fundamental growth mechanisms. The perspective of such samples is to enable the investigation of exciting physical phenomena or to offer new tailored functionalities that may inspire innovative devices. In general, we fabricate our samples in the bottom-up approach, i.e. in a process of adding material by growth in contrast to removing material by etching. Thus, for the desirable high level of control over fabrication it is mandatory to understand the underlying growth mechanisms. Moreover, these mechanisms are often highly fascinating by themselves. The standard technique for the fabrication of samples at PDI is molecular beam epitaxy (MBE). Hence, our samples are usually grown as epitaxial thin films on crystalline substrates, and different materials may be stacked on top of each other to form heterostructures of considerable complexity. In addition, we also grow on substrates whose surface has been pre-patterned by lithography to induce lateral variations in growth, and self-organization phenomena can be employed for the deliberate formation of three-dimensional structures like quantum wires instead of two-dimensional planar films. The samples that we aim to fabricate are novel in at least one of the following aspects:

- A material of this chemical composition has not been synthesized before, or at least not in this crystalline quality and/or chemical purity.
- Different materials are monolithically integrated to form an unprecedented hybrid structure.

Das Thema dieses Forschungsschwerpunktes ist die Herstellung neuartiger kristalliner dünner Schichten und Nanostrukturen und die Untersuchung fundamentaler Wachstumsmechanismen. Solche Proben dienen dazu, spannende physikalische Phänomene zu untersuchen oder aber neue, maßgeschneiderte Funktionalitäten zu ermöglichen, die innovative Anwendungen inspirieren können. Generell werden die Proben in einem sogenannten ‚bottom-up‘-Ansatz (englisch für ‚von unten nach oben‘) hergestellt. Dies bedeutet, dass während des Herstellungsprozesses Material durch Wachstum hinzugefügt wird – im Unterschied zu Verfahren, bei denen aus einer größeren Probe Material durch Ätzprozesse abgetragen wird. Daher ist es für das angestrebte hohe Maß an Kontrolle bei der Probenherstellung unabdingbar, die zugrundeliegenden Wachstumsmechanismen genau zu verstehen – ganz abgesehen davon, dass diese Mechanismen per se faszinierend sind.

Die Standardmethode, die wir am PDI für die Probenherstellung verwenden, ist die Molekularstrahlepitaxie (englisch molecular beam epitaxy, MBE). Infolgedessen werden unsere Proben gewöhnlich als epitaktische dünne Schichten auf kristallinen Substraten gezüchtet. Hierbei können unterschiedliche Materialien als Schichtsystem übereinander gewachsen werden und bilden dann Heterostrukturen von hoher Komplexität. Darüber hinaus wird auf Substraten gewachsen, deren Oberflächen mittels lithographischer Techniken vorstrukturiert sind. Somit können laterale Änderungen im Wachstum induziert werden. Außerdem werden Phänomene der Selbstorganisation ausgenutzt, um die Ausbildung dreidi-

- A known material or combination of materials is structured on the nanoscale in a new way, i.e. the sample is shaped in at least one dimension to a new type of geometry, or a heterostructure of exceptional complexity or precision is created.

Typical examples are extending the range of compositions over which films can be grown in high quality, the use of novel substrates, and the heteroepitaxy of dissimilar materials.

In general, all growth mechanisms are governed by the interplay between thermodynamics and kinetics. At the nanoscale, the role of surface and interface effects is often crucial. In heterostructures, differences between the crystal lattices induce strain which affects crystal growth and is often accommodated by the formation of defects. Hence, the elucidation of growth mechanisms is inextricably linked to the investigation of surface structure, interface formation, and in general the microstructure of the sample. Therefore, the close collaboration with the core research area *Nanoanalytics* is indispensable for the understanding of growth mechanisms and the successful fabrication of nanostructures. Where needed, experiments are complemented by theoretical calculations.

Our research is based on the longstanding expertise of PDI in the MBE of III-As and III-N compound semiconductors, but more and more we study the growth of other materials. In the following, the material systems that are currently under investigation will be presented.

The epitaxial growth of *group-III-arsenide* heterostructures serves as the backbone of various internal and external research projects, due to the unique structural quality of the (Al,Ga)As material system and its very abrupt interfaces even in complex heterostructures. In general, advancements in growth enable the fabrication of tailored structures in particular in the core research

mensionaler Strukturen – wie zum Beispiel Quantendrähten – anstelle von planaren Schichten zu ermöglichen.

Die Proben, deren Herstellung wir anstreben, sind unter mindestens einem der folgenden Gesichtspunkte neuartig:

- Ein Material dieser chemischen Zusammensetzung wurde zuvor noch nicht synthetisiert – zumindest nicht in dieser kristallinen Qualität oder chemischen Reinheit.
- Unterschiedliche Materialien werden monolithisch integriert, um eine bislang nicht existierende Hybrid-Struktur zu erzeugen.
- Ein bekanntes Material oder eine Materialkombination wird auf der Nanoskala auf neuartige Weise strukturiert – d.h. die Probe wird entlang zumindest einer Raumrichtung zu einer neuartigen Geometrie geformt, oder eine Heterostruktur von außergewöhnlicher Komplexität oder Präzision wird erschaffen.

Typische Beispiele sind die Verwendung neuartiger Substrate, die Erweiterung des Zusammensetzungsbereichs, in dem Schichten in hoher Qualität gezüchtet werden können, und die Heteroepitaxie von sich stark unterscheidenden Materialien.



areas *Intersubband Emitters: GaAs-based Quantum-Cascade Lasers* and *Control of Elementary Excitations by Acoustic Fields*. In this respect, an important goal for us is to enhance the resolution for the lateral shallow patterning and subsequent overgrowth leading to structured microcavities. Specifically, the trapping of single polaritons in such structures requires a lateral trap dimension size on the order of  $(0.5 \mu\text{m})^2$  which is below the resolution limit of conventional photolithography of about  $(1.0 \mu\text{m})^2$ . A promising way to realize such small-scale lateral structures inside a microcavity is by maskless milling using focused Ga ion beams. This technique offers a resolution of down to  $0.01 \mu\text{m}$  and avoids any wet-chemical treatment. The latter can impede the necessary overgrowth after patterning due to contamination or enhanced surface roughness. This year, we have started a collaboration with K. Höflich (Helmholtz Zentrum für Materialien und Energie, Berlin) to develop this idea towards the realization of arrays of single polariton traps.

One particularity of *group-III nitrides* is that the common growth direction is polar, and that this polarity has profound implications for the properties of heterostructures. In this context, we carry out studies to compare Ga- and N-polar (In,Ga)N/GaN and GaN/(Al,Ga)N quantum wells. Furthermore, we fabricate custom heterostructures for the investigation of fundamental material properties. As an extension of the set of alloys typically considered as group-III nitrides, we have started growth efforts on hexagonal BN (h-BN). This research builds up on the growth of h-BN with a thickness of few monolayers in the framework of our activity on two-dimensional (2D) materials. Beyond that class of materials, h-BN is an interesting semiconductor with many unusual properties that has recently attracted increasing attention.

The fabrication of ferromagnet semiconductor hybrid structures in high crystal perfection is a prerequisite for the investiga-

tion of spin transport phenomena relevant for spintronic device concepts. Our focus is on the growth of half-metallic Heusler alloys on GaAs-related structures. As a new research direction, in a close collaboration with the core research area Control of Elementary Excitations by Acoustic Fields the non-reciprocal transmission of surface acoustic waves along epitaxial  $\text{Fe}_3\text{Si}/\text{GaAs}$  hybrid structures has been studied. In addition, the preparation of fully crystalline thin film stacks consisting of a semiconducting channel sandwiched between two ferromagnetic layers constitutes a prerequisite for a new vertical device type. In order to overcome the challenges associated with the growth of a semiconductor on a metal, we have continued to develop solid-phase epitaxy as an approach where an amorphous film of Ge is deposited on  $\text{Fe}_3\text{Si}$  and then crystallized slowly by thermal annealing. Previous comprehensive structural analysis of  $\text{Fe}_3\text{Si} / \text{Ge}(\text{Fe},\text{Si}) / \text{Fe}_3\text{Si}$  thin-film stacks grown this way showed that the  $\text{Ge}(\text{Fe},\text{Si})$  films crystallize in the well-oriented, layered tetragonal structure  $\text{FeGe}_2$ , which does not exist as a bulk material and is a promising candidate for studies of 2D magnetism. In a close collaboration with the core research area Nanoanalytics, the antiferromagnetism in such  $\text{FeGe}_2$  interlayers and its influence on the magnetic interlayer coupling in vertical spin valve structures has been continued to be explored. Furthermore, in order to characterize this new material individually, eliminating the underlying  $\text{Fe}_3\text{Si}$  film is essential. Through a detailed optimization of the solid phase epitaxy process we have been able to synthesize single-crystalline, layered  $\text{FeGe}_2$  films with higher structural and interface perfection on  $\text{GaAs}(001)$  substrates. Superconducting quantum interference device measurements have revealed low-temperature ferromagnetism in such a film. Additionally, in a close collaboration with the core research area Nanoanalytics the disorder-order transition in epitaxially stabilized  $\text{FeGe}_2$  has been studied by in-situ transmission electron microscopy. Hence,  $\text{FeGe}_2$  pro-

vides an interesting framework to study the interplay between chemical bonding and magnetism, and could open new ways for applications involving ferromagnetic layered materials.

Transparent (*semi*)conducting oxides are widely used in devices. For example, n-type  $\text{In}_2\text{O}_3$ ,  $\text{Ga}_2\text{O}_3$ ,  $\text{SnO}_2$ , and  $\text{NiO}$  traditionally serve as active material in conductometric gas sensors and—highly doped— as transparent contact layers in solar cells, displays, and LEDs. The requirements on material quality for these traditional applications are low, and usually met by polycrystalline, sputtered material. During the last decade, however, transparent semiconducting oxides have been re-discovered as true wide-band-gap semiconductors by virtue of their synthesis to semiconductor standards (single crystalline, highly pure with well-defined doping). This development enables the investigation of the underlying physics of these materials and their applications. It further opens up the possibility for novel and improved conventional oxide-semiconductor-based devices by rational design. For example, based on its large band gap of  $E_g=4.5$  eV, single crystalline  $\text{Ga}_2\text{O}_3$  is a promising material for next generation power electronics as well as solar-blind ultra violet sensors. Combined with  $\text{In}_2\text{O}_3$  ( $E_g=2.7$  eV) and  $\text{Al}_2\text{O}_3$  ( $E_g=8.8$  eV), band gap engineering and heterostructures with large band offsets are foreseeable. Compared to traditional compound semiconductors, semiconducting oxides are at an early stage of development with many open fundamental questions. Our efforts to answer these questions are embedded in the Leibniz ScienceCampus GraFOx, lead by PDI. The main contribution of our core research area in this context is the growth of semiconducting oxides by MBE, a proven tool to synthesize high-quality semiconductor thin films, and to investigate their properties.

$\text{Ga}_2\text{O}_3$  cannot be doped p-type, which precludes the implementation of p-type functionalities based on this material, in partic-

ular technologically important *pn*-junctions which are building blocks for many types of devices. To make up for this shortcoming, we have prepared a *pn*-junction by combining the naturally p-type semiconducting oxide  $\text{SnO}$  with  $\text{Ga}_2\text{O}_3$ . The resulting *pn*-heterodiodes revealed a diode-like current-voltage characteristics with high rectification and low ideality factor, indicating a high-quality *pn*-junction. The related *pn*-junction isolation bears the potential for decoupling the p-type functionality in lateral transport devices made of  $\text{SnO}$  from that of the underlying n-type  $\text{Ga}_2\text{O}_3$  substrate, and the *pn* junctions may further contribute to field management required to reach higher voltage capabilities in  $\text{Ga}_2\text{O}_3$  devices.

*Phase change materials* (PCM) are unique compounds employed in non-volatile random access memory thanks to the rapid and reversible transformation between the amorphous and crystalline states that display large differences in electrical and optical properties. Our unique approach in this field is the use of MBE for the fabrication of epitaxial PCM, which makes possible advanced studies on the properties of these materials. The epitaxial growth of GeSbTe alloys is quite demanding as an interplay between composition, phase and ordering occurs. Control over those three parameters is mandatory to obtain material with well defined physical properties. In the framework of the EU project BeforeHand we are actively involved in the development of high temperature and long data retention PCMs complying with the requirements of automotive applications. In this context, epitaxial Ge-rich GeSbTe alloys and heterostructures are currently under investigation. In addition, we have established the epitaxial growth of the metastable phase of GaTe on Si(111) and more recently graphene. GaTe belongs to the class of monochalcogenides that have emerged as a new class of layered materials beyond graphene and transition metal dichalcogenides. Finally, we are currently exploring the epitaxy of 2D tellurium on Si(111).

Graphene, h-BN, and other 2D materials are promising building blocks for several applications, and are thus anticipated to play a major role in future technologies. In addition, combining them to so-called van der Waals (vdW) heterostructures enables new properties and functionalities which are not observed in the single materials. For technological implementation, it is mandatory to synthesize them with high thickness precision and structural quality in a scalable manner. For this purpose, we have investigated MBE large-area synthesis of graphene and h-BN. Beyond epitaxy of graphene on different substrates, we have achieved MBE of atomically thin h-BN films on Ni templates. The high structural quality of our MBE-grown h-BN (similar to that of state-of-the-art h-BN flakes) has for instance permitted to successfully employ this material as a vdW substrate for the 2D semiconductors MoS<sub>2</sub> and MoSe<sub>2</sub>. Moreover, we have conducted research on the epitaxial growth of graphene/h-BN vdW heterostructures. Our studies have allowed us to identify unconventional phenomena such as defect-mediated vdW growth of h-BN on graphene. The latter has served as the basis for the recent development of a novel approach to realize selective-area vdW epitaxy of 2D heterostructures, which is based on defect engineering in 2D materials via focused ion beam irradiation.

Parallel to MBE, we operate a furnace in which Si is desorbed from SiC to induce epitaxial graphene formation. This is an established method which enables us to fabricate continuous or nanostructured graphene (single layer to multi-layer thick). The high crystalline quality, inertness, and atomic flatness of epitaxial graphene make it an ideal substrate for the development of growth protocols for vdW epitaxy.

# Nanoanalytics / Nanoanalytik

Dr. Achim Trampert

Dr. Stefan Fölsch – Scanning tunneling microscopy and spectroscopy

Dr. Michael Hanke – Synchrotron studies

Dr. Achim Trampert – Transmission electron microscopy and spectroscopy

The ongoing miniaturization in semiconductor technology calls for precise information on the structural and compositional quality of low-dimensional systems and nanoscale devices. Accordingly, the central aim is to clarify the fundamental structure-property relation in semiconductor materials. Our work program is based on the development and application of sophisticated experimental and modeling tools for materials analysis with highest sensitivity and resolution down to the single-atom level.

Research within this CReA addresses the following key aspects:

- Interfaces in epitaxial heterostructures
- Order-disorder phenomena and phase transitions
- Microstructure of metastable and nanoscale systems
- Manipulation and spectroscopy of materials at the single-atom scale.

At our PHARAO beamline at the Berlin synchrotron BESSYII, Helmholtz-Zentrum für Materialien und Energie, Berlin, synchrotron x-ray diffraction (XRD) is performed for the in-situ investigation of epitaxial layers during growth. Advanced transmission electron microscopy (TEM) and scanning (S)TEM techniques including diffraction, imaging and spectroscopy as well as scanning tunneling microscopy (STM) and spectroscopy are applied to quantitatively analyze the structural, chemical and electronic properties of the material systems with highest spatial resolution. Experimental results are compared with computer simulations and supported by theoretical modeling. Aside from the analytical aspect, the CReA uses operational tools to deliberately modify material structure by the

Die stetige Miniaturisierung in der Halbleitertechnologie erfordert präzise Information über die strukturelle Qualität und die chemische Zusammensetzung niedrigdimensionaler Halbleitersysteme und Nanomaterialien. Das zentrale Ziel der CReA ist daher die Klärung der Struktur-Eigenschaftsbeziehung in Halbleitermaterialien. Unser Arbeitsprogramm basiert auf der Entwicklung und Anwendung anspruchsvoller experimenteller Werkzeuge und Modellierungsverfahren für die Materialanalyse mit höchster Empfindlichkeit und Auflösung bis hinunter auf die Einzel-Atom-Ebene.

Nanoanalytik behandelt folgende Themen:

- Grenzflächen in epitaktischen Heterostrukturen
- Ordnungs-Unordnungsphänomene und Phasenübergänge
- Mikrostruktur von metastabilen und nanoskaligen Systemen
- Manipulation und Spektroskopie von Materialien auf der Skala von Einzelatomen

An unserer PHARAO-Beamline am Berliner Synchrotron BESSYII, Helmholtz-Zentrum für Materialien und Energie, Berlin, wird Synchrotron-Röntgendiffraktometrie (XRD) zur in-situ-Untersuchung von Epitaxieschichten während des Wachstums durchgeführt. Moderne Transmissionselektronenmikroskopie (TEM) und Raster (S)TEM-Techniken, einschließlich Beugung, Bildgebung und Spektroskopie, sowie Rastertunnelmikroskopie (STM) und -spektroskopie (STS) werden eingesetzt, um die strukturellen, chemischen und elektronischen Eigenschaften der Materialsysteme mit höchster räumlicher Auflösung zu ana-

focused ion beam (FIB) technique on the length scale between micron to nanometer and by STM on the scale of single atoms.

A central goal in preparing modern artificial heterostructures and nanomaterials is the control of *interfaces* and the understanding of their building principles. Interfaces have a crucial effect on both, physical properties and device performance, in particular as structure sizes become smaller. Epitaxial hetero-interfaces are generally classified as coherent or semi-coherent, depending on the epitaxial strain state. We are studying the character of epitaxial strain and strain relieving mechanisms as well as the atomic configuration and translation state of coherent interfaces between dissimilar materials.

For some time, we have continuously improved our understanding of interfaces in axial and radial III-V nanowires, two-dimensional (2D) layered materials, and, especially, in planar III-V heterostructures and quantum wells. Extensive and systematic structural investigations of interfaces in III-V compounds have demonstrated that these interfaces inherently have a finite width with respect to their chemical composition. Only recently, we have methodologically extended this strategy of interface investigation to complex, non-common-atom, heterovalent interfaces such as in II-VI/III-V heterosystems, which pose extreme challenges for structure determination. In cooperation with Arizona State University, USA, the CdTe/InSb interface has been analyzed as case study. Our methodology based on TEM 002 dark-field imaging provides quantitative compositional profiles for all atom types on all relevant length scales. The results offer a new strategy to analyze such heterovalent interfaces with non-common atoms.

Interfaces in semiconductor heterostructures are almost never atomically abrupt and perfectly flat and consequently have a certain degree of three-dimensional (3D)

lyisieren. Experimentelle Ergebnisse werden mit Computersimulationen verglichen und durch theoretische Modellierung unterstützt. Über den analytischen Aspekt hinaus nutzt die CReA Werkzeuge zur gezielten Modifikation der Materialstruktur, und zwar durch die fokussierte Ionenstrahltechnik auf der Längenskala zwischen Mikro- und Nanometer, sowie durch STM auf der Skala einzelner Atome.

extension. Therefore, the interpretation of 2D (S)TEM projections of those interfaces can be very challenging. Most recently, we have demonstrated that electron tomography allows an accurate and quantitative determination of the 3D structural and chemical roughness of buried interfaces in III-V multilayer samples. For the tomography experiment, well-defined needle-shaped specimens have to be fabricated by FIB techniques allowing full 180° rotation for tilt series acquisition of 2D STEM images. The tomographic reconstruction data yield isoconcentration surfaces which describe the locations of the average concentrations of the adjacent III-V layers. They are exploited to obtain topographic height maps revealing the interface morphology. By applying the height-height correlation function, we are able to quantitatively determine important interfacial properties such as the root mean square (RMS) roughness and the lateral correlation length of various interfaces of the technologically significant (Al,Ga)As/GaAs system. In addition, height difference maps that correspond to 30% and 70% of the total concentration difference along the interfaces were used to generate topographic maps of the chemical interface width, which in turn can be used to calculate an average width of the interface transition. Electron tomography thus proves to be a valuable tool for the comprehensive structural description of buried interfaces.

Apart from these interface studies, we strengthened our research on weakly coupled large-area van der Waals heterostructure films, a work that has been performed at our PHARAO end station at Berlin synchrotron BESSYII (HZB). During previous experiments we have successfully demonstrated that synchrotron-based scattering on heterostructures made of light elements as graphene, hexagonal boron nitride as well as molybdenum disulfide provides a sufficiently intense scattering signal to observe the in-plane orientation of the various sublayers and to quantita-

tively determine a potential in-plane strain therein. Grazing incidence diffraction has been applied which effectively suppresses the scattering from the substrate and thus makes this method highly surface sensitive. In 2020 we moved on to heterosystems formed of the layered ferromagnet  $\text{Fe}_{5-x}\text{GeTe}_2$  (FGT) and graphene grown on SiC substrates. In order to understand magnetic properties a detailed knowledge on layer morphology, individual orientation, elastic strain, and vertical inheritance through the heterostructure becomes essential. In an initial experiment we found that the starting graphene layer appears very well aligned but 30° off the symmetry given by the underlying SiC(0001) substrate with a full width at half maximum (FWHM) of only 0.3°, while the orientation of the FGT layer coincides with that of the substrate, however with a less pronounced sticking reflected by a FWHM of about 7.8°. This observation demonstrates that to some extent a vertical inheritance of the in-plane symmetry takes place even across interfaces between weakly-coupled heterostructures.

The physical properties of ferromagnetic Heusler alloys or semiconducting oxide layers depend on their *structural order* and *phase stability*. The stability limitations and phase transformation processes are studied in dependence on internal parameters like chemical composition and strain state as well as external parameters given by temperature and growth kinetics. The degree of order/disorder and their spatial distribution in thin films are determined quantitatively by X-ray diffraction and electron microscopy – in-situ and ex-situ.

We have continued our work on solid phase epitaxy of amorphous Ge on  $\text{Fe}_3\text{Si}$  films on GaAs(001) substrates. Based on X-ray and TEM data, it was conclusively shown that an ordered metastable phase of  $\text{FeGe}_2$  is formed at the end of the solid phase epitaxy process. In-situ TEM has been introduced to directly observe the amorphous-crystalline solid phase transition with high spatial res-

olution and in real time. In the early stage of crystallization nucleation started at the interface to the  $\text{Fe}_3\text{Si}$ . From there growth proceeded in a layer-by-layer mode forming a film of disordered  $\text{FeGe}_2$  with a crystal structure similar to the CsCl lattice but with a high amount of vacancies in the Fe sublattice. This crystallization process is shown to be limited by the diffusion of Fe towards the growth front. After the formation of 2-3 nm a second phase transition happened to the ordered  $\text{FeGe}_2$ , which is accompanied with the rearrangement of Fe atoms and vacancies on their shared sublattice into the tetragonal layered structure. This disorder-order transition, which could only be determined on the basis of our in-situ TEM study, is explained by an epitaxial strain minimization process.

In the last years, nanofocus synchrotron radiation has developed into a powerful technique for characterizing *local strain and chemical composition* as well as morphological properties of individual low-dimensional objects. As a direct result of a steadily improved x-ray optics, beam foci as small as 50 nm or below with high photon flux ( $10^{10}$  photons/sec) at hard X-ray energies (10–30 keV) are nowadays available at third-generation synchrotron facilities like PETRA III at DESY in Hamburg or the European Synchrotron Radiation Facility (ESRF) in Grenoble.

Due to the pandemic in 2020 many experiments at international large-scale facilities had to be canceled or performed as remote experiment. Our proposal on locally resolved strain fields caused by surface acoustic waves has been granted at the ESRF and could be performed in a remote way. As a major outcome we could demonstrate for the first time a standing wave of surface phonons with 250 nm period. Applying the so-called k-map-technique, we were able to record five-dimensional data sets containing the three-dimensionally resolved diffusely scattered intensity in reciprocal space taken on a 2D grid in real space with an x-ray spot of 50 nm diameter. This

set of data contains the full information of the elastic strain along all three directions. The local strain  $\Delta a/a$  is in the order of  $10^{-4}$ . The combination of locally resolved access to phonon-induced elastic strain might pave the way to more complex functional structures involving phonons.

The functionality of metastable semiconductor alloys and nanoscale materials is controlled by their *microstructure*, i.e., the structural perfection and chemical homogeneity on the atomic to mesoscopic scale. Materials are analyzed with respect to their structural, chemical, and mechanical properties on various length scales with the final goal of determining the structure-property relation. The research in this area is accordingly driven by a further methodology development in line with current material issues.

The complete 3D microstructure information is essential for the quality improvement of monolithically integrated optoelectronic components. In this light, we have successfully applied electron tomography in conjunction with sophisticated FIB-based sample preparation to gain insight into the 3D defect arrangement and defect interaction process. Highly lattice-mismatched epitaxial III-(Sb,As) layers were grown on Si(001) substrates. This material system is exemplary for the challenges of monolithically integrating III-V compound semiconductors with Si. We have continued our study on electron tomography of threading dislocation arrangements, and the reconstruction of the displacement field around individual dislocations for getting access to a complete analysis of their 3D properties.

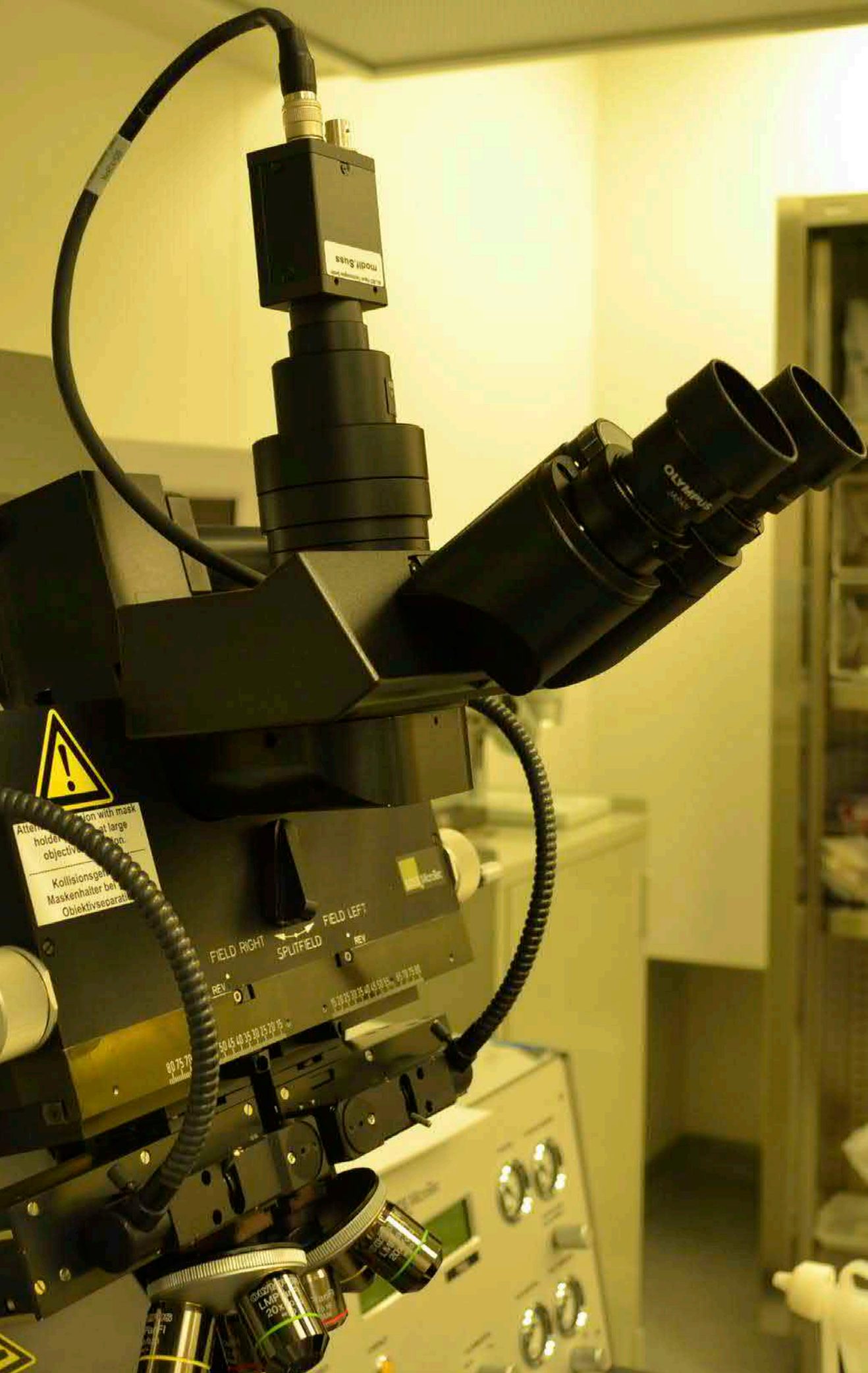
A further example of our detailed microstructural analysis deals with small-angle x-ray scattering from GaN nanowires grown on Si(111) and on TiN that has been measured in grazing incidence geometry and modeled by means of a Monte Carlo simulation taking into account the orientational distribution of the faceted nanowires and the roughness of their side facets. It has been found that the scattering inten-

sity at large wave vectors does not follow Porod's law. The intensity depends on the orientation of the side facets with respect to the incident x-ray beam. It is maximum when the scattering vector is directed along a facet normal, as a reminiscence of the surface truncation rod scattering. At large wave vectors, the scattering intensity has been found to be decreased by surface roughness. A RMS roughness of about 0.9 nm, which is the height of just 3-4 atomic steps per micron long facets, already gives rise to a strong intensity reduction.

As a further topic of our CReA we employ *atom manipulation* by cryogenic scanning tunneling microscopy (STM) to explore individual quantum dots and quantum-dot assemblies with precisely controlled properties. The dots are built up from single adatoms on an InAs surface and induce carrier confinement. The long-term goal is to implement suchlike artificial structures in electronic quantum circuits for quantum information processing. On that path we currently investigate hexagonal quantum-dot molecules and larger assemblies of those, the latter reproducing honeycomb lattice symmetry. We also started to investigate 1D assemblies with sublattice symmetry, namely quantum-dot dimer chains hosting symmetry-protected electronic boundary states. Aside from the atom-by-atom fabrication approach, we utilize the high sensitivity, spatial resolution, and spectroscopic means of STM to investigate the structure-property relation in 2D materials. Here, transition-metal dichalcogenide (TMD) layers grown on epitaxial graphene formed on SiC(0001) are studied to explore surface and interface effects in heterostructures. For example, we created homojunctions in TMD monolayers by patterning the graphene substrate and found quantum-confined electronic states emerging from strain-driven Moiré effects in heterobilayers composed of molybdenum disulfide and tungsten diselenide. Understanding such basic phenomena is essential to control carrier transport in TMD hetero-

structures – the potential building blocks of 2D electronics devices.





Modul Süss

OLYMPUS



Attention: Collision with mask holder at large objective separation.  
Kollisionserfahrungsgefahr bei Maskenhalter bei Objektivseparat

FIELD RIGHT SPLITFIELD FIELD LEFT

REV

REV

10 15 20 25 30 35 40 45 50

OLYMPUS LMP 20x

# Control of Elementary Excitations by Acoustic Fields / Kontrolle von elektronischen Anregungen in Halbleiter-Nanostrukturen

Dr. Paulo V. Santos

Dr. Alberto Hernández-Mínguez

This core research area explores dynamic acoustic fields for the control of electronic excitations in semiconductor nanostructures. We use, for that purpose, elastic vibrations in the bulk (bulk acoustic waves, BAW) or along the surface of a solid (surface acoustic waves, SAW), in most cases a semiconductor nanostructure. These waves resemble seismic waves created during earthquakes, but have much smaller (micrometer-sized) wavelengths. Both types of waves can be electrically generated using piezoelectric transducers, a standard technique widely used in signal processing, sensors, and acoustooptical modulation.

The recent years have witnessed a growing interest in the application of acoustic waves for the control of electronic effects in semiconductors. Here, one takes advantage of the dynamic and spatially dependent character of the acoustic fields, which are composed of a dynamic strain component and, in piezoelectric semiconductors, a piezoelectric component. Both components induce a time- and spatially dependent modulation, which can be exploited to control different types of excitations (e.g., photons, electrons, holes, spins, etc.). In addition, acoustic potentials are mobile and can thus be used for the confinement and transport of electronic excitations. Interestingly, the dynamic fields produced by high-frequency acoustic waves in the GHz range have wavelengths on the order of one micrometer, thus being comparable to the dimensions of semiconductor components. The acoustic and acoustoelectric effects can, furthermore, be exploited for novel device functionalities. Quite naturally the studies also include the development of piezoelectric materials compatible with semiconduc-

In dieser Core Research Area werden dynamische akustische Felder zur Steuerung elektronischer Anregungen in Halbleiternanostrukturen untersucht. Hierfür verwenden wir elastische Schwingungen, die sich als Volumenwellen (Bulk Acoustic Waves, BAW) oder entlang der Oberfläche eines Festkörpers als akustische Oberflächenwellen (Surface Acoustic Waves, SAW) ausbreiten. Diese Wellen ähneln seismischen Wellen, die während Erdbeben erzeugt werden, haben jedoch viel kleinere (mikrometergroße) Wellenlängen. Beide Arten von Wellen können zum Beispiel mit piezoelektrischen Wandlern elektrisch erzeugt werden. Diese Standardtechnik für Schwingungsanregung wird häufig in der Signalverarbeitung, bei Sensoren und bei der akustooptischen Modulation verwendet.

In den letzten Jahren ist das Interesse, akustische Wellen zur Kontrolle elektronischer Effekte in Halbleitern einzusetzen, gewachsen. Hierbei wird ausgenutzt, dass sich diese Felder aus einer dynamischen Verzerrungskomponente und, in piezoelektrischen Halbleitern, auch aus einer dynamischen elektrischen Komponente zusammensetzen. Beide Komponenten induzieren eine zeit- und ortsabhängige Modulation der Bandstruktur des Halbleiters. Darüber hinaus sind akustische Potentiale mobil und können somit zur Einsperrung und Transport elektronischer Anregungen genutzt werden. Interessanterweise haben die Felder, die durch hochfrequente Schallwellen im GHz-Bereich erzeugt werden, Wellenlängen in der Größenordnung von einem Mikrometer und sind damit mit den Abmessungen von Halbleiterbauelementen vergleichbar. Die akustischen und akustoelektrischen Effekte können darüber hinaus für neuartige Bau-

tors as well as efficient processes for the electrical excitation of acoustic waves in non- or only weakly piezoelectric materials (such as, e.g., Si and SiC).

The activities addressed in this report include investigations of (i) the non-reciprocal propagation control of SAW beams via the magnetoacoustic interaction, (ii) the generation of anti-bunched photons at GHz frequencies by acoustically pumped single exciton centers in GaAs, and (iii) the triggered generation of correlated photons by parametrically scattered microcavity polaritons (MP). We highlight here three contributions from this Core Research Area.

The first report (by A. Hernández-Mínguez and co-workers) addresses the on-demand control of SAW propagation in ferromagnet/semiconductor hybrid structures. We have demonstrated an acoustic diode based on the non-reciprocal propagation of SAWs along a GaAs substrate coated with an epitaxial Fe<sub>3</sub>Si film. The preferential propagation along one direction arises from the excitation of spin waves in the Fe<sub>3</sub>Si film by the chiral effective magnetic field induced by the SAW strain, which depends on the relative orientations of the film magnetization and SAW propagation direction. The resulting propagation non-reciprocity, defined as the difference between the transmitted acoustic power for forward and backward SAW propagation, reaches values up to 20% and can be further enhanced by optimization of the sample design. The unidirectionality provided by the non-reciprocity can be exploited for the efficient interfacing of solid-state quantum systems using SAWs, as well as in elastooptics and electronic devices for signal processing.

The second contribution (by M. Yuan and co-workers) addresses functionalities for the optical processing of quantum information based on SAWs. Quantum networks require the on-chip transfer and manipulation of single particles as well

elementfunktionalitäten genutzt werden. Selbstverständlich umfassen die Studien auch die Entwicklung von halbleiterkompatiblen piezoelektrischen Materialien sowie von effizienten Prozessen zur elektrischen Anregung von Schallwellen in nicht- oder nur schwachen piezoelektrischen Materialien (wie zum Beispiel Si und SiC).

Die in diesem Bericht angesprochenen Aktivitäten umfassen Untersuchungen zu (i) der nicht-reziproken Ausbreitungskontrolle von SAW-Strahlen durch die magnetakustische Wechselwirkung, (ii) der Erzeugung von gebündelten Photonen bei GHz-Frequenzen durch akustisch gepumpte Einzel-Exzitonen-Zentren in GaAs und (iii) die ausgelöste Erzeugung korrelierter Photonen durch parametrisch gestreute Mikrokavitäts-polaritonen (MP).

Der erste Beitrag (von A. Hernández-Mínguez et al.) berichtet über die durchstimmbare Kontrolle der Propagation von SAWs in Ferromagnet/Halbleiter-Hybridstrukturen. Wir haben eine akustische Diode demonstriert, die auf der nicht reziproken Ausbreitung von SAWs auf einem GaAs-Substrat basiert, das mit einem epitaktischen Fe<sub>3</sub>Si-Film beschichtet ist. Die bevorzugte Ausbreitung entlang einer Richtung ergibt sich aus der Anregung von Spinwellen im Fe<sub>3</sub>Si-Film durch das SAW-Ausdehnungsfeld. Letzteres erzeugt ein chirales effektives Magnetfeld, das von den relativen Orientierungen der Filmmagnetisierung und der SAW-Ausbreitungsrichtung abhängt. Die resultierende Nichtreziprozität der Ausbreitung, definiert als die Differenz zwischen der übertragenen Schalleistung entlang entgegengesetzten Richtungen, erreicht Werte von bis zu 20% und kann durch Optimierung des Probendesigns weiter verbessert werden. Die durch die Nicht-Reziprozität durchstimmbare Unidirektionalität kann für die effiziente Verbindung von Festkörper-Quantensystemen unter Verwendung von SAWs sowie in Elastooptiken und elektronischen Geräten zur Signalverarbeitung ausgenutzt werden.

as their interconversion to single photons for long-range information exchange. We show that flying excitons propelled by GHz SAWs are outstanding messengers to fulfill these requirements due to their intrinsic interface to photons. A main challenge for the implementation of flying excitonic qubits is the creation of two-level centers for the storage of single excitons, which can be connected by transport channels. We achieved a major step towards this goal by demonstrating the transport of excitons along narrow channels to a single-exciton center by GHz SAWs. The stored excitons recombine emitting anti-bunched photons synchronously with the SAW frequency. The studies thus demonstrated an acoustically driven single-photon source on GaAs-based semiconductor platform operating at a record frequency of 3.6 GHz.

The last contribution (by A. Kuznetsov and co-workers) exploits SAW fields for the fine-tuning of confined polariton structures, which enables scalable and complex on-chip functionalities. Polaritons are light-matter particles, which behave as atomic states when confined in  $\mu\text{m}$ -sized traps defined on a GaAs chip. Unlike real atoms, these solid-state analogues suffer from the disorder associated with fluctuations in material properties and structural dimensions, which impair their exploitation for advanced functionalities. Here, a particularly challenging example are optical parametric oscillators (OPOs) based on confined polariton states, which involve the non-linear coherent coupling of three confined states (denoted as pump, signal, and idler states). In an OPO, an optically excited, two-polariton pump state is reversibly converted to a signal and an "idler" states with different energies. OPOs are relevant for optical amplification and generation of correlated photons. They require, however, a high degree of fine tuning of the energy and symmetry of the confined states of a trap, which is difficult to reach due to unavoidable fluctuations. We recently introduced a robust approach to overcome these constraints based on

Der zweite Beitrag (von M. Yuan et al.) befasst sich mit SAW-basierten Funktionalitäten für die optische Verarbeitung von Quanteninformationen. Kompakte Quantennetzwerke erfordern die on-Chip Manipulation von einzelnen Teilchen sowie deren Umwandlung in einzelne Photonen für Informationsübertragung über große Entfernungen. Die von GHz-SAWs transportierten Exzitonen (Fliegende Exzitonen) bilden aufgrund ihrer intrinsischen Grenzfläche zu Photonen hervorragende Botenstoffe, um diese Anforderungen zu erfüllen. Eine Hauptherausforderung für die Implementierung fliegender exzitonischer Qubits ist die Realisierung von Two-Level-Zentren für die Speicherung einzelner Exzitonen, die über Transportkanäle miteinander verbunden sind. Wir haben einen wichtigen Schritt in Richtung dieses Ziels erreicht, indem wir den Transport von Exzitonen durch GHz-SAWs entlang einem schmalen Kanal zu einem Two-Level-Zentrum für Exzitonen demonstriert haben. Die im Two-Level-Zentrum gespeicherten Exzitonen rekombinieren und emittieren „anti-bunched“ Photonen synchron mit der SAW-Frequenz. Die Studien zeigten somit eine akustisch angetriebene Einzelphotonenquelle auf einer GaAs-basierten Halbleiterplattform, die bei einer Rekordfrequenz von 3,6 GHz arbeitet.

Der letzte Beitrag (von A. Kuznetsov und Mitarbeitern) nutzt SAW-Felder zur Feinabstimmung von eingeschlossenen „Microcavity-Polaritons“ (MP), eine Funktionalität, die skalierbare und komplexe On-Chip-Funktionen ermöglicht. MP sind gemischte Licht-Materie-Teilchen in einem Halbleiter-Mikroresonator, die atom-ähnliche Zustände bilden, wenn sie in Mikrometer-Große Traps eingeschlossen sind. Im Gegensatz zu realen Atomen sind diese Festkörperanaloge auf Schwankungen in der Materialeigenschaften und Strukturdimensionen sehr empfindlich, was deren Nutzung für fortgeschrittene Funktionalitäten beeinträchtigt. Ein herausforderndes Beispiel sind optische parametrische Oszillatoren (OPOs),

the modulation of confined OPOs by SAW fields. The acoustic modulation can dynamically finetune a whole array of polariton traps to trigger OPOs in all array sites, thus enabling a complex and scalable functionality in an all-semiconductor structure.

die auf eingesperrten MP-Zuständen basieren. OPOs entstehen durch die nichtlineare kohärente Kopplung von drei eingesperrten Trap-Zustände: dabei werden zwei optisch angeregten MP in einem Pumpzustand in MPs in einen Signal- und einen Idler-Zustand mit unterschiedlichen Energien umgewandelt. OPOs sind relevant für die optische Verstärkung sowie für die Erzeugung korrelierter Photonen. Die Realisierung einer OPO erfordert jedoch ein hohes Maß an Feinabstimmung der Energie und Symmetrie der eingesperrten Trap-Zustände, das aufgrund unvermeidbarer Schwankungen schwer zu erreichen ist. Wir haben kürzlich einen neuartigen Ansatz zur Überwindung dieser Einschränkungen eingeführt, der auf der Modulation eingesperrter OPOs durch SAW-Felder beruht. Letzteres ermöglicht die dynamische Durchstimmung von ganzen Arrays von OPOs und, dadurch, die Realisierung von einer komplexen und skalierbaren Funktionalität auf einer Halbleiterplattform.

# III-V Nanowires for Optoelectronics / III-V-Nanodrähte und deren Anwendung in der Optoelektronik

Dr. Lutz Geelhaar  
Dr. Oliver Brandt

Semiconductor nanowires are structures with an extremely high aspect ratio and a diameter typically smaller than 100 nm. In bottom-up approaches, feature sizes down to 10 nm and below can be achieved without any lithography. Complementary top-down approaches offer higher level of control, in particular for the fabrication of regular nanowire arrays. The quasi-one-dimensional shape and the nanometric size of nanowires result in unique properties, often independently of the concrete nanowire material. Their characteristics make nanowires an exciting subject for fundamental studies and offer many conceptual advantages for various applications.

The goal of our research is to inspire and demonstrate new functionalities for optoelectronic applications by employing III-V nanowires. To this end, we investigate fundamental nanowire properties that crucially influence such applications to assess nanowire suitability. We grow both group-III-nitride and group-III-arsenide nanowires by molecular beam epitaxy but pursue also top-down approaches. We analyze nanowire microstructure and optical as well as electronic properties, and we employ technology to guide growth, enable electrical measurements, and process demonstrator devices.

Three different *synthesis* methods represent our platform for both fundamental investigations aimed at elucidating formation mechanisms and the fabrication of nanowire samples for dedicated studies of material properties and applications. First, the best-known bottom-up method resulting in uniaxial growth of nanowires utilizes

Halbleiter-Nanodrähte sind Strukturen mit extrem hohem Aspektverhältnis und Durchmesser von typischerweise weniger als 100 nm. In sogenannten ‚bottom-up‘-Ansätzen (englisch für ‚von unten nach oben‘) werden Nanodrähte hergestellt, indem Material durch Wachstum hinzugefügt wird. Auf diese Weise können Strukturgrößen bis hinunter zu 10 nm ohne lithographische Prozesse erzielt werden. Komplementäre ‚top-down‘-Verfahren (‚von oben nach unten‘), bei denen aus einer größeren Probe Material durch Ätzprozesse abgetragen wird, ermöglichen ein größeres Maß an Kontrolle, insbesondere für die Herstellung von regelmäßigen Nanodraht-Arrays. Die quasi eindimensionale Form und die Größe im Bereich von Nanometern resultieren in einzigartigen Eigenschaften von Nanodrähten, oftmals unabhängig von deren konkretem Material. Ihre Besonderheiten machen Nanodrähte zu einem spannenden Objekt für grundlegende Untersuchungen und bieten zahlreiche konzeptionelle Vorteile für unterschiedliche Anwendungen.

Unser Forschungsziel ist es, durch den Einsatz von III-V-Nanodrähten neue Funktionalitäten für optoelektronische Anwendungen zu inspirieren und zu demonstrieren. Dazu untersuchen wir fundamentale Nanodraht-Eigenschaften, die solche Anwendungen entscheidend beeinflussen, und beurteilen die Eignung von Nanodrähten. Wir züchten Gruppe-III-Arsenid- und -Nitrid-Nanodrähte mittels Molekularstrahlepitaxie aber verfolgen auch ‚top-down‘-Ansätze. Wir analysieren die Mikrostruktur sowie die optischen und elektronischen Eigenschaften von Nanodrähten und nutzen Technologie für die Herstellung regelmäßiger Nano-

the vapor-liquid-solid mechanism in which the formation of a solid nanowire from the vapor phase is mediated by a tiny liquid metal droplet. We employ this approach (using Ga as the metal) for the synthesis of group-III-arsenide nanowires on Si(111) substrates. Selective area vapor-liquid-solid growth is readily obtained by patterning these substrates by electron beam lithography and reactive ion etching, leading to ordered nanowire arrays.

Second, an alternative bottom-up approach exists for materials that exhibit the tendency to form nanowires under suitable growth conditions spontaneously, i. e., without any external guidance. GaN is one of these materials, and is prone to the spontaneous formation of nanowires on a wide variety of substrates, including amorphous and crystalline insulators, semiconductors, and metals. We are currently focusing on the growth of group-III nitride nanowires on metallic substrates, and in particular on TiN – both as sputtered film and flexible foil – and graphene. In either case, ensembles of vertical GaN nanowires with excellent structural and optical properties can be obtained.

Spontaneously formed GaN nanowires invariably grow along the  $[000\bar{1}]$ -direction, i.e., they are N polar. In order to synthesize Ga-polar group-III-nitride nanowires, we utilize as our third synthesis method a top-down process. In particular, we fabricate ordered arrays of nanowires from high-quality group-III-nitride layers and heterostructures by selective area sublimation. This complementary approach allows us to study phenomena depending on, for example, nanowire diameter in a systematic fashion.

In our studies of nanowire *properties*, we pay special attention to phenomena that are a direct consequence of the peculiar wire-like shape and nanometric size and are independent of the material the nanowires consist of. For example, the high surface-to-volume

draht-Arrays, um elektrische Messungen zu ermöglichen und um Demonstrator-Bau-elemente zu prozessieren.

ratio of nanowires has several important consequences. In particular, lattice-mismatched axial heterostructures relax their strain elastically at the free sidewalls, and the formation of dislocations is avoided. For radial heterostructures, a new type of structure only possible due to the nanowire geometry, the strain is shared between core and shell. In both cases, the strain distribution is very complex. Since many semiconductor properties depend sensitively on strain, the dedicated investigation of strain in nanowires is crucial for an understanding of their optoelectronic properties.

Another consequence of sidewall surfaces are radial electric fields induced by surface states. The strength of these fields depends on the doping density in the nanowire and may be large enough to dissociate excitons. Electric fields and doping crucially affect device design and are thus important topics of investigation.

Furthermore, nanowires are not ideal single crystals but exhibit structural defects. Some of these defects, such as twin boundaries, stacking faults, and inversion domain boundaries, act as two-dimensional radiative defects that may dominate luminescence. Others, such as dislocations created by the coalescence of nanowires in close vicinity, act as nonradiative defects. Non-radiative recombination also occurs at the free surface or interfaces and at point defects. Investigations of the microstructure and internal quantum efficiency are thus essential to elucidate the actual potential of group III-V nanowires for optoelectronic applications.

In general, our research relates to *applications* based on either light emission or light absorption, e. g. optical data transmission or energy harvesting. Since the nanowire geometry facilitates the integration of dissimilar materials, substrates with attractive properties can be employed that were excluded for planar growth. Furthermore, the spectral region of optoelectronic de-

vices can be widened. Also, radial nanowire heterostructures drastically increase the size of the active region, which is associated with stronger light emission and absorption. In addition, light-matter interaction can be tailored by design of nanowire dimensions and their arrangement in arrays.

Currently, we work towards a laser monolithically integrated on Si. Such a laser is of strategic relevance for the application field Si photonics. Our concept will provide the direct coupling of light between arrays of vertical III-V nanowires and planar Si waveguides. This project (MILAS) is funded by the Federal Ministry of Education and Research, and our partner is Technical University of Berlin.

In the nanowire geometry, the chemical composition can be changed in both the axial and the radial direction, leading to corresponding heterostructures and / or doping profiles. Such design concepts still strongly resemble established planar structures. Beyond those strategies, we investigate more *advanced structures* with the aim to tailor functionality in entirely new directions. For example, we synthesize nanowire heterostructures that are bent in a pre-defined way and employ the resulting complex strain gradients to influence radiative recombination processes. In addition, in many III-V nanowires both the wurtzite and zincblende crystal structure form. We exploit this polytypism to study crystal phase quantum structures of various dimensionalities with inherently atomically sharp interfaces and free from alloy disorder. In combination with compositional heterostructures, we realize complex topologies like quantum rings. Furthermore, we utilize dielectric confinement to modify radiative recombination in ultrathin nanowires.

In this year, we have introduced a way to control the density of self-assembled GaN nanowires over several orders of magnitude. We use reactively sputtered TiN films as an inert substrate on which GaN



nanowires do not nucleate under standard conditions, and deliberately create seeds for nucleation by the in-situ deposition of a submonolayer of Si prior to GaN growth. On these engineered surfaces, ultrathin (20 nm diameter) GaN nanowires form with a density that can be tuned from  $4 \times 10^6$  to  $2 \times 10^9$  cm<sup>-2</sup>. These low densities enable us to address individual nanowires with conventional optics. This possibility and the dielectric exciton confinement in GaN nanowires of such low diameters make these ensembles an attractive base for the realization of nanowire heterostructures for single photon emission.

Spectroscopic investigations of ultrathin GaN nanowires on sputtered TiN reveal unprecedentedly long bound exciton decay times. Surprisingly, we have found the decay time to systematically increase with decreasing nanowire diameter, apparently ruling out surface recombination as the main nonradiative decay channel. We have shown that this finding can be understood by considering exciton dissociation in the radial electric fields in the nanowire followed by rapid hole capture by surface states. Ultimately, nonradiative recombination of electrons and holes thus occurs at the surface after all, but the field ionization of excitons is the rate-limiting step determining the effective nonradiative lifetime. This two-step process provides a framework for a unified understanding of the exciton decay times observed for GaN nanowires of arbitrary diameter.

Many properties of GaN nanowires depend on their diameter, but an accurate and statistically meaningful determination of the diameter distribution of ensembles of GaN nanowires is challenging, particularly for small diameters and low nanowire densities. For this task, we have established grazing-incidence small-angle x-ray scattering (GISAXS) as a powerful alternative to electron microscopy. In conjunction with Monte Carlo modeling, this method has been shown to provide not only accurate values of the nanowire diameters, even for

mean diameters below 10 nm and low ensemble densities, but also information on their actual cross-sectional shapes and the atomic-scale roughness of their side facets. GISAXS is thus uniquely suited for a full morphological characterization of nanowire ensembles.

Complementary to the self-assembly of GaN nanowires, we pursue two different top-down approaches for the fabrication of ordered GaN nanowire arrays. The first of these techniques (ICP-KOH) relies on inductively coupled plasma etching followed by an anisotropic wet etching step with a KOH solution to remove the dry etch damage, while the second one (SAS) is based on thermal sublimation, and is thus not expected to cause any damage to the nanowire sidewalls. We have compared these two top-down fabrication techniques with the focus on the uniformity of the nanowire arrays. A statistical analysis of top-view secondary electron micrographs has shown that both techniques deliver arrays with a yield of 99.9% and a positioning as well as a diameter accuracy better than 5 nm. The ICP-KOH approach has, however, the decisive advantage of offering a much higher throughput than the SAS method.

GaAs/(In,Ga)As core-shell nanowire heterostructures could be the basis for light emitters monolithically integrated on a Si photonics platform. Towards this application, we have compared the luminescence properties of such nanowires comprising either quantum wells or dot-in-well heterostructures. The emission of the quantum wells is much narrower, in particular when grown under a Bi flux. In contrast, the luminescence efficiency of the dot-in-well structures is substantially higher, especially for high In content leading to a similarly long emission wavelength as for the dot-in-well nanowires. For employment as active region in a laser for the near-infrared spectral region, either quantum dot fluctuations associated with spectral broadening must be reduced or the quantum efficiency of quantum wells enhanced.

# Intersubband Emitters: GaAs-based Quantum-Cascade Lasers / Intersubbandemitter: GaAs-basierte Quantenkaskadenlaser

Prof. Dr. Holger T. Grahn  
Dr. Lutz Schrottke

The excellent state of semiconductor science and technology allows for the development and application of sophisticated devices such as quantum-cascade lasers (QCLs). These devices rely on the comprehensive understanding and the high-quality growth of complex planar heterostructures. For the terahertz spectral region, which typically ranges from 0.1 to 10 THz and bridges the electronics-based microwave region with the optics-based infrared region, GaAs/(Al,Ga)As-based heterostructures are the material of choice. The THz region is of great current interest for spectroscopic applications, since rotational states of many molecules, impurity transitions in semiconductors, and fine-structure transitions in atoms as well as ions can result in THz absorption or emission. The advantages of THz QCLs, covering at present the emission frequency range of about 1 to 5 THz, originate from their extremely narrow emission lines and optical output powers of typically several mW to several tens of mW. Therefore, THz QCLs are already used as local oscillators in heterodyne receivers and are promising sources for high-resolution absorption spectroscopy, for instance for the precise determination of the absolute density of atoms and ions in technologically relevant plasma processes. In particular, QCLs for local oscillators at 4.75 THz are currently unrivaled for heterodyne detection of atomic oxygen, which is important in planetary and interstellar science. Currently, the implementation of stabilized THz QCLs for future space missions based on passive cooling is of great interest.

Der hervorragende Stand der Halbleiterwissenschaft und -technologie erlaubt die Entwicklung und Anwendung von anspruchsvollen Bauelementen wie Quantenkaskadenlasern (QCLs). Diese Bauelemente erfordern ein umfassendes Verständnis komplexer planarer Heterostrukturen und deren Wachstum von hoher Qualität. Für den Terahertz-Spektralbereich, der typischerweise von 0,1 bis 10 THz reicht und den Bereich der elektronisch erzeugten Mikrowellenstrahlung mit dem der optisch erzeugten Infrarotstrahlung verbindet, sind GaAs/(Al,Ga)As-Halbleiterheterostrukturen das bevorzugte Materialsystem. THz-Strahlung ist derzeit für spektroskopische Untersuchungen von großem Interesse, da Rotationszustände vieler Moleküle, Übergänge in Fremdatomen in Halbleitern sowie Feinstrukturübergänge in Atomen und Ionen zu Absorption oder Emission in diesem Spektralbereich führen können. Die Vorteile von QCLs, deren Frequenzbereich sich derzeit von ca. 1 bis 5 THz erstreckt, haben ihren Ursprung in ihren extrem schmalen Emissionslinien und Ausgangsleistungen von typischerweise einigen mW bis zu einigen 10 mW. Deshalb werden diese Laser bereits als Lokaloszillatoren in Heterodyn-Empfängern für astronomische Untersuchungen verwendet und sind vielversprechende Quellen für die hochauflösende Absorptions-Spektroskopie, unter anderem für die genaue Bestimmung der absoluten Dichte von Atomen und Ionen in technologisch relevanten Plasmen. Insbesondere sind zur Zeit QCLs als Lokaloszillatoren bei 4,75 THz für den Nachweis von

In contrast to conventional interband semiconductor lasers, QCLs are so-called intersubband emitters, since the lasing transition takes place within the conduction band rather than across the energy gap. Therefore, they are unipolar lasers, i. e., only one type of carrier, typically electrons, is injected into the laser structure. In order to obtain population inversion between subbands in the conduction band, a rather complex semiconductor heterostructure with typically 6 to 20 layers with thicknesses in the range of a few to about 20 nanometers has to be realized, which is repeated about 100 times forming a semiconductor superlattice with a complex unit cell. The total thickness of the complete structure typically amounts to about 10  $\mu\text{m}$ . The realization of such a structure requires both, a design strategy based on appropriate modeling and a highly accurate growth technique such as molecular beam epitaxy with a very good stability of the growth parameters over up to 20 hours. In-situ continuous spectral reflectivity measurements are used during growth to achieve a better growth control on these complex structures, since this operation mode is found to enhance the reproducibility and precision of the growth runs. This growth expertise is one of the core competences of our institute. After growth, the wafers are processed using wet chemical or dry etching to form edge-emitting Fabry-Pérot ridge lasers. For single-mode operation, distributed-feedback lasers using lateral gratings of different order, two-section cavity lasers, or very short Fabry-Pérot cavities are realized. Typical dimensions of the laser ridges are widths of 15 to 200  $\mu\text{m}$  and lengths of 0.5 to 7.5 mm.

Our activities in the field of THz QCLs cover the design, the growth, the fabrication, and the determination of the operating parameters of these lasers. Since 2014, QCLs developed in our institute have been used as local oscillators in the German REceiver for Astronomy at Terahertz frequencies (GREAT) on board the Stratospheric Ob-

atomarem Sauerstoff, der in der Planeten- und Weltraumforschung wichtig ist, konkurrenzlos. Gegenwärtig ist die Realisierung stabilisierter, für passive Kühlung geeigneter THz-QCLs für zukünftige Raumfahrtmissionen von großem Interesse.

Im Gegensatz zu konventionellen Interband-Halbleiterlasern sind QCLs Intersubbandemitter, da der Laserübergang innerhalb des Leitungsbands und nicht über die Energielücke erfolgt. Deshalb sind QCLs unipolare Halbleiterlaser, das heißt nur eine Ladungsträgerart, typischerweise Elektronen, wird in die Laserstruktur injiziert. Um Besetzungsinversion zwischen den Subbändern im Leitungsband zu erreichen, wird eine komplexe Heterostruktur mit etwa 100 Perioden, die typischerweise innerhalb einer Periode 6 bis 20 Schichten mit Dicken zwischen etwa 1 und 20 nm enthält und insgesamt etwa 10  $\mu\text{m}$  dick ist, realisiert. Die Entwicklung von THz-QCLs erfordert sowohl das Design auf der Grundlage geeigneter Modellierung der Laser als auch die Herstellung komplexer Heterostrukturen. Dafür wird eine sehr präzise Wachstumsmethode wie die Molekularstrahl-Epitaxie mit einer guten Stabilität der Wachstumsparameter über bis zu 20 Stunden benötigt. Kontinuierliche In-situ-Messungen der spektralen Reflexion werden während des Wachstums eingesetzt, um eine bessere Kontrolle des Wachstums dieser komplexen Strukturen zu erreichen, da dieser Arbeitsmodus die Reproduzierbarkeit und Genauigkeit der Wachstumsabläufe erhöht. Das Wachstum mittels Molekularstrahl-Epitaxie ist eine der Kernkompetenzen unseres Instituts. Die Laser werden anschließend mittels nass-chemischer Verfahren oder Trockenätzen als kantenemittierende Fabry-Pérot-Laserstreifen hergestellt. Für den Einzelmodenbetrieb werden Resonatoren mit verteilter Rückkopplung unter Verwendung von lateralen Gittern verschiedener Ordnungen, Zweisektionslaser oder sehr kurze Fabry-Pérot-Resonatoren verwendet. Typische Abmessungen der Laserstreifen sind Breiten von 15 bis 200  $\mu\text{m}$  und Längen von 0,5 bis 7,5 mm.

servatory For Infrared Astronomy (SOFIA) for the detection of the fine-structure transition of interstellar neutral atomic oxygen (OI) at 4.7448 THz. Currently, a QCL with improved operating parameters is employed in an advanced astronomical THz receiver based on multichannel detection (upGREAT). So far, our QCLs have been used in about 50 missions, covering approximately 450 flight hours. The key challenges for applications continue to be the increase of the practical operating temperature, i. e., the temperature at which the lasers emit powers of at least 1 mW, beyond 75 K and of the wall plug efficiency to reduce the necessary cooling power so that miniature mechanical cryocoolers or even passive cooling in satellite-based instruments can be employed.

QCLs for the THz spectral region are usually based on GaAs/Al<sub>x</sub>Ga<sub>1-x</sub>As heterostructures with  $0.1 \leq x \leq 0.25$ . In 2016, we realized GaAs/AlAs QCLs operating at 4.75 THz, which exhibit an about three times higher wall plug efficiency than GaAs/Al<sub>0.25</sub>Ga<sub>0.75</sub>As QCLs with an almost identical design. Substituting AlAs for the Al<sub>0.25</sub>Ga<sub>0.75</sub>As barriers leads to a larger energy separation between the subbands so that the probability for leakage currents through parasitic states and the reabsorption of the laser radiation can be reduced. Since then, we have successfully enlarged the frequency range of THz QCLs based on GaAs/AlAs heterostructures so that frequencies between 2.3 and 5.6 THz are now available. Starting from a laser structure operating at 4.75 THz, we developed GaAs/AlAs QCLs in this frequency range by a gradual scaling of the layer structure toward lower and higher frequencies. The corresponding frequencies of the gain maxima are achieved by an adjustment of the quantum well thicknesses and a fine tuning of the thicknesses of some particular barriers. In particular between 2.3 and 5.0 THz, several frequencies are of interest. In atmospheric science, the rotational transition of the hydroxyl radical (OH) at 3.55 THz and the fine-structure

Unsere Aktivitäten auf dem Gebiet der THz-QCLs beinhalten das Design, das Wachstum, die Herstellung und die Bestimmung der Betriebsparameter dieser Laser. Seit 2014 werden von uns entwickelte QCLs im German REceiver for Astronomy at Terahertz frequencies (GREAT) während der Beobachtungsflüge des Stratospheric Observatory For Infrared Astronomy (SOFIA) für den Nachweis eines Feinstrukturübergangs in interstellarem neutralem atomarem Sauerstoff (OI) bei 4,7448 THz verwendet. Gegenwärtig wird in einem weiterentwickelten astronomischen THz-Empfänger auf der Grundlage von Mehrkanal-Detektion (upGREAT) ein QCL mit verbesserten Betriebsparametern betrieben. Unsere QCLs sind bisher in rund 50 Missionen mit insgesamt annähernd 450 Flugstunden eingesetzt worden. Die Kernherausforderungen für Anwendungen bestehen nach wie vor in der Erhöhung der praktischen Betriebstemperatur, d.h. der Temperatur, bei der die Laser eine Ausgangsleistung von mindestens 1 mW aufweisen, über 75 K hinaus und in der Verbesserung des Gesamtwirkungsgrades, um die notwendige Kühlleistung zu reduzieren, so dass miniaturisierte mechanische Kühler oder sogar passive Kühlsysteme in Satelliten-gestützten Instrumenten verwendet werden können.

THz-QCLs beruhen üblicherweise auf GaAs/Al<sub>x</sub>Ga<sub>1-x</sub>As-Heterostrukturen mit  $0,1 \leq x \leq 0,25$ . Im Jahr 2016 haben wir GaAs/AlAs-Laser für 4,75 THz mit einem mehr als dreifachen Gesamtwirkungsgrad im Vergleich zu GaAs/Al<sub>0,25</sub>Ga<sub>0,75</sub>As-Lasern realisiert. Der Ersatz der Al<sub>0,25</sub>Ga<sub>0,75</sub>As- durch AlAs-Barrieren führt zu einem größeren Energieabstand der Subbänder, so dass die Wahrscheinlichkeit von Leckströmen durch parasitäre Zustände und Reabsorption der Laserstrahlung reduziert wird. Seitdem haben wir erfolgreich den Frequenzbereich der GaAs/AlAs-QCLs erweitert, so dass nun Frequenzen zwischen 2,3 und 5,6 THz erreichbar sind. Ausgehend von einer Laserstruktur für 4,75 THz haben wir

line of OI at 4.75 THz are important. Both can be measured with QCL-based heterodyne receivers. For fundamental research and industrial applications, high-resolution absorption spectroscopy based on fine-structure transitions in Si, Al, N<sup>+</sup>, and O at 2.31, 3.36, 3.92, and 4.75 THz, respectively, is expected to allow for the quantitative determination of the atom and ion densities in plasma processes. Furthermore, QCLs emitting in the atmospheric windows around 3.43, 4.32, and 4.92 THz are of interest for applications if the THz radiation has to be transmitted through air over a distance of up to 10 m.

For high-resolution spectroscopy, QCLs with active regions that exhibit the maximum of the optical gain at the respective target frequency are required. Due to a lateral inhomogeneity of the growth rate, the frequency of the gain maximum varies across the wafer. For three wafers based on GaAs/AlAs heterostructures with target frequencies of 3.36 and 3.92 THz, we observed a blue shift of the emission frequency from the center to the edge of the wafer. This blue shift is attributed to a decrease of the thickness of the QCLs, which can be determined with spectroscopic techniques. The location-dependent thickness is used to calculate a position-dependent frequency of the gain maximum for the active region. The correlation of the calculated frequencies with the emission frequencies of lasers fabricated from different locations on the wafer, which exhibits a universal behavior, allows us to establish an effective method for the fabrication of THz QCLs emitting at a particular target frequency.

The optical gain of QCLs is generated by intersubband transitions, which also affect the effective refractive index of the waveguides. Using the spacing of the laser modes in the emission spectra, we have determined the effective group refractive index  $n_{g,eff}$  for more than one hundred THz QCLs with Fabry-Pérot resonators based on single-plasmon waveguides. The exper-

GaAs/AlAs-QCLs in diesem Frequenzbereich durch eine graduelle Skalierung der Schichtstruktur zu niedrigeren und höheren Frequenzen hin entwickelt. Die jeweiligen Maxima der optischen Verstärkungsspektren wurden durch eine Anpassung der Quantenschichtdicken und eine Feinabstimmung einiger Barrierendicken erreicht. Insbesondere zwischen 2,3 und 5,0 THz sind mehrere Frequenzen von Interesse. In der Atmosphärenforschung sind der Rotationsübergang des Hydroxyl-Radikals (OH) bei 3,55 THz und die Feinstrukturlinie von OI bei 4,75 THz von Bedeutung. Beide Übergänge können mittels QCL-basierten Heterodyn-Empfängern detektiert werden. Sowohl für die Grundlagenforschung als auch für industrielle Anwendungen ist die hochauflösende Absorptionsspektroskopie der Feinstrukturübergänge in Si, Al, N<sup>+</sup> und O bei 2,31, 3,36, 3,92 und 4,75 THz ein vielversprechender Ansatz zur quantitativen Analyse der Atom- bzw. Ionendichten in Plasmaprozessen. Weiterhin sind QCLs, die in den atmosphärischen Fenstern um 3,43, 4,32 und 4,92 THz emittieren, für Anwendungen interessant, in denen die Strahlung über eine Entfernung von bis zu 10 m übertragen werden muss.

Für die hochauflösende Spektroskopie werden QCLs mit aktiven Regionen, die das Maximum der optischen Verstärkung bei der entsprechenden Zielfrequenz aufweisen, benötigt. Infolge einer lateralen Inhomogenität der Wachstumsrate variiert die Frequenz des Maximums der optischen Verstärkung über den Wafer. Für drei Wafer mit GaAs/AlAs-Heterostrukturen mit den Zielfrequenzen 3,36 und 3,92 THz haben wir eine Blauverschiebung der Emissionsfrequenz von der Mitte des Wafers zum Rand hin beobachtet. Diese Blauverschiebung wird einer Abnahme der Dicke der QCLs zugeschrieben, die mittels spektroskopischer Methoden bestimmt werden kann. Die ortsabhängige Dicke wird für die Berechnung der ortsabhängigen Frequenz des Verstärkungsmaximums der aktiven Region verwendet. Die Korrelation der berechne-

imentally obtained values of  $n_{g,\text{eff}}$  for emission frequencies between 2.5 and 5.6 THz generally follow the trend of the value derived from electromagnetic simulations. However, for a certain number of QCLs, the experimental values of  $n_{g,\text{eff}}$  exhibit a rather large deviation from the general trend and the simulation results. From a thorough analysis, we conclude that differences in the optical gain/loss spectra are responsible for this deviation, which lead to a modification of the dispersion in the active region and consequently to altered values of  $n_{g,\text{eff}}$ . The analysis also provides evidence that these differences in the gain/loss spectra originate from both, the details of the design and the gain broadening due to interface roughness. A detailed understanding of the behavior of  $n_{g,\text{eff}}$  is expected to be important for the development of THz frequency combs for high-resolution spectroscopy.

In collaboration with the Leibniz-Institut für Plasmaforschung und Technologie (INP Greifswald), we are developing a spectrometer based on our THz QCLs for the detection of different species of atoms and ions in plasmas, which are crucial for the plasma-assisted deposition of Si-based films and AlN layers. The density of Si, Al, N<sup>+</sup>, and O can be directly determined using their fine-structure transitions at 2.31, 3.36, 3.92, and 4.75 THz, respectively, in a transmission setup. For that purpose, single-mode THz QCLs emitting precisely at these frequencies are required. In order to also cover broadened absorption lines at elevated pressures, a tuning range of at least 5 GHz is desirable for each frequency. While a QCL for 2.31 THz has still to be optimized, we have already provided QCLs emitting at 3.36, 3.92, and 4.75 THz to the INP Greifswald, which are being used in their spectrometer.

The QCLs emitting at 3.55 and 4.75 THz are continuously improved in order to increase their practical operating temperature and to reduce the requirements for the cooling of the lasers, in particular for future appli-

ten Frequenzen mit Emissionsfrequenzen von an verschiedenen Positionen auf dem Wafer hergestellten Lasern, die ein universelles Verhalten aufweist, hat die Etablierung einer effektiven Methode für die Herstellung von THz-QCLs mit bestimmten Zielfrequenzen erlaubt.

Die optische Verstärkung der QCLs wird durch Intersubband-Übergänge, die auch den effektiven Brechungsindex der Wellenleiter beeinflussen, erzeugt. Unter Verwendung der Modenabstände in den Emissionsspektren haben wir den effektiven Gruppenbrechungsindex  $n_{g,\text{eff}}$  für über einhundert THz-QCLs mit Fabry-Pérot-Resonatoren und Einzel-Plasmonen-Wellenleitern bestimmt. Die experimentell ermittelten Werte für  $n_{g,\text{eff}}$  im Frequenzbereich von 2,5 bis 5,6 THz folgen im Allgemeinen dem Verlauf der Werte, die von elektromagnetischen Simulationen abgeleitet wurden. Jedoch weisen für eine gewisse Zahl von QCLs die experimentellen Werte für  $n_{g,\text{eff}}$  eine ziemlich große Abweichung von dem allgemeinen Verlauf und den berechneten Ergebnissen auf. Durch eine gründliche Analyse schließen wir auf Unterschiede in den optischen Verstärkungs-/Verlustspektren als Ursache für diese Abweichung, da sie zu einer Modifikation der Dispersion im aktiven Bereich und folglich zu veränderten Werten für  $n_{g,\text{eff}}$  führen. Die Analyse zeigt auch, dass die Unterschiede in den optischen Verstärkungs-/Verlustspektren sowohl von Details des Designs als auch von einer Verbreiterung des Verstärkungsspektrums infolge von Grenzflächenrauigkeiten herrühren. Wir erwarten, dass ein genaueres Verständnis des Verhaltens von  $n_{g,\text{eff}}$  wichtig für die Entwicklung von THz-Frequenzkämmen für die hochauflösende Spektroskopie ist.

In Zusammenarbeit mit dem Leibniz-Institut für Plasmaforschung und Technologie (INP Greifswald) entwickeln wir ein Spektrometer für die Detektion verschiedener Atom- und Ionenarten in Plasmen, die für die Plasma-gestützte Abscheidung von Si-

cations in spaceborne instruments. Output powers of up to 9 and 8 mW, respectively, have been demonstrated. For both frequencies, a practical operating temperature above 75 K has been achieved. Since THz QCLs can be conveniently operated in liquid-coolant-free mechanical coolers, new paths have been opened toward various applications. These lasers have been provided to the Institut für Optische Sensorsysteme of the Deutsches Zentrum für Luft- und Raumfahrt in Berlin for a heterodyne receiver, for which their frequency is stabilized using harmonic mixers. Finally, the high level of design and growth of THz QCLs in our institute is demonstrated by several requests for scientific and commercial applications of our QCLs in various systems.

basierten Filmen und AlN-Schichten sehr wichtig sind. Die Dichten von Si, Al, N<sup>+</sup> und O können direkt unter Verwendung ihrer Feinstrukturübergänge bei 2,31, 3,36, 3,92 und 4,75 THz in einem Transmissionsaufbau bestimmt werden. Hierfür sind THz-QCLs, die im Einzelmodenbetrieb genau bei diesen Frequenzen emittieren, notwendig. Um auch verbreiterte Absorptionslinien bei höheren Drücken abzudecken, ist für jede Frequenz ein Abstimmbereich von wenigstens 5 GHz wünschenswert. Während ein QCL für 2,31 THz noch weiter optimiert werden muss, haben wir dem INP Greifswald bereits QCLs für 3,36, 3,92 und 4,75 THz, die in deren Spektrometer verwendet werden, zur Verfügung gestellt.

Die QCLs, die bei 3,55 und 4,75 THz emittieren, werden fortlaufend verbessert, um ihre praktische Betriebstemperatur zu erhöhen und die Erfordernisse für ihre Kühlung, insbesondere für den zukünftigen Einsatz in Weltraum-gestützten Instrumenten, zu reduzieren. Ausgangsleistungen von 9 bzw. 8 mW wurden demonstriert. Für beide Frequenzen haben wir eine praktische Betriebstemperatur oberhalb von 75 K erreicht. Da die THz-QCLs problemlos in mechanischen Kühlern ohne kryogene Flüssigkeiten betrieben werden können, eröffnen sich neue Anwendungsmöglichkeiten. Wir haben diese Laser dem Institut für Optische Sensorsysteme des Deutschen Zentrums für Luft- und Raumfahrt in Berlin für einen Heterodyn-Empfänger zur Verfügung gestellt, bei dem die Laserfrequenz durch Verwendung von harmonischen Mixern stabilisiert wird. Schließlich zeigt sich das hohe Niveau des Designs und des Wachstums von THz-QCLs in unserem Institut durch mehrere Anfragen für wissenschaftliche und kommerzielle Anwendungen unserer Laser in verschiedenen Systemen.

Te2.t

Te2HL.t

window

W5 W5% +  
W 26%R -

P

Q

R

Q

A





# Brief Reports Kurzberichte

In-situ control of molecular beam epitaxial growth by spectral reflectivity analysis . . . . .	66
SnO/ $\beta$ -Ga <sub>2</sub> O <sub>3</sub> pn-heterojunction diodes grown by plasma-assisted molecular beam epitaxy . . . . .	70
Towards Ge-rich Ge-Sb-Te alloys fabricated by molecular beam epitaxy . . . . .	74
Artificial quantum dot molecules assembled by atom manipulation . . . . .	78
In situ transmission electron microscopy of disorder-order transition in epitaxially stabilized FeGe <sub>2</sub> . . . . .	81
Nature of nonradiative recombination at threading dislocations in GaN . . . . .	85
Antiferromagnetism in $\alpha$ -FeGe <sub>2</sub> spacer layers and its influence on the magnetic interlayer coupling in spin valve structures . . . . .	89
Realistic potential shape of quantum point contacts . . . . .	93
Comparison of top-down approaches for the fabrication of highly ordered GaN nanowire arrays . . . . .	96
Unified understanding of nonradiative recombination in GaN nanowires . . . . .	100
Tuning the density of self-assembled GaN nanowires over three orders of magnitude with Si seeds on metallic TiN . . . . .	104
Luminescence properties of coaxial GaAs/(In,Ga)As nanowire heterostructures with and without quantum dots grown using a Bi surfactant . . . . .	108
Small-angle x-ray scattering from self-assembled GaN nanowires . . . . .	112
Triggered generation of correlated photons by parametrically scattered polaritons at MHz frequencies . . . . .	116
Remotely pumped, GHz anti-bunched emission from single-exciton centers in GaAs . . . . .	119
Correlation between the frequency, growth rate, and location on the wafer for terahertz quantum-cascade lasers . . . . .	123
Effective group dispersion of terahertz quantum-cascade lasers . . . . .	127

# In-situ control of molecular beam epitaxial growth by spectral reflectivity analysis

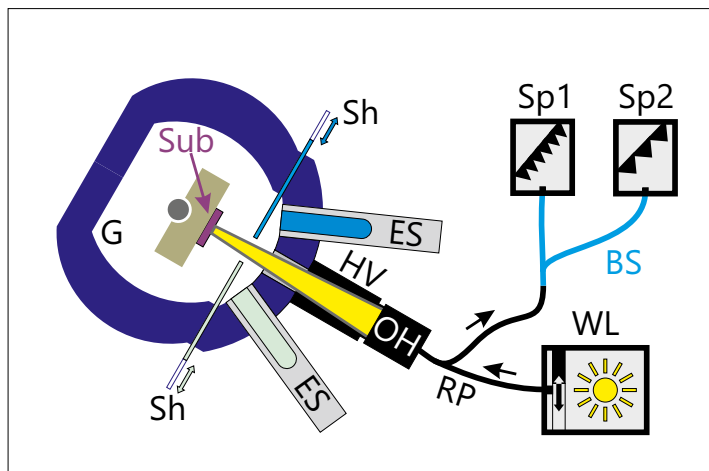
K. Biermann, P. L. J. Helgers, A. Crespo-Poveda, A. S. Kuznetsov, A. Tahraoui, B. Röben, X. Lü, L. Schrottke, P. V. Santos, H. T. Grahn

During the last eight years, in-situ spectral reflectivity measurements carried out continuously during molecular beam epitaxial growth have regularly been applied to the fabrication of complex GaAs-based heterostructures such as microcavities (MCs) and terahertz (THz) quantum-cascade lasers (QCLs). This technique exhibits beneficial effects on precision and reliability of the growth when using research-and-development (R&D) molecular beam epitaxy (MBE) systems.

The experimental setup for the in-situ reflectivity measurements is sketched in Fig. 1 showing a schematic side view of the MBE growth chamber. The former consists of a heatable viewport and an adjustable optical head to focus light guided through a standard, y-shaped reflectivity probe fiber

from a halogen light source onto the sample surface. The light reflected from the sample surface is coupled into the outgoing segment of the reflectivity probe fiber and is then divided by a fiber beam splitter to a spectrometer for shorter wavelengths (650 to 1,100 nm) and another one for longer wavelengths (1,000 to 1,700 nm). The computer which controls these spectrometers is communicating via a local area network with the one controlling the MBE system. During growth, reflectivity spectra are collected every 20 to 30 seconds, which corresponds to typically 4 to 6 rotations of the substrate. The procedure includes averaging and selecting of single spectra (acquisition time of 0.3 s) to compensate for signal fluctuations due to the substrate rotation. The spectra are additionally normalized with respect to their integrated intensities, and, in general, a baseline spectrum recorded before growth is subtracted.

**Fig. 1.** Sketch of the employed in-situ reflectivity measurement setup. G: growth chamber, Sub: substrate, Sh: shutter, ES: effusion source, HV: heatable viewport, OH: optical head, RP: reflectivity probe fiber, BS: fiber beam splitter, WL: halogen light source, Sp1 and Sp2: short- and long-wavelength range spectrometer, respectively.



QCLs are unipolar intersubband emitters which contain multiple cascaded active regions in such a way that a single charge carrier could, in principle, trigger the emission of one photon in each traversed period of the cascade. Due to the long emission wavelengths of THz QCLs, waveguide structures have to be designed with rather large thicknesses of about 10 to 12  $\mu\text{m}$  consisting of 1,000 to 2,000 single layers. At our usual low growth rate of 0.13 nm/s, this leads to extended growth times of roughly 25 hours for a complete QCL structure. While we found that the run-to-run Al flux is very stable, the Ga flux reduces significantly during such long growth times. Therefore, we deduce the actual growth rate from the reflectivity data and adjust the Ga flux by means of an automated feed-back control loop. To this end, the

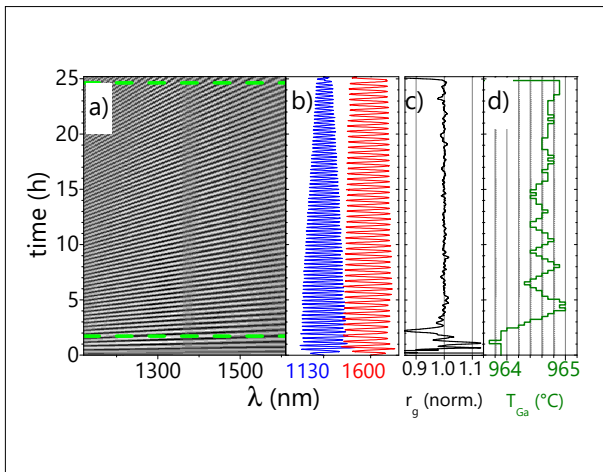


**Fig. 2.** Growth control of a QCL structure. (a) Difference reflectivity map [linear scale from  $-1.0$  (dark) to  $1.0$  (bright)]. (b) Vertical cross-section of (a) at  $1,130$  and  $1,600$  nm. (c) Normalized growth rate  $r_g$  (measured divided by nominal growth rate). (d) Controlled temperature  $T_{Ga}$  of the Ga source.

growth of the QCL structure begins with a  $110$ -nm-thick  $(Al,Ga)As$  refractive-index contrast layer with an  $AlAs$  content of  $90\%$ . Since the average  $AlAs$  content of the following active region is only a few percent, the difference in the refractive indices leads to Fabry-Pérot oscillations in the temporal evolution of the reflectivity, which are directly related to the growth rate.

Figure 2 displays the measurement data recorded during the deposition of a  $4.7$ -THz QCL structure. Figure 2(a) shows the difference reflectivity map. At time  $t = 0$ , the  $Al_{0.9}Ga_{0.1}As$  refractive-index contrast layer was deposited, and, subsequently, a Si-doped  $700$ -nm-thick GaAs contact layer was grown until  $t = 1.7$  h (lower horizontal dashed line). Then, for the next  $23$  hours, the cascaded active region of the QCL was grown (up to the upper dashed line). Finally, the Si-doped GaAs top contact layer was deposited. During the whole time, clear Fabry-Pérot oscillations can be observed. Figure 2(b) displays two vertical cross-sections of the difference reflectivity map shown in Fig. 2(a) for the wavelengths of  $1,130$  and  $1,600$  nm. Typically, the time

traces corresponding to the wavelengths  $1,130, 1,135, \dots, 1,600$  nm are analyzed individually for the present growth rate, and the obtained values are averaged to adjust the temperature of the Ga source accordingly. Figure 2(c) shows the measured growth rate normalized with respect to the nominal growth rate of  $0.13$  nm/s. It is kept very close to the intended value during deposition of the cascaded active region. The corresponding automated adjustment of the Ga source temperature is illustrated in Fig. 2(d).

Figure 3 shows the effective normalized growth rates, which are deduced from the period lengths determined by ex-situ X-ray diffraction scans, for  $197$  THz QCL structures. The dots (triangles) in Fig. 3 correspond to samples grown in an  $8$ -port VG V80H MBE system from  $1990$  ( $10$ -port Oxford V80H MBE system from  $2012$ ). The grey areas mark downtimes of the  $8$ -port VG system due to maintenance work as well as software upgrades such as adding safety control routines (monitoring liquid nitrogen, cooling water, compressed air) that allow for unattended growth of THz

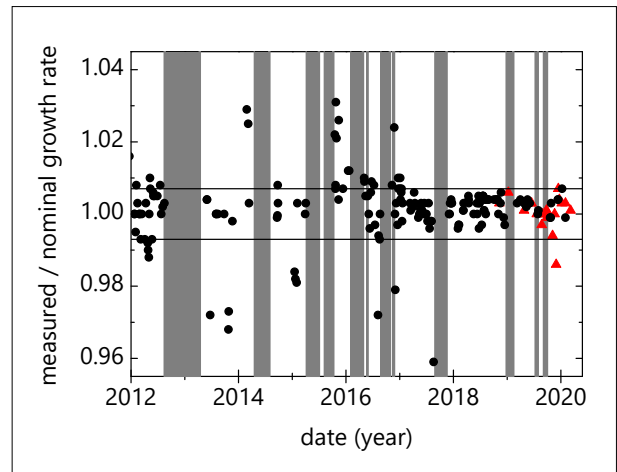


**Fig. 3.** Effective normalized in-situ controlled growth rates of QCL structures. The dots (triangles) correspond to samples grown in a VG V80H (Oxford V80H) MBE system. The grey areas mark the downtimes of the VG V80H system.

QCLs overnight and on weekends. Some measurement points with increased deviation, which can be found adjacent to one of the grey areas, are attributed to a poor calibration after maintenance work or software changes. For the samples grown in the VG V80H system (dots) from the beginning of 2018 (57 QCL structures), we obtain a mean normalized growth rate of 1.0022 with a standard deviation of 0.0027. This precision of 0.3% is the margin we expect to maintain on both MBE systems.

Close control of the growth process is also mandatory for the deposition of exciton polariton MCs. MCs usually consist of a lower and an upper distributed Bragg reflector (DBR), which enclose the cavity spacer. In our case, the spacer contains quantum wells (QWs), which act as the source of excitons interacting with the microcavity optical field. The DBRs and the cavity spacer are designed for a specific center wavelength ( $\lambda_c$ ),

which should match the excitonic emission wavelength such that the cavity photons strongly couple to the QW excitons to form exciton polaritons (EPs). While the DBRs are normally assembled of  $\lambda_c/4$  stacks of two materials with different refractive indices  $n$ , the spacer layer in between the DBRs has an optical thickness equal to a multiple integer of  $\lambda_c/2$ . Due to the geometries of our MBE systems, the growth rate across a two-inch wafer decreases from the center to the edge by a few percent. Thus, the cavity resonance wavelength exhibits a blue shift from the center to the edge in the same way, which is much larger than the blue shift of the emission wavelength of our typically 8- to 20-nm-thick QWs. As a consequence, perfect matching of the exciton and cavity resonance wavelengths will take place only at a specific distance  $d_0$  from the center of the wafer. Preferably, the matching should take place half way between the center and the edge, in order to provide re-

**Fig. 4.** Growth control of a microcavity structure. (a) Difference reflectivity map [linear scale from -0.3 (dark) to 1.0 (bright)]. (b) Horizontal crosssections. (c) Controlled Ga (blue) and Al (red) source temperatures. Between (a) and (b), the time spans of the growth of the DBRs and the cavity spacer (CS) are indicated. The green areas between (b) and (c) indicate the time spans of active feedback control.

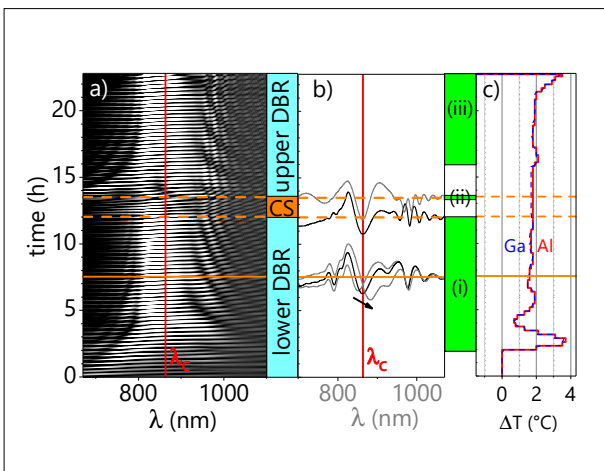
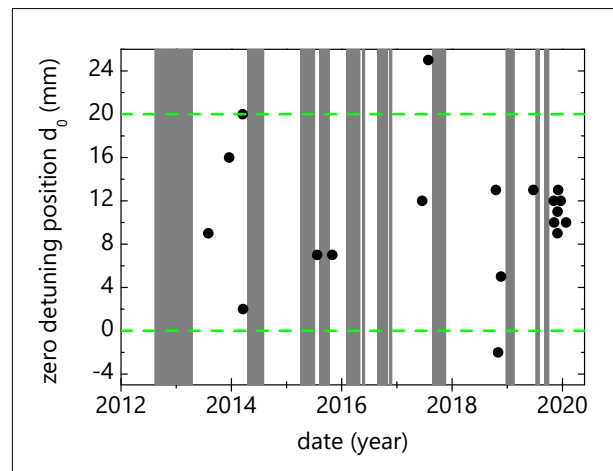


**Fig. 5.** Zero detuning position  $d_0$  measured from the center of two-inch wafers at low temperatures (5 – 20 K). The horizontal lines enclose the maximum tolerable range. The  $d_0$  value of -2 mm of one point corresponds to an estimated value of a positively detuned MC. The grey areas (same as in Fig. 3) mark the downtimes of the MBE system.



gions with negative, zero, and positive detuning of the EPs.

The evolution of the difference reflectivity during a controlled growth run of an MC structure is illustrated in Fig. 4. Figure 4(a) shows the result of the overall measurement of the difference reflectivity. The structure contains a  $3\text{-}\lambda$  cavity spacer with 5 pairs of 15-nm-thick GaAs QWs positioned close to the antinodes of the resonant cavity light field. The DBRs consist of pairs of  $\text{Al}_{0.90}\text{Ga}_{0.10}\text{As}$  and  $\text{Al}_{0.15}\text{Ga}_{0.85}\text{As}$  layers. In contrast to the in-situ control mechanism of QCLs discussed above, the control of MCs is based on the characteristic spectral reflectivity signatures of the DBRs and the cavity spacer. Therefore, at specific growth stages the measured spectral positions of the reflectivity minima are analyzed. For DBRs, this takes place after completing the low- $n$   $\lambda/4$  layers. This is illustrated in Fig. 4(b) by the horizontal line corresponding to 7.5 h. The arrow indicates the temporal red-shift of the measured reflectivity minimum nearest to  $\lambda_C$ . Analysis of these spectral positions after low- $n$   $\lambda/4$  layers allows for an automated control of the Ga and Al source temperature, as depicted in Fig. 4(c), to adjust the stopbands of the DBRs around  $\lambda_C$ .

The automated control of the cavity spacer thickness works very similar. Corresponding reflectivity spectra are shown in Fig. 4(b) close to the upper dashed horizontal line. In this case, the growth is effectively slowed down some tens of nm before nominally

completing the cavity spacer, and the slowly varying reflectivity minimum is observed while approaching  $\lambda_C$ . The deposition of the spacer layer is then terminated by the control loop. For this sample, photoluminescence spectra scans at 10 K across the wafer (not shown) determined a zero detuning distance from the wafer center of  $d_0 = 12$  mm and a Rabi splitting of 6 meV. During the last eight years, we have grown 53 MC structures. The zero photon-exciton detuning distances  $d_0$  at low temperatures of 19 MC structures are displayed in Fig. 5. The maximum usable range for  $d_0$  spans from 0 to about 20 mm (horizontal lines in Fig. 5). Out of the depicted 19 MC samples in Fig. 5, only two are clearly detuned. A certain number of the overall 53 MC growth runs failed due to software errors, hardware failures, or overgrowth problems, which might occur in the case of intra-cavity patterned MCs. These results show that, even with such an in-situ control, the growth of well-tuned MC structures remains challenging. However, exact tuning of an MC sample without any in-situ control in an R&D MBE system appears considerably more difficult.

We have demonstrated the implementation and application of in-situ spectral reflectivity measurements in order to control the growth of complex heterostructures for MCs and THz QCLs. Although this in-situ tool is rather straightforward, it has demonstrated to improve substantially the reproducibility and precision of extended growth runs in an R&D MBE system.

# SnO/ $\beta$ -Ga<sub>2</sub>O<sub>3</sub> *pn*-heterojunction diodes grown by plasma-assisted molecular beam epitaxy

M. Budde, D. Splith<sup>1</sup>, P. Mazzolini, A. Tahraoui, O. Bierwagen

During the last decade, transparent semi-conducting oxides (TSOs) have become a widely investigated class of materials whose transparency and wide band gaps are especially suitable for optoelectronics and power electronics applications. Most studied TSOs are *n*-type such as Ga<sub>2</sub>O<sub>3</sub>, In<sub>2</sub>O<sub>3</sub>, or SnO<sub>2</sub>. Out of these, Ga<sub>2</sub>O<sub>3</sub>, with the thermodynamically stable monoclinic polymorph  $\beta$ -Ga<sub>2</sub>O<sub>3</sub>, is predicted to outperform GaN and SiC for high-voltage power electronics. This is related to its ultra-wide band gap of  $\approx 4.8$  eV providing a high breakdown field of  $\approx 8$  MV/cm and a reasonably high electron mobility around 200 cm<sup>2</sup>/Vs enabling a sufficiently low on-resistance. In addition, the availability of bulk  $\beta$ -Ga<sub>2</sub>O<sub>3</sub> single crystals provides the substrate basis for low-defect  $\beta$ -Ga<sub>2</sub>O<sub>3</sub> devices as required for ultimate performance. Edge-termination to manage field crowding in high-voltage power electronic devices is ideally realized by *pn*-junctions. Since bipolar doping is not possible for most TSOs, including  $\beta$ -Ga<sub>2</sub>O<sub>3</sub>, *n*-type TSOs need to be combined with suitable *p*-type TSOs to form *pn*-heterojunctions.

SnO has a high hole mobility for this class of materials ( $\mu \approx 1\text{--}30$  cm<sup>2</sup>/Vs) but is known to be metastable with respect to Sn and SnO<sub>2</sub>, making its growth challenging. Previously, we determined the growth window for the formation of stoichiometric SnO by plasma-assisted molecular beam epitaxy (MBE): SnO was grown by a controlled Sn/O-plasma flux ratio at temperatures  $\leq 400$  °C, resulting in *p*-type conductivity with hole mobilities up to 6.0 cm<sup>2</sup>/Vs, and

rapid thermal annealing (RTA) experiments in different atmospheres revealed a stability up to at least 300 °C [M. Budde *et al.*, Phys. Rev. Mater. **4**, 124602 (2020)]. The fabrication of SnO/ $\beta$ -Ga<sub>2</sub>O<sub>3</sub> *pn*-heterojunctions has not been reported to date.

In this study, we fabricate and characterize vertical *pn*-heterojunction diodes using MBE-grown SnO layers on unintentionally *n*-type doped ( $n \approx 3 \cdot 10^{17}$  cm<sup>-3</sup>),  $\approx 680$   $\mu$ m-thick  $\beta$ -Ga<sub>2</sub>O<sub>3</sub> ( $\bar{2}01$ ) substrates grown from the melt [A. Kuramata *et al.*, Jpn. J. Appl. Phys. **55**, 1202A2 (2016)]. 5 mm  $\times$  5 mm-large pieces diced from the  $\beta$ -Ga<sub>2</sub>O<sub>3</sub> ( $\bar{2}01$ ) substrate wafer were metallized by electron beam evaporation with 20 nm Ti/100 nm Au followed by a rapid thermal annealing for 1 minute at 470 °C in nitrogen atmosphere to form an ohmic back contact to the *n*-type Ga<sub>2</sub>O<sub>3</sub>. Prior to growth the substrates were *in situ* cleaned using an oxygen plasma [0.5 standard cubic centimeters per minute (sccm), 300 W] at a substrate heater temperature of 400 °C. Higher temperatures could be critical for the backside metallic contacts. Two samples (G015 and G016) were grown at 400 °C using oxygen fluxes of 0.15 sccm and 0.16 sccm, respectively. For both runs a plasma power of 300 W and a metallic Sn flux with a beam equivalent pressure of  $\approx 1 \cdot 10^{-7}$  mbar and a growth time of 40 minutes were used. A piece of (insulating) *c*-plane Al<sub>2</sub>O<sub>3</sub> was co-loaded in each run as a reference sample (A015, A016).

The X-ray diffraction measurements shown in Fig. 1 confirm the presence of SnO in all

<sup>1</sup> Felix-Bloch-Institut für Festkörperphysik, Universität Leipzig, Leipzig, Germany

samples. Laser reflectometry was measured on the reference films A015 and A016 during growth, indicating a total SnO thickness of about 200 nm and 170 nm, respectively. Hall measurements in the van-der-Pauw geometry indicate a sheet resistance of 184 k $\Omega$  and 46 k $\Omega$  for the SnO films of samples A015 and A016, respectively. *P*-type transport was confirmed for both samples, with a lower hole concentration ( $p$ ) for A015 ( $p=1.1 \cdot 10^{18} \text{ cm}^{-3}$ ,  $\mu=1.6 \text{ cm}^2/\text{Vs}$ ) compared to A016 ( $p=1.0 \cdot 10^{19} \text{ cm}^{-3}$ ,  $\mu=0.8 \text{ cm}^2/\text{Vs}$ ). Due to parallel conduction in the Ga<sub>2</sub>O<sub>3</sub> substrate (with sheet resistance on the order of few Ohms) such measurements would not provide meaningful results on samples G015 and G016, for which we, however, expect SnO transport properties similar to those of samples A015 and A016, respectively.

Square shaped,  $55 \times 55 \mu\text{m}^2$ - and  $180 \times 180 \mu\text{m}^2$ -large 20 nm Ti/100 nm Au top contacts were lithographically defined on the *p*-type SnO layer of samples G015 and G016 using a photoresist mask, electron beam evaporation, and lift-off. No post-an-

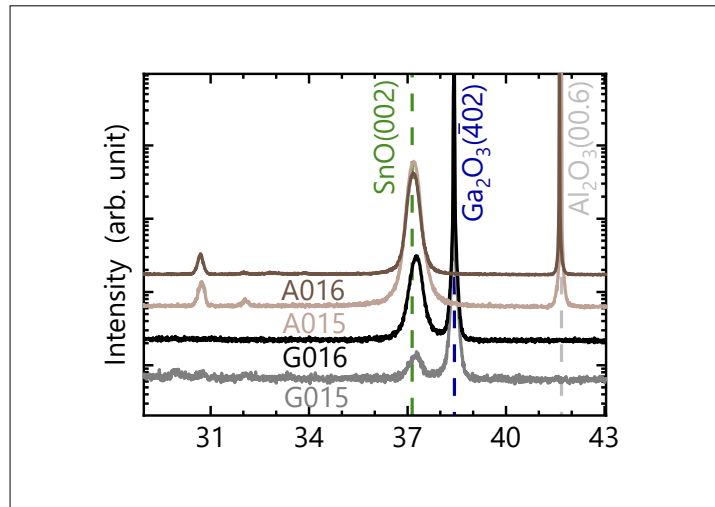
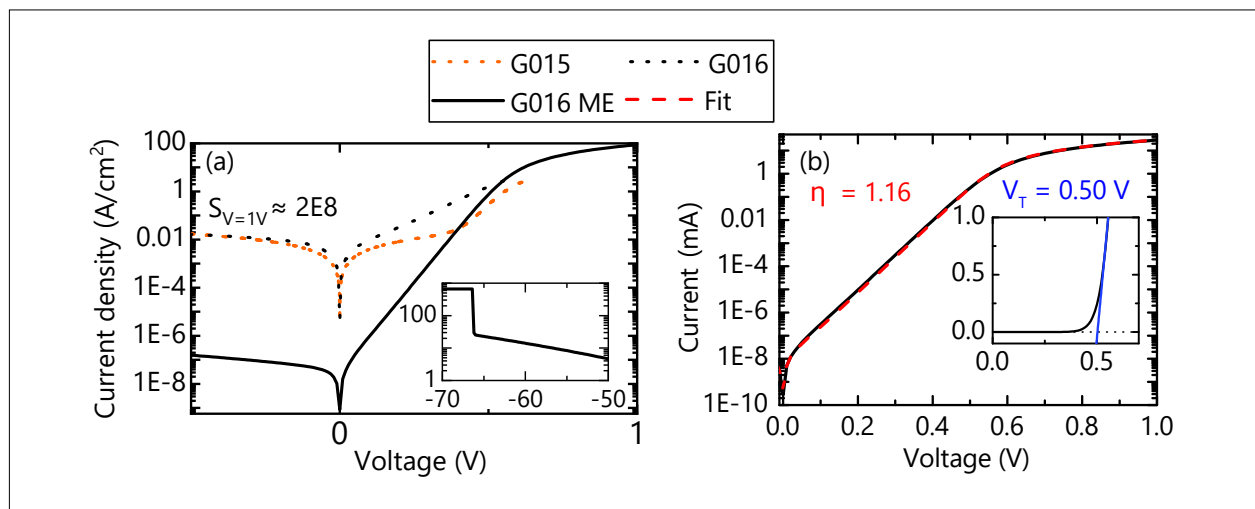


**Fig. 1.**  $2\theta$ - $\omega$  scans of samples A015, A016, G015 and G016. The reflexes of Ga<sub>2</sub>O<sub>3</sub>, Al<sub>2</sub>O<sub>3</sub> and SnO are indicated with blue, grey and green dashed lines, respectively.

nealing was conducted on the top contacts to prevent the transformation of the *p*-type SnO layer into *n*-type SnO<sub>2</sub>. Current-voltage (IV) curves of *pn*-heterojunction diodes fabricated on samples G015 and G016 with voltage applied to the  $180 \times 180 \mu\text{m}^2$  top

**Fig. 2.** (a) IV curves of samples G015, G016 and G016 ME (mesa etched) measured on  $180 \times 180 \mu\text{m}^2$  contacts in a semi-logarithmic plot including the rectification ratio for G016 ME at 1V. The insets show a micrograph of a contact after mesa etching and the breakdown of a  $55 \times 55 \mu\text{m}^2$  diode at  $-66\text{V}$ . (b) IV curve of sample G016 ME together with the fit (red) using the Shockley equation. The inset shows the curve on a linear scale including a linear fit (blue) to determine the turn-on voltage ( $V_T$ )



contacts and grounded bottom contact are shown in Fig. 2(a) and indicate the rectification expected for a  $pn$ -diode but with a high reverse leakage current and thus low rectification. Despite a slightly different turn-on behavior, no distinct differences between both samples are visible. Thus, for further characterization of the diodes, we will focus on sample G016 in this report.

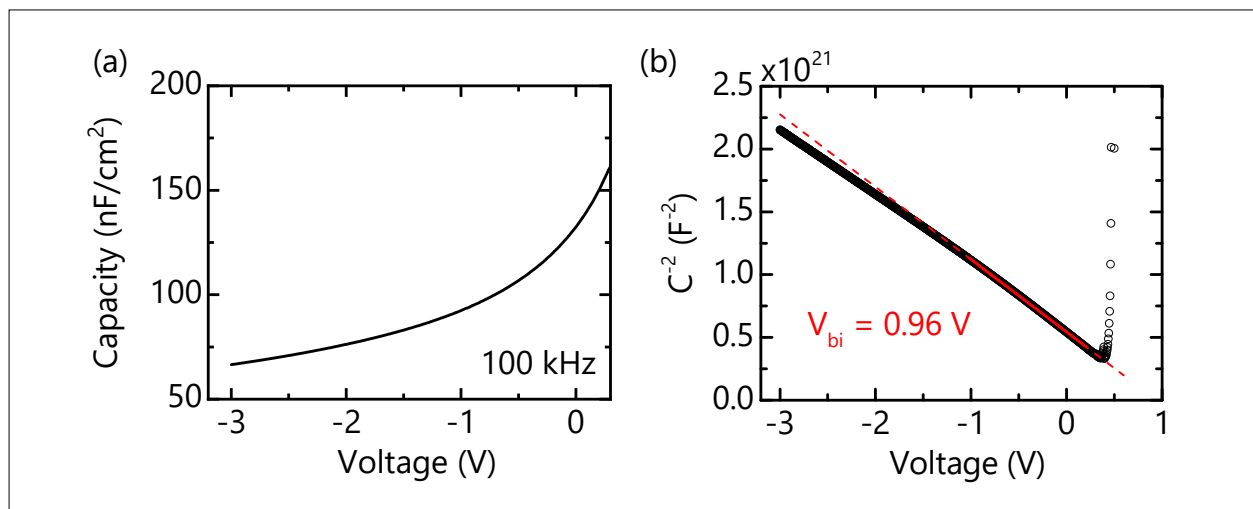
Mesa etching of the SnO layer was performed to isolate the top contacts using a lithographically-defined resist mask and an inductively coupled plasma inside a reactive ion etching system. As a result, a drastic decrease of the reverse (leakage) current [see the curve for sample G016 ME in Fig. 2(a)] and a high rectification ratio of about  $2 \cdot 10^8$  at 1 V were achieved. This improvement can be explained by reverse current spreading in the SnO layer with an effective area for reverse leakage on the order of the entire substrate area for the unetched sample compared to only the mesa size for the mesa-isolated top contacts.

The IV characteristics of this mesa-isolated diode can be described by the Shockley

equation, resulting in the fit shown by a red dashed line in Fig. 2(b). An ideality factor of 1.16 can be extracted for sample G016 ME. The extracted rectification ratio and ideality factor both indicate a high quality of the grown  $pn$ -heterostructures. In addition, a series resistance of  $12 \Omega$  (corresponding to a differential specific on-resistance of  $3.9 \text{ m}\Omega \text{ cm}^2$ ) and a turn-on voltage ( $V_T$ ) of about 0.5 V were determined for the diode.  $V_T$  was extracted using a linear fit of the forward bias [see inset of Fig. 2(b)].

A capacitance-voltage (CV) measurement at 100 kHz, shown in Fig. 3(a), is also in qualitative agreement with the presence of a  $pn$ -junction. In Fig. 3(b) the reciprocal of the square of the capacitance is plotted, allowing the evaluation of the built-in voltage ( $V_{bi}$ ) and the net doping density ( $N_t$ ).  $V_{bi}$  is about 0.96 V and  $N_t$  about  $2.3 \cdot 10^{17} \text{ cm}^{-3}$ . The latter is mainly defined by the doping density in  $\text{Ga}_2\text{O}_3$  as a result of the significantly higher hole density of the SnO layer, placing the depletion region mainly into the  $\text{Ga}_2\text{O}_3$ . Reverse breakdown of a mesa-isolated ( $55 \mu\text{m}$ )<sup>2</sup> diode on sample G016 occurred at  $-66 \text{ V}$  [see inset of Fig. 2(a)]. At this voltage

**Fig. 3.** (a) Capacitance-voltage measurements of sample G016 ME on a  $180 \times 180 \mu\text{m}^2$  diode at 100 kHz up to a forward bias of 0.3V. (b) Plot of  $1/C^2$  over the voltage including a linear fit (red) to calculate the built-in voltage ( $V_{bi}$ ) and net doping concentration  $N_t$ .





and a donor concentration equalling the extracted  $N_d$ , approximately 570 nm of the  $\text{Ga}_2\text{O}_3$  are depleted, resulting in average and peak breakdown electric fields of 1.15 and 2.30 MV/cm within the  $\text{Ga}_2\text{O}_3$ . These values are appreciable but well below the theoretical limit of  $\text{Ga}_2\text{O}_3$  (8 MV/cm), likely related to field spikes at the corners of the square shaped contacts as well as missing field plates.

In summary, we have demonstrated that SnO forms a  $pn$ -heterodiode with  $\beta\text{-Ga}_2\text{O}_3$ . After mesa isolation a rectification of  $2 \cdot 10^8$  at  $\pm 1$  V, an ideality factor of 1.16, differential

specific on-resistance of  $3.9 \text{ m}\Omega \text{ cm}^2$ , built-in voltage of 0.96 V, and a reverse breakdown voltage of 66 V (average breakdown field of 1.15 MV/cm in the depletion region) were measured. By reducing the donor concentration of the  $\text{Ga}_2\text{O}_3$  (to increase the depletion layer thickness) as well as improving the contact geometry (to reduce field crowding) the breakdown voltage can be increased towards values required in high-voltage devices.

This work was performed within the Leibniz-ScienceCampus "GraFOx", funded by the Leibniz Association.

# Towards Ge-rich Ge-Sb-Te alloys fabricated by molecular beam epitaxy

S. Cecchi, D. Kriegner<sup>1,2</sup>, F. Arciprete<sup>3</sup>, E. Zallo, V. Holy<sup>1,4</sup>, R. Calarco

An important part of near future information technology will be based on the implementation of a giant network of electronic smart systems known as Internet of Things. The huge amount of generated data needs to be stored by efficient embedded non-volatile memory devices. Memories based on phase change materials are suitable candidates in most cases. For automotive application, however, the well known ternary alloy  $\text{Ge}_2\text{Sb}_2\text{Te}_5$  (GST225) is not compatible, as it would suffer from poor data retention. Instead, Ge-rich Ge-Sb-Te (GST) alloys are the most promising materials to match the higher working temperature requirements. In this context, the goal of the present study is to explore the synthesis of epitaxial Ge-rich GST films by molecular beam epitaxy (MBE). Epitaxial GST films have been shown to exhibit superior structural quality and offer thus a unique platform to investigate film properties with very precise control over composition. Moreover, MBE allows the fabrication of complex heterostructures.

The epitaxial GST films described in the following were fabricated by MBE on  $\text{Si}(111)-(\sqrt{3} \times \sqrt{3})\text{R}30^\circ\text{-Sb}$  passivated surfaces. Starting from the deposition conditions for the composition GST225, well-established in our lab [S. Cecchi *et al.*, *APL Mater.* **5**, 026107 (2017)], an about three times larger flux of Ge was provided. All the other growth parameters were unchanged. The epitaxial quality during growth was checked by reflection high-energy electron

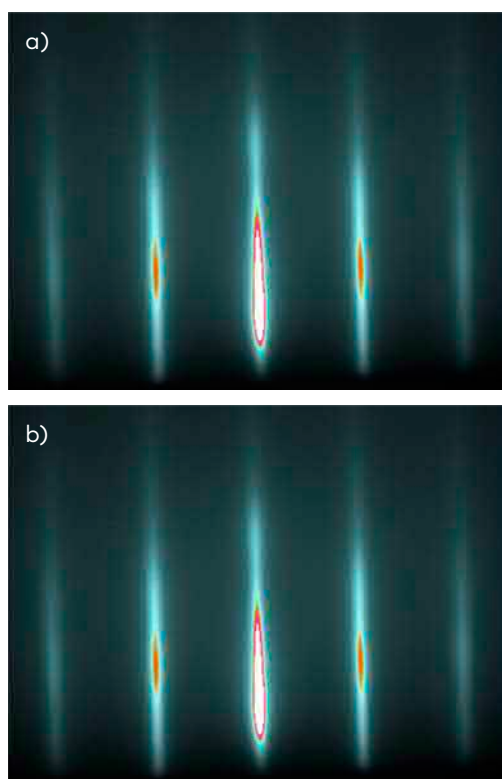


**Fig. 1.** RHEED images of (a) GST225 and (b) Ge-rich GST epitaxial films along a  $\text{Si}(1\bar{1}0)$  azimuth of the  $(\sqrt{3} \times \sqrt{3})\text{R}30^\circ\text{-Sb}$  passivated surface. The images were taken at the end of each deposition.

diffraction (RHEED). RHEED images acquired after growth are shown in Figure 1. A well defined streaky pattern characterizes the reference GST225 sample [see Fig. 1(a)], testifying its optimized quality. Figure 1(b) presents the image obtained for Ge-rich conditions. In this case, broader streaks are

1 Department of Condensed Matter Physics, Faculty of Mathematics and Physics, Charles University, Praha, Czech Republic.

2 Institute of Solid State and Materials Physics, Technische Universität Dresden, Dresden, Germany.

3 Dipartimento di Fisica, Università di Roma “Tor Vergata”, Rome, Italy.

4 CEITEC at Masaryk University, Brno, Czech Republic.

superposed on weak ring features, a clear sign of reduced epitaxial quality.

To characterize the structural properties of the grown material, we performed X-ray diffraction (XRD) and Raman spectroscopy measurements. The XRD radial scans of the samples are shown in Fig. 2 (dotted curves). The curve of the GST225 sample has the common features of epitaxial GST, as reported in previous studies [V. Bragaglia *et al.*, *Sci. Rep.* **6**, 23843 (2016)]. Remarkably, the XRD profile of the second sample is qualitatively similar. The sharp peaks at  $\approx 2, 4$  and  $6 \text{ \AA}^{-1}$  correspond to the 111, 222, and 333 Bragg reflections of the Si substrate, respectively. Together with the main reflections of the GST crystal at  $\approx 1.8, 3.6$  and  $5.4 \text{ \AA}^{-1}$ , additional broader features are present. This pattern results from the layered structure typical of MBE grown GST, in which ordered layers of vacancies (VL) are formed. The separation between the main and VL reflections is inversely proportional to the average thickness of the GST blocks in the film, providing a simple tool to estimate its average composition (shown in the figure). Notably, the smaller  $Q_z$  separation found for the sample grown with higher Ge flux (dark red curve) corresponds to a composition close to  $\text{Ge}_5\text{Sb}_2\text{Te}_8$  (GST528). In agreement with the RHEED data, the reduced crystal quality of the GST528 sample is revealed here by its broader and less intense main reflections.

In analogy to our previous modeling of  $\text{Sb}_{2+x}\text{Te}_3$  epitaxial films [S. Cecchi *et al.*, *Adv. Funct. Mater.* **29**, 1805184 (2019)], we developed simulations of the diffraction signal of layered GST films. This task is particularly complex, since epitaxial GST samples are characterized by a certain degree of compositional disorder, i. e. different  $\text{Ge}_x\text{Sb}_2\text{Te}_{3+x}$  blocks are stacked in the film. The model is based on the description of random sequences of  $\text{Ge}_x\text{Sb}_2\text{Te}_{3+x}$  blocks in the framework of kinematical theory. Following recent density functional theory (DFT) calculations (not shown here), mirror-sym-

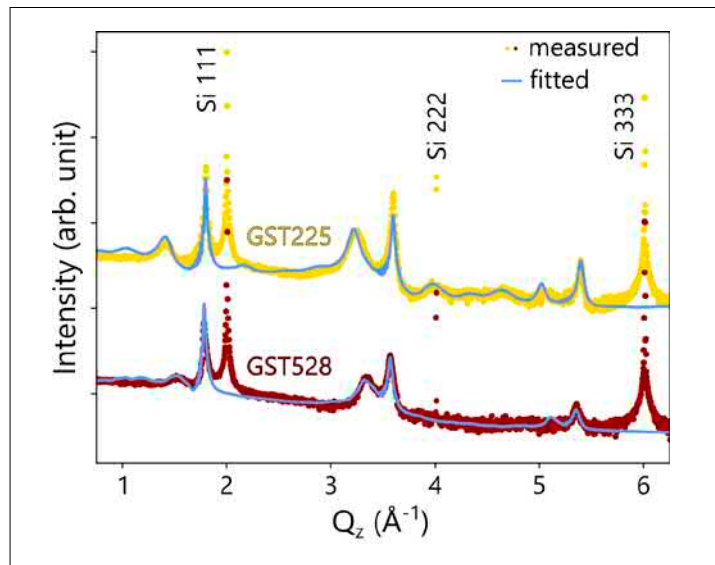


**Fig. 2.** XRD radial scans of the GST films grown on Si(111). The curves are plotted on a logarithmic scale and vertically shifted for clarity. The fitted curves (solid light blue) are superposed on the measurements. The estimated alloy compositions are also shown.

metric building blocks were considered. A simplified description of the  $\text{Ge}_x\text{Sb}_2\text{Te}_{3+x}$  lamellas, consisting of five atomic plane distances, was adopted. The GST composition in the sequences is set in the model by a distribution function, given as an entry parameter. In this work, the  $\text{Ge}_x\text{Sb}_2\text{Te}_{3+x}$  block distributions measured by scanning transmission electron microscopy (STEM) for GST225 and GST528 samples (not shown here) were used.

The fitted curves are plotted in Fig. 2 (solid light blue lines) along with the experimental ones. The main features in the radial scans of the two samples are well reproduced. It is noteworthy that these simulations reveal differences in the atomic distances between the two compositions. As an example, a slight increase of the Te-Te distance at the gap between neighboring blocks was recorded for the GST528 sample, which is in agreement with DFT predictions. Hence, the present analysis may shed light on the average structure of  $\text{Ge}_x\text{Sb}_2\text{Te}_{3+x}$  lamellas

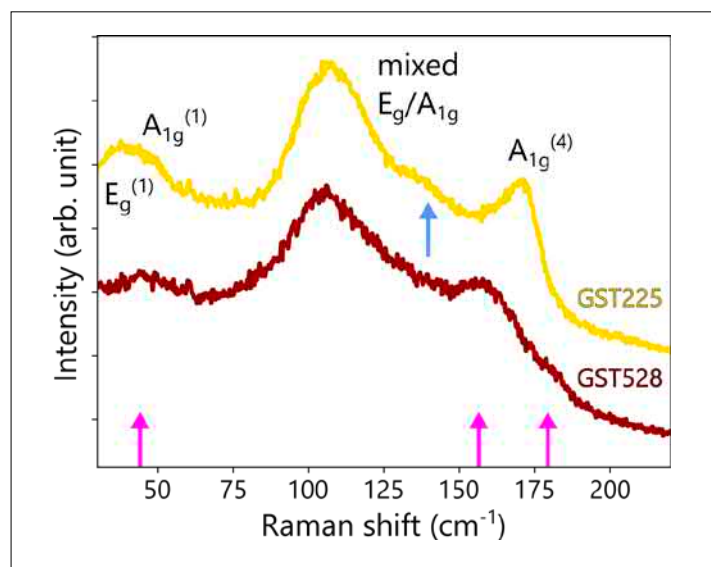


**Fig. 3.** Raman spectra of the GST films grown on Si(111). The spectra of GST225 and GST528 samples are plotted in yellow and dark red, respectively. The curves are vertically shifted for clarity. The main differences between the samples are indicated with arrows (light blue and magenta).

as a function of composition, which can hardly be gained directly from STEM micrographs.

In the past, we have successfully used Raman spectroscopy to analyze the structure of Ge-Sb-Te materials and heterostructures. Interestingly, for epitaxial  $\text{Sb}_{2+x}\text{Te}_3$  alloys we achieved a rapid assessment of the film composition [S. Cecchi *et al.*, *Adv. Funct. Mater.* **29**, 1805184 (2019)]. Here, we show the potential to develop a similar compositional analysis based on Raman spectroscopy also for epitaxial GST films. The experimental Raman spectra of the GST225 (yellow curve) and GST528 (dark red curve) samples are shown in Fig. 3.

The spectrum of GST225 is characterized by two major contributions, a broader mode at  $\approx 108 \text{ cm}^{-1}$  (overlap of  $E_g$  and  $A_{1g}$  modes) and a sharper one at  $\approx 172 \text{ cm}^{-1}$  ( $A_{1g}^{(4)}$  mode). At low frequency, two additional phonons are predicted, the  $E_g^{(1)}$  mode at  $33 \text{ cm}^{-1}$  and the  $A_{1g}^{(1)}$  mode at  $48 \text{ cm}^{-1}$ , which are expect-

ed in the experimental spectra only for samples with higher degree of structural ordering (or after thermal annealing). In Fig. 3 the features in the spectrum of the GST225 sample are labeled correspondingly. The modes at low frequency are not well defined, which highlights the residual intrinsic disorder affecting this material system. An additional broad feature is seen at  $\approx 138 \text{ cm}^{-1}$  (see light blue arrow), which does not correspond to the predicted vibrations of GST alloys. Instead, as reported by Cecchi *et al.* [2019, *op. cit.*], in this region the  $E_g$  mode of Sb layers is located, suggesting a possible slight excess of Sb in the sample.

The change in composition has a clear effect on the spectrum of GST528 (see magenta arrows). For frequencies above  $150 \text{ cm}^{-1}$  at least two vibrations are active at  $\approx 156 \text{ cm}^{-1}$  and  $\approx 180 \text{ cm}^{-1}$ . The peak at higher frequency has most likely the same character as the  $A_{1g}^{(4)}$  mode of GST225, and it blueshifts in accord with the thicker average GST block in the GST528 film. The origin of the more intense mode at lower frequency is at present under investigation. The central part of the spectrum appears broader and less intense, a result of the superposition of more features compared to GST225, while no significant shift is measured. Thus, this feature is consistent with the structural complexity exhibited by GST alloys with larger average block size. The increased disorder occurring in this sample, as shown by RHEED and XRD measurements, weakens the low frequency contributions. Still, in this region a weak mode is visible at  $\approx 44 \text{ cm}^{-1}$ .

In summary, we reported on the first investigation of epitaxial GST films far from the well known GST225 alloy. A straightforward approach to achieve Ge-rich compositions was attempted. A GST528 film with reduced epitaxial quality was obtained. We developed and tested XRD simulations suitable for the analysis of layered GST films as an important tool for studies of epitaxial GST with substantial deliberate variations in composition. Raman spectroscopy is

shown to be very sensitive to the compositional changes in the samples. The support of DFT calculations (ongoing) is necessary to attribute the additional vibrations found in the spectrum of GST528. In the future we will explore more elaborate epitaxial strategies to grow Ge-rich GST alloys.

The present work has been supported by the European Union in the framework of the project BeforeHand. This project has received funding from the European Union's Horizon 2020 research and innovation programme under grant agreement No 824957.

# Artificial quantum dot molecules assembled by atom manipulation

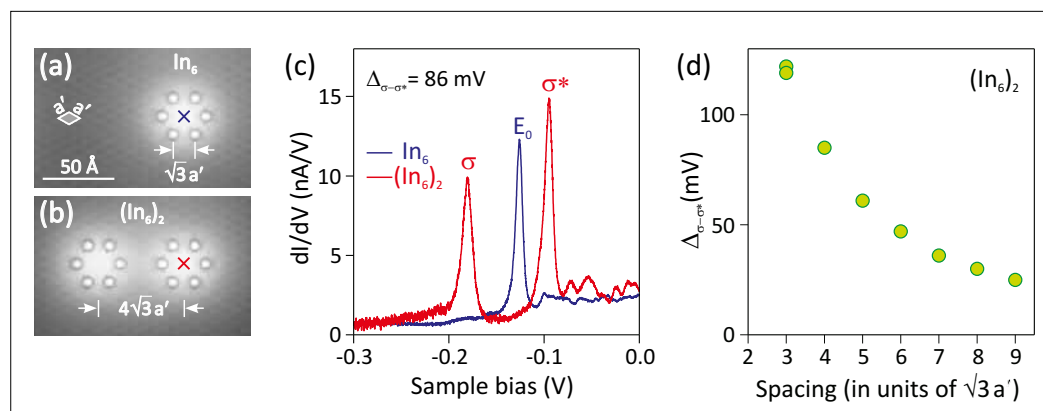
V. D. Pham, S. C. Erwin<sup>1</sup>, K. Kanisawa<sup>2</sup>, S. Fölsch

In our effort to create artificial quantum structures on semiconductor surfaces we continued to explore quantum dot molecules of strictly defined size, composition, and symmetry. Here, we highlight current activities on quantum dot hexamers resembling the structure of benzene. The experimentally observed energy level structure is indeed consistent with hexagonal symmetry. These artificial benzene molecules may serve as building blocks for extended assemblies with honeycomb structure, offering a way to realize artificial graphene on a semiconductor surface.

To fabricate the molecules we apply our well-proven approach of atom manipula-

tion on the InAs(111)A surface using scanning tunneling microscopy (STM) at a sample temperature of 5 K. This surface offers two important ingredients for the fabrication of atomic-scale quantum dots, namely an intrinsic surface state and the presence of native In adatoms (concentration roughly 0.005 monolayers) that can be repositioned by the STM tip with sub-Ångström precision. The In adatoms are positively charged and thereby confine surface-state electrons. InAs(111)A exhibits a  $2 \times 2$  In vacancy reconstruction with a hexagonal surface unit cell and a lattice constant of  $a' = 8.57 \text{ \AA}$ . The In vacancies define the allowed sites of native In adatoms.

**Fig. 1.** (a) Constant-current STM topography image (0.1 nA, 0.1 V) of an InAs(111)A surface area with a hexagon-shaped dot assembled from six In adatoms, the side length is  $\sqrt{3}a'$  with  $a' = 8.57 \text{ \AA}$  the lattice constant of the  $2 \times 2$  reconstructed surface. (b) Same as (a) with a second  $\text{In}_6$  dot added at a center-to-center spacing of  $4\sqrt{3}a'$ . (c) Conductance spectra recorded with the STM tip fixed above the center of the first  $\text{In}_6$  dot (a) before (blue curve) and (b) after adding the second  $\text{In}_6$  dot (red curve); the isolated dot (artificial atom) exhibits a single "atomic" state at  $E_0 = -126 \text{ meV}$  whereas a bonding ( $\sigma$ ) and an antibonding state ( $\sigma^*$ ) emerge for the dimer. (d)  $\sigma - \sigma^*$  splitting  $\Delta_{\sigma-\sigma^*}$  measured for the  $(\text{In}_6)_2$  dimer versus spacing between the two  $\text{In}_6$  dots.



<sup>1</sup> Center for Computational Materials Science, Naval Research Laboratory, Washington DC, USA.

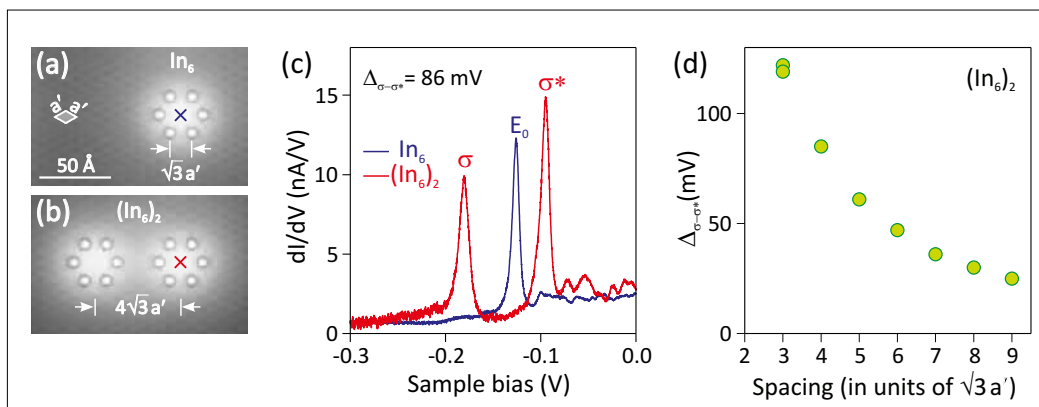
<sup>2</sup> NTT Basic Research Laboratories, NTT Corporation, Atsugi, Kanagawa, Japan.

The STM topography image in Fig. 1(a) shows six In adatoms arranged into a hexagon with a side length of  $\sqrt{3}a'$ . The increased apparent height within the hexagon-shaped  $\text{In}_6$  dot is due to the electrostatic potential induced by the charged adatoms which locally increases the density of states available for the tunnel process. Holding the tip fixed at the  $\text{In}_6$  dot center and recording the differential tunneling conductance  $dI/dV$  (as a measure for the density of electronic states) yields a sharp resonance peak [blue spectrum in Fig. 1(c)] indicating a confined state at  $E_0 = -126$  meV below the Fermi level of the sample. This observation is in line with our previous findings for quantum dots in terms of linear In adatom chains showing that for short chains ( $N \geq 6$ ) the lowest-lying state first emerges at about 0.1 eV below the Fermi level [S. Fölsch *et al.*, Nat. Phys. **9**, 505 (2014)]. In the following, we will employ the  $\text{In}_6$  dot in Fig. 1(a) as an artificial atom that provides a well-defined “atomic” state.

The simplest case of a quantum dot molecule is a dimer of two artificial atoms placed side by side, see the STM image in Fig. 1(b) where the center-to-center spacing was chosen to be  $4\sqrt{3}a'$ . The corresponding spectrum in panel (c) reveals the emergence of a bonding ( $\sigma$ ) and an antibonding ( $\sigma^*$ ) state due to the quantum coupling between the two artificial atoms. For this specific spacing the  $\sigma - \sigma^*$  splitting amounts to  $\Delta_{\sigma-\sigma^*} = 86$  mV. Figure 1(d) shows the smoothly decreasing quantum coupling as the center-to-center spacing is increased from 3 to 9 in units of  $\sqrt{3}a'$ . All these observations are consistent with our earlier findings for dimers of linear  $\text{In}_6$  chains.

Given this, we are in a position to construct more complex molecules. Consider, for example, the molecule in Fig. 2(a) which consists of six artificial atoms ( $\text{In}_6$  dots with  $\sqrt{3}a'$  side length) in a hexagonal arrangement, thus resembling the structure of benzene. The center-to-center spacing is again

**Fig. 2.** (a) STM topography image (0.1 nA, 0.1 V) of a hexagonal  $(\text{In}_6)_6$  molecule composed of six artificial atoms in terms of  $\text{In}_6$  dots. The spacing between the artificial atoms is again  $4\sqrt{3}a'$ . (b) Conductance spectra taken with the STM tip fixed above (blue curve) and in between of the artificial atoms (red curve); the energies of the four lowest states associated with the peaks labeled #1 to #4 are consistent with the LCAO energies assuming an on-site energy  $\alpha = -180$  meV and a hopping energy  $\beta = -45$  meV, the latter being roughly half of the  $\sigma - \sigma^*$  splitting found for the bare dimer (Fig. 1). The two peaks at higher energy are attributed to confined states whose wave function symmetry is equivalent to p atomic orbitals in  $\sigma$  bonding configuration, with the state labeled p- $\sigma$  having fully bonding character. (c) Energy level structure within the simple LCAO picture.



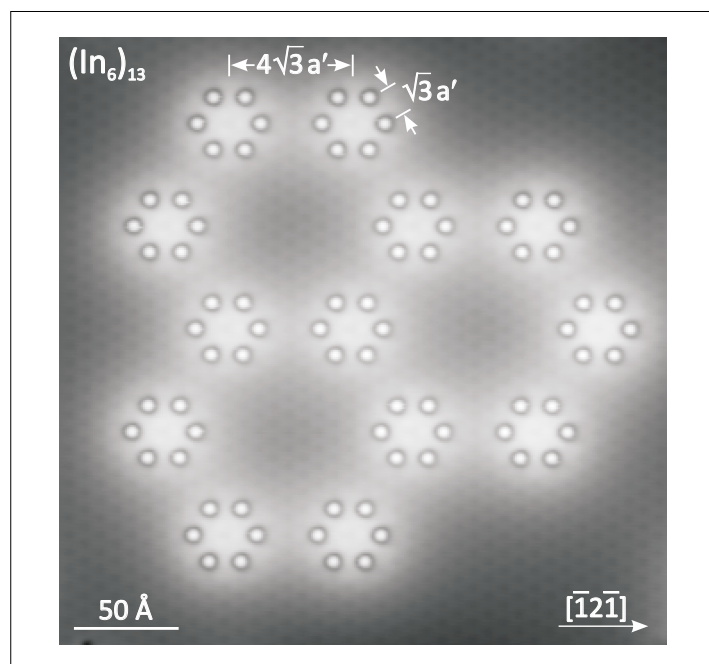


**Fig. 3.** STM topography image (0.1 nA, 0.1 V) of thirteen  $\text{In}_6$  dots arranged into threefold symmetry to resemble the structure of the polycyclic molecule phenalene. The spacing between the artificial atoms ( $\text{In}_6$  dots) is  $4\sqrt{3}a'$ , as in Figs. 1 and 2.

$4\sqrt{3}a' = 59.37 \text{ \AA}$  as for the dimer in Fig. 1(a). The spectra in Fig. 2(b) were taken on top (blue curve) and in between of the artificial atoms (red curve). They reveal a series of conductance peaks of which the four lowest (numbered #1 to #4) can be associated with the level structure of a hexamer with hexagonal symmetry. The level structure – shown in Fig. 2(c) and indicated by vertical bars in Fig. 2(b) – is derived from a simple linear-combination-of-atomic-orbitals (LCAO) picture assuming  $s$  “atomic” orbitals. This assumption is reasonable because the corresponding state labeled  $E_0$  in Fig. 1(b) is the ground state associated with the confining quantum dot potential. Fitting the observed energies to this level structure yields a hopping energy of  $\beta = -45 \text{ meV}$ . This value is in good agreement with the hop-

ping energy  $-e\Delta_{\sigma-\sigma^*}/2 = -43 \text{ meV}$  found for the dimer in Figs. 1(a) and (b). The two conductance peaks above peak #4 in Fig. 2(b) we attribute to confined states with a wave function symmetry equivalent to  $p$  orbitals in  $\sigma$  bonding geometry. This is especially apparent for the state labeled  $p-\sigma$  because it shows zero (maximum) probability density on top of (between) the artificial atoms, consistent with fully bonding  $p$  orbital character. Similar behavior we observed in hexagonal ring structures on  $\text{InAs}(111) \text{ A}$  [V. D. Pham *et al.*, *Phys. Rev. Lett.* **123**, 066801 (2019)] which exhibit quantum coupling along a close path just like the artificial molecule depicted in Fig. 2(a).

Figure 3 demonstrates a first step towards more extended polycyclic molecules. Here, thirteen artificial atoms (involving  $13 \times 6 = 78$  In adatoms in total) were assembled into a threefold arrangement resembling the structure of real phenalene. Also for this extended artificial molecule, we find that the level structure can be understood within LCAO. In this case, however, the coordination of the artificial atoms within the molecule is not equivalent [contrasting the bare hexamer case in Fig. 2(a) where the coordination of all artificial atoms is equivalent]. This makes it necessary to consider the effect of the local electrostatic potential induced by the charged In adatoms. Technically this is done by (i) calculating the potential screened by the surface-state electrons, and (ii) accounting for the varying potential by implementing different on-site energies of the respective artificial atoms in the LCAO eigenvalue problem. Our ongoing work shows that this calculation scheme is successful to rationalize the observed level structure of various different kinds of quantum dot assemblies, emphasizing the importance to include the effect of electrostatics in the description of artificial quantum structures integrated on a semiconductor surface.



# *In situ* transmission electron microscopy of disorder-order transition in epitaxially stabilized FeGe<sub>2</sub>

M. Terker, L. Nicolai, S. Gaucher, J. Herfort, A. Trampert

Metastable crystalline phases can be stabilized in thin films by means of epitaxial constraint imposed by hetero-interfaces. One such example has been observed in the case of solid-phase epitaxy of semiconducting Ge on ferromagnetic Fe<sub>3</sub>Si. For this nominally lattice matched cube-on-cube system strong diffusion of Fe into the Ge film is detected at relatively low crystallization temperatures and instead of pure Ge with a diamond structure an epitaxially stabilized phase of vacancy ordered tetragonal FeGe<sub>2</sub> described by the P4mm space group was obtained.

*In situ* high-resolution transmission electron microscopy (HRTEM) was used to observe the dynamics of the solid phase epitaxy process inside the microscope. Based on this study we have found that initial crystallization does not immediately result in the ordered FeGe<sub>2</sub> structure, but that there exists an intermediate state lacking the periodicity corresponding to the vacancy layers of the P4mm phase. In this work we present our *in situ* TEM study of the disorder-order transition to shed light on the role of underlying strain and atomic diffusion during the solid phase epitaxy processes. The initial and final states of the heating experiment are also investigated with atomic resolution high-angle annular dark-field scanning transmission electron microscopy (HAADF STEM) and energy dispersive x-ray spectroscopy (EDX).

For the present study samples were prepared in a molecular beam epitaxy chamber. First, a 3 nm thin cubic Fe<sub>3</sub>Si film is epitax-

ially grown on GaAs (001) substrate. Last, an amorphous (a-) Ge film is deposited at room temperature inside the same growth chamber. Specimens for *in situ* TEM investigations were then prepared using a hybrid approach. For this preparation technique, a cross-sectional sample is first conventionally prepared by mechanical grinding, dimpling and Ar<sup>+</sup>-ion milling. Afterwards, a focused ion-beam (FIB) device is utilized to cut out a lamella from the specimen and transfer it to a MEMS *in situ* heating chip. This avoids the lamella preparation by FIB which generally causes surface damage to the sample.

In order to initiate the crystallization and ordering process the sample is heated from room temperature to 300 °C within 1 min and kept at this temperature. Figure 1(a) summarizes a sequence of HRTEM images of this isothermal annealing experiment taken at different times between 0 and 60 min after reaching the target temperature. At the beginning of the *in situ* recording directly after reaching 300 °C a thin layer has already crystallized at the Ge/Fe<sub>3</sub>Si interface, while the rest of the Ge is still in the amorphous state. This means that a heterogeneous nucleation has taken place whereby the crystallized region appears as thin, coherently grown epitaxial layer, with the crystal structure showing no sign of the vacancy ordered FeGe<sub>2</sub> phase. After 15 min annealing a large part of the Ge film has transformed to the crystalline disordered FeGe<sub>2</sub> phase. At the same time, in the pre-existing FeGe<sub>2</sub> film near the interface to the Fe<sub>3</sub>Si, the occurrence of a periodic modula-

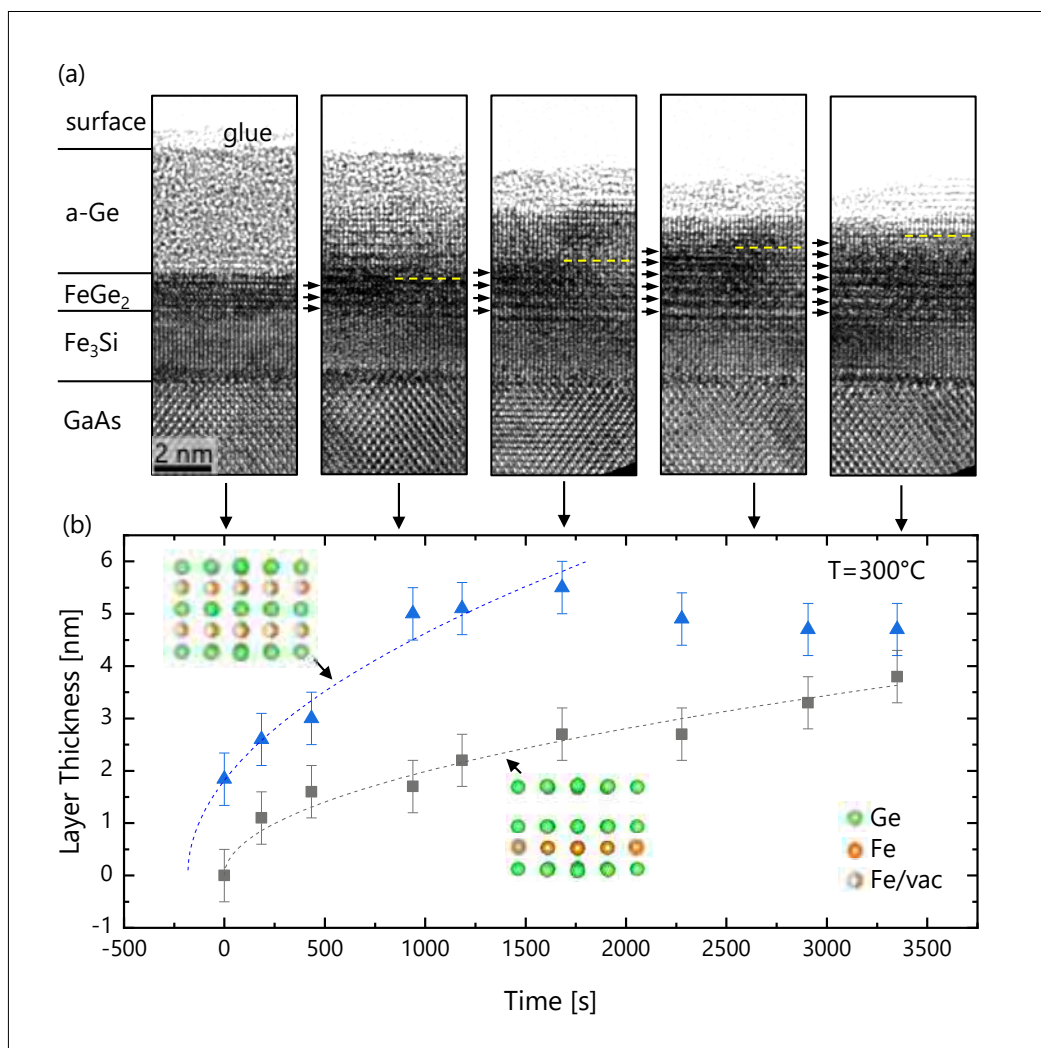


**Fig. 1.** (a) The depicted images show snapshots of an *in situ* annealing experiment at 300 °C. Image after just reaching the target temperature, after 15 min, after 30 min, after 45 min and after 60 min at 300 °C. The yellow dashed line indicates the transformation front of the vacancy ordering and black arrows indicate the periodic layers. (b) The thickness of the different layers in the center of the images is plotted against annealing time. Models showing the atomic structure of the disordered and ordered phase are depicted next to the respective lines in the plot.

tion in the HRTEM contrast becomes visible, which is characteristic for the emergence of the vacancy ordered  $\text{FeGe}_2$  structure. Within the next 15 min the amorphous film has completely crystallized. The remaining amorphous material near the surface results from the epoxy adhesive. The ordered area of the  $\text{FeGe}_2$  layer has also slowly expanded further in a layer-by-layer-like manner. During the next 30 min this process continues until nearly the entire film is

in the ordered phase. The transformation front is marked in the TEM images by a yellow dashed line. The layer-by-layer nature of this disorder-order transition indicates a higher in-plane than out-of-plane transformation rate.

Figure 2(b) summarizes the results of the kinetics of the amorphous-crystalline as well as the disorder-order phase transformations by plotting the thickness of the re-

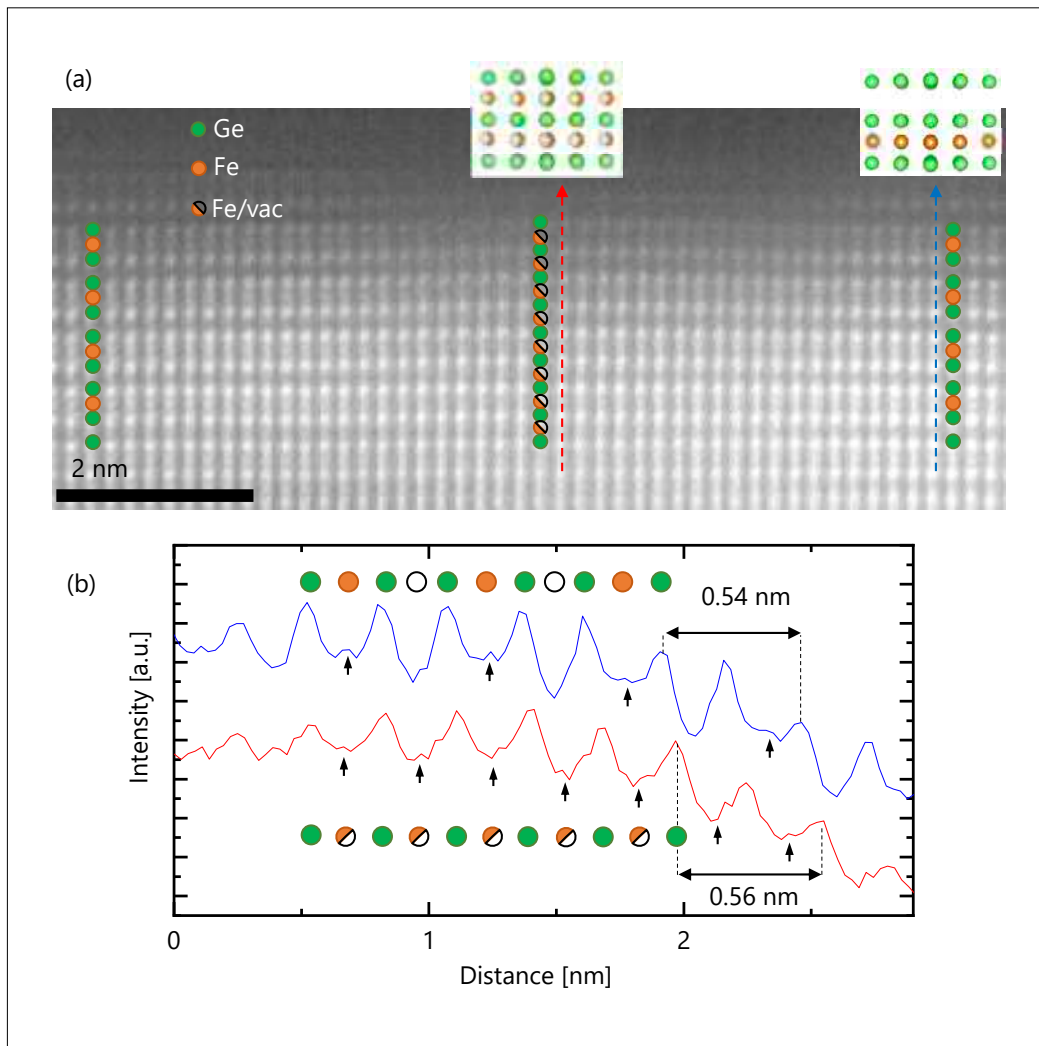


**Fig. 2.** Fourier filtered image, showing a small section of disordered  $\text{FeGe}_2$  surrounded by the layered phase as indicated by green and orange dots. Insets show models of the vacancy ordered and the disordered structure of  $\text{FeGe}_2$ . (b) Intensity line scans along the red and blue arrows in (a). Black arrows indicate the position of Fe peaks.

spective newly formed phase as a function of time. In agreement to our previous observation [M. Terker *et al.* *Semicond. Sci. Technol.* 34, 124004(2019)], the crystallization kinetics can be described by a square root time behavior. The small reduction in thickness after around 30 min can be attributed to a rearrangement of the front morphology by flattening the sample surfaces towards extended (001) terraces. There is a one unit cell reduction in thickness of

the  $\text{Fe}_3\text{Si}$  during the early crystallization of the  $\alpha\text{-Ge}$ . This means that the  $\text{FeGe}_2$  phase does not only grow into the  $\alpha\text{-Ge}$  but also into the  $\text{Fe}_3\text{Si}$  quasi-substrate due to the interdiffusion of Fe and of Ge. As a consequence, an additional  $\text{FeGe}_2$  layer is formed at the interface. The second phase transformation however, is not obviously accompanied by a further  $\text{Fe}_3\text{Si}$  thickness reduction. Therefore, it can be concluded that no significant persistent diffusion of Fe into the

crystallized film is necessary for the transition to the ordered structure. This fact is in agreement with the assumption that the disordered phase has already the  $\text{FeGe}_2$  stoichiometry. On the other hand, the kinetics of the disorder-order phase transformation shows a much slower course compared to the crystallization, except for the start of the annealing where the precrystallized film rapidly changes to the ordered phase. This transition continues after the crystallization process has finished until only a few atomic layers without the ordered structure remain after 60 min.

Figure 2(a) shows a Fourier filtered HAADF STEM image of the sample after the annealing. Towards the left and right side of the image the triple-layer ordering of the  $\text{P4mm FeGe}_2$  phase [see inset in Fig. 2(a)] can be clearly observed. However, in the central part of the image the ordering process doesn't seem to have occurred. Instead Fe and vacancies randomly share the sublattice as depicted in the atomic model at the top of Fig. 2(a). The difference between the center and the edges of the depicted section becomes apparent when looking at the intensity line scans along the red and blue arrow shown in Fig. 2(b). While the blue line again shows the three distinct intensity levels for vacancy, Fe and Ge the red line varies only between two intensities i.e. Ge and Fe/vacancy. Interestingly, these disordered sections reflect a bulging. This demonstrates, that the observed second

phase transition consists of more than just a rearrangement of the Fe and the vacancies. Also the Ge lattice transforms, from equidistant horizontal planes with a spacing of  $0.28 \pm 0.01$  nm to  $0.25 \pm 0.01$  nm across vacancy layers and  $0.29 \pm 0.01$  nm for Fe filled layers. This means that the spacing of two subsequent Ge-layers in the ordered structure is 0.02 nm smaller compared to two layers of the disordered one. Due to the coherent nature of the epitaxial interface an effect on the in-plane lattice spacing is not observed, however, due to the expected larger lattice constant of the disordered crystal the associated epitaxial strain could stimulate the phase transition if that reduced the mismatch towards the  $\text{Fe}_3\text{Si}$ . This would explain why the transformation starts at the interface. Further, the strain at the interface region between the ordered and disordered region could cause the much faster in-plane transformation rate resulting in the layer-by-layer-like transition.

Comparison of the *in situ* TEM results with no-illumination conditions and MBE annealed samples show that the hybrid preparation approach yielded high quality sample with minimal contamination and surface damage while the electron beam only had the effect of additionally heating the sample. Therefore, this hybrid approach could help to apply *in situ* TEM to more atomic level investigations of planar heterostructures.

# Nature of nonradiative recombination at threading dislocations in GaN

J. Lähnemann, V. M. Kaganer, K. K. Sabelfeld<sup>1</sup>, A. E. Kireeva<sup>1</sup>, U. Jahn, C. Chèze, R. Calarco, O. Brandt

GaN-based light-emitting diodes are known to be unaffected by threading dislocation densities on the order of  $10^8 - 10^9 \text{ cm}^{-2}$ , which would prevent any emission in conventional III-V semiconductors. This finding has entailed a long-standing discussion on whether and which types of dislocations in GaN are nonradiatively active. The presence of threading dislocations in GaN layers can be directly visualized by dark spots observed in cathodoluminescence (CL) maps of the layer surface. This lack of emission is commonly taken as direct proof for the nonradiative activity of threading dislocations. However, we have recently shown for dislocations with an edge component that the observed contrast actually stems from the piezoelectric field related to the three-dimensional strain relaxation when the dislocation reaches the surface [V. M. Kaganer *et al.*, *Appl. Phys. Lett.* **112**, 122101 (2018); *ibid.* *Phys. Rev. Appl.* **12**, 054038 (2019)]. To draw conclusions on the nonradiative activity, we have to thus probe dislocations in the bulk of the layer away from the surface, at depths relevant for light-emitting devices.

To address this question, we have recorded CL maps of a GaN/In<sub>0.16</sub>Ga<sub>0.84</sub>N single quantum well (QW) sample in a top-view geometry with the QW buried at a depth of about 650 nm, as sketched in Fig. 1. By varying the acceleration voltage and thus the excitation depth, as well as by comparing the CL intensity profiles around a dislocation for both the emission of the GaN layer and the buried QW, we can examine the role of the dislocation. To quantitatively un-

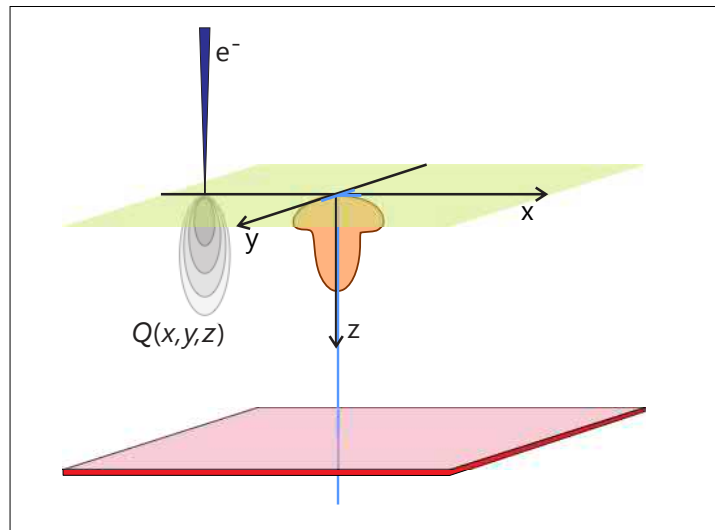


**Fig. 1.** Configuration of the top-view CL experiment at the GaN(0001) surface (upper plane) with the electron beam scanning across the outcrop of a dislocation (vertical line), surrounded by a piezoelectric field (mushroom-like shape) induced by the strain relaxation near the surface. The QW (bottom plane) is buried at a depth of 650 nm.

derstand the dependence of these profiles on acceleration voltage  $V$  and temperature  $T$ , we employ an advanced Monte Carlo scheme to simulate the three-dimensional drift and diffusion of carriers.

Profiles of the CL intensity around an isolated dislocation are obtained from monochromatic maps of the CL intensity and displayed in Fig. 2 for different acceleration voltages and sample temperatures. The broad detection window encompasses the energy range of the near-band-edge emission of either GaN or the QW emission band. The profiles are always extracted along the

<sup>1</sup> Institute of Computational Mathematics and Mathematical Geophysics, Russian Academy of Sciences, Novosibirsk, Russia.

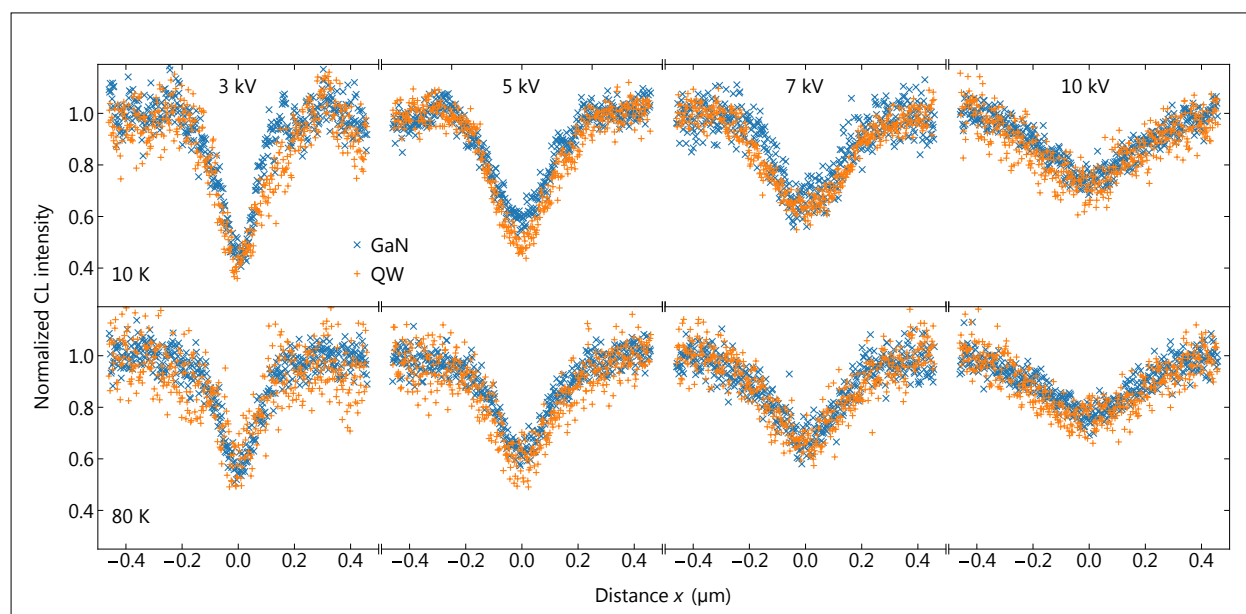
same direction. At both temperatures, the CL intensity contrast decreases with increasing acceleration voltage. Comparing the profiles at the two temperatures, we observe a higher intensity contrast at 10 K.

The increasing contrast with decreasing temperature would be difficult to understand without our Monte Carlo simulations (see below). In fact, both the diffusion length and the generation volume become larger when the temperature is reduced, which should lead to a *decreasing* intensity contrast as the contribution of carriers recombining away from the dislocation is enhanced. However, this effect is overcompensated by the increasing influence of exciton drift in the strain field close to the dislocation outcrop with decreasing temperature. The impact of drift is strongest at 3 kV, where the generation volume does not extend beyond the reach of the strain field, which explains why the temperature dependence is strongest at this acceleration voltage.

The reduced contrast for higher acceleration voltages is a direct consequence of the larger probe volume and the fact that an increasing portion of carriers recombines far from the dislocation. However, this argument applies to both the piezoelectric field close to the surface as well as to the dislocation line itself. As we increase the acceleration voltage, the electrons are scattered to a greater depth beyond the reach of the piezoelectric field, but their lateral spread also increases. With the present experiments alone, we cannot distinguish these two scenarios. Therefore, in the following, we focus on the dislocation-induced contrast in the emission of the buried QW in order to resolve the question whether the dislocation line is nonradiatively active or not.

The intensity profiles for the GaN and the QW emission shown in Fig. 2 coincide, within the accuracy of the measurement, for all measurement conditions. As a first step toward an understanding of these profiles, it

**Fig. 2.** Comparison of CL intensity profiles across a dislocation obtained from monochromatic images of both the GaN emission at 3.48 eV (x) and the (In,Ga)N QW emission centered at 2.7 eV (+) for different temperatures and acceleration voltages as indicated.



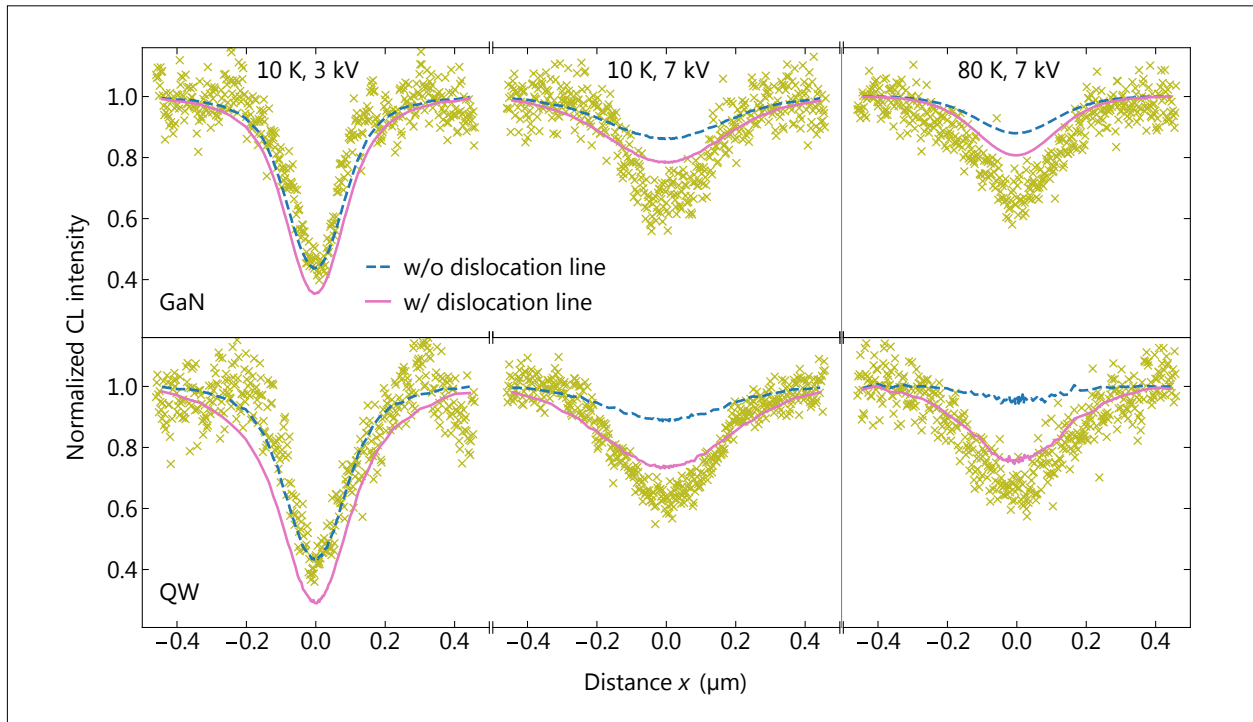


**Fig. 3.** Experimental (symbols) and simulated (lines) profiles of the CL intensity across a dislocation at different temperatures and acceleration voltages for both the GaN emission (top) and the QW emission (bottom). The dashed lines show the results of Monte Carlo simulations that take into account drift, diffusion and the carrier dissociation in the piezoelectric field of the dislocation, while nonradiative recombination at the dislocation line is ignored. For the solid lines, a 3-nm-thick cylinder with infinite recombination velocity representing the dislocation line is added.

is important to recall that in CL spectroscopy excitation is local, but detection is integral. The carrier loss in the piezoelectric field at the surface or at the dislocation line in the GaN matrix is thus also reflected in the QW signal. In contrast, the dislocation line in the QW itself has no directly detectable influence on the QW signal, since only an insignificant fraction of carriers will actually reach the QW at the position of the dislocation after traversing a distance of 650 nm by diffusion. On first sight, it thus seems plausible that the intensity profiles for GaN and the QW are identical. However, on closer examination, the mechanisms contributing to the GaN and QW CL contrasts are actually different.

To understand the profiles quantitatively, we employ a Monte Carlo drift-diffusion model [V.M. Kaganer 2019, *op. cit.*]. Our

model includes the drift of excitons in the strain field of an edge type threading dislocation and accounts for the dissociation of excitons in the resulting piezoelectric field. Additionally, the buried QW is integrated as perfect (radiative) sink for carriers, i. e., we assume that any trajectory reaching the QW plane counts toward the QW emission. Thus, we can concurrently simulate the CL intensity profiles for emission from the top GaN layer and the QW. In the simulations, the experimentally determined generation volume, as well as experimental values for the diffusion length and lifetimes obtained on the same sample are used. For the GaN signal, the depth-dependent reabsorption of the emission in the layer is also accounted for.

In Fig. 3, simulated profiles of the CL intensity, both for the GaN and the QW

emission, are compared to a selection of experimental profiles measured across the dislocation. Two different situations are simulated. First, as above, only the strain field near the surface is considered, and the recombination velocity at the dislocation line is set to zero. Second, the nonradiative recombination at the dislocation is included by adding a cylinder with infinite recombination velocity around the dislocation line. Note that both, the experimental and simulated profiles, are always normalized to the intensity far from the dislocation to highlight the intensity contrast. A lower contrast should not be confused with a higher absolute emission intensity.

As expected, the simulated curves at  $V = 3$  kV, where the generation volume does not extend beyond the reach of the piezoelectric field, are only weakly affected by nonradiative recombination at the dislocation line. However, for an acceleration voltage of 7 kV and especially at  $T = 80$  K, the difference between the simulated curves with active or inactive dislocation line becomes more pronounced, particularly for the QW emission. Here it is of importance that the QW is not directly excited by the scattered electrons, but only by carriers diffusing from the generation volume to the QW. Thus carriers have to traverse up to 650 nm to contribute to the QW emission, while the GaN emission originates from shallower depths.

The simulations ignoring the dislocation line are governed by the impact of the piezoelectric field (dashed lines in Fig. 3). At 7 kV, a large portion of carriers is generated beyond the reach of this field. Due to the shorter diffusion path (average trajectory length) compared with carriers gen-

erated closer to the surface, these carriers contribute more significantly to the QW emission. As a result, the QW emission exhibits a lower intensity contrast compared with the GaN emission. This difference is even more pronounced for a smaller diffusion length, and, at  $T = 80$  K, the simulated profile for the QW is almost flat, which implies that even far from the piezoelectric field only few carriers reach the QW. The small diffusion length at 80 K thus leads to a weak QW signal, and we had to increase the number of trajectories by a factor of 10 compared to the corresponding simulations at 10 K to obtain an adequate statistics, while still having a higher noise level in the simulated profiles. In fact, for  $T > 80$  K, the diffusion length becomes too small to lead to a detectable CL signal of the buried QW at the investigated acceleration voltages, both theoretically and experimentally.

The simulations with active dislocation line (solid lines in Fig. 3) show the opposite behavior. The intensity contrast is higher for the QW compared with the GaN emission. This higher sensitivity of the QW emission for the impact of the dislocation line is again due to the long diffusion path: carriers reaching the QW plane have a higher chance to interact with the dislocation line. This path becomes even longer when the diffusion length is reduced at  $T = 80$  K.

Overall, the experimental intensity contrast, particularly that of the QW signal, can only be explained by assuming that the dislocation line acts as an efficient nonradiative recombination channel. In buried heterostructures such as used in light-emitting devices, the impact of the dislocation line on the luminous efficiency is then controlled by the diffusion length in the active region.



# Antiferromagnetism in $\alpha$ -FeGe<sub>2</sub> spacer layers and its influence on the magnetic interlayer coupling in spin valve structures

D. Czubak, L. Oppermann, S. Gaucher, H. T. Grahn, J. Herfort, M. Ramsteiner

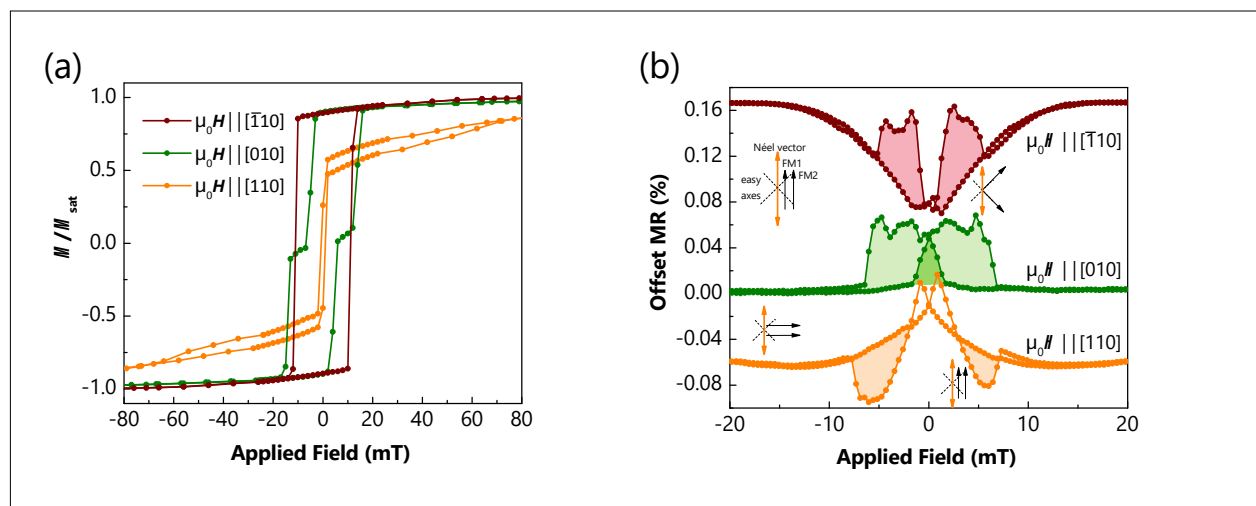
The metastable material  $\alpha$ -FeGe<sub>2</sub> with a layered tetragonal structure is one of the few promising candidates regarding the search for two-dimensional magnetic materials. Previously, we have shown a successful vertical spin valve operation at room temperature of trilayer structures comprising  $\alpha$ -FeGe<sub>2</sub> spacer layers (SL) sandwiched between ferromagnetic Fe<sub>3</sub>Si electrodes (FM1 and FM2), and we were able to identify a strong dependence on the magnetic interlayer coupling between FM1 and FM2.

Here, we study the symmetry of the interlayer coupling in Fe<sub>3</sub>Si/ $\alpha$ -FeGe<sub>2</sub> bilayer as well as Fe<sub>3</sub>Si/ $\alpha$ -FeGe<sub>2</sub>/Fe<sub>3</sub>Si trilayer structures by magnetometry and magnetoresistance measurements in order to gain a deeper insight in the magnetic properties

of  $\alpha$ -FeGe<sub>2</sub>. The Fe<sub>3</sub>Si films are grown by molecular beam epitaxy on GaAs(001) substrates and the  $\alpha$ -FeGe<sub>2</sub> SL by a solid-phase epitaxial process involving interdiffusion between an amorphous Ge layer and an underlying Fe<sub>3</sub>Si layer. For the fabrication of vertical spin valve devices, photolithography and wet etching are used to define quadratic pillars with a surface area of 1  $\mu\text{m}^2$ .

Utilizing  $\alpha$ -FeGe<sub>2</sub>/Fe<sub>3</sub>Si bilayer structures on GaAs(001), we investigated the influence of  $\alpha$ -FeGe<sub>2</sub> on the magnetization reversal of Fe<sub>3</sub>Si films using superconducting quantum interference device (SQUID) magnetometry. Figure 1(a) shows room-temperature magnetization curves of such a bilayer structure with the magnetic field  $\mu_0\mathbf{H}$  applied in the surface plane

**Fig. 1.** (a) Normalized SQUID magnetization curves of a  $\alpha$ -FeGe<sub>2</sub>/Fe<sub>3</sub>Si bilayer along three in-plane crystallographic axes. The hysteresis loops reveal a clear magnetic anisotropy induced by  $\alpha$ -FeGe<sub>2</sub>. (b) Magnetoresistance for a Fe<sub>3</sub>Si/ $\alpha$ -FeGe<sub>2</sub>/Fe<sub>3</sub>Si trilayer structure along the same crystallographic directions (vertically offset for clarity). The spin valve signals (shaded areas) confirm the anisotropy and exhibit even a sign reversal (see negative signal along the [110] direction)



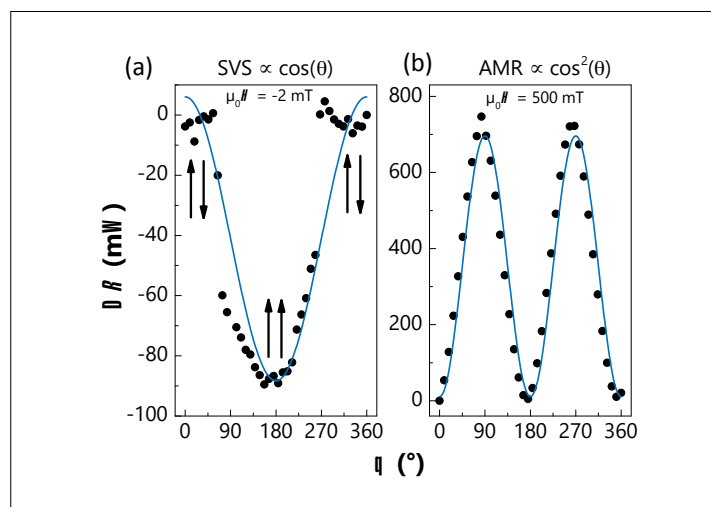


**Fig. 2.** Resistance curve with respect to a 360°-angle scan of the applied magnetic field at room-temperature where the 0° direction corresponds to the  $[\bar{1}10]$  direction. (a) At  $-2$  mT, after saturation at high fields, the magnetization of FM2 is considered as fixed, whereas FM1 is able to rotate. The result deviates from the expected cosine dependence due to the Néel vector pinning effect. (b) At 500 mT, only the AMR effect is detected by the characteristic  $\cos^2$  dependence.

along three crystallographic axes of the GaAs(001) substrate. For all magnetic field orientations, characteristic hysteresis loops of a ferromagnetic film are detected. For the high-symmetry axis [010], the magnetization switches in two steps with a plateau at zero magnetization. The hysteresis loops along the [110] and  $[\bar{1}10]$  directions exhibit single steps, and their coercive fields strongly deviate from each other. Such an uniaxial anisotropy is in strong contrast to the commonly observed magnetization behaviour of single  $\text{Fe}_3\text{Si}$  films on GaAs substrates with easy axes along  $\langle 100 \rangle$  directions. As no total magnetization in single  $\alpha\text{-FeGe}_2$  films can be detected at room temperature, we assume  $\alpha\text{-FeGe}_2$  to be antiferromagnetic with its Néel vector along  $[\bar{1}10]$  having a strong influence on neighboring ferromagnets. Consequently, we explain the observed magnetization behavior by proximity effects, which induce an additional magnetic easy axis along the  $[\bar{1}10]$  direction in the  $\text{Fe}_3\text{Si}$  film.

In order to verify the antiferromagnetic order in  $\alpha\text{-FeGe}_2$  films and the accompanied contribution of an uniaxial anisotropy, we studied the angular dependence of the magnetoresistance in trilayer structures. Figure 1(b) displays the magnetoresistance MR as a function of an external magnetic field ( $\mu_0\mathbf{H}$ ) swept along different crystallographic directions. For the  $\mu_0\mathbf{H} \parallel [\bar{1}10]$  and  $\mu_0\mathbf{H} \parallel [010]$ , characteristic features (shaded areas) are detected as signatures of successful spin valve operation. The low resistance states correspond to the parallel magnetization configuration (FM1 vs. FM2), whereas high resistances are attributed to misaligned magnetizations. Note that the spin valve signals are superimposed on the anisotropic magnetoresistance (AMR) caused by the lateral transport in the ferromagnetic bottom electrode  $\text{Fe}_3\text{Si}$ . Most strikingly, negative spin valve features are detected for  $\mu_0\mathbf{H} \parallel [110]$ . This sign reversal between the spin valve signals confirms the magnetometry results regarding the uniaxial anisotropy introduced by the  $\alpha\text{-FeGe}_2$  spacer layer.

Assuming an antiferromagnetic order in  $\alpha\text{-FeGe}_2$ , we propose a model in which the uniaxial Néel vector of  $\alpha\text{-FeGe}_2$  influences the magnetization reversal in the ferromagnetic electrodes and the corresponding spin valve signals. For the electrodes FM1 and FM2, the [010] and [100] orientations of the GaAs(001) substrate are expected to be the easy axes of magnetization, as commonly observed. In contrast, the Néel vector indicating the antiparallel spin alignment in  $\alpha\text{-FeGe}_2$  is presumed to remain with its fixed orientation the  $[\bar{1}10]$  direction of the GaAs(001) substrate. Close to zero field, the interlayer coupling due to exchange coupling leads to spin flop transitions between a parallel magnetization configuration of the electrodes FM1 and FM2 (along the Néel vector) and a tilted magnetization configuration (towards [010] and [100]). As a consequence, the magnetization reversal for the ferromagnetic electrodes proceeds according to the sequences indicated in

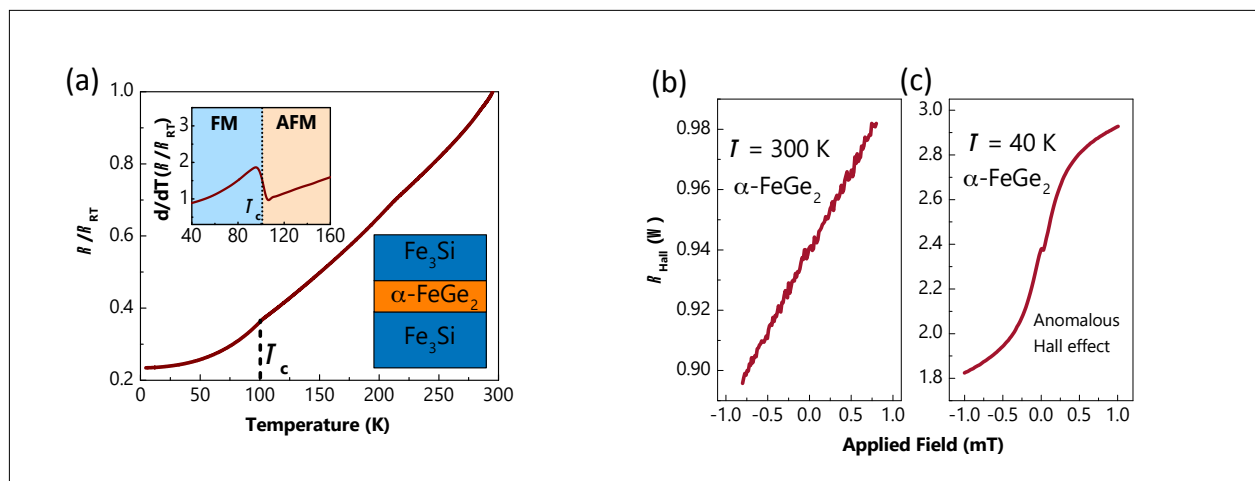
Fig. 1(b) for the different orientations of the external magnetic field. The trilayer resistance is expected to increase with increasing magnetization misalignment between FM1 and FM2. The lowest trilayer resistance corresponds to the configuration in which the magnetizations of FM1 and FM2 are aligned parallel along the Néel vector as we expect a minimum in the spin relaxation rate in  $\alpha$ -FeGe<sub>2</sub> along this direction.

The spin valve signal (resistance at low magnetic field, see Fig. 1(b)), in contrast, exhibits a single extremum around 180° as shown in Fig. 2(a), where  $\theta$  describes the relative magnetization directions of FM1 and FM2. Typical spin valve signals show a  $\cos(\theta)$  dependence but here pinning of the magnetization along the Néel vector of FeGe<sub>2</sub> leads to a nearly constant resistance around 0° and 180°. This result exactly reflects our expectation based on our above model with antiferromagnetic order in the  $\alpha$ -FeGe<sub>2</sub> spacer layer. The corresponding evolution of the magnetization dynamics in the individual films is indicated by arrows in Fig. 2(a), representing the magnetization

directions of FM1 and FM2. The angular dependence on the in-plane field of the AMR background signal (resistance at magnetic saturation, see Fig. 1(b)) exhibits the typical  $\cos^2$  dependence, as shown in Fig. 2(b).

The temperature dependence of the spin valve device resistance exhibits characteristic features which can be attributed to low-temperature ferromagnetic phase transitions. Figure 3(a) displays the resistance normalized by the resistance at room temperature  $R/R_{RT}$  as a function of temperature. A characteristic change in the  $R/R_{RT}(T)$  curvature occurs at 100 K. The corresponding peaks in the temperature derivatives [cf. top inset in Fig. 3(a)] can be explained by spin disorder scattering, which starts to decrease below the Curie temperature  $T_C$ , where a phase change into a ferromagnetic state occurs. Fig. 3 (b) and (c) show Hall measurements on a single  $\alpha$ -FeGe<sub>2</sub> film, which reveal a normal Hall effect at 300 K with no sign of ferromagnetism and an anomalous Hall effect at 40 K demonstrating the proof of the ferromagnetic state at low temperatures.

**Fig. 3.** (a) Temperature dependence of the resistance for a trilayer Fe<sub>3</sub>Si/ $\alpha$ -FeGe<sub>2</sub>(6 nm)/Fe<sub>3</sub>Si device structure. The derivative of the  $R(T)$ -curve (upper inset) indicates an AFM to FM phase transition at 100 K. (b) Hall resistance of a single  $\alpha$ -FeGe<sub>2</sub> film measured at 300 K and (c) anomalous Hall effect measured at 40 K indicating the ferromagnetic phase for  $\alpha$ -FeGe<sub>2</sub>.



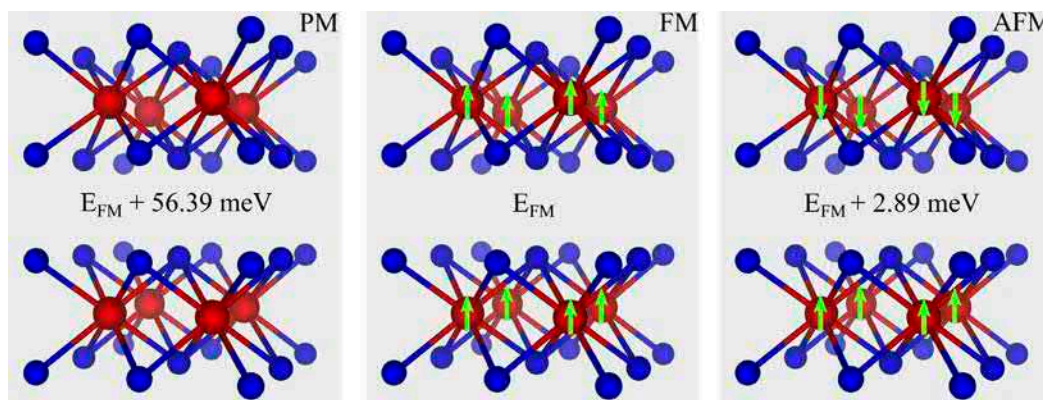


**Fig. 4.** Relative total energies of different magnetic phases in bulk  $\alpha$ -FeGe<sub>2</sub> (PM: paramagnetic, FM: ferromagnetic, AFM: antiferromagnetic) calculated by DFT. Red spheres represent Fe atoms and blue spheres Ge atoms, whereas the Ge atoms are not connected to each other in order to illustrate the layered structure. DFT calculations were done in cooperation with K. Zollner and J. Fabian from the University of Regensburg. The result supports our experimental findings.

Furthermore, results from density functional theory (DFT) calculations on the total energy for different magnetic phases of bulk  $\alpha$ -FeGe<sub>2</sub> indicate the ferromagnetic phase as the energetically most favourable ground state and hence expected to occur at low temperatures, as summarized in Fig. 4(b). We consider three different configurations: (i) paramagnetic (PM) phase, where the atoms are considered to have no collective magnetization axis; (ii) ferromagnetic (FM) phase, in which all Fe atoms have aligned magnetic moments along the c-axis; and (iii) antiferromagnetic (AFM) phase, where the ferromagnetic Fe sheets within  $\alpha$ -FeGe<sub>2</sub> form sublattices with antiparallel order. Interestingly, the AFM phase is only about 2.9 meV higher in energy (or about 0.36 meV per unit cell) than the FM phase, which makes a phase change FM to

AFM highly probable by increasing the temperature. The PM phase is expected to occur at an energy of about 56 meV (or about 7 meV per unit cell).

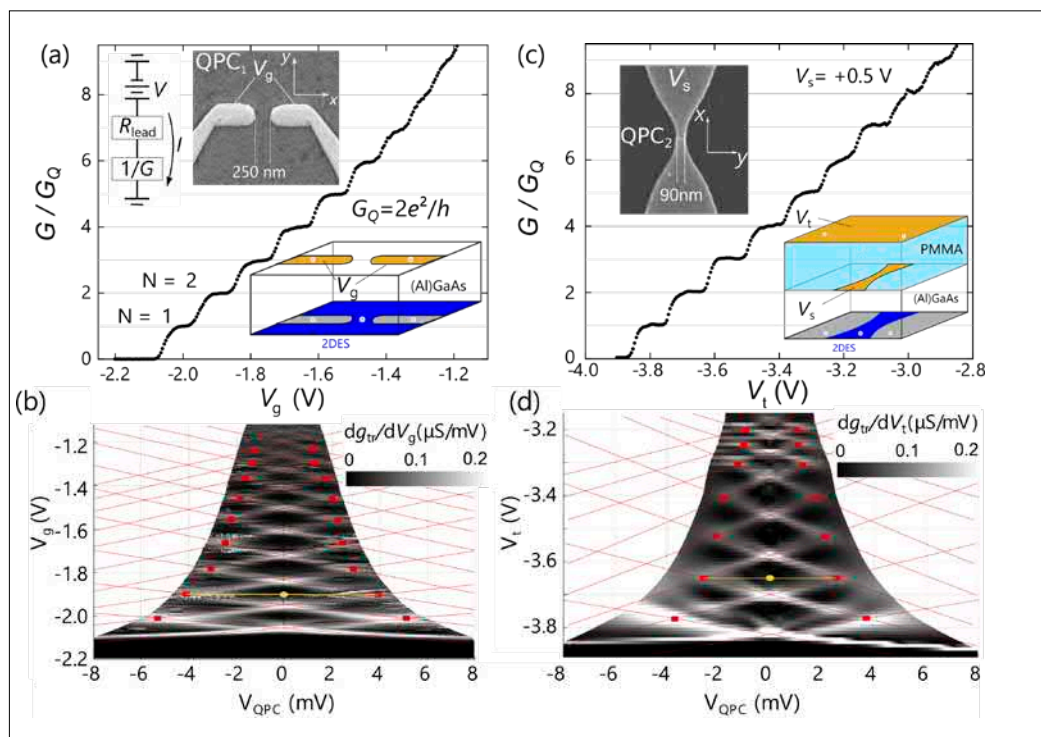
In summary, all our results are consistent with antiferromagnetic ordering in  $\alpha$ -FeGe<sub>2</sub> films at room temperature and an AFM to FM phase transition at low temperatures. The antiferromagnetic order leads to strong interlayer coupling between the ferromagnetic electrodes of the vertical spin valve structure, and a sign reversal in the spin valve signal reflects the uniaxial anisotropy between the  $\langle 110 \rangle$  directions. The small difference between the total energies of the AFM and FM phases might enable the tailoring of magnetic properties, for example by strain engineering.

# Realistic potential shape of quantum point contacts

J. Freudenfeld, M. Geier<sup>1</sup>, J. T. Silva, V. Umansky<sup>2</sup>, D. Reuter<sup>3</sup>, A. D. Wieck<sup>3</sup>, P. W. Brouwer<sup>1</sup>, S. Ludwig

Quantum point contacts (QPCs) are the shortest possible one-dimensional (1D) constrictions of nanoelectronic quantum circuits and their most fundamental components. Roughly speaking, a QPC can be described in terms of a longitudinal barrier in the direction of current flow and a lateral confinement perpendicular to it. The latter defines the mode structure of the 1D channel, while the coupling of the 1D modes to the QPC's environment is governed by the longitudinal barrier shape. The coherent

**Fig. 1.** (a) and (c) Pinch-off curves of QPC<sub>1</sub> and QPC<sub>2</sub> respectively, corrected for lead resistances [simplified circuit diagram is shown as inset in (a)]. Lower insets: sketches of split gate device versus screen gate device, which contains an insulating PMMA layer between screen and top gate. Metal gates at voltages  $V_g$ ,  $V_t$  and  $V_s$  are marked gold. Sufficiently negative values of  $V_g$  or  $V_t$  deplete the 2DES below (blue is conducting, gray depleted). Upper insets: scanning electron micrographs of the sample surfaces (top gate not yet included). (b) and (d) Differential transconductance  $dg_{tr}/dV_g$  for QPC<sub>1</sub> and  $dg_{tr}/dV_t$  for QPC<sub>2</sub> respectively as a function of the voltage drop over the respective QPC  $V_{QPC} = V - R_{lead}I$ . Red lines and squares are a guide to the eye.



<sup>1</sup> Dahlem Center for Complex Quantum Systems and Physics Department, Freie Universität Berlin, Berlin, Germany.

<sup>2</sup> Department of Condensed Matter Physics, Weizmann Institute of Science, Rehovot, Israel.

<sup>3</sup> Angewandte Festkörperphysik, Ruhr-Universität Bochum,

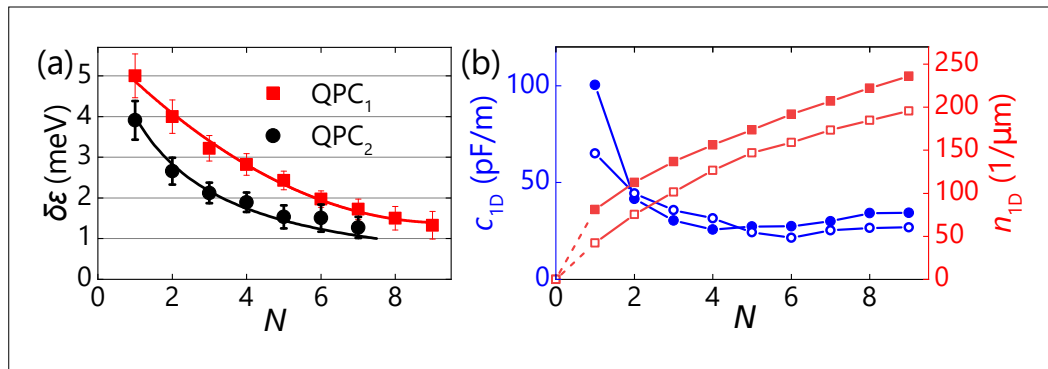
dynamics of charge carriers depends on the details of the electrostatic potential, which is important for quantum technology applications. The prediction of the electrostatic potential shape of a QPC is not trivial, because it requires a three-dimensional solution of the combination of the Poisson and the Schrödinger equations, while the boundary conditions are a priori not well known. Instead, simplified models are used. Here, we experimentally demonstrate the limits of this simplifying approach and the importance of Coulomb screening, which substantially changes the effective potential shape of QPCs as the 1D constriction is populated with charge carriers.

We study QPCs of two very different designs, both defined using the electric field effect in a two-dimensional electron system (2DES) embedded 107 nm beneath the surface of a (Al,Ga)As/GaAs heterostructure. The Fermi energy and mobility of the 2DES measured at cryogenic temperatures are  $E_F \approx 10.9$  meV and  $\mu_e \approx 2.6 \times 10^6$  cm<sup>2</sup>/Vs respectively for QPC<sub>1</sub> and similar for QPC<sub>2</sub>. To define QPC<sub>1</sub>, shown in the insets of Fig. 1(a), we apply a negative voltage  $V_g$  to two metal gates arranged in the usual split-gate layout. To create the second QPC<sub>2</sub>, shown in the inset of Fig. 1(c), we use a global top

gate to deplete a large area of the 2DES. However, below a screen gate placed between the top gate and the 2DES, a finite carrier density remains inside the 2DES. The screen gate shapes the QPC between the 2D leads. We control its conductance and the carrier density of its 2D leads by a combination of the voltages  $V_t$  and  $V_s$  applied to the top gate and screen gate, respectively. In Fig. 1(a) and Fig. 1(c), we present example pinch-off curves of both QPCs, showing their conductances as a function of gate voltages measured at temperatures near  $T = 250$  mK like all data presented here.

The pinch-off curves feature the expected conductance plateaus at  $G = N2e^2/h$ , where  $N$  is a positive integer,  $e$  the elementary charge, and  $h$  the Planck constant. Smooth transitions between the plateaus indicate reflectionless contacts between the QPC and its leads and point to a parabolic longitudinal potential barrier in the current direction. Another often observed feature of the pinch-off curves are almost equidistant steps between the quantized plateaus. It is tempting to interpret these in terms of a parabolic lateral confinement potential with equally spaced eigen energies. Below, we prove this common interpretation wrong and present an improved model.

**Fig. 3.** (a) Energy difference between subsequent eigen modes of the QPCs  $\delta\varepsilon(N)$  extracted from Figs. 1(b,d). (b) Blue circles, left axis: 1D capacitance and red squares, right axis: 1D carrier density of QPC<sub>1</sub>, deduced from  $\delta\varepsilon(N)$  for a hard-wall confinement potential (filled symbols) and a parabolic potential (open symbols).



To determine the energy differences  $\delta\varepsilon(N)$  between subsequent 1D modes, characteristic for the lateral confinement, we plot the differential transconductances  $dg_{\text{tr}}/dV_g$  for QPC<sub>1</sub> in Fig.1(b) and  $dg_{\text{tr}}/dV_g$  for QPC<sub>2</sub> in Fig.1(d), where  $g_{\text{tr}} = dI/dV_{\text{QPC}}$  with  $V_{\text{QPC}} = V - R_{\text{leed}}I$  is the portion of the source-drain voltage dropping across the respective QPC accounting for the resistance  $R_{\text{leed}}$  in series with each QPC. Steps of the conductance appear as lines of positive differential transconductance (white areas of the measured data range, emphasized by straight red lines). Along the  $N$ th line of positive (negative) slope counted from the bottom of the plot, the energy of the  $N$ th 1D subband bottom is equal to the chemical potential in the source (drain) lead,  $\varepsilon_N = \mu_S$  ( $\varepsilon_N = \mu_D$ ). At intersection points at finite  $V_{\text{QPC}}$  [red squares in Figs. 2(b,d)] the chemical potential drop across a QPC equals the energy spacing between the corresponding 1D modes,  $\mu_S - \mu_D = eV_{\text{QPC}} = \varepsilon_N - \varepsilon_{N-1} \equiv \delta\varepsilon(N)$ .

As we show in Fig.2(a), the different geometries give rise to different subband spacings of the two QPCs. However, for both QPCs, we observe a strong decrease of  $\delta\varepsilon(N)$  as they are populated with electrons by increasing  $N$ . This result contradicts the assumption of a parabolic confinement potential with a constant curvature predicting a constant  $\delta\varepsilon(N)$ . Comparing the measured  $\delta\varepsilon(N)$  with the respective predictions assuming specific potential shapes [M. Geier *et al.*, Phys. Rev. B **101**, 165429 (2020)] allows us to perform a reality check. As a

result, we find that a parabolic lateral confinement with variable curvature is realistic for small  $N$ , but is impossible for  $N > 4$ . The potential shape is strongly influenced by the increased Coulomb screening as the 1D constriction is populated with carriers. It flattens the lateral potential thereby instigating the transition toward a hard-wall potential.

Such a transition is supported by the data shown in Fig.2(b), where we present the 1D carrier density  $n_{1D}(N)$  and the related capacitance  $c_{1D}(N) = e\delta n_{1d} / \delta V_g$  (circles) between the 1D channel and the top gate as a function of  $N$  for QPC<sub>1</sub>, assuming a truncated hard-wall potential (filled symbols) and a parabolic potential (open symbols). As the carrier density increases, the capacitance drops rapidly for  $N < 4$ . It indicates the above discussed strong increase of screening with  $N$ . For  $N \geq 4$ , the capacitance remains constant indicating a fully screened, hence, flat bottom of the potential well.

In summary, we studied two different gate-defined QPCs and find that their longitudinal potential barrier can be described as a smooth parabola, while the lateral confinement undergoes a transition from a parabolic toward a hard-wall potential well, as the constriction is populated with carriers. These findings will facilitate the design of future on-chip quantum circuits as the coherent dynamics of carriers depends on the details of the electrostatic potential landscape.

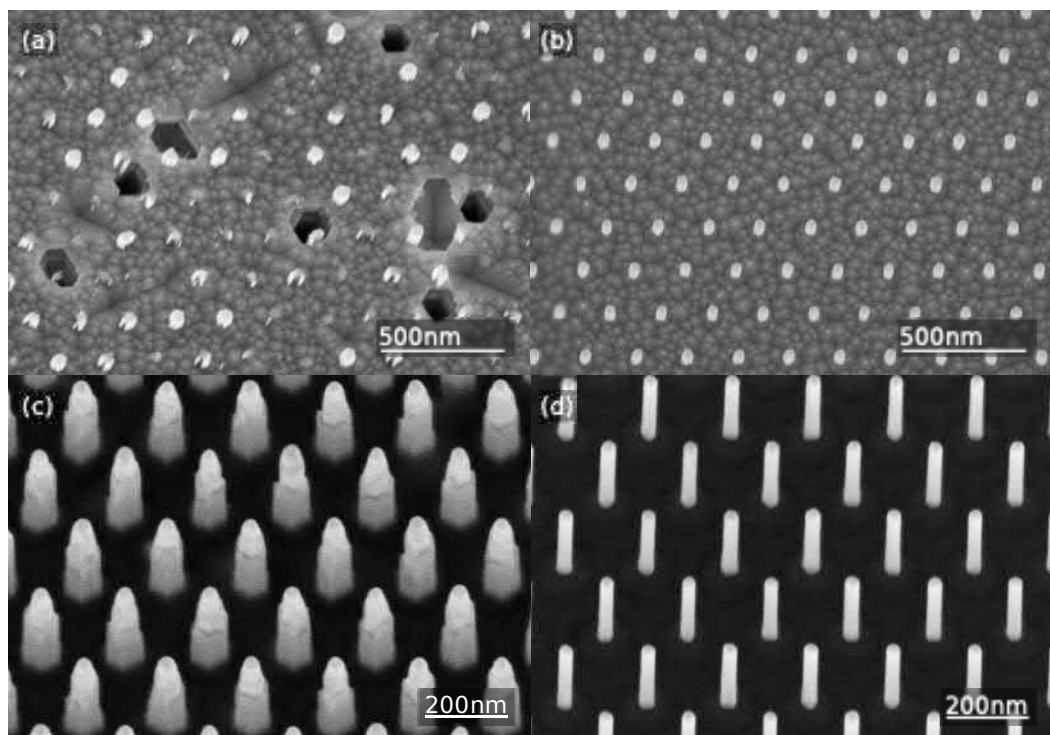
# Comparison of top-down approaches for the fabrication of highly ordered GaN nanowire arrays

M. Oliva, A. Tahraoui, T. Auzelle, J. Lähnemann, L. Geelhaar, O. Brandt

Light-emitting diodes based on GaN nanowire (NW) arrays have several potential advantages over their planar counterparts. For very thin NWs (< 50 nm), for example, strain in axial NW heterostructures may relax elastically, resulting in a reduction of internal piezoelectric fields. Moreover, light is extracted more efficiently for NWs of sub-wavelength diameter. In addition, an array of such NWs may be designed to act

as a photonic crystal for obtaining a light extraction efficiency near unity. In practice, these functionalities require exceedingly homogeneous arrays of thin NWs with highly uniform NW diameters and spacings. The best-established top-down fabrication technique to obtain such NW arrays for GaN relies on inductively coupled plasma (ICP) etching followed by an anisotropic wet etching step with a KOH solution to

**Fig. 1.** Bird's-eye view ( $15^\circ$  tilt from top-view) scanning electron micrographs of NW arrays with a diameter and pitch of 30 and 200 nm, respectively. The arrays in (a) and (b) were fabricated by SAS without and with a KOH etching step before the thermal annealing, respectively. In these images, we can perceive the characteristic  $\{1\bar{1}03\}$  facets obtained by thermally decomposing a GaN(0001) surface (S. Fernández-Garrido, *op. cit.*). (c) and (d) illustrate the different steps of the ICP-KOH etching processes: (c) shows the typical morphology of the NWs after ICP etching and (d) the NWs obtained by subsequent KOH etching.





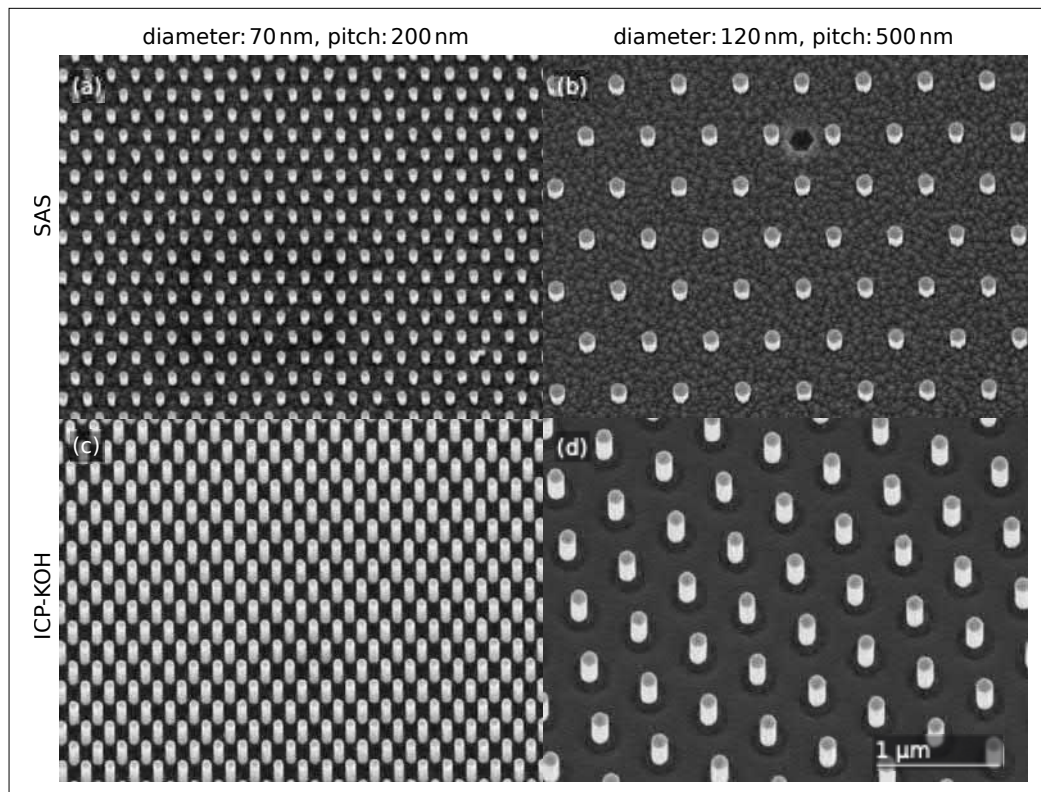
remove the dry-etch damage [Q. Li *et al.*, *Opt. Express* **19**, 25528 (2011)]. As a gentle alternative to this two-step chemical etching approach (ICP-KOH), B. Damilano *et al.* [*Nano Lett.* **16**, 1863 (2016)] recently introduced a new top-down fabrication method coined as selective area sublimation (SAS). This technique is not based on chemical etching, but on purely thermal sublimation, and is thus not expected to cause any damage to the NW sidewalls.

In the present work, we compare these two top-down fabrication techniques with the focus on the uniformity of the NW arrays. The uniformity is quantitatively assessed by a statistical analysis of top-view scanning electron micrographs for NW arrays from two samples, both of which contain microfields with a nominal NW center-to-center

distance (pitch) of 200 nm and nominal NW diameters of 30, 40, 50, 60, and 70 nm, yielding the distributions of the NW diameter, the circularity, and the pitch. Our samples are fabricated utilizing GaN(0001) templates covered by a  $\text{Si}_x\text{N}_y$  layer, which is patterned by electron beam lithography. The pattern comprises  $50 \times 50 \mu\text{m}^2$  fields of hexagonal arrays of circular patches defining the positions of the NWs.

Figure 1(a) depicts an ordered NW array fabricated by SAS following the procedures established by S. Fernández-Garrido *et al.* [*Nanoscale Adv.* **1**, 1893 (2019)]. Prior to thermal annealing, the sample is briefly etched by ICP to eliminate residual surface contamination from previous fabrication steps. SAS is then carried out in a molecular beam epitaxy (MBE) system for 20 min

**Fig. 2.** Bird's-eye view ( $15^\circ$  tilt from top-view) scanning electron micrographs of NW arrays fabricated by SAS and ICP-KOH with different diameters and pitches as indicated in the figure. The scale bar in (d) applies to all microfields.



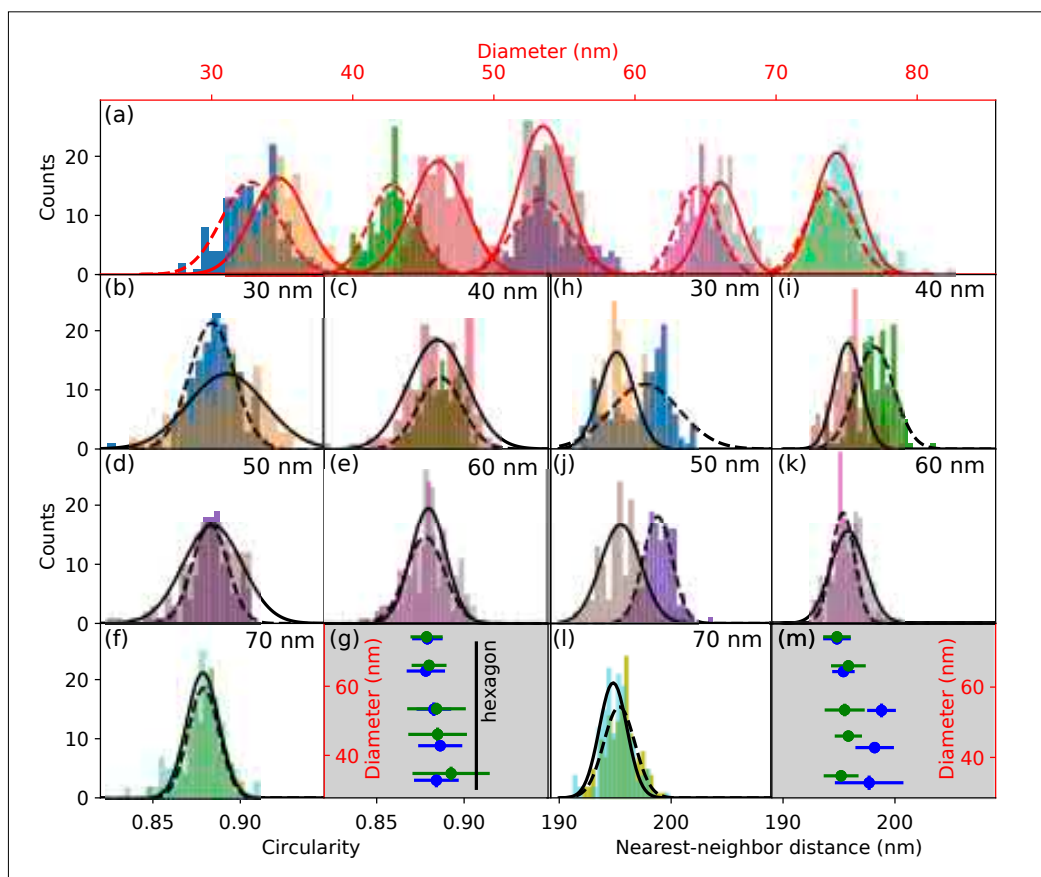


**Fig. 3.** Distribution of the (a) equivalent disk diameter, (b)–(f) circularity, and (h)–(l) nearest-neighbor distance of NW arrays fabricated by both, ICP-KOH and SAS. Each histogram corresponds to a particular field characterized by a nominal NW diameter as indicated in the figure. The histograms are fitted by a normal distribution with dashed and solid lines indicating that the field was fabricated by ICP-KOH and SAS, respectively. Panels (g) and (m) display the mean values (symbols) and standard deviations (bars) of the circularity and the nearest-neighbor distance, respectively, as well as of the equivalent equivalent disk diameters of NW arrays fabricated by ICP-KOH (blue) or SAS (green). The vertical line in (g) indicates the circularity of a perfect hexagon.

at a thermocouple temperature of 980 °C. At these conditions, we reproducibly obtain NWs with a length of 100–150 nm. Upon increasing the SAS time to 60 min, NWs with lengths of 250–300 nm are achieved.

Samples produced in this way are characterized by a nonregular cross-sectional shape as well as prominent craters in the GaN template, decreasing the NW yield substantially [see Fig.1(a)]. These features were also observed in the previous works by B. Damilano (*op. cit.*), P.-M. Cou-

lon [Microsyst. Nano Eng. **5**, 52 (2019)] and S. Fernández-Garrido (*op. cit.*), and the craters were attributed in the latter work to threading dislocations in the GaN template. In fact, the crater density corresponds to the density of threading dislocations ( $\approx 5 \times 10^8 \text{ cm}^{-2}$ ) in these GaN/Al<sub>2</sub>O<sub>3</sub> layers. In this work, we show that homogeneous NW arrays free of craters can be obtained if the sublimation process is preceded by an etch step in 6.9 M KOH (aq) for 2 min at 60 °C. The resulting samples, of which an example is shown in Fig. 1(b),

exhibit a much improved NW morphology and are entirely free of craters, suggesting that the craters are actually *not* related to threading dislocations.

The SAS fabrication process relies on sublimation in an ultra-high vacuum (UHV) chamber and is thus much more time-consuming than the ICP-KOH technique. Figure 1(c) depicts an ordered array of cones with a length of 500–600 nm obtained after ICP-RIE etching for 3 min using a mixture of Ar, Cl<sub>2</sub>, and BCl<sub>3</sub> gases. Other lengths can be obtained by adjusting the etching time. After a subsequent etching of the sample in 6.9 M KOH (aq) for 2 min at 60 °C, perfectly straight NWs as depicted in Fig. 1(d) are obtained. NWs with the same length, diameter, and morphology can be achieved for temperatures of 40–80 °C and can also be reproduced for widely different *n*-type doping densities (10<sup>16</sup> and 10<sup>18</sup> cm<sup>-3</sup>) of the template. These results demonstrate that the KOH-based wet etching is robust, self-limited, and only removes the damage layer created by dry etching.

Figure 2 depicts scanning electron micrographs of representative microfields containing NW arrays with different diameters and pitches, fabricated with the optimized SAS [Figs. 2(a) and 2(b)] and ICP-KOH [Figs. 2(c) and 2(d)] fabrication techniques. We have investigated 150–175 NWs from each microfield and found a yield of straight and ordered NWs of 99.9 %, independent of the NW diameter and fabrication technique.

The distribution of the equivalent disk diameter, circularity, and nearest-neighbor distance (from center-to-center) is shown in Fig. 3. For both top-down approaches, the NW diameter distributions peak close to the nominal value and exhibit standard deviations of 3–4 nm. The circularity of the NWs of 0.88–0.89 is close to that of a regular hexagon (0.91), independent of the diameter of the NWs, and only slightly less for ICP-KOH as compared to SAS. Likewise, the

nearest-neighbor distance is close to the nominal value with a standard deviation of 2–6 nm. Thus, the uniformity of the arrays is almost identical and is clearly mostly limited by the patterning precision.

Both investigated techniques thus allow the fabrication of highly ordered and uniform GaN NW arrays. The ICP-KOH approach has the decisive advantage of offering a much higher throughput than the SAS method. However, the dry etching step inevitably creates surface defects that may be difficult to eliminate completely by the KOH step, hence resulting in nonradiative surface recombination. Such defects are not expected for the SAS approach, which relies purely on thermal decomposition. A side-by-side comparison of the radiative efficiency of these NW arrays is thus of great interest to judge the suitability of these competing fabrication techniques for optoelectronic applications based on NW arrays.

# Unified understanding of nonradiative recombination in GaN nanowires

T. Auzelle, T. Flissikowski, M. Azadmand, H. T. Grahn, L. Geelhaar, O. Brandt

The recombination dynamics in GaN nanowire (NW) ensembles synthesized by molecular beam epitaxy is governed by non-radiative processes even at cryogenic temperatures. In fact, the typical decay times of the donor-bound exciton in GaN NWs with diameters between 30 and 200 nm range from 0.1 to 0.25 ns, i. e., significantly shorter than the radiative lifetime of the bound exciton state in bulk GaN of at least 1 ns. The most obvious candidate for a fast nonradiative process is the NW surface. Indeed, the so far longest exciton decay times (about 0.5 ns) have been observed for exceptionally thick GaN NWs with a diameter of 400 nm [J. B. Schlager *et al.*, *J. Appl. Phys.* **103**, 124309 (2008); *ibid.* **109**, 044312 (2011)]. At the same time, these NW ensembles are also remarkable for their low density, and the individual NWs are thus free of coalescence and the associated boundary defects. These defects are found in abundance in GaN NW ensembles with high densities, and are a second plausible candidate for the origin of the fast nonradiative process in GaN NWs. However, C. Hauswald *et al.* [*Phys. Rev. B* **90**, 165304 (2014)] found that the decay time for typical GaN NW ensembles with diameters between 30 and 200 nm does not exhibit any obvious trend with either the surface-to-volume ratio or the coalescence degree and thus suggested that the nonradiative channel originates from point defects. In a subsequent work, J. Zettler *et al.* [*Nano Lett.* **16**, 973 (2016)] observed an *increase* of the decay time from 0.14 to 0.36 ns upon *thinning* NWs by partial thermal decomposition of a NW ensemble. This unexpected result seemed to definitely rule out surface recombination and was tentatively attributed to a reduction of the density of native point defects

by the high-temperature annealing of the thinned NWs during sublimation.

In the present work, we report unprecedentedly long bound exciton decay times (up to 0.72 ns) for samples with ensembles of ultrathin (14–24 nm) GaN NWs fabricated on sputtered TiN films by molecular beam epitaxy. The decay time is found to systematically *increase* with *decreasing* NW diameter. This striking finding can be understood by considering exciton dissociation in the radial electric fields in the NWs followed by rapid hole capture by surface states. Ultimately, nonradiative recombination of electrons and holes thus occurs at the surface after all, but the field ionization of excitons is the rate-limiting step determining the effective nonradiative lifetime. We show that this two-step process provides a framework for a unified understanding of the exciton decay times observed for GaN NWs of arbitrary diameter.

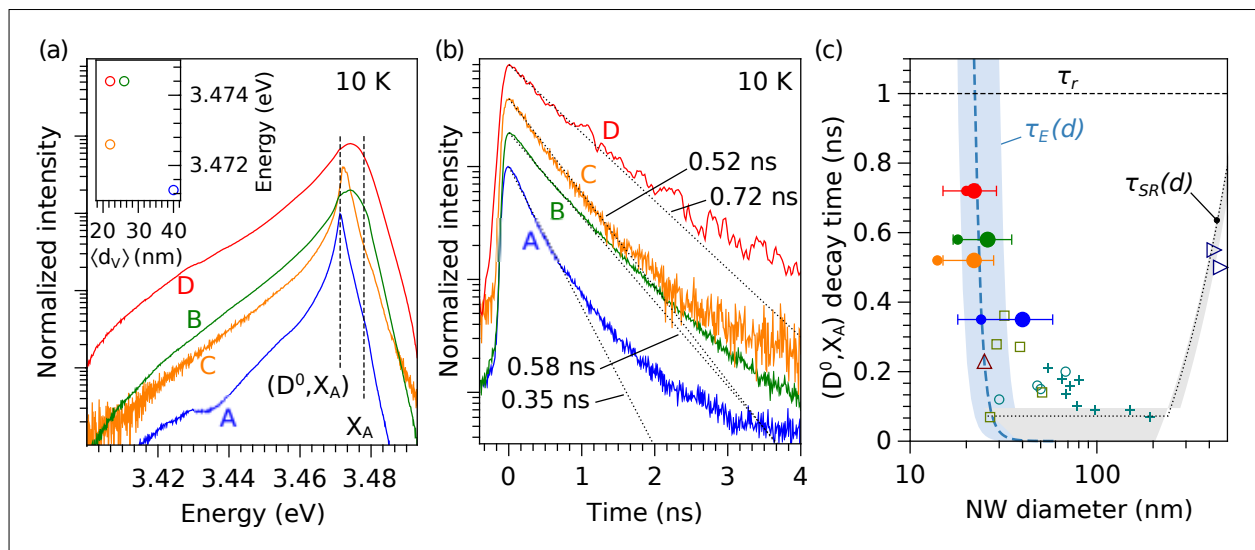
Figure 1(a) displays the photoluminescence (PL) spectra of our samples recorded under continuous-wave (cw) excitation at 10 K. The energy of the respective emission band identifies the transitions as being due to the radiative decay of the free  $X_A$  and the donor-bound-bound ( $D^0, X_A$ ) exciton. However, the emission energy is diameter dependent and not identical to that of bulk GaN as usually observed for NWs with larger diameters, but exhibits on average a blueshift with decreasing diameter (see inset). Several mechanisms have been identified that can shift the transition energy for thin NWs, namely, surface donor-bound excitons [O. Brandt *et al.*, *Phys. Rev. B* **81**, 045302 (2010); P. Corfdir *et al.*, *Phys. Rev. B* **90**, 205301 (2014)], sur-

face stress [G. Calabrese *et al.*, *Acta Mater.* **195**, 87 (2020)], and dielectric confinement [J. Zettler, *op. cit.*]. Since the shift depends on the diameter, all of these mechanisms result in a broadening of the ensemble spectra as primarily observed here for samples B and D. In addition, NWs with a very small volume may not contain even a single donor [C. Pfüller *et al.*, *Nano Res.* **3**, 881 (2010)] so that the free-exciton transition may appear to be strongly enhanced in low-temperature ensemble spectra as seen here particularly for sample B.

PL intensity transients of the  $(D^0, X_A)$  line obtained upon pulsed excitation at 10 K are presented in Fig. 1(b). The biexponential decay was previously shown [C. Hauswald *et al.*, *Phys. Rev. B* **88**, 075312 (2013)] to arise

from a coupling of the exciton states with the initial decay time reflecting the actual lifetime of the  $(D^0, X_A)$  state that so far remained mostly in the range from 0.1 to 0.25 ns. For the present samples, exceptionally long initial decay times between 0.35 and 0.72 ns are observed, with the thinnest NWs actually exhibiting the longest value and vice versa. In fact, a comparatively clear trend is evident when correlating the decay time with the volume-weighted mean diameter  $\langle d_v \rangle$ , as shown in Fig. 1(c), suggesting that the decay time systematically *increases* with *decreasing* diameter. As mentioned above, we have observed the same behavior for thermally thinned NWs and attributed it to an effect of NW annealing on the point defect density. These results indicate that the key parameter is

**Fig. 1.** (a) cw-PL spectra and (b) band-edge PL transients integrated ( $\pm 15$  meV) over the  $(D^0, X_A)$  line of samples A–D. The inset in (a) shows the peak energy vs. the volume-weighted mean diameter of the NWs. The dotted lines in (b) are mono-exponential fits of the initial decay, with the resulting decay times indicated in the figure. (c)  $(D^0, X_A)$  decay time versus the average NW diameter for samples A–D and samples from other experimental studies. Large filled circles with horizontal error bars correspond to the volume-weighted mean diameter  $\langle d_v \rangle$ , whereas small filled circles refer to the bare mean diameter  $d$ . Values from other publications (open symbols) are used as reported.  $\tau_E(d)$  is the calculated dissociation time of the free exciton in the electric field at the NW sidewall surface.  $\tau_{SR}(d)$  denotes the calculated time of excitons to reach the surface electric field by diffusion.  $\tau_r$  indicates the radiative lifetime in bulk GaN. The horizontal dotted line is a guide to the eye.



the NW diameter itself, calling for a reevaluation of the mechanism responsible for the nonradiative exciton decay in GaN NWs.

At this point, it is important to recall that band bending occurs in GaN NWs due to the presence of surface states at their oxidized  $\{1\bar{1}00\}$  sidewall facets. A reduction of the band bending was observed to enhance the intensity of the  $(D^0, X_A)$  line [C. Pfüller *et al.*, Phys. Rev. B **82**, 45320 (2010)], suggesting that the electric field associated with the band bending triggers the nonradiative decay of the  $(D^0, X_A)$  state, while more strongly bound excitons remain unaffected [P. Corfdir *et al.*, Phys. Rev. B **90**, 195309 (2014)]. These findings can be understood when taking into account that the actual nonradiative decay takes place via the free exciton due to the strong coupling of free and bound exciton states [C. Hauswald 2014, *op. cit.*]. The nonradiative decay is thus initiated by the field ionization of the free exciton, i. e., the tunneling of an electron out of the Coulomb potential created by the hole. Subsequently, holes are driven to the surface, recombine with filled surface states, followed by electrons filling the now empty states once more. The hole capture process is ultrafast, and field ionization thus represents the rate-limiting step for nonradiative recombination.

For a continuous and homogeneous charge distribution and assuming the NW to be fully depleted, the electrostatic potential within the NW is parabolic<sup>1</sup>. The maximum electric field  $F_m$  then occurs at its sidewall facets, and increases linearly with the NW diameter and the doping density. To obtain the field ionization rate  $1/\tau_E(d)$ , we first calculate  $F_m$  by solving the Poisson equation for a GaN cylinder with a given doping density, and then proceed analogously to

the calculation of the field ionization probability (per unit time) of the hydrogen atom [V. M. Kaganer *et al.*, Appl. Phys. Lett. **112**, 122101 (2018)]. Figure 1(c) compares the measured  $(D^0, X_A)$  decay times for samples investigated in the present work (filled circles) and previous investigations (open symbols) with  $\tau_E(d)$  for a donor density of  $8 \times 10^{16} \text{ cm}^{-3}$ . The calculated ionization time is seen to steeply increase from essentially zero for diameters above 40 to values of 1 ns and more for diameters below 20 nm. This steep increase coincides with the longest decay times observed in the present and previous work for thin NWs.

Below a critical diameter  $d_c$ , the NW is fully depleted, resulting in  $F_m \propto d$ . In sufficiently thin NWs, the decay time is thus not affected by the electric field, but represents the actual lifetime of the  $(D^0, X_A)$  state. The 0.72 ns decay time for sample D approaches the longest values measured for state-of-the-art GaN layers (1 ns), and even thinner NWs may thus help to settle the question whether this value represents the true radiative lifetime. With increasing diameter up to  $d_c$ , a dead zone develops close to the NW surface, since the surface electric field becomes strong enough to ionize excitons virtually instantaneously. Radiative recombination can then only occur in the NW core, in which the radial field stays sufficiently small. For example, for a doping density of  $8 \times 10^{16} \text{ cm}^{-3}$ , the electric field does not exceed 10 kV/cm (corresponding to  $\tau_E = 0.12 \text{ ns}$ ) within the inner 26 nm of the NW. For NWs with a diameter  $d > d_c$ , the surface electric field is determined only by the doping level, and the space charge layer occupies an increasingly smaller portion of the NW. Field ionization of excitons is then limited by their diffusion toward the NW sidewalls, and the nonradiative lifetime

<sup>1</sup> Note that this approximation holds only above a certain NW diameter for any given doping density. Below this value, the potential becomes nonparabolic and eventually entirely irregular due to the discrete and random position of donors. However, the *average* electric field in the NW still decreases with decreasing diameter, and our arguments thus remain valid even for NWs with nonparabolic potential.

$\tau_{\text{SR}}(d)$  becomes proportional to the NW diameter, resembling surface recombination. The resulting slowdown of nonradiative recombination with increasing NW diameter is consistent with the long decay times of about 0.5 ns observed for NWs with a diameter of 400 nm [cf. Fig. 1(c)].

The mechanism detailed above also accounts for other experimental results. For example, the nonradiative lifetime in GaN NWs was observed to be essentially independent of both temperature (between 10 and 300 K) and excitation density (over four orders of magnitude) (C. Hauswald 2014, *op. cit.*), which cannot be understood within the conventional framework of defect-mediated nonradiative recombination. When considering field ionization of excitons as the rate-limiting step, both findings are easily understood: first, the band bending in the NWs originates from the charge transfer from the bulk into surface states and is thus essentially independent of temperature. Second, and equally important, the exciton binding energy in GaN is sufficiently high for excitons still dominating the spontaneous emission at room tempera-

ture. Third, the number of surface states in a NW is very high compared to that of point defects in its bulk, rendering the nonradiative channel hard to saturate.

Having identified the origin for the highly effective nonradiative channel for GaN NWs, the remedy becomes obvious. Since the nonradiative decay is mediated by the field ionization of excitons, the radial electric fields should be eliminated or at least reduced. This task can be achieved by either reducing unintentional doping or, perhaps more practical, by a suitable surface passivation. We stress that the mechanism described in this work is not restricted to GaN NWs, but applies to nano- and microstructures in general. In fact, the occurrence of electric fields (either due to charge transfer or strain) is hard to avoid in such structures, and they may affect materials with lower exciton binding energy such as, for example, GaAs, even more severely. Unless measures are taken to counteract them, electron-hole separation in these fields may thus very well limit the performance of devices such as micro-light-emitting diodes and single-photon emitters regardless of the specific material.

# Tuning the density of self-assembled GaN nanowires over three orders of magnitude with Si seeds on metallic TiN

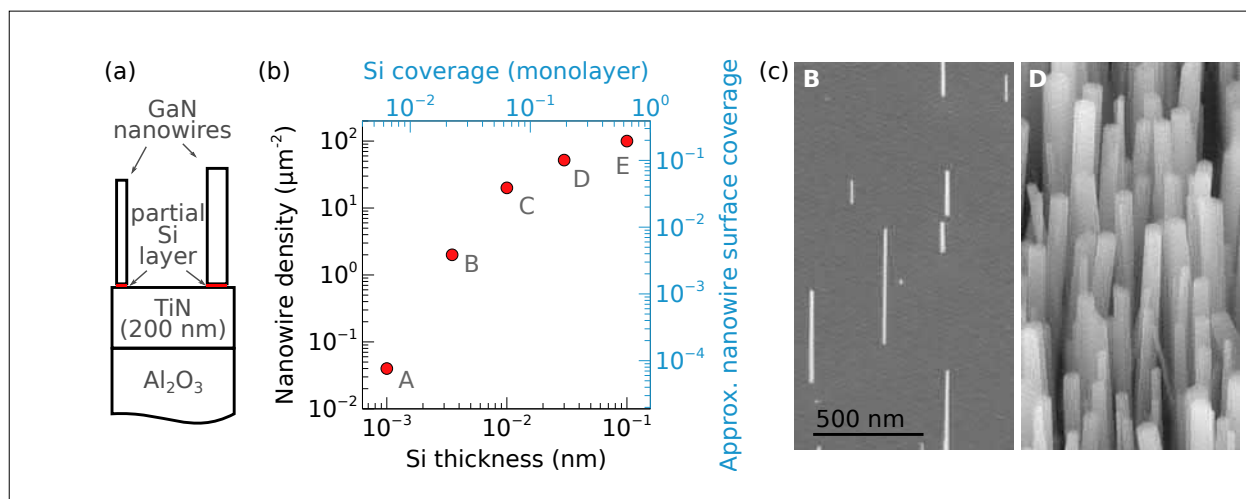
T. Auzelle, L. Geelhaar, O. Brandt

Ultralow densities of GaN nanowires ( $<1 \mu\text{m}^{-2}$ ) are essential for applications and fundamental studies requiring nanowires to be individually addressable with conventional optics. Such low densities can be obtained by selective area growth, but this approach requires the costly pre patterning of substrates at the nanoscale. In contrast, the self-assembly of GaN nanowires with excellent luminescence properties is readily achieved on unpatterned substrates by plasma-assisted molecular beam epitaxy (PAMBE). However, in this case high-density ensembles are invariably produced, even for growth on graphene or TiN, both of which provide very large adatom diffusion lengths. Here, we introduce a facile way of engineering nucleation sites prior to growth and demonstrate control over the nanowire

density on unpatterned TiN substrates down to extraordinarily low values. Our approach builds upon the prior work of Z. de Souza Schiaber *et al.* [Nano Lett. **17**, 63 (2017)], where Si was used to induce GaN nanowire nucleation on Ga-polar GaN substrates. However, the investigation of these nanowires by optical means was impeded by the presence of the GaN substrate.

GaN nanowire ensembles are grown by PAMBE on stoichiometric TiN films prepared in vacuo by reactive sputtering on  $\text{Al}_2\text{O}_3$  substrates. On such bare TiN surfaces, the incubation time preceding nanowire nucleation is found to exceed 5 h for conventional nanowire growth conditions. We attribute this exceptionally long incubation time to the low reactivity of TiN, as well as

**Fig. 1.** Schematic of the investigated samples. (b) Density of GaN nanowires obtained for a total growth duration of 155 min on the Si/TiN surface with different Si coverages. The samples are labeled A to E as indicated in the figure. (c) Bird's eye view scanning electron micrograph of two GaN nanowire ensembles obtained with two different Si coverages.





to the absence of surface contaminants and surface defects which would otherwise induce nucleation. On this surface, we deliberately create seeds for nucleation by *in situ* depositing a submonolayer of Si prior to GaN growth as schematically depicted in Fig. 1(a). Note that Si deposition occurs in ultra-high vacuum, but a reaction of Si with N (to form  $\text{Si}_x\text{N}_y$ ) is likely as soon as GaN growth is initiated. The Si coverage is varied from 0.006 to 0.6 monolayers and GaN is subsequently grown for 155 min.

On all samples with a finite Si coverage, GaN nanowires form, in contrast to the case of a pristine TiN surface. Their density directly correlates with the Si coverage, ranging from 0.04 to  $100 \mu\text{m}^{-2}$  as shown in Fig. 1(b). This result demonstrates the ability of a submonolayer of Si to effectively seed the growth of GaN nanowires on TiN. The scanning electron micrographs in Fig. 1(c) displaying two nanowire ensembles induced by different Si coverages evidence the strong changes in the ensemble density and nanowire diameter. Furthermore, no parasitic GaN layer is grown in between the nanowires, facilitating the optical investigation of these nanowires as opposed to those fabricated by the approach of Z. de Souza Schiaber (*op. cit.*), where the GaN substrate entirely dominates the optical response of the structure.

The nanowire dimensions for the various ensembles grown on Si are shown in the histograms of Fig. 2. For a Si coverage of 0.06 monolayers and below, the nanowires feature an average diameter of 15 nm with a narrow distribution ( $\pm 5$  nm). Further pre-deposition of Si leads to the appearance of thicker nanowires resulting in a strong broadening of the diameter distribution. This peculiar asymmetric distribution is a signature of the occurrence of coalescence between neighboring nanowires by bundling. This process becomes energetically favorable when the nanowires exceed a certain critical length or density [V. M. Kaganer *et al.*, *Nano Lett.*, **16**, 3717 (2016)], as

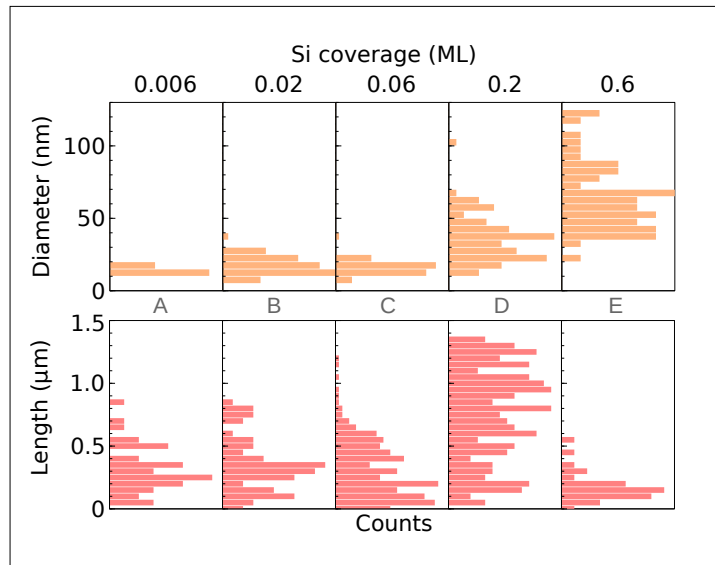


**Fig. 2.** Histograms of the GaN nanowire dimensions for the nanowire ensembles grown on Si/TiN with different Si coverages. The labels refer to the data points in Fig. 1(b).

induced here by increasing the Si coverage. Hence, the apparent correlation between the Si coverage and the nanowire diameter is primarily a consequence of the different nanowire densities. It is important to note that nanowire bundling leads to strain and dislocations in the coalesced nanowire aggregates, and should thus be avoided for preserving the high structural perfection of single GaN nanowires. The narrow diameter distribution for a Si coverage of and below 0.06 monolayers reflects the absence of bundling, meaning that the nanowires in these ensembles are entirely free of strain and dislocations.

The nanowire length distributions shown in Fig. 2 are broad even for the lowest Si coverage, and become narrow only for the highest Si coverage for which the nanowire density is very high. The mean nanowire length is neither constant, nor does it systematically depend on the Si coverage. Actually, we would expect that once nucleated, the elongation rate of GaN nanowires corresponds to the impinging N flux.

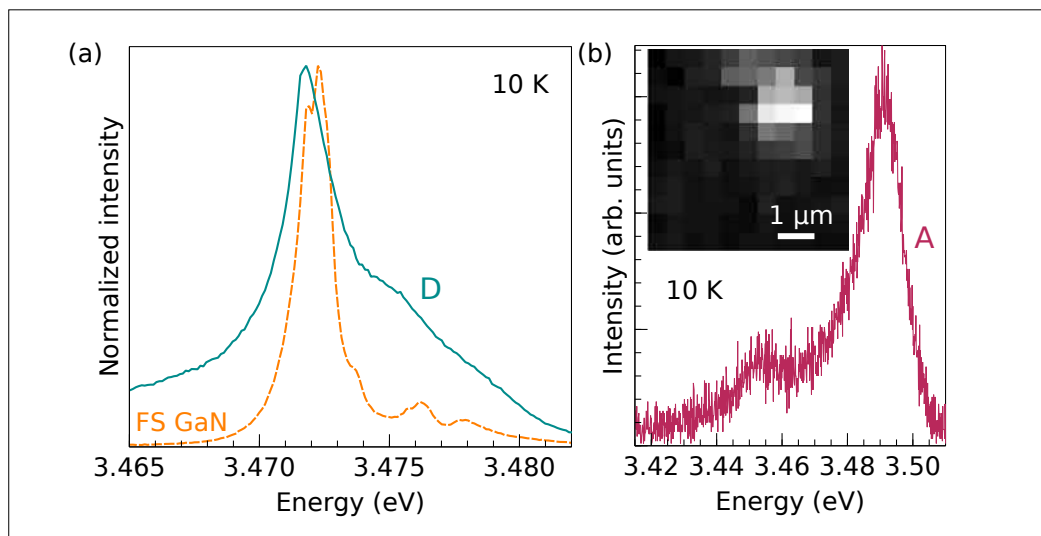


**Fig. 3.** (a) Near-band-edge PL spectrum of sample D and a freestanding (FS) GaN(0001) substrate. Due to the high density of the ensemble ( $50 \mu\text{m}^{-2}$ ), the  $3 \mu\text{m}$  excitation spot results in the excitation of about 350 nanowires. The excitation density was set to  $1 \text{ Wcm}^{-2}$ . (b) Near-band-edge PL of sample A. The extremely low density of the ensemble ( $0.04 \mu\text{m}^{-2}$ ) allows the excitation of single nanowires. The grey scale map in the inset shows the GaN PL intensity around the single nanowire. The excitation density amounts to  $1 \text{ kWcm}^{-2}$ .

A nanowire nucleating at the beginning of growth would thus reach a length of about  $2.1 \mu\text{m}$  after 155 min of growth, which is well above the maximum lengths found experimentally (see Fig. 2). This finding implies the existence of a delayed nanowire nucleation. This so-called incubation time can be directly measured for high-density ensembles by *in situ* monitoring the nanowire nucleation, using, for example, reflection high energy electron diffraction. In the present case, the very low nanowire density inhibits the observation of the nucleation onset. It is, however, clear that the incubation time must be substantial when comparing the mean length with the expected one.

The existence of an incubation time as well as the broad nanowire length distribution is reminiscent of GaN nanowires on Si substrates covered with amorphous  $\text{Si}_x\text{N}_y$ , for which both properties are observed as well. The broad length distribution reflects that GaN nanowires form spontaneously on the

amorphous  $\text{Si}_x\text{N}_y$  film at different points in time, in contrast to selective area growth that takes place on pre-defined sites rapidly inducing supersaturation, resulting in virtually instantaneous nanowire nucleation and a homogeneous length distribution. Hence, our present results resemble spontaneous nanowire formation rather than selective area growth. In addition, it is conceivable that the seeds forming by Si deposition and nitridation have a widely differing ability to induce nucleation due to different composition and size.

As mentioned above, the absence of a GaN substrate as well as parasitic growth allows direct optical investigations of the freestanding GaN nanowires. Figure 3(a) compares photoluminescence (PL) spectra of sample D and freestanding GaN. The position of their band edge is comparable and determined by the respective donor-bound exciton transition. The broadening observed for the nanowire sample is characteristic for

GaN nanowires and has several contributions, all related to the presence of the free surface. Figure 3(b) shows that for sample A with the lowest density, we can easily address single nanowires optically even with a low-magnification (15 ×) microscope objective. The PL peak energy indicates that the emission is due to free excitons experiencing a 10 meV blueshift due to dielectric confinement in the ultrathin nanowires. The intensity distribution in the PL map reflects the spatial resolution obtained with this objective.

In conclusion, the *in situ* deposition of Si on reactively sputtered TiN provides the unique possibility of tuning the density of self-assembled GaN nanowires down to ultralow values without GaN parasitic layer. In comparison to the pre patterning of substrates, this approach offers the advantage that nanowires with much smaller diameters (well below 20 nm) can be obtained. Such diameters are adequate for the realization of heterostructures providing zero-dimensional exciton confinement for achieving, for instance, single photon emission.

# Luminescence properties of coaxial GaAs/(In,Ga)As nanowire heterostructures with and without quantum dots grown using a Bi surfactant

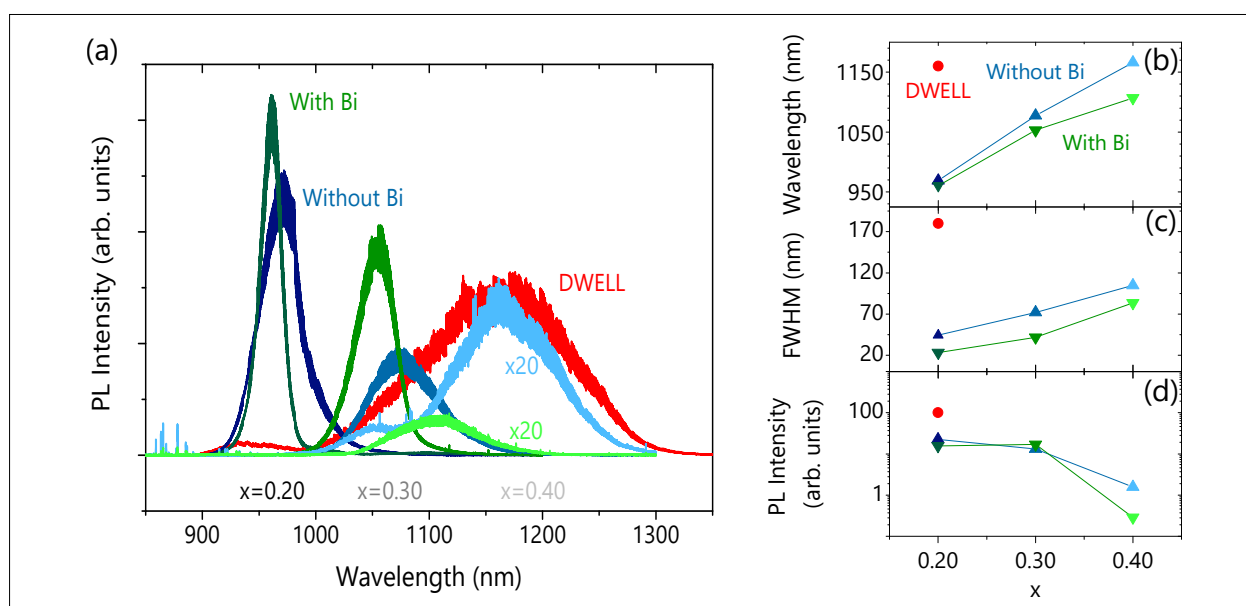
J. Herranz, M. Góra, J. Lähnemann, M. Oliva, R. B. Lewis, O. Brandt, L. Geelhaar

We have recently introduced a coaxial GaAs/(In,Ga)As dot-in-well (DWELL) nanowire (NW) heterostructure that extends the emission of GaAs-based NWs up to the telecommunication O band (1.26–1.36  $\mu\text{m}$ ) at room temperature, which could pave the way towards monolithically integrated light sources for Si photonics [J. Herranz *et al.*, ACS Appl. Nano Mater. **3**, 165 (2020)]. The formation of quantum dots (QDs) is promoted by Bi acting as a surfactant [R. Lewis *et al.*, Nano Letters **17**, 4255 (2017)]. Whereas the achieved emission wavelength is attractive for applications, the DWELL emission is very broad. In this respect, coaxial GaAs/(In,Ga)As quantum well (QW) NW heterostructures could be more promising.

Because, in such NW heterostructures, the strain induced by lattice mismatch is shared between core and shell, in principle higher In contents than in analogous planar QWs could be reached without deterioration in luminescence efficiency. Furthermore, supplying Bi as surfactant could potentially be beneficial also for QW NW heterostructures. Here, we present a comprehensive comparative study of coaxial GaAs/(In,Ga)As NW heterostructures comprising QWs with In composition up to 40%, grown with and without Bi supply, and the DWELLs integrating Bi-induced QDs.

All investigated samples were grown by molecular beam epitaxy (MBE) on Si(111) sub-

**Fig. 1.** (a) Low temperature (10 K) PL spectra of  $\text{In}_x\text{Ga}_{1-x}\text{As}$  QW NW samples with different In content  $x$ , grown with (green shades) and without a Bi flux (blue shades), and a DWELL NW sample (red) with an averaged In content of 20%. (b) Peak emission wavelength, (c) FWHM, and (d) integrated PL intensity corresponding to the spectra presented in (a).



strates patterned by electron beam lithography for selective area growth. Both QW and DWELL heterostructures were deposited around GaAs core NWs synthesized by the self-assisted growth method with a diameter of about 100 nm and predominantly zinc-blende crystal structure. Two series of QW NW samples were fabricated. They consist of a 10 nm thick  $\text{In}_x\text{Ga}_{1-x}\text{As}$  QW shell with In contents  $x = 0.20, 0.30$  and  $0.40$ , grown under nominally identical conditions, with and without additional Bi flux. An outer GaAs shell completes the structure. The DWELL shell consists of InAs QDs embedded in a 9 nm thick  $\text{In}_{0.15}\text{Ga}_{0.85}\text{As}$  QW shell. A Bi flux was employed to promote the formation of the QDs. Thus, the NW geometry is similar in all samples.

Low temperature photoluminescence (PL) spectra of all studied samples are presented in Fig. 1(a). The peak emission wavelength, full width at half maximum (FWHM) and integrated PL intensity are summarized in Fig. 1(b), Fig. 1(c) and Fig. 1(d), respectively. Increasing the In content  $x$  in the QW extends the emission towards long wavelengths as expected, with the  $\text{In}_{0.40}\text{Ga}_{0.60}\text{As}$  QW NW samples reaching similar peak emission wavelengths as the DWELL NW structure [Fig. 1(b)]. The QW NW samples grown with Bi supply show a relative blue-shift with respect to those grown without. Simultaneous to the redshift of the emission with increasing In content  $x$ , we observe an increase of FWHM [Fig. 1(c)] for the QW NW samples. Nevertheless, for all QW NWs the FWHM values are lower than for the DWELL NW sample. The broad emission of the DWELL NW heterostructure is characteristic for a large distribution in QD size and/or In content. Interestingly, the FWHM is reduced by a factor of approximately two for the QW NW samples grown with a Bi flux. In addition, Fig. 1(d) reveals that the integrated PL intensity of the QW NW samples decreases drastically with increasing In content  $x$ , both for the series grown with and without Bi supply. Consequently, the intensity of the  $\text{In}_{0.40}\text{Ga}_{0.60}\text{As}$  QW NW

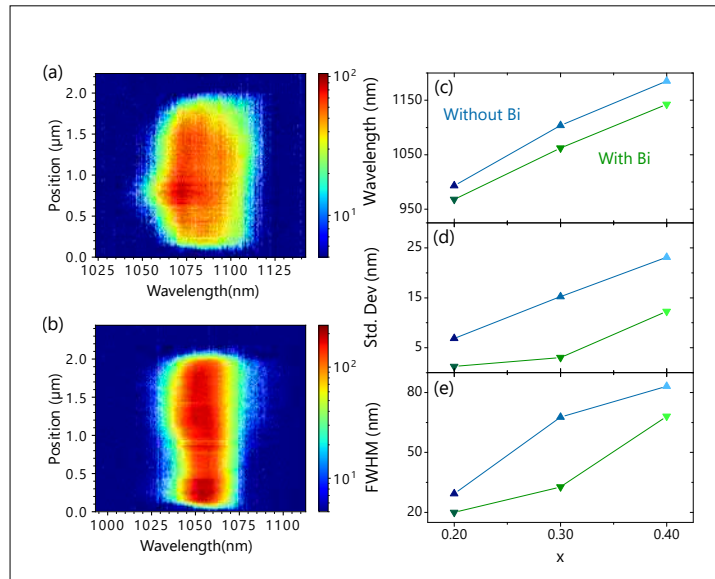


**Fig. 2.** Hyperspectral CL linescans acquired at 10 K for a single  $\text{In}_{0.30}\text{Ga}_{0.70}\text{As}$  QW NW grown (a) without and (b) with Bi flux. (c–d) Statistical analysis of the CL for 7 to 10 NWs on each QW NW sample, shown are (c) the average peak emission wavelength, (d) its standard deviation, and (e) the average FWHM of single NWs.

samples is much lower than the one of the DWELL NW sample, which exhibits a similar peak emission wavelength. Plastic relaxation of the QW shells might be responsible for the degradation of the emission properties of the  $\text{In}_x\text{Ga}_{1-x}\text{As}$  QW NW samples for high In content. A complex strain relaxation mechanism with simultaneous coherent shell growth and plastically relaxed growth of three-dimensional mounds has been reported for such  $\text{In}_x\text{Ga}_{1-x}\text{As}$  shells with higher In contents [R. Lewis *et al.*, *Nano Letters* **17**, 136 (2017)].

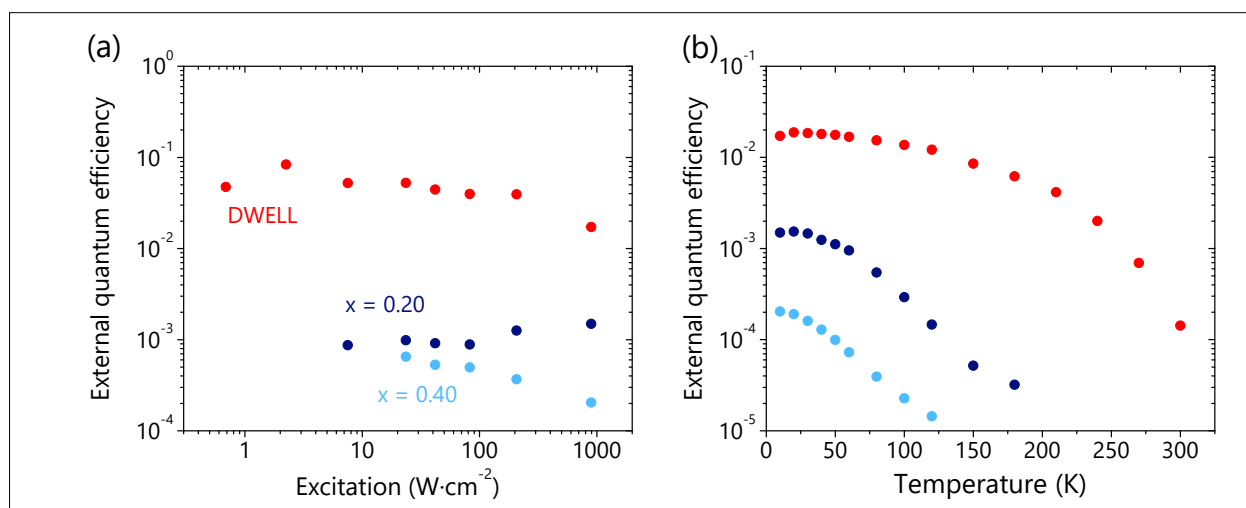
In order to investigate the width of the emission in more detail, we employ cathodoluminescence (CL) spectroscopy. Representative hyperspectral linescans are shown in Fig. 2 for an  $\text{In}_{0.30}\text{Ga}_{0.70}\text{As}$  QW NW grown without [panel (a)] and with Bi flux [panel (b)], respectively. These linescans reveal that the emission along individual NWs is in both cases fairly homogeneous. Also, the emission is less broad

for the QW NW grown with Bi. We carried out a statistical analysis of the integrated emission of 7 to 10 single NWs for each QW NW sample, and the average peak emission wavelength, its standard deviation, and the average FWHM are presented in Fig. 2(c), (d), and (e). We note that the average FWHM of single NWs on a given sample is indicative of QW fluctuations within one NW, whereas the standard deviation of the peak emission wavelength is caused by variations from NW to NW. Both parameters are reduced with a supply of Bi, consistent with the reduced FWHM observed in the ensemble PL measurements [Fig. 1(a)]. Interestingly, we observe that the ensemble width is dominated by single NW broadening, while NW to NW variations are smaller, even if we assume a gaussian distribution for these variations [FWHM =  $2.355 \cdot \sigma$ , where  $\sigma$  is the standard deviation presented in Fig. 2(d)]. The reduction in both types of broadening can be explained by enhanced surface diffusion between different sidewall facets under the influence of Bi.

Finally, we evaluate the external quantum efficiency (EQE) for the DWELL NW het-

erostructure, as well as for the  $\text{In}_x\text{Ga}_{1-x}\text{As}$  QW NW heterostructures with In composition  $x = 0.20$  and  $0.40$ . Using an ideal diffuse reflector (Zenith Polymer) as a standard for an EQE of unity, the measurement of absolute PL intensities provides a method to assess the EQE of the investigated NWs. Figure 3 summarizes the experimental EQE results. Figure 3(a) presents the EQE at low temperature (10 K) as a function of the excitation power. The EQE is one to two orders of magnitude higher for the DWELL NW sample than for the QW NW samples. For high excitation, the DWELL NW efficiency decreases as a result of the saturation of the QD emitters. A similar behaviour is also observed for the  $\text{In}_{0.40}\text{Ga}_{0.60}\text{As}$  QW NW sample, which, in this case, could be attributed to the saturation of localized states stemming from compositional fluctuations. Figure 3(b) depicts the EQE data as a function of temperature. The DWELL NW sample emits light up to room temperature, while no emission is detected for the QW NW samples above 180 K and 120 K for  $x = 0.20$  and  $0.40$ , respectively. The former result indicates that the confinement of carriers in the QDs of

**Fig. 3.** Experimental EQE at low temperature (10 K) as a function of (a) excitation power and (b) temperature for the DWELL NW (red),  $\text{In}_{0.20}\text{Ga}_{0.80}\text{As}$  QW NW (blue) and  $\text{In}_{0.40}\text{Ga}_{0.60}\text{As}$  QW NW (light blue) samples. The excitation power for the measurements in (b) was  $300 \text{ Wcm}^{-2}$ .



the DWELL heterostructure provides effective protection from capture at non-radiative recombination centers. We should note that the studied NWs exhibit similar dimensions and, therefore, similar absorption properties. Thus, the measured EQE trends correspond directly to trends in the internal quantum efficiency (IQE) of these heterostructures.

Our comparative study demonstrates a high radiative efficiency for the DWELL NW heterostructure, with an EQE up to 8.3% at low temperature and low excitation power and only a comparatively moderate decrease of emission intensity up to room temperature. In contrast, the radiative efficiency of the  $\text{In}_x\text{Ga}_{1-x}\text{As}$  QW NW structures is much lower, in particular for high In content, corresponding to a similar emission wavelength as for the DWELL NWs. At the

same time, the QWs offer a much narrower emission, in particular when grown under a Bi flux. For the active region of a NW laser monolithically integrated on a Si photonics platform, the high efficiency of the DWELL heterostructure is promising. Nevertheless, its broad emission presents a limitation for this purpose, since it implies that only a fraction of the QDs can contribute to lasing at a certain wavelength. Furthermore, due to their low density, QDs are easily saturated. Towards GaAs-based NW heterostructures optimal for lasing in the near-infrared spectral region, either QD fluctuations must be reduced or the quantum efficiency of the QWs improved.

The authors acknowledge funding from the German Federal Ministry of Education and Research BMBF in the framework of project MILAS.

# Small-angle x-ray scattering from self-assembled GaN nanowires

V. Kaganer, D. van Treeck, G. Calabrese, J. K. Zettler, O. Brandt, S. Fernández-Garrido, O. Konovalov<sup>1</sup>

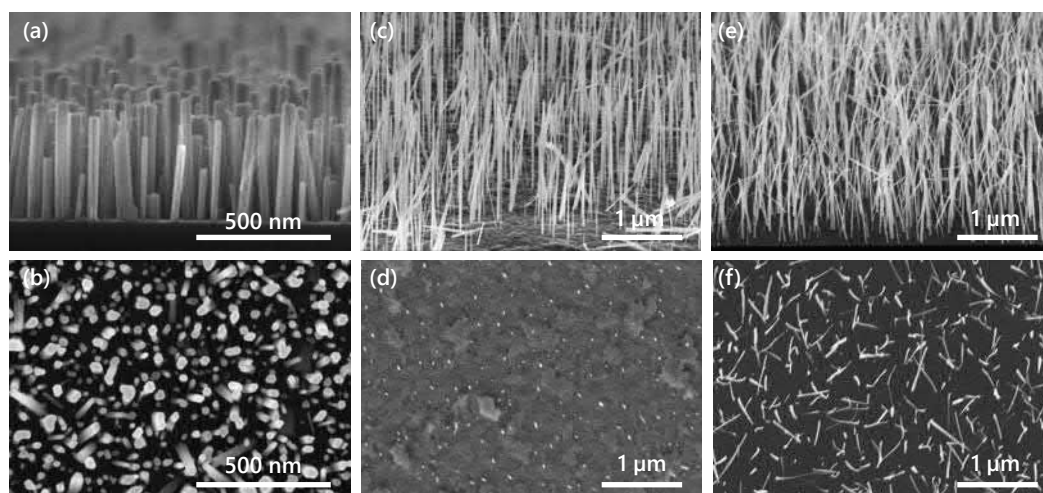
GaN nanowires (NWs) spontaneously form in plasma-assisted molecular beam epitaxy on various substrates at elevated temperatures under an excess of N. On the most common substrate Si(111), they grow in dense ensembles ( $> 10^{10} \text{ cm}^{-2}$ ) and experience massive coalescence during their growth. Using the metallic ceramics TiN as a substrate enables us to obtain long NWs with a density below  $10^9 \text{ cm}^{-2}$  free from coalescence and as thin as 20 nm. As-grown GaN NWs can be thinned further by thermal decomposition at elevated temperatures for investigating diameter-dependent phenomena. Figure 1 exemplifies three NW ensembles. GaN NWs on Si(111) are presented in Figs. 1(a) and 1(b). Their diameter distribution can be obtained from the top-view secondary electron micrographs. This

is, however, hardly possible for NWs on TiN [Figs. 1(c) and 1(d)] because of the low NW density or for thermally decomposed NWs [Figs. 1(e) and 1(f)] because of their bending.

Grazing incidence small-angle x-ray scattering (GISAXS) is well suited for the determination of diameter distributions of NWs, treated in this context as orientationally aligned cylindrical objects. Moreover, smaller diameters give rise to larger scattering angles, which simplifies the analysis. Figure 2(a) presents the GISAXS intensity distribution for GaN NWs on Si(111). The Yoneda streak ("Y") is located at the critical angle for total external reflection. For the present study, the intensity streaks around the transmitted (labeled "T") and reflect-

<sup>1</sup> European Synchrotron Radiation Facility, Grenoble, France.

**Fig. 1.** Bird's eye view (top) and top-view (bottom) secondary electron micrographs of GaN NWs (a) and (b) on Si(111), (c) and (d) on TiN, (e) and (f) on Si(111) after thermal decomposition.





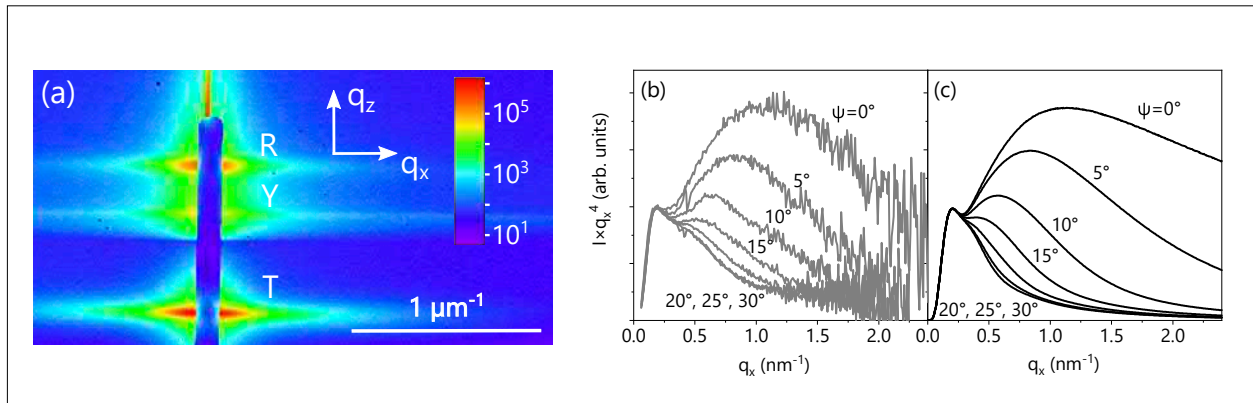


**Fig. 2.** (a) GISAXS intensity from GaN NWs on Si(111) as measured by a two-dimensional detector. The vertical blue bar in the middle of the scattering pattern is the beamstop. The color-coded scale bar represents the intensity in counts. (b) Measured intensities along the "T" streak on the intensity map and (c) Monte Carlo modeling of the scattering intensity.  $\psi$  is the angle between the incident beam and the side facets of the NWs. The intensities are displayed as  $I(q_x)q_x^4$  versus  $q_x$  to highlight the deviations from Porod's law.

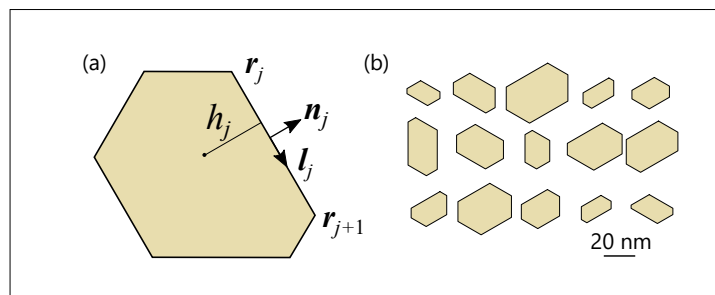
ed beams ("R") are important. Since they possess the same intensity distributions, we use more the intense "T" streak for the analysis described in the following.

The intensity distribution is expected to be described by Porod's law, which states that the small-angle scattering intensity from objects with rigid borders follows, at large wave vectors  $q$ , the universal dependence  $I \propto q^{-4}$ . This law is directly related to Fresnel's law for scattering from planar surfaces and is as general. In Fig. 2(b), we plot the measured intensities as  $I(q_x)q_x^4$  versus  $q_x$ , for which a constant is expected at large  $q_x$ . However, we find systematic deviations from Porod's law, depending on the rotation angle  $\psi$  of the sample about the substrate normal. This dependence is explained by the epitaxial relation of NWs to the substrate: the side facets of NWs are aligned with respect to the substrate: GaN(1100) || Si(112). The intensity is maximum when the scattering vector is along the facet normal,  $\psi = 0^\circ$ , similarly to the surface truncation rod scattering for planar surfaces.

We calculate the scattering amplitude from a NW treating it as a prism with an arbitrary

distorted hexagonal cross section, as shown in Fig. 3(a). The form factor of a faceted crystal can be expressed through the coordinates of its vertices [von Laue, Ann. Phys. **26**, 55 (1936)]: the integral over the NW volume is reduced, using Gauss' theorem, to the integrals over the facets; application of Gauss' theorem to these area integrals reduces them to integrals over the edges, which, in turn, can be taken by parts and expressed through the coordinates of

**Fig. 3.** A hexagon with vertices  $\mathbf{r}_j$  and unit vectors  $\mathbf{l}_j$  and  $\mathbf{n}_j$  along and normal to the side facet, respectively. The distance from the hexagon center to its side facet is  $h_j$ . (b) Examples of randomly generated hexagons used to simulate the scattering from GaN NWs on Si(111).



the vertices. For a planar polygon, the form factor reads

$$A(\mathbf{q}) = \frac{1}{q^2} \sum_j \frac{\mathbf{q} \cdot \mathbf{n}_j}{\mathbf{q} \cdot \mathbf{l}_j} \left( e^{i\mathbf{q} \cdot \mathbf{r}_{j+1}} - e^{i\mathbf{q} \cdot \mathbf{r}_j} \right), \quad (1)$$

where the sum runs over the vertices and, as illustrated in Fig. 3(a),  $\mathbf{r}_j$  are coordinates of the vertices,  $\mathbf{l}_j$  and  $\mathbf{n}_j$  are unit vectors along the polygon side between the vertices  $\mathbf{r}_j$  and  $\mathbf{r}_{j+1}$  and normal to it, respectively.

With the form factor defined by the positions of the vertices according to Eq. 1, we are not restricted to regular hexagons but can take into account the actual cross-sectional shapes of the NWs. Since the side facets of the NWs are GaN  $\{1\bar{1}00\}$  planes making an angle of  $60^\circ$  to each other, we build the hexagons as shown in Fig.3(a): random heights  $h_j$  are taken in the directions normal to the facets. Then, we check that the generated hexagon is convex, and discard it otherwise. Figure 4(b) presents examples of randomly generated hexagons with the same orientation of their sides. This distribution of the hexagons is used to simulate the ensemble of GaN NWs on Si(111).

The side facets of GaN NWs are atomically flat but may have atomic steps. The radial

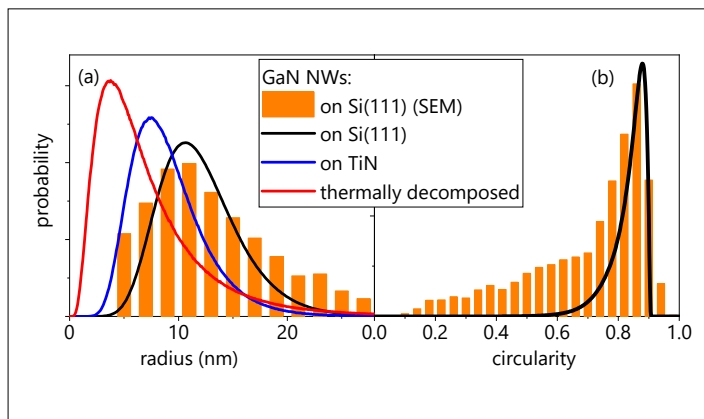
growth of these NWs presumably proceeds by step flow, with the motion of steps from the NW top, where they are nucleated, down along the side facets. Random steps across the side facets can be treated as facet roughness in the same way as it is done in the calculation of crystal truncation rods. A step of height  $d_0$  shifts the  $j$ th side of the polygon in Fig. 3(a) by a vector  $d_0 \mathbf{n}_j$  in the direction of the facet normal. Hence, the  $j$ th term in the sum (1) acquires an additional factor  $\exp(i d_0 \mathbf{q}_\perp \cdot \mathbf{n}_j)$ . Random steps give rise to a factor  $R_j = R(\mathbf{q}_\perp \cdot \mathbf{n}_j)$ , where the function  $R(q)$  is defined as  $R(q) = \sum_{m=0}^{\infty} p_m \exp(imqd_0)$ , here  $p_m$  are the probabilities of the shift of the side facet by  $m$  steps. Hence, the function  $R(q)$  is the characteristic function of the probabilities  $p_m$ .

We found that the geometric probability distribution  $p_m = (1-\beta)\beta^m$  adequately describes the experimental profiles. It corresponds to a flat surface with a fraction  $\beta < 1$  one step higher, a fraction  $\beta$  on these terraces again one step higher, and so on. The corresponding characteristic function is  $R(q) = (1-\beta) / [1-\beta \exp(iqd_0)]$ , and the root mean squared (rms) roughness is  $\sigma = d_0 \sqrt{\beta} / (1-\beta)$ .

Figure 2(c) presents the results of the Monte Carlo modeling of the GISAXS intensity. For the simulations, the NW length, tilt, orientation of side facet (twist), cross-sectional size and shape are random parameters, with the distributions of NW lengths, tilt and twist angles being determined in independent prior experiments. The parameters of the NW ensemble to be determined from the modeling are the mean width of the side facets, its variation, as well as the variation of the cross-sectional shapes of the NWs, and the roughness of the side facets.

The x-ray scattering profiles obtained by the Monte Carlo modeling are presented in Fig. 2(c). Figure 4 compares the distributions of NW radii and circularities obtained from the Monte Carlo simulations of the

**Fig. 4.** Distributions of NW radii (a) and circularity (b) obtained from the analysis of the top-view secondary electron micrographs of NWs on Si(111) (bars) and the results of the Monte Carlo modeling of the GISAXS profiles (lines).



GISAXS profiles with the distributions obtained from the analysis of top-view secondary electron micrographs. In both cases, the area  $A$  and the perimeter  $P$  of each NW were determined to obtain the equivalent-disk radius  $R$  from  $A = \pi R^2$  and the circularity  $C = 4\pi A/P^2$ . The deviation for larger radii and lower circularities mainly stems from the fact that GISAXS resolves even coalesced aggregates into their individual constituents, and thus represents the actual single NW shape rather than the one of coalesced aggregates. The rms roughness obtained from the Monte Carlo modeling amounts to  $\sigma = 0.9$  nm, i.e., 3–4 atomic steps on a  $1 \mu\text{m}$  long GaN(1 $\bar{1}$ 00) facet.

The results for the GaN NW ensemble on TiN and the thermally decomposed one on Si(111) are presented in Figs. 5(a) and 5(b). The intensity profiles are adequately described by regular hexagons of circularity  $C = \pi\sqrt{3}/6$ , which agrees with the absence of the coalescence in these NW ensembles. Smaller scattering volumes of NWs and larger parasitic scattering from the substrate roughness limits the  $q$ -range of the intensity profiles. However, the average NW radius  $R$  can be directly obtained from the position of the maximum  $q_m$  in the  $Iq_x^4$  versus  $q_x$  profiles as  $R \approx 1.9/q_m$ . Thus, we can obtain the NW radii distributions for these samples as presented in Fig. 4(a).

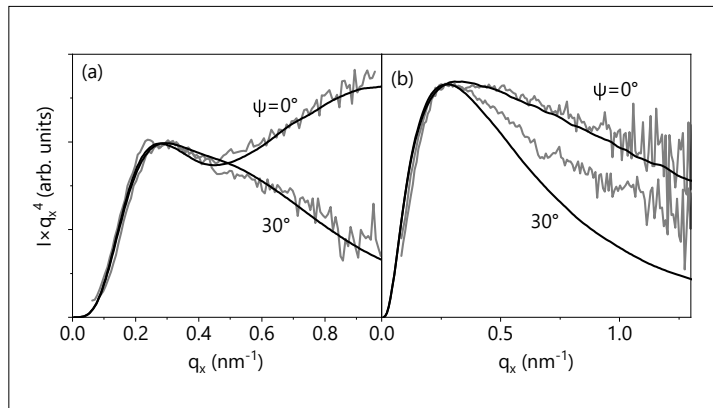


Fig. 5. The measured GISAXS intensity (gray lines) and Monte Carlo simulations (black lines): (a) GaN NWs on TiN and (b) thermally decomposed GaN NWs on Si(111).

Concluding, we have shown that GISAXS, in conjunction with the Monte Carlo modeling of the intensity profiles, is well suited for the determination of the distributions of the cross-sectional sizes of the NWs, their actual shapes, and the atomic-scale roughness of their side facets. Particularly the latter quantity cannot be easily extracted from electron micrographs, making GISAXS uniquely suited for a full morphological characterization of NW ensembles. Moreover, the methods developed in the present work are not specific to GaN NW, but can be applied to any other materials systems and NW arrangements.

# Triggered generation of correlated photons by parametrically scattered polaritons at MHz frequencies

A. S. Kuznetsov, G. Dagvadorj<sup>1,2</sup>, K. Biermann, M. H. Szymanska<sup>2</sup>, P. V. Santos

Many fundamental physical concepts developed for atoms can be conveniently emulated by confined solid-state systems with discrete energy levels. Unlike real atoms, these solid-state analogues suffer from disorder associated with fluctuations of material properties and structural dimensions, which impair their exploitation for complex and scalable functionalities. A particular example, which is relevant for optical amplification and generation of correlated photons, is the effect of optical parametric oscillation (OPO) – the non-linear coherent coupling of an optically excited two particle pump state to a signal and an idler states with different energies. An OPO requires multiple optoelectronic states with well-defined symmetries and precise energy configuration. The latter challenges, together with the unavoidable fluctuations in dimensions and material properties of real structures, considerably limit OPO's practical implementations. This work introduces a way to overcome these constraints based on the fine-tuning of confined states using dynamic acoustic fields in an all-semiconductor structure.

We use the molecular beam epitaxy (MBE) technique to grow a laterally structured high-quality optical (Al,Ga)As microcavity (MC) with embedded multiple GaAs QWs, schematically shown in Fig. 1(a). The properties of the MC give rise to the strong coupling between photons and QW excitons, resulting in exciton-polaritons (sim-

ply, polaritons) – half-light, half-matter quasiparticles. Confinement of polariton states originates from  $\mu\text{m}$ -sized intra-cavity traps created within the spacer layer of the MC. The traps were produced by etching the spacer layer of the MC between MBE growth steps. During the first stage of the MBE growth run, the lower distributed Bragg reflector (DBR) and the MC spacer region containing three pairs of 15 nm-thick GaAs QWs centered at the antinodes of the optical field were grown with an additional 120 nm thick (Al,Ga)As layer. The latter is needed to protect the QWs and to match their position to an antinode of the optical field. The sample was then removed from the MBE chamber and patterned by means of photolithography and wet chemical etching to form 12-nm high and a few  $\mu\text{m}$  wide mesas with different shapes. For the final growth step, the sample was reinserted in the MBE chamber for the deposition of the upper DBR. The etching of the MC spacer layer results in a blueshift of the bare optical mode of the MC by a few nm. As a consequence, the energy of the lower polariton mode in the etched regions becomes higher than the one in the non-etched areas. Polariton traps with the desired energy barrier height can then be formed by enclosing a  $\mu\text{m}$  sized non-etched region by etched areas [A. S. Kuznetsov *et al.*, Phys. Rev. B **97**, 195309 (2018)].

An array of such intra-cavity traps was placed within an acoustic resonator formed

<sup>1</sup> Department of Physics, University of Warwick, Coventry, United Kingdom.

<sup>2</sup> Department of Physics and Astronomy, University College London, London, United Kingdom.

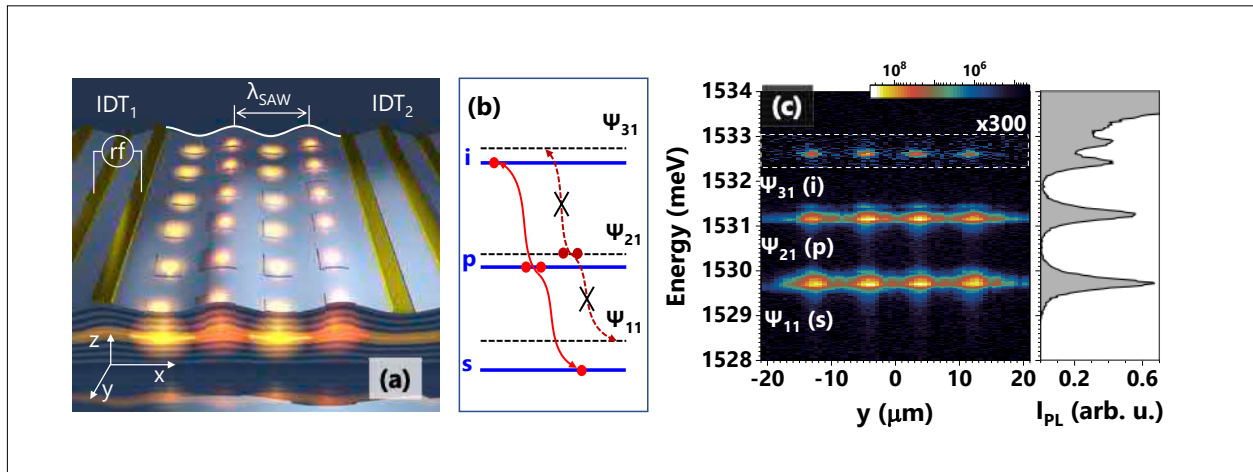


**Fig. 1.** (a) A sketch showing the acoustic modulation of an array of intra-cavity polariton traps. The traps are positioned at the antinodes of the standing field of an acoustic resonator consisting of a driving interdigital transducer (IDT<sub>1</sub>) and a passive reflecting one (IDT<sub>2</sub>). The coloured spots represent emission of polariton condensates excited optically. (b) A sketch of confined levels of a single trap in the absence (dashed line) and under a SAW (solid lines). The SAW induces level-dependent energy shifts that enable an OPO where two pump polaritons injected in the pump state (p,  $\Psi_{21}$ ) scatter into signal (s,  $\Psi_{11}$ ) and idler (i,  $\Psi_{31}$ ) states equidistantly spaced with respect to the pump. (c) Photoluminescence map of a row of traps of the OPO array. The array consists of nominally  $3 \times 3 \mu\text{m}^2$  intra-cavity traps with a pitch of  $9 \mu\text{m}$ . The traps are resonantly excited into  $\Psi_{21}$ . The signal and idler states are clearly visible. The right-most panel displays the spatially integrated PL spectrum of a single trap recorded under weak non-resonant excitation. All measurements were done at 10 K.

by two opposing interdigital piezoelectric transducers (IDTs) with the array sites located on the antinodes of the standing acoustic field as illustrated in Fig. 1(a). The IDTs were designed for launching surface acoustic waves (SAWs) along the  $x \parallel [\bar{1}10]$  surface direction with a wavelength of  $8 \mu\text{m}$  (corresponding to the acoustic frequency  $f_{\text{SAW}} = 383.66 \text{ MHz}$  at 10 K). Only one of the two IDTs was driven. The other one acted as a passive acoustic reflector. The delay line forms an acoustic resonator with a quality factor of 4700. In the absence of the acoustic excitation, the energy configuration of the trap levels does not fulfill the energy and symmetry matching conditions for OPO excitation as illustrated schematically by the dashed lines in Fig. 1(b). In contrast, in the presence of the acoustic field, the optical pumping of the confined state  $\Psi_{21}$  triggers Bose-Einstein OPO condensates (BECs) on all sites of the array as shown by the spectral photoluminescence

(PL) map of Fig. 1(c). The OPO manifests itself as signal and idler PL signatures redshifted and blueshifted, respectively, about the pump energy. The photons emitted by the signal and idler states are correlated in energy, i.e., two pump polaritons are transformed into one signal and one idler polariton, thus conserving the total energy:  $2E_{\text{pump}} = E_{\text{signal}} + E_{\text{idler}}$ , where  $E_{\text{pump}}$  is the pump energy, and  $E_{\text{signal}}$  and  $E_{\text{idler}}$  are the energies of the signal and idler states, respectively. [A. S. Kuznetsov et al, *Optica* 7, 12, 1673-1681 (2020)]

The results of Fig. 1(c) represent a novel concept, reported in this work, which is the dynamic control of the scattering pathways of resonantly excited confined polariton BECs based on the modulation by the spatially and time-varying potentials produced by SAWs. The effect of the SAW is primarily due to the strain modulation of the QW exciton energy [A. S. Kuznetsov et al., *Phys.*

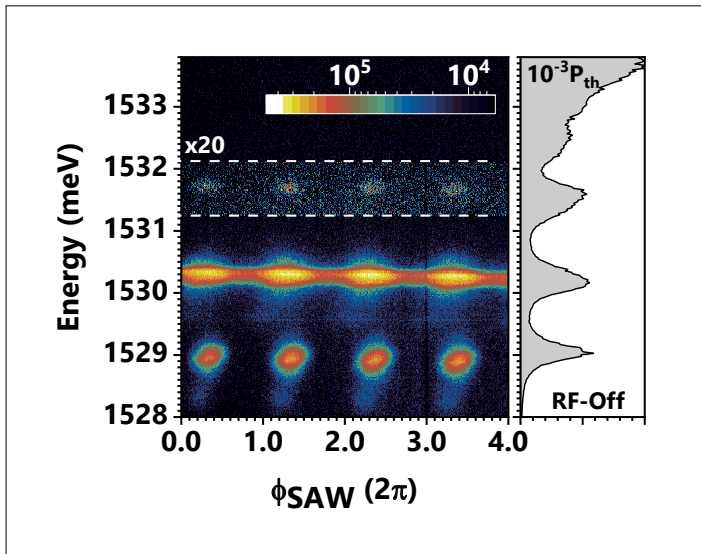


**Fig. 2.** Time-resolved PL map of a nominally  $4 \times 4 \mu\text{m}$  trap recorded under acoustic modulation at  $f_{\text{SAW}} = 383.69 \text{ MHz}$  at 10 K. The map shows the OPO excitation by resonant pumping of the second confined level. The optical excitation power density was  $2P_{\text{th}}$ , where  $P_{\text{th}}$  is the threshold power for the condensation. The right panel displays the trap PL spectrum in the absence of the SAW and optical excitation power of  $10^{-3} P_{\text{th}}$ .

Rev. Res. **1**, 023030 (2019)]. The spatially dependent SAW fields dynamically control the energy of the individual confined polariton states. In this way, the SAW matches the energies of the levels with the appropriate symmetry to act as signal, pump, and idler OPO states.

The dynamic character of the SAW-induced OPO is revealed in the time-resolved PL map of a single trap shown in Fig. 2, which demonstrates the activation of the OPO once per SAW period  $T_{\text{SAW}} \approx 2.6 \text{ ns}$ . The temporal width of each OPO pulse is

$\Delta t_{\text{OPO}} = 690 \pm 50 \text{ ps}$ . This map shows that a continuous optical signal can be transformed into a train of coherent ps pulses and proves that, in addition to the energy correlation, the signal and idler photons are correlated in time. The findings are in excellent agreement with advanced calculations carried out using a driven-dissipative theoretical framework that captures the non-linear physics of the OPO processes. The latter opens a way to accurately predict the dynamic properties of such arrays.

In summary, the work demonstrates a scalable semiconductor platform for the triggered generation of correlated photon pairs as well as for the ultrafast modulation of optical signals. Our approach offers several benefits for the realization of OPO devices and nanophotonic circuits. Firstly, the OPO can be electrically triggered with high repetition rate by rf pulses of about 400 MHz. This allows to start and stop the generation of correlated photons on demand. Secondly, we demonstrated that OPOs can be synchronously excited on all sites of an array of traps using a single acoustic beam. This opens a way for the realization of scalable non-linear on-chip systems. Here, the benefits are two-fold: (a) the SAW modulation of the individual polariton traps in the array appropriately tunes the confined levels and counteracts unavoidable fluctuations in dimensions and material properties; and (b) the OPO emission from the array sites is time-correlated by the SAW phase.

We acknowledge the financial support by German DFG (grant 359162958) and QuantERA grant Interpol (EU-BMBF grant nr. 13N14783).

# Remotely pumped, GHz anti-bunched emission from single-exciton centers in GaAs

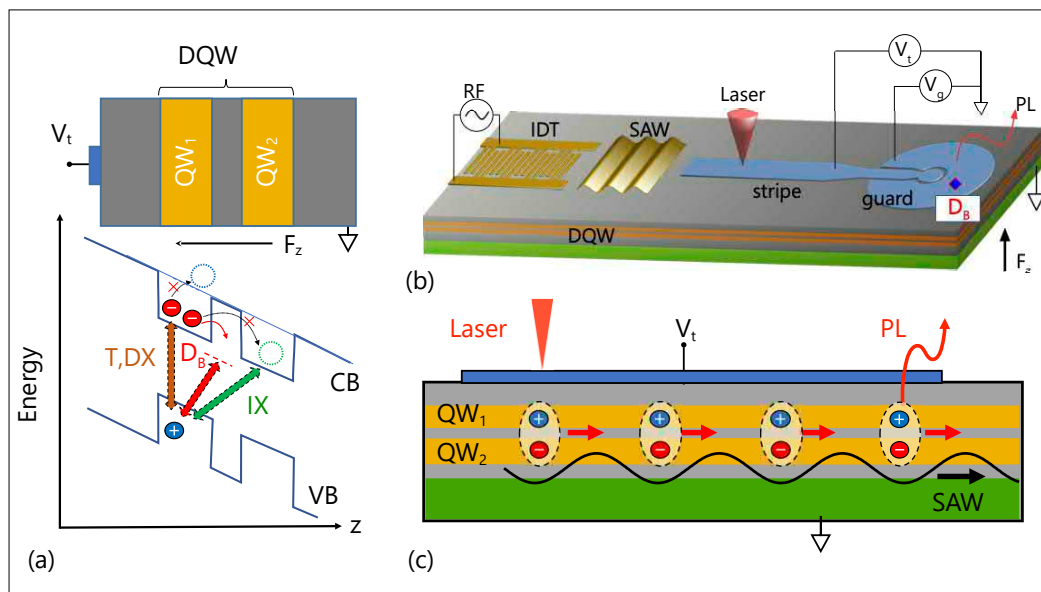
M. Yuan, K. Biermann, S. Takada<sup>1,2</sup>, C. Bäuerle<sup>2</sup>, P. V. Santos

Scalable quantum networks require the on-chip transfer and manipulation of single particles as well as their interconversion to single photons for long-range information exchange. Flying excitons propelled by GHz surface acoustic waves (SAWs) are outstanding messengers to fulfill these requirements. A main challenge for the implementation of flying excitonic qubits is the creation of two-level excitonic states interconnected by a transport channel, which

can store single particles and convert them to photons. Here, we realize a major step towards this goal by demonstrating the acoustic manipulation and remote pumping of single-exciton centers by flying indirect excitons (IXs) propelled by GHz-SAWs in a GaAs-based semiconductor platform.

The studies were carried out in a GaAs/(Al,Ga)As double quantum well (DQW) structure consisting of two GaAs QWs coupled

**Fig. 1.** (a) IX formation via the dissociation of direct excitons (DXs) or trions (Ts) by the electric field ( $F_z$ ) induced electron tunneling between the quantum wells (QWs). Within a narrow field range ( $\sim 1$  kV/cm), the trion dissociation into IXs (dashed circles) is blocked leading to the selective excitation of bound exciton states ( $D_B$ ). (Dissociation of a DX is also possible but less favourable energetically.) (b) and (c) Sketches of the samples for acoustic IX transport. The IX are formed in the DQW regions underneath a stripe-like semitransparent gate subjected to a bias  $V_t$ . The stripes ends in a small circular trap area with a guard gate biased by  $V_g$ . An interdigital transducer (IDT) launches a SAW, which captures and transports the optically excited IXs along the stripe. The IX distribution is probed by collecting the spatially resolved photoluminescence (PL) intensity along the path.



1 National Institute of Advanced Industrial Science and Technology (AIST), National Metrology Institute of Japan (NMIJ), Tsukuba, Ibaraki, Japan.

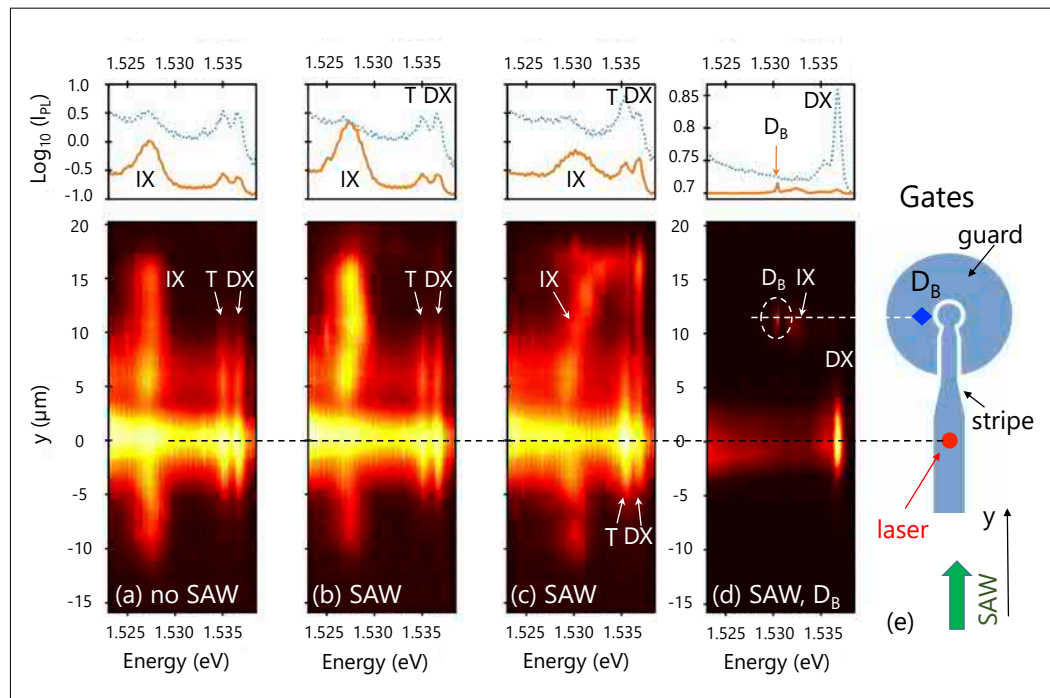
2 Univ. Grenoble Alpes, CNRS, Grenoble INP, Institut Néel, Grenoble, France.

by a thin barrier grown by molecular beam epitaxy on an  $n$ -type doped GaAs(001) substrate [cf. Fig. 1(a)]. An electric field  $F_z$  induced by the bias  $V_t$  applied across the structure drives photoexcited electrons into  $QW_2$  and holes into  $QW_1$ , resulting in IX formation. The DQW structure can thus hold both direct (or intra-QW, DX) and indirect (inter QW) excitons with transition energies indicated by the brown and green arrows in Fig. 1(a), respectively. The structure can also hold single shallow impurities (denoted as  $D_B$ ), which can bind single excitons (red arrow). Under weak optical excitation and biases  $V_t$  close to the onset of IX formation, photoexcited electron-hole pairs bind to free residual carriers to form trions (Ts). The conversion of trions to IXs via electron tunneling through the DQW barrier requires

the excitation of a free electron to the band states. As illustrated in Fig. 1(a), the resonant tunneling to single  $D_B$  becomes energetically favorable to the IX formation.

IXs can be confined and transported along a  $\mu\text{m}$ -wide channel defined by a biased stripe gate using the mobile band gap modulation produced by the SAW strain field, as illustrated in Figs. 1(b) and 1(c). We use interdigital acoustic transducers (IDTs) to launch SAWs with a wavelength of  $\lambda_{\text{SAW}} = 800 \text{ nm}$ , corresponding to a frequency of  $f_{\text{SAW}} = 3.58 \text{ GHz}$ . Optically detected IX transport experiments were carried out at 4 K with a spatial resolution of approx.  $1 \mu\text{m}$ . The excitons were excited by a spot from a pulsed laser (wavelength of  $770 \text{ nm}$ , pulse width of  $270 \text{ ps}$ , synchronized

**Fig. 2.** (Lower panels) Spatially resolved photoluminescence maps on a log intensity scale in the absence (a) and in the presence of a SAW for (b)  $P_{\text{rf}} = -9 \text{ dBm}$  and  $V_t = V_g = 0.2 \text{ V}$  and (c)  $P_{\text{rf}} = -11 \text{ dBm}$ , for  $V_t = 0.23 \text{ V}$ , and  $V_g = 0.31 \text{ V}$ . (d) Corresponding map with a  $D_B$  on the transport path and biasing conditions to enhance the impurity PL ( $P_{\text{rf}} = -14 \text{ dBm}$  and  $V_t = V_g = 0.4 \text{ V}$ ). (e) Sketch of the transport path defined by electrostatic gates. The upper panels in (a)–(d) display profiles of the PL intensity integrated around the excitation region ( $|y| < 3 \mu\text{m}$ , dotted) and along the transport path ( $y > 3 \mu\text{m}$ , solid).





with the SAW) focused by a microscope objective onto the semitransparent stripe.

We observe long-range transport of IXs, which enables the remote pumping of  $D_B$  centers. The lower panel of Fig. 2(a) displays a spectrally resolved photoluminescence (PL) map of the exciton distribution under the electrostatic stripe gates using optical excitation by a laser spot at  $y = 0$  [cf. sketch of Fig. 2(e)]. This map was recorded in the absence of the SAW under a transverse field  $F_z = 5$  kV/cm. The PL around the excitation spot (dotted line in the upper panel, integrated for  $|y| < 3 \mu\text{m}$ ) shows the characteristic emission lines from DX, T, and IXs superimposed on a broad PL background from the doped layers and emission centers in the substrate (note that the intensity of the DX and T lines become strongly suppressed under  $F_z$ ). Away from the generation area the PL is dominated by the emission from IXs, which, due to the long recombination lifetime, can diffuse up to the top region of the guard gate (solid line).

Figure 2(b) displays a PL map recorded under the same conditions as in Fig. 2(a), but now under the SAW propagating along the  $y$  direction. The acoustic field pushes the IXs upwards leading to a strong increase of the IX PL intensity for positive  $y$  (cf. solid line in the upper panel) and a reduction for negative  $y$ . The recombination energy and location of the transported IXs can be controlled by changing the bias applied to the gates. As an example, Fig. 2(c) shows a map recorded by increasing the guard bias by 0.08 V relative to  $V_t$ . The IX emission energy blueshifts when IXs enter the guard gate as well as when the particles are pushed by the SAW beyond the guard, where they become converted to DXs or trions. The additional energy for this conversion is provided by the moving SAW field.

The IX transported over tens of  $\lambda_{\text{SAW}}$  can remotely activate  $D_B$  as shown in Fig. 2(d). Here, the SAW amplitude and gate bias-

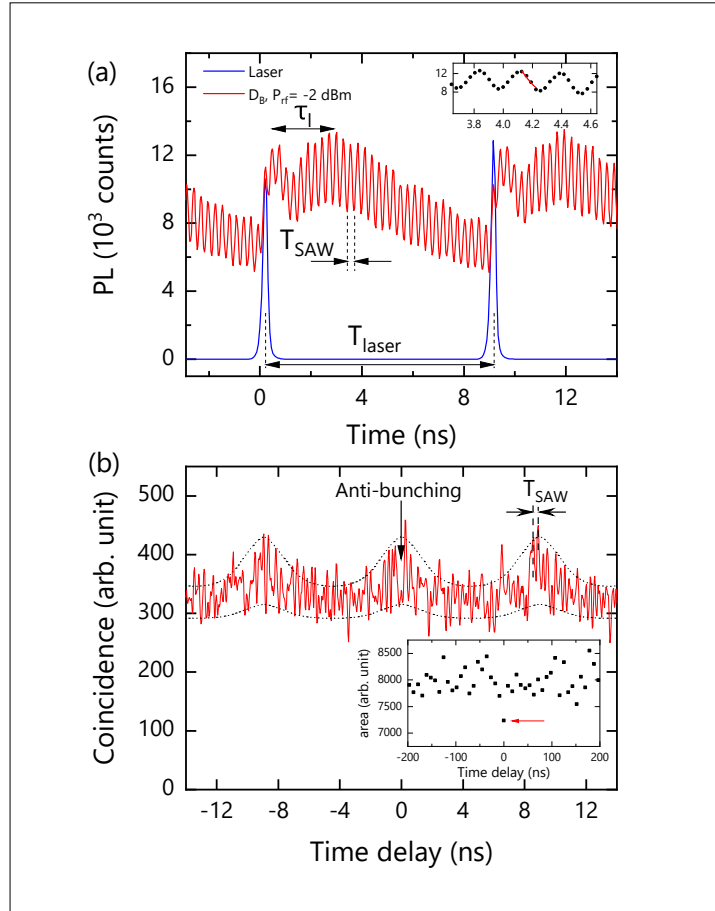


**Fig. 3.** (a) Time-resolved laser (blue) and PL emission (red) from a  $D_B$  remotely ( $8 \mu\text{m}$  away) excited by a  $P_{\text{rf}} = -2$  dBm SAW (red). The inset shows a close up of the signal with a time constant of 110 ps. (b) Second-order photon autocorrelation  $g^{(2)}(\tau_c)$  for the  $D_B$  under acoustic excitation ( $P_{\text{rf}} = -3$  dBm). The excitation spot was  $1 \mu\text{m}$  away. The dashed envelopes are guides to the eye. The inset shows the averaged  $\bar{g}^{(2)}$  around the delays corresponding to multiples of the laser period.

ing conditions were selected to enhance the emission of a  $D_B$  center under the guard gate approx.  $12 \mu\text{m}$  (corresponding to  $15\lambda_{\text{SAW}}$ ) away from the excitation spot (dashed ellipse). The SAW-propelled flying IXs travel along the stripe, bind to the impurity, and subsequently recombine to emit photons.

The excitation of the  $D_B$  centers by GHz SAW fields induces a strong time modulation of their optical emission. The red line in Fig. 3(a) displays the time-resolved

PL trace recorded on a  $D_B$  center located about  $\ell \sim 8 \mu\text{m}$  away from the laser excitation spot. The blue curve reproduces, for comparison, a time-resolved profile of the exciting laser spot (not to scale), which consist of pulses with a repetition time of  $T_{\text{laser}} = 9 \text{ ns}$ . The short-period oscillations in the  $D_B$  response (red curve) correspond to the SAW period  $T_{\text{SAW}} = 0.28 \text{ ns}$ . A close up of the oscillations (upper inset) reveals that the  $D_B$  emission decays with a time constant of approx. 110 ps, thus demonstrating that the PL signal from these centers can follow the fast varying acoustic field.

The envelope of the oscillations features two maxima: the first immediately after the laser pulse and the second at a delay of approximately  $\tau_\ell \sim 2.6 \text{ ns}$  (referencing the first maximum). The first maximum is attributed to the drift of hot excitons propelled by repulsive exciton interaction within the high-density cloud around the excitation spot [A. Violante *et al.*, *New. J. Phys.* **16**, 033035 (2014)]. The rise time of about 0.4 ns is attributed to the long lifetime of the IXs. The second maximum is assigned to carriers transported by the SAW, which reach the  $D_B$  after a subsequent delay  $\tau_\ell = \ell / v_{\text{SAW}}$ , where  $v_{\text{SAW}} = 2960 \text{ m/s}$  is the SAW velocity.

The photon emission statistics of the  $D_B$  centers was addressed by recording photon autocorrelation  $g^{(2)}$  histograms under acoustic excitation using a Hanbury-Brown and Twiss setup. The results obtained after corrections for spurious background emission are shown in Fig. 3(b). As in Fig. 3(a), the short- and long-period oscillations are associated with the repetition periods of the SAW and the laser pulses, respectively. The histogram shows a clear suppres-

sion of the coincidence rate at the time delay  $\tau_c = 0$ . In order to confirm the selective suppression at  $\tau_c = 0$ , the inset displays the averaged value  $\bar{g}^{(2)}(\tau_c)$  for  $g^{(2)}(\tau_c)$  over a time interval of 0.64 ns around time delays multiple of the laser repetition period. The latter shows that the suppression of coincidences at  $\tau_c = 0$  (red arrow) is well below the fluctuations, thus proving the emission of anti-bunched photons. The autocorrelation  $g^2(0) = 0.75 \pm 0.03$ , which corresponds to the simultaneous emission of 4 photons, is probably an upper limit determined by photon collection from the neighboring areas of the center.

In conclusion, we have investigated the transport and dynamic modulation of excitons by high-frequency, sub-micron-wavelength SAWs on GaAs DQW structures. In particular, we show that a GHz SAW field can pump single-exciton states bound to impurities, which act as two-level states emitting anti-bunched photons. The centers can follow the high-frequency acoustic pumping rate leading to the emission of anti-bunched photons synchronized with the SAW phase. The results thus demonstrate the feasibility of exciton manipulation as well as of exciton-based, high-frequency single-photon sources using acoustic waves. Finally, multiple single-exciton centers can potentially be excited by a single SAW beam, thus providing a pathway for scalable arrays of synchronized single-photon emitters.

We acknowledge financial support from the French National Agency (ANR) and Deutsche Forschungsgesellschaft (DFG) in Project No. ANR-15-CE24/DFG SA-598-12/1: SingleEIX.

# Correlation between the frequency, growth rate, and location on the wafer for terahertz quantum-cascade lasers

X. Lü, B. Röben, L. Schrottke, K. Biermann, H. T. Grahn

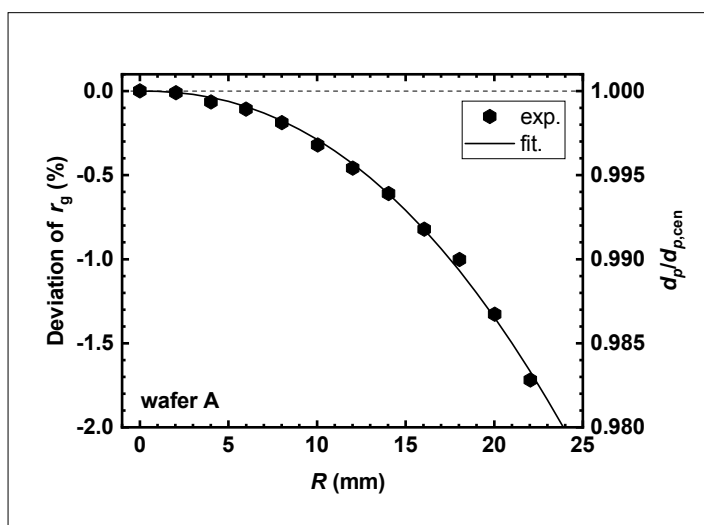
High-resolution absorption spectroscopy in the terahertz (THz) range requires radiation sources with well-defined emission frequencies as well as sufficient frequency tunability of several gigahertz (GHz). Due to the comparatively high wall plug efficiencies and large tuning ranges, GaAs/AlAs THz quantum-cascade lasers (QCLs) based on hybrid designs are promising sources for these applications. However, it is not straightforward to obtain a THz QCL emitting exactly at the target frequency, since the emission frequencies of THz QCLs correlate with the growth conditions and their respective location on the wafer. Understanding the correlation between the emission frequency, growth rate, and location on the wafer is beneficial for the optimization of the operating parameters such as the emission frequency, tuning range, and wall plug efficiency. Here, we investigate GaAs/AlAs THz QCLs from three wafers A–C using both, measurements and simulations. The target frequency for wafer A is 3.36 THz while it is 3.92 THz for wafers B and C. These lasers are intended to be used for the quantitative determination of the density of Al atoms and  $N^+$  ions, respectively, in plasma processes.

The QCLs were grown on two-inch wafers by molecular beam epitaxy under continuous wafer rotation so that only the growth rate along the radial direction has to be considered. Figure 1 depicts the deviation from the normalized growth rate  $r_g$  (= measured/nominal growth rate) of wafer A, which is obtained from reflectivity measurements, as a function of the distance  $R$  from the center of the wafer. The deviation of  $r_g$  corresponds to the relative

period length, i.e.  $d_p/d_{p, cen}$ , where  $d_p$  ( $d_{p, cen}$ ) denotes the period length of the QCL in the central (non-central) area of the wafer, which is indicated on the right-hand ordinate in Fig. 1. The relation between the deviation of  $r_g$  and  $R$  can be well reproduced by a power law given by  $1-d_p/d_{p, cen} \propto R^{2.22}$ , which is indicated by the solid line in Fig. 1.

The lasers were processed by photo-lithography and standard wet chemical etching. The lasers, which are based on single-plasmon waveguides, were investigated under continuous-wave (cw) or pulsed operation in a helium flow cryostat. The lasing spectra were recorded using a Fourier-transform infrared spectrometer, while the output power was determined using a calibrated power meter. We measured eight QCLs

**Fig. 1.** Deviation from the normalized growth rate  $r_g$  as a function of the distance  $R$  from the center of wafer A. The corresponding relative period length ( $d_p/d_{p, cen}$ ) is also given on the right-hand ordinate.



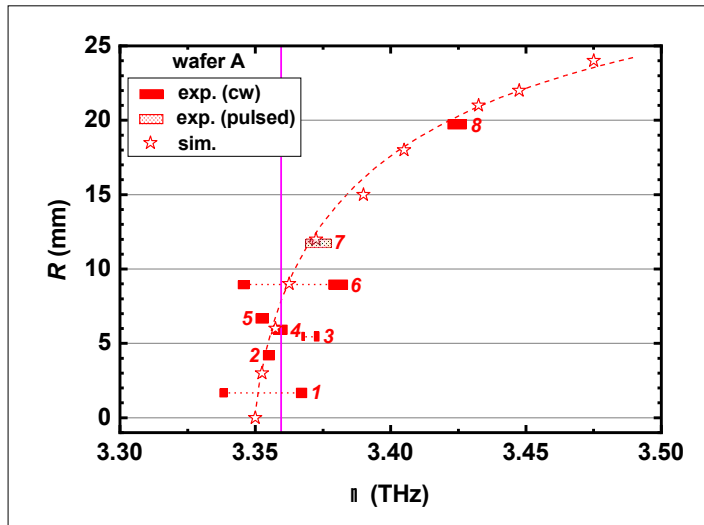


**Fig. 2.** The location of the QCLs on wafer A as a function of frequency measured at a heat sink temperature of 30 K for cw operation (filled rectangles) or 60 K for pulsed operation (hatched rectangle). The dotted lines depict the dominant peaks for lasers A1, A3, and A6 under cw operation. The simulated results are indicated by asterisks. The vertical line marks the target frequency of 3.36 THz, while the dashed line serves as a guide to the eye.

from wafer A, which are located in different regions of the wafer ( $1 \text{ mm} < R < 20 \text{ mm}$ ). Figure 2 displays the distance  $R$  from the center of the wafer for the QCLs on wafer A as a function of frequency. To use a similar temperature in the QCL active regions, the results under cw operation were measured at a heat sink temperature of 30 K, while the results under pulsed operation were recorded at a heat sink temperature of 60 K. The widths of the rectangles in Fig. 2 depict the current tuning ranges of the laser modes. The QCLs have ridge dimensions of approximately  $0.12 \times 1.0 \text{ mm}^2$ , exhibit one or two dominant modes, and are operated in cw mode (filled rectangles) except for laser A7, which has a ridge size of  $0.20 \times 3.0 \text{ mm}^2$ , exhibits multi-mode spectra, and is investigated in pulsed mode. For the laser A7, the mode at the maximum of the spectral envelope was selected (hatched rectangle).

For the QCLs with a cavity length of about 1 mm, there are only a few emission peaks

due to the large mode spacing, and the gain maxima may be located between the dominant emission peaks. The frequencies of QCLs with two dominant peaks are connected by dotted lines to demonstrate this possibility (lasers A1, A3, and A6). These results show that the variation of the growth rate from the center to the edge of the wafer leads to a blue shift of the emission frequency. The frequency range of laser A4 (3.357–3.362 THz) includes the target frequency of 3.36 THz.

To understand the frequency shift along the radial direction of the wafer, we calculated the gain spectra and determined the frequency of the gain maxima in the framework of a self-consistent Fourier-transform-based transport model. We slightly rescaled the period length of the nominal design ( $d_p^{\text{des}}$ ) so that the simulated frequency of the gain maximum ( $\nu_m^{\text{sim}}$ ) is close to a frequency between the two dominant peaks of laser A1. We label this thickness  $d_{p,\text{cen}}^{\text{sim}} (=1.017 d_p^{\text{des}})$ . Then, we simulate the QCLs for different values of  $d_p^{\text{sim}} (< d_{p,\text{cen}}^{\text{sim}})$  and obtain the frequency as a function of  $d_p^{\text{sim}}/d_{p,\text{cen}}^{\text{sim}}$ . According to the relation between  $d_p/d_{p,\text{cen}}$  and the distance  $R$  (cf. Fig. 1), we obtain the simulated frequency as a function of  $R$ . The simulated results are indicated in Fig. 2 as asterisks. We found that the simulated frequencies agree well with the experimental results.

We also investigated two more wafers (wafer B and C), which are designed for the target frequency of 3.92 THz. Figure 3 displays the location of six (four) QCLs on wafers B (C) as a function of frequency. For wafer B (blue symbols in Fig. 3), the change of the frequency with increasing distance  $R$  from the center of the wafer has the same tendency as that for wafer A. By applying a similar procedure as for wafer A, we obtain  $d_{p,\text{cen}}^{\text{sim}} = 1.028 d_p^{\text{des}}$ , and the simulated frequencies along the radial direction are labelled as asterisks in Fig. 3. The simulated frequencies are again in agreement with the experimental frequencies. The

design of wafer C is similar to that of wafer B, but with a thicker AIAs barrier and larger Si doping density. For wafer C (red symbols in Fig. 3), the frequency shift behaves similarly as the ones for wafers A and B. The frequency range of one lasing mode of laser C1 (3.919–3.924 THz) includes the target frequency of 3.92 THz. By using  $d_{p,\text{cen}}^{\text{sim}} = 1.032 d_{p,\text{cen}}^{\text{des}}$ , the experimental frequencies can be well reproduced by the simulations, which shows the wide applicability of our model.

We can also employ the simulations to predict the covered frequency range across a wafer. For a new QCL wafer, we firstly determine the frequencies of one or two lasers from the center of the wafer so that we can determine the value of  $d_{p,\text{cen}}^{\text{sim}}$  using the procedure described for wafer A. By employing the relation between the distance  $R$  from

the center of the wafer and  $d_p/d_{p,\text{cen}}$ , which is obtained from reflectivity measurements, we can calculate the possible values of  $d_p^{\text{sim}}/d_{p,\text{cen}}^{\text{sim}}$  across the wafer. We then use  $d_p^{\text{sim}}$  as the input parameter for the simulations and obtain the simulated frequencies across the wafer. If the simulated frequency range includes the target frequency, we can convert the corresponding value of  $d_p^{\text{sim}}$  into the distance  $R_{\text{target}}$  using the power law for the deviation from the normalized growth rate. At the distance  $R_{\text{target}}$  from the center of the wafer, the QCL may emit at the target frequency.

**Fig. 3.** The location of the QCLs on wafers B (blue symbols) and C (red symbols) as a function of frequency measured at a heat sink temperature of 30 K for cw operation (filled rectangles) or 60 K for pulsed operation (hatched rectangles). The dotted lines depict the dominant peaks for lasers B2, C1, and C3 under cw operation. The simulated results are indicated by asterisks. The vertical line marks the target frequency of 3.92 THz, while the dashed lines serves as a guide to the eye.

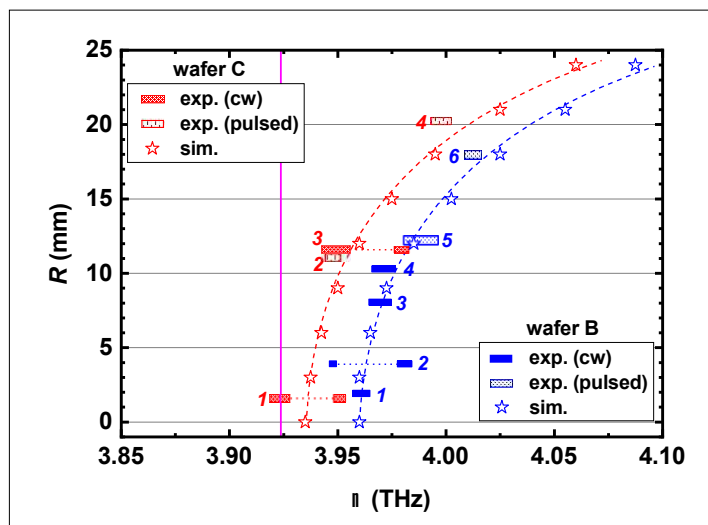
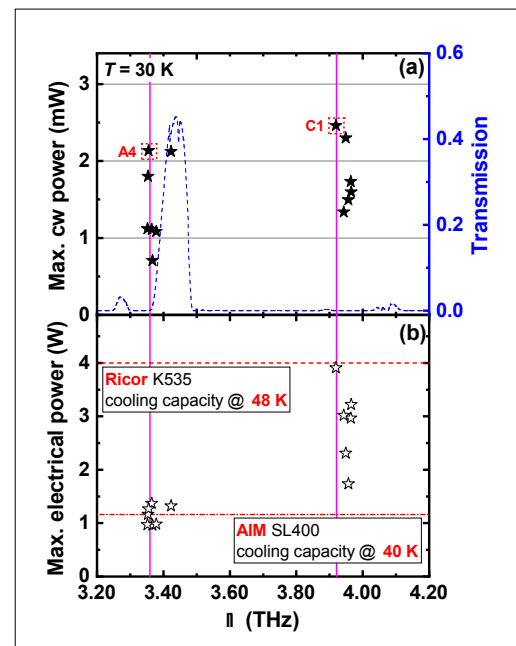


**Fig. 4.** (a) Maximum output power and (b) maximum electrical pump power as a function of the emission frequency for 13 GaAs/AIAs QCLs (asterisks) from wafers A, B, and C under cw operation measured at a heat sink temperature of 30 K. The vertical lines indicate the target frequencies of 3.36 and 3.92 THz. The dashed line depicts a simulated transmission spectrum of air based on the HITRAN database for ambient conditions corresponding to the USA model, mean latitude, summer, and an optical path length of 10 m.



For the application of THz QCLs, the optical output power and the electrical pump power are also important operating parameters. Figure 4 summarizes the maximum output power and the electrical pump power of 13 GaAs/AlAs QCLs from wafers A, B, and C as a function of the emission frequency. The typical output powers of these lasers (except A3) are larger than 1 mW. For the 3.36-THz QCLs, the maximum electrical pump power is below 1.5 W, while for the 3.92-THz QCLs it is below 4 W. The cooling capacity of the Stirling cryocooler (Ricor K535) at 48 K is 4 W [dashed line in Fig. 4 (b)], which means that all the lasers can be operated in a cryocooler. Some of the 3.36-THz QCLs may also be operated in a miniature cryo-

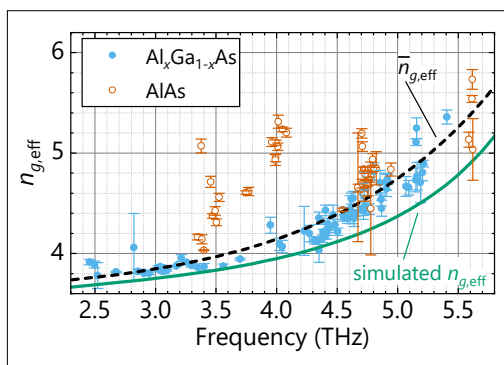
cooler (AIM SL400). The wall plug efficiencies for lasers A4 and C1 reach values larger than  $1.6 \times 10^{-3}$  and  $0.6 \times 10^{-3}$ , respectively. Since wafers A, B, and C are our first attempts to reach 3.36 and 3.92 THz, the wall plug efficiencies may be further improved by optimizing the design and the growth. The intrinsic tuning ranges of lasers A4 and C1 amount to 5.0 and 5.4 GHz, respectively. The frequency ranges of lasers A4 and C1 at an operating temperature of 30 K include the target frequencies 3.36 and 3.92 THz, respectively. Due to a sufficient output power, a low electrical pump power, and an adequate frequency tunability, lasers A1 and C1 can be applied to high-resolution absorption spectroscopy.

# Effective group dispersion of terahertz quantum-cascade lasers

B. Röben, X. Lü, K. Biermann, L. Schrottke, H. T. Grahn

Chromatic dispersion—often expressed in terms of the refractive index—determines the phase and group velocity of electromagnetic radiation as a function of its optical frequency. In modern optics, dispersion is important for optical waveguides, since it determines effects such as pulse broadening and chirping. In waveguide lasers, dispersion influences the spectral emission parameters such as the mode spacing. One of the most recent developments among waveguide lasers is the terahertz (THz) quantum-cascade laser (QCL). It is based on a cascaded semiconductor heterostructure within a single-plasmon or metal-metal waveguide. THz QCLs are very attractive for spectroscopy, since they are compact and exhibit output powers of several mW as well as very narrow linewidths in the MHz to kHz range.

**Fig. 1.** Effective group refractive index  $n_{g,\text{eff}}$  of different THz QCLs with  $\text{Al}_x\text{Ga}_{1-x}\text{As}$  (dots) and AlAs (circles) barriers. The vertical error bars signify twice the standard deviation of the mean. The general trend is well described by the dashed line, which represents an average function  $\bar{n}_{g,\text{eff}}(\nu)$  of the measured values for  $n_{g,\text{eff}}$ . The solid line corresponds to a simulated curve for  $n_{g,\text{eff}}$ .



Just as for other waveguide lasers, the dispersion of THz QCLs is an important fundamental parameter. In this work, we investigate the effective group refractive index  $n_{g,\text{eff}}$  for more than one hundred THz QCLs with emission frequencies between 2.5 and 5.6 THz based on active regions with both,  $\text{Al}_x\text{Ga}_{1-x}\text{As}$  ( $x \leq 0.25$ ) and AlAs barriers. For the determination of  $n_{g,\text{eff}}$ , we employ the emission spectra of THz QCLs based on Fabry-Pérot resonators with lengths  $L$  between 3 and 3.5 mm operated in pulsed mode, which typically exhibit multiple emission modes. From the frequency spacing  $\Delta\nu$  of two adjacent modes,  $n_{g,\text{eff}}$  can be obtained according to the equation

$$n_{g,\text{eff}} = \frac{c}{2L\Delta\nu}, \quad (1)$$

where  $c$  denotes the speed of light. For maximum accuracy, we calculate the mean value of  $n_{g,\text{eff}}$  based on all mode pairs within each spectrum for all investigated injection currents of a particular QCL.

Figure 1 shows the effective group refractive index  $n_{g,\text{eff}}$  of 121 different QCLs based on more than 800 spectra in total. Every dot represents one of the 79 QCLs with  $\text{Al}_x\text{Ga}_{1-x}\text{As}$  barriers ( $x \leq 0.25$ ) and every circle one of the 42 QCLs with AlAs barriers. Most values of  $n_{g,\text{eff}}$  follow a general trend, which is well described by the average function  $\bar{n}_{g,\text{eff}}(\nu)$  obtained by fitting all data points for  $n_{g,\text{eff}}$  in Fig. 1 excluding the values for the GaAs/AlAs QCLs below 4.5 THz, since these values clearly represent a rather large deviation from the general trend.

The average function  $\bar{n}_{g,\text{eff}}(\nu)$ , representing the experimentally observed general trend for  $n_{g,\text{eff}}$ , agrees rather well with the curve

obtained from electromagnetic simulations as shown in Fig. 1. A possible reason for the deviation between these two curves is an unreliable data set for the material dispersion, since there is rather little literature on low-temperature values of the dispersion of the (Al,Ga)As system in the THz frequency range. The deviation may also be related to the cavity pulling effect.

As also shown in Fig. 1, the measured values of  $n_{g,\text{eff}}$  for the QCLs with AlAs barriers between 3.4 and 4.1 THz deviate substantially from the general trend described by  $\bar{n}_{g,\text{eff}}(\nu)$  and from the simulated curve for  $n_{g,\text{eff}}$ . We ruled out a significant correlation between this deviation and different structural parameters such as the Al content and the thickness of the active regions. We also excluded a significant correlation with the performance characteristics such as the output power. Instead, we found that  $n_{g,\text{eff}}$  varies for different active-region designs.

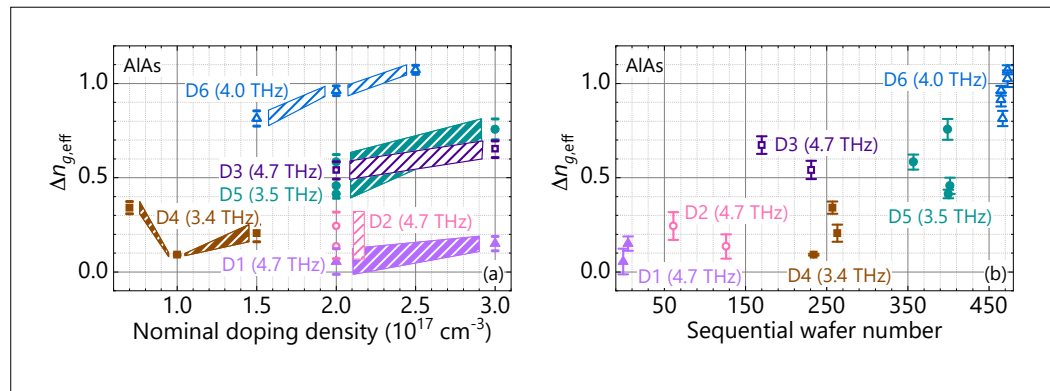
Figure 2(a) shows the deviation  $\Delta n_{g,\text{eff}} = n_{g,\text{eff}} - \bar{n}_{g,\text{eff}}$  from the general trend as a function of the nominal doping density for QCLs with different designs of the layer sequence denoted D1 to D6. Large differences in  $\Delta n_{g,\text{eff}}$  occur mainly between QCLs of different de-

signs of the layer sequence, while the doping density has a smaller influence on  $\Delta n_{g,\text{eff}}$ . There also appears to be no correlation between  $\Delta n_{g,\text{eff}}$  and the emission frequency.

Additionally, we investigated whether  $\Delta n_{g,\text{eff}}$  depends on the date of growth. Figure 2(b) shows  $\Delta n_{g,\text{eff}}$  as a function of a sequential wafer number. Wafers with a larger sequential number were grown later. We observe a tendency toward larger values of  $\Delta n_{g,\text{eff}}$  with increasing sequential wafer number. This result indicates a corresponding variation of the growth conditions over time, which may affect the structural quality of the THz QCLs such as the interface roughness.

The results shown in Figs. 2(a) and 2(b) indicate that details of the design and of the actual active region depending on the growth process have an influence on  $\Delta n_{g,\text{eff}}$ . In order to investigate possible mechanisms for these results, Fig. 3(a) shows an example of the simulation results for the gain and the group refractive index  $n_{g,\text{ar}}$  of an active region (ar) for emission at 3.5 THz. The value of  $n_{g,\text{ar}}$  is increased at the frequency  $\nu_M$  of the gain maximum, which is due to the relationship between gain and refractive-

**Fig. 2.** (a) Deviation  $\Delta n_{g,\text{eff}} = n_{g,\text{eff}} - \bar{n}_{g,\text{eff}}$  from the general trend of different QCLs with AlAs barriers as a function of the nominal doping density. Same symbols indicate the results for identical designs of the layer sequence denoted D1 to D6. For designs D2 and D5, the error ranges are merged for clarity. The hatched areas connect the data points of the same designs and serve as a guide to the eye. (b) Deviation  $\Delta n_{g,\text{eff}}$  from the general trend as a function of a sequential wafer number for QCLs with AlAs barriers.





dex as described by the Lorentz oscillator model. According to further simulations, the value of  $n_{g,ar}$  at  $\nu_M$  varies with the particular active-region design. However, our simulation results of  $n_{g,eff}$  do not quantitatively agree with the experimental results displayed in Fig. 2(a), although we also took into account waveguide dispersion using electromagnetic simulations. We attribute the rather limited predictability of our model to the comparatively complex subband structure of our active-region designs.

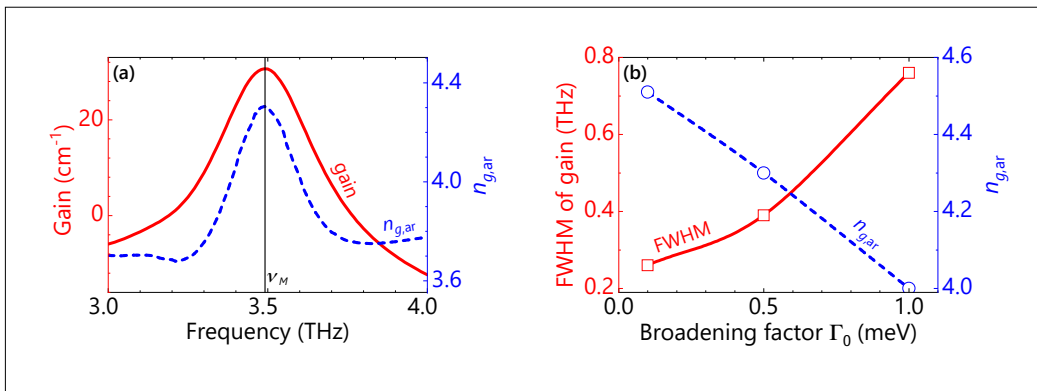
An important parameter also affecting  $n_{g,ar}$  is the inhomogeneous broadening of the gain spectra, which is attributed to interface roughness including alloy disorder and lateral fluctuations of the doping density. Figure 3(b) shows simulation results for the full width at half maximum (FWHM) of the gain and for  $n_{g,ar}$  as a function of the broadening factor  $\Gamma_0$ . Smaller values for  $\Gamma_0$ , which correspond to a reduced interface roughness, lead to a narrower gain curve and to larger values for  $n_{g,ar}$ . Consequently, the increase of  $\Delta n_{g,eff}$  with the sequential wafer number (i.e., with time) as displayed in Fig. 2(b) may be due to a reduction in the interface roughness over time, which may be related to an improvement of the growth conditions. An experimental verification of the correspondence between a

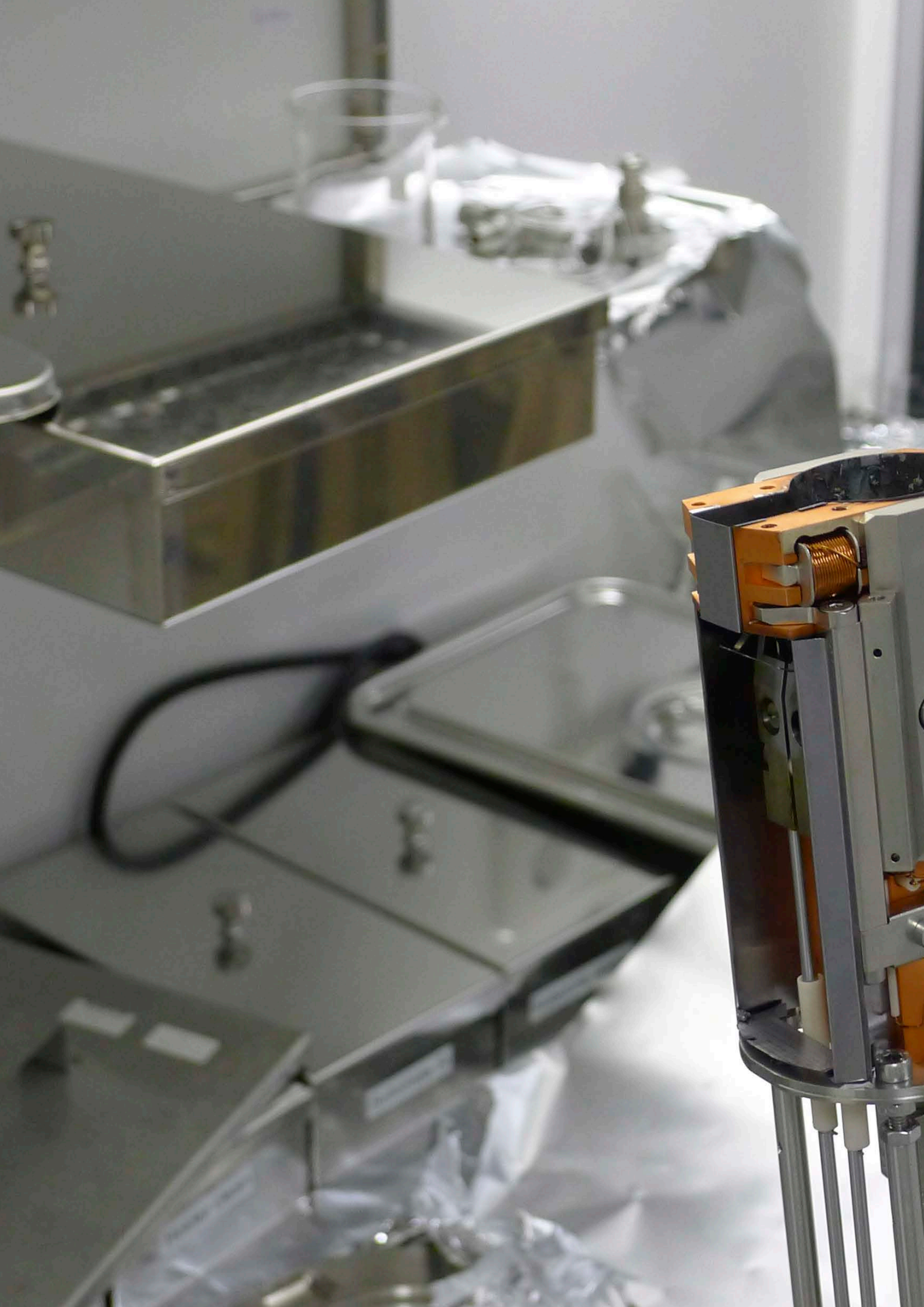
larger value for  $n_{g,eff}$  and a reduced interface roughness will be subject to further experimental studies including examinations of QCL structures by transmission electron microscopy.

In conclusion, we have investigated the effective group refractive index  $n_{g,eff}$  for a large number of THz QCLs by analyzing their emission spectra. The values for  $n_{g,eff}$  as a function of emission frequency follow a general trend for most of the GaAs/ $Al_xGa_{1-x}$ As and GaAs/AlAs QCLs. However, a considerable number of GaAs/AlAs QCLs exhibit substantial deviations from this trend. Our analysis provides evidence for the dependence of  $n_{g,eff}$  on the gain spectra resulting from intersubband transitions in the active region. According to our simulations, the details of the active-region designs and the interface-roughness affect  $n_{g,eff}$ , which may explain the experimental results. If the influence of the interface roughness on  $n_{g,eff}$  is confirmed by further experimental techniques such as transmission electron microscopy, the determination of  $n_{g,eff}$  may provide a straightforward path to assess the structural quality of THz QCLs.

Partial financial support of this work by the Leibniz-Gemeinschaft under Grant No. K54/2017 is gratefully acknowledged.

**Fig. 3.** (a) Prototypical example of the simulation results for the gain and the group refractive index  $n_{g,ar}$  of an active region (ar) for 3.5 THz. The vertical line indicates the frequency  $\nu_M$  of the gain maximum. (b) Simulation results for the full width at half maximum (FWHM) of the gain curve (rectangles) and for  $n_{g,ar}$  (circles) at the frequency  $\nu_M$  as a function of the broadening factor  $\Gamma_0$ .







# Departments Abteilungen

Department Epitaxy Abteilung Epitaxie.....	132
Department Semiconductor Spectroscopy Abteilung Halbleiterspektroskopie.....	137
Department Microstructure Abteilung Mikrostruktur.....	144
Department Technology and Transfer Abteilung Technologie und Transfer .....	150

# Department Epitaxy

## Abteilung Epitaxie

Head of Department: Dr. Lutz Geelhaar, [geelhaar@pdi-berlin.de](mailto:geelhaar@pdi-berlin.de)



The overall competence of this research department is the growth of crystalline thin films and nanostructures with extremely well-defined properties by epitaxy. Epitaxy is a process in which one crystal, the adsorbate, is grown on another crystal, the substrate, in such a way that there is a unique relation between the orientations of the two crystal lattices. Typically, the adsorbate is at most a few micrometers thick. Compared to the growth of bulk crystals, epitaxy offers several advantages: First, epitaxy allows the synthesis of materials that are only metastable and cannot be grown as bulk crystals at all. Thus, materials can be grown with specific and tailored properties that could not be obtained in any other way. Second, during epitaxy the composition of the growing crystal can be changed very abruptly—on the atomic scale—so that heterostructures consisting of different materials can be fabricated. In such heterostructures quantum phenomena can be observed, and by tailoring the heterostructures quantum phenomena can be manipulated and new functionalities can be achieved. Therefore, epitaxy is a means to realize nanostructured materials as well as artificial low-dimensional semiconductor systems and to tune their mechanical, optical, electronic, and magnetic properties.

The research activities in the epitaxy department are directed at two complementary tasks. On the one hand, our experimental contribution to the overall research of the institute is the fabrication of custom-designed nanostructured samples. On the other hand, the underlying growth mechanisms themselves are investigated, both for their own scientific sake and in order to optimize properties that are investigated in the core research areas. Our comprehensive expertise is based on the long tradition for

Die Kernkompetenz dieser Abteilung ist die Züchtung kristalliner Schichten und Nanostrukturen mit äußerst präzise definierten Eigenschaften mittels Epitaxie. Mit Epitaxie bezeichnet man den Prozess, in dem ein Kristall – das Adsorbat – auf einem anderen Kristall – dem Substrat – mit einer eindeutigen Beziehung zwischen den Kristallorientierungen gezüchtet wird. Dabei ist das Adsorbat typischerweise nicht dicker als einige Mikrometer. Epitaxie weist einige Vorteile im Vergleich zu der Züchtung von Volumenkristallen auf. So lassen sich mittels Epitaxie auch Materialien herstellen, die nur metastabil und als Volumenkristall gar nicht zu züchten sind. Auf diese Weise können besondere Materialien mit spezifischen, maßgeschneiderten Eigenschaften hergestellt werden. Der zweite wichtige Vorteil der Epitaxie liegt in der Möglichkeit, während des epitaktischen Wachstums die Zusammensetzung des Kristalls sehr abrupt – auf atomarer Skala – zu ändern, so dass sogenannte Heterostrukturen erzeugt werden können, die aus unterschiedlichen Materialien bestehen. In solchen Heterostrukturen können Quantenphänomene beobachtet und durch definiertes Einstellen der Strukturparameter manipuliert werden. Dies ermöglicht die Realisierung und Untersuchung neuer Funktionalitäten, die für Anwendungen interessant sein können. Epitaxie ist somit ein Werkzeug, mit dem nanostrukturierte Materialien wie auch künstliche niedrigdimensionale Halbleitersysteme mit einstellbaren mechanischen, optischen, elektronischen und magnetischen Eigenschaften hergestellt werden können.

Die Forschungsaktivitäten in der Epitaxie-Abteilung konzentrieren sich auf zwei komplementäre Linien. Auf der einen Seite werden für ein breites Spektrum an weiterführenden Forschungsaktivitäten am

the fabrication of two-dimensional heterostructures comprising III-V semiconductors, but in addition we work on more and more other materials. Furthermore, research on the vertical growth of III-V nanowires has become a major activity of this research department.

The technique for crystal growth that we employ at PDI is molecular beam epitaxy (MBE). In MBE, growth takes place under extremely pure conditions in ultra-high vacuum. Crystal growth is fed by beams of neutral atoms or molecules that are typically obtained by evaporating source material in effusion cells. Due to the low pressure, these atoms or molecules do not scatter or interact with each other before they reach the substrate. In order to modify the kinetics of crystal growth, the substrate temperature is adjusted. In general, MBE offers a very high level of control over the growth conditions, and growth can be monitored in situ by several characterization techniques.

Arguably the most mature class of compound semiconductors is formed by the group-III arsenides GaAs, AlAs, InAs, and their alloys. Very complex heterostructures can be realized in this material system with impressive precision and reproducibility. Such samples are fabricated for investigation in the core research areas *Intersubband Emitters: GaAs-based Quantum-Cascade Lasers* and *Control of Elementary Excitations by Acoustic Fields*.

The performance and functionality of future semiconductor devices will be enhanced by making use of three-dimensional nanostructures. Our efforts in this direction concentrate on the creation of such structures directly by growth, i. e. in a bottom-up approach with the help of self-organization mechanisms. In particular, we grow both group-III arsenides and nitrides not only as planar layers but also in the form of nanowires. Nanowires are structures with an extremely high aspect ratio and a diameter of the order of 100 nm. Their formation, prop-

stitut maßgeschneiderte nanostrukturierte Proben hergestellt. Auf der anderen Seite werden die Wachstumsmechanismen selbst untersucht – aus wissenschaftlichem Interesse an den zugrundeliegenden Prozessen und um die Materialeigenschaften, die in den Forschungsschwerpunkten untersucht werden, zu optimieren. Unsere umfassende Expertise basiert auf einer langen Tradition der Herstellung zweidimensionaler Heterostrukturen, die aus III-V-Halbleitern bestehen. Mittlerweile arbeiten wir aber auch intensiv an weiteren Materialsystemen. Zudem hat sich das senkrechte Wachstum von III-V-Nanodrähten zu einer Kernaktivität der Abteilung entwickelt.

Am PDI setzen wir als Methode für Kristallzüchtung die Molekularstrahlepitaxie (MBE für englisch molecular beam epitaxy) ein. Bei diesem Verfahren findet das Wachstum unter äußerst reinen Bedingungen im Ultrahochvakuum statt. Das Kristallwachstum wird durch Atom- oder Molekülstrahlen versorgt, die typischerweise durch das Verdampfen von Quellmaterial in Effusionszellen erzeugt werden. Aufgrund des niedrigen Drucks in der Wachstumskammer streuen die Atome beziehungsweise Moleküle nicht und erfahren auch keine Wechselwirkung untereinander, bis sie auf das Substrat treffen. Um die Kinetik des Kristallwachstums zu modifizieren, wird die Substrattemperatur geregelt. Generell bietet MBE ein sehr hohes Maß an Kontrolle über Wachstumsbedingungen, und das Wachstum kann in situ mittels mehrerer Charakterisierungstechniken überwacht werden.

Die wohl am weitesten entwickelte Klasse von Verbindungshalbleitern wird von den Gruppe-III-Arseniden GaAs, AlAs, InAs und deren Legierungen gebildet. In diesem Materialsystem lassen sich sehr komplexe Heterostrukturen mit beeindruckender Präzision und Reproduzierbarkeit herstellen. Solche Proben werden für weitere Untersuchungen in den Forschungsschwerpunkten *Intersubband-Emitter: GaAs-basierte Quantenkaskadenlaser* und *Kontrolle von Elemen-*

erties, and applications are the subject of the core research area *III-V Nanowires for Optoelectronics*.

Research activities with the focus on the synthesis of materials are carried out in the core research area *Nanofabrication*. At present, the epitaxy of group-III arsenides, group-III nitrides, ferromagnetic Heusler alloys like  $\text{Co}_2\text{FeSi}$  in hybrid structures with group-III arsenide heterostructures and MgO, transparent semiconducting oxides ( $\text{Ga}_2\text{O}_3$ ,  $\text{In}_2\text{O}_3$ , NiO, and SnO), phase-change alloys in the material system Ge-Sb-Te, graphene (the two-dimensional allotrope of carbon), and hexagonal BN is investigated. This research takes place in close collaboration with the core research area *Nanoanalytics* in which the emphasis of the research is on materials properties.

In practice, the key features of MBE described before can only be achieved by combining a considerable number of different technical components, and hence MBE systems are fairly complex. The core component of such systems is a chamber made from stainless steel in which ultra-high vacuum is maintained and the actual crystal growth takes place. In order to preserve ultra-purity and avoid cross-contamination, each material system requires its own, dedicated MBE chamber. For the two main material systems of PDI, group-III arsenides and group-III nitrides, we can pursue the multitude of research projects only by operating more than one MBE chamber each. In total, there are at present eleven MBE systems in use. For the fabrication of hybrid structures comprising different materials, growth on the same sample has to take place subsequently in more than one MBE chamber. In order to avoid contamination of the interface between two materials, such samples have to be transported from one MBE chamber to the other under ultra-high vacuum conditions. Thus, some of our MBE chambers are connected as cluster systems. As an alternative, mobile ultra-high vacuum shuttle chambers are

*taranregungen durch akustische Felder hergestellt.*

Die Leistung und Funktionalität zukünftiger Halbleiter-Bauelemente wird durch die Verwendung von dreidimensionalen Nanostrukturen verbessert werden. Unsere Bemühungen in diesem Zusammenhang konzentrieren sich auf die Ausbildung solcher Strukturen direkt während des Wachstums, das heißt durch Ausnutzung von Selbstorganisationsphänomenen. Insbesondere züchten wir sowohl Gruppe-III-Arsenide als auch -Nitride nicht mehr nur als planare Schichten, sondern auch als Nanodrähte. Nanodrähte sind Strukturen, die ein äußerst hohes Aspektverhältnis und einen Durchmesser in der Größenordnung von 100 nm aufweisen. Die Bildung, die Eigenschaften und die Anwendungen von Nanodrähten sind Untersuchungsgegenstand des Forschungsschwerpunkts *III-V-Nanodrähte für Optoelektronik*.

Die Synthese von Materialien steht hingegen im Fokus des Forschungsschwerpunkts *Nanofabrikation*. Gegenwärtig werden hier die Epitaxie von Gruppe-III-Arseniden und -Nitriden, ferromagnetischen Heusler-Legierungen wie  $\text{Co}_2\text{FeSi}$  in Hybridstrukturen mit Gruppe-III-Arsenid-Heterostrukturen und MgO, transparenten halbleitenden Oxiden ( $\text{Ga}_2\text{O}_3$ ,  $\text{In}_2\text{O}_3$ , NiO und SnO), Phasenwechsel-Materialien des Systems Ge-Sb-Te, Graphen (das zweidimensionale Allotrop von Kohlenstoff) und hexagonalem BN untersucht. Diese Forschung wird in enger Zusammenarbeit mit dem Forschungsschwerpunkt *Nanoanalytik* durchgeführt.

In der Praxis lassen sich die beschriebenen Schlüsselmerkmale von MBE nur erreichen, wenn eine beträchtliche Anzahl unterschiedlicher technischer Komponenten kombiniert wird. Daher sind MBE-Anlagen recht komplex. Die Kernkomponente eines solchen Systems ist eine Kammer, die aus Edelstahl gefertigt wird. Hier findet das eigentliche Kristallwachstum statt. Um die extreme Reinheit zu erhalten und wech-

also employed to transfer samples between MBE systems.

As a distinctive experimental feature, PDI owns three special MBE chambers that allow the in-situ, real-time analysis of growth processes by x-ray diffraction. To this end, these chambers can be connected to our own beamline at the synchrotron BESSY II (Helmholtz-Zentrum Berlin für Materialien und Energie). The successful operation of such a setup critically depends on the continuous stationary operation of the MBE system at the synchrotron, since a high quality of the epitaxial layers and interfaces is imperative for a reliable quantitative analysis. Consequently, at least one of these special MBE chambers is always located at the synchrotron. Currently, a system equipped for the study of semiconducting oxides is installed there.

This year, we have put into operation an x-ray and ultraviolet photoelectron spectroscopy system. This system will be beneficial for research at PDI in multiple ways. We can analyze chemical bonding states close to the surface, which is particularly relevant for van der Waals materials and heterostructures. Also, the composition of novel complex alloys like ternary oxides can be determined, and in combination with a sputter source depth profiles can be extracted. Likewise, interfacial reactions in extreme heterostructures, e. g. involving metals and semiconductors, can be analyzed. In addition, we can study the work function of novel materials, and investigate band bending and band offsets. We are excited about these new opportunities for our research and look forward to such studies.

seitige Verunreinigungen zu vermeiden, braucht jedes Materialsystem seine eigene, dedizierte Wachstumskammer. Für die zwei zentralen Materialsysteme des PDI, Gruppe-III-Arsenide und -Nitride, lässt sich die Vielfalt der Forschungsprojekte nur durchführen, wenn jeweils mehr als eine Kammer zur Verfügung steht. Insgesamt sind am Institut zurzeit elf MBE-Anlagen in Betrieb. Wenn hybride Strukturen aus unterschiedlichen Materialien hergestellt werden sollen, muss das Wachstum an derselben Probe nacheinander in mehr als einer MBE-Kammer stattfinden. Um eine Verunreinigung der Grenzfläche zwischen zwei Materialien zu vermeiden, müssen diese Proben zwischen MBE-Kammern unter Ultrahochvakuumbedingungen transportiert werden. Deshalb sind einige unserer MBE-Anlagen als Cluster-Systeme konzipiert. Alternativ verwenden wir kleine mobile Ultrahochvakuumkammern, um den Probentransfer zwischen MBE-Kammern zu gewährleisten.

Als experimentelle Besonderheit stehen dem PDI drei spezielle MBE-Anlagen zur Verfügung, die In-situ-Studien der Wachstumsprozesse mittels Röntgenbeugung in Echtzeit ermöglichen. Hierfür können die Kammern mit unserem eigenen Strahlrohr am Synchrotron BESSY II (Helmholtz-Zentrum Berlin für Materialien und Energie) verbunden werden. Der erfolgreiche Betrieb eines derartigen Aufbaus hängt wesentlich vom kontinuierlichen, stationären Einsatz der MBE-Anlage am Synchrotron ab. Infolgedessen befindet sich mindestens eine dieser speziellen MBE-Anlagen stets am Synchrotron. Zurzeit wird dort eine MBE-Anlage betrieben, die für die Analyse halbleitender Oxide eingerichtet ist.

In diesem Jahr nahmen wir ein System für Röntgen- und Ultraviolett-Photoelektronenspektroskopie in Betrieb. Dieses System wird für die Forschung am PDI in mehrfacher Hinsicht von Nutzen sein. Wir können chemische Bindungszustände nahe der Oberfläche analysieren, was insbeson-

dere für van der Waals-Materialien und -Heterostrukturen relevant ist. Außerdem können die Zusammensetzung neuartiger komplexer Legierungen wie ternärer Oxide bestimmt und in Kombination mit einer Sputterquelle Tiefenprofile extrahiert werden. Ebenso können Grenzflächenreaktionen in extremen Heterostrukturen, zum Beispiel aus Metallen und Halbleitern, analysiert werden. Zudem können wir die Austrittsarbeit neuartiger Materialien untersuchen und Bandverbiegungen und Bandkantensprünge untersuchen. Wir sind begeistert über diese neuen Möglichkeiten für unsere Forschung und freuen uns auf solche Studien.



# Department Semiconductor Spectroscopy

## Abteilung Halbleiterspektroskopie

Head of Department: Prof. Dr. Holger T. Grahn, htgrahn@pdi-berlin.de

The overall competence of this research department lies in the physics and applications of semiconductor hetero- and nanostructures, in particular with regard to their electronic and optical properties. The research topics include elementary excitations in solids controlled by surface acoustic waves, the optical properties of III-V nanowires and heterostructures, terahertz quantum-cascade lasers, spin generation and transport in ferromagnet/semiconductor hybrid structures, quantum transport in semiconductor-based nanoscale systems, and topological insulators. Dedicated spectroscopic and magneto-transport techniques are used to determine the electronic, optical, and transport characteristics of these semiconductor hetero- and nanostructures.

- Elementary excitations controlled by acoustic fields are investigated in solids by optical spectroscopy. Photons, electrons, and spins can be manipulated at gigahertz frequencies using surface acoustic waves opening new perspectives for applications in optoelectronic devices.
- The optical properties of III-V nanowires and heterostructures are investigated by spatially and time-resolved photoluminescence spectroscopy as well as by cathodoluminescence spectroscopy in a scanning electron microscope. Of particular importance is the correlation between structural defects and optical properties in III-V nanowires.
- Quantum-cascade lasers for the terahertz spectral region are designed, their optical as well as transport properties are simulated, complete lasers are realized, and their lasing properties are investigated. These lasers are compact sources,

Die übergreifende Kompetenz dieser Forschungsabteilung liegt in der Physik und den Anwendungen von Hetero- und Nanostrukturen aus Halbleitern, insbesondere bezüglich ihrer elektronischen und optischen Eigenschaften. Die Forschungsthemen umfassen Elementaranregungen in Festkörpern kontrolliert durch akustische Oberflächenwellen, optische Eigenschaften von III-V-Nanodrähten und -Heterostrukturen, Terahertz-Quantenkaskadenlaser, Spinerzeugung und -transport in Ferromagnet/Halbleiter-Hybridstrukturen, Quantentransport in nanoskaligen Halbleiter-Systemen und topologische Isolatoren. Dedizierte spektroskopische und Magnetotransport-Methoden werden zur Bestimmung der elektronischen, optischen und Transport-Charakteristika dieser Hetero- und Nanostrukturen aus Halbleitern verwendet.

- Elementaranregungen kontrolliert durch akustische Felder werden in Festkörpern mittels optischer Spektroskopie untersucht. Photonen, Elektronen und Spins können bei Gigahertz-Frequenzen mittels akustischer Oberflächenwellen manipuliert werden, was neue Perspektiven für Anwendungen in optoelektronischen Bauelementen eröffnet.
- Die optischen Eigenschaften von III-V-Nanodrähten und -Heterostrukturen werden mit räumlich und zeitlich aufgelöster Photolumineszenz-Spektroskopie sowie Kathodolumineszenz-Spektroskopie in einem Rasterelektronenmikroskop untersucht. Von besonderer Bedeutung ist die Korrelation von strukturellen Defekten mit den optischen Eigenschaften von III-V-Nanodrähten.
- Quantenkaskadenlaser werden für den Terahertz-Spektralbereich entwickelt,



can be operated in single mode, exhibit typical optical output powers between several mW and several tens of mW, and function at temperatures, which do not require cooling with liquid helium.

- The generation and the transport of spins in ferromagnet/semiconductor hybrid structures are studied by analyzing their magneto-optical and magneto-transport properties. In order to achieve spin control, all-electrical spin injection and detection are investigated using lateral and vertical spin valve devices.
- The electronic and spin properties of semiconductor-based nanoscale systems such as nanowires and quantum dots defined laterally in heterostructures are studied by quantum-transport experiments aiming at the development of new strategies for information processing.
- The electronic transport properties of topological insulators, in which charges are only transported on the surface and not in the bulk, are investigated by examining the weak antilocalization effect due to spin orbit coupling and the electron-electron interaction.

The facilities for optical spectroscopy include Raman spectroscopy to study the vibrational modes in semiconductor films, heterostructures, and nanowires as well as in topological insulators and graphene. Continuous-wave photoluminescence and photoluminescence excitation spectroscopy from the ultraviolet (244 nm) to the near-infrared spectral region (1.7  $\mu\text{m}$ ) are used to investigate III-V films, heterostructures, and nanowires. The spectroscopic techniques for the near-infrared to ultraviolet spectral regions such as Raman and photoluminescence spectroscopy can also be used with a spatial resolution down to about 0.5  $\mu\text{m}$  and in magnetic fields up to 8 T. With cathodoluminescence spectroscopy and imaging in a scanning electron microscope, the spatial resolution can be enhanced into the range

deren optische und Transport-Eigenschaften werden berechnet, vollständige Laser werden realisiert und deren Lasereigenschaften werden untersucht. Diese Laser sind kompakte Quellen, erlauben Einzelmodenbetrieb, besitzen typische optische Ausgangsleistungen zwischen einigen mW und einigen zehn mW, und funktionieren bei Temperaturen, die keine Kühlung mit flüssigem Helium erfordern.

- Die Erzeugung und der Transport von Spins werden in Ferromagnet/Halbleiter-Hybridstrukturen untersucht, indem ihre magneto-optischen und Magnetotransport-Eigenschaften analysiert werden. Um Kontrolle über Spins in einem Halbleiter zu erhalten, wird die rein elektrische Injektion und Detektion von Spins mit lateralen und vertikalen Spinventil-Bauelementen untersucht.
- Die elektronischen und Spin-Eigenschaften von nanoskaligen Halbleiter-Systemen wie beispielsweise Nanodrähte und Quantenpunkte, die lateral in Heterostrukturen definiert sind, werden mittels Quantentransportexperimenten für die Entwicklung neuer Strategien in der Informationsverarbeitung untersucht.
- Die elektronischen Transporteigenschaften von topologischen Isolatoren, in denen Ladungsträger nur an der Oberfläche und nicht im Volumen transportiert werden, werden durch Analyse der schwachen Antilokalisierung infolge der Spin-Bahn-Kopplung und der Elektron-Elektron-Wechselwirkung untersucht.

Im Bereich der spektroskopischen Messmethoden steht uns die Ramanspektroskopie für Untersuchungen der Schwingungsmoden in Halbleiterschichten, Heterostrukturen, Nanodrähten, topologischen Isolatoren und Graphen zur Verfügung. Darüber hinaus werden III-V-Schichten, -Heterostrukturen und -Nanodrähte mittels Photolumineszenz- und Photolumineszenzanregungs-Spektroskopie vom ultravioletten (244 nm) bis zum nah-infraroten (1,7  $\mu\text{m}$ ) Spektralbereich untersucht. Die spektro-

of ten nanometers. In addition, element identification is achieved by energy- and wavelength-dispersive x-ray spectroscopy, and the crystallographic orientation as well as the strain state can be determined using electron backscatter diffraction. Time-resolved photoluminescence spectroscopy on a pico- to microsecond time scale from the ultraviolet (240 nm) to the near-infrared spectral region (1.3  $\mu\text{m}$ ) and pump-and-probe spectroscopy with a sub-picosecond time resolution are employed to investigate the carrier and polarization dynamics in III-V films, heterostructures, and nanowires. Fourier-transform spectroscopy is used in the far-infrared or terahertz spectral region to record the lasing parameters of quantum-cascade lasers and in the mid-infrared region to study vibrational modes. The magneto-transport experiments on ferromagnet/semiconductor hybrid devices, semiconductor-based nanoscale systems, and topological insulators can be performed in magnetic fields up to 16 T and at temperatures down to 20 mK.

In 2020, acoustically driven spin resonances have been identified at room temperature in atomic-scale centers in silicon carbide. Specifically, a surface acoustic wave cavity has been used to selectively address spin transitions with magnetic quantum number differences of  $\pm 1$  and  $\pm 2$  in the absence of external microwave electromagnetic fields. These spin-acoustic resonances reveal a nontrivial dependence on the static magnetic field orientation, which is attributed to the intrinsic symmetry of the acoustic fields combined with the peculiar properties of a half-integer spin system. A microscopic model of the spin-acoustic interaction has been developed, which describes the experimental results without any fitting parameters. Furthermore, it is predicted that traveling surface waves lead to a chiral spin-acoustic resonance that changes upon magnetic field inversion. These results establish silicon carbide as a highly promising hybrid platform for on-chip spin-optomechanical quantum

skopischen Methoden für den nah-infraroten bis ultravioletten Spektralbereich wie die Raman- und Photolumineszenz-Spektroskopie können auch mit einer räumlichen Auflösung von bis zu 0,5  $\mu\text{m}$  und in Magnetfeldern von bis zu 8 T eingesetzt werden. Mit der Kathodolumineszenz-Spektroskopie in Kombination mit den Abbildungsmöglichkeiten eines Rasterelektronenmikroskops kann die Ortsauflösung bis in den Bereich von zehn Nanometern verbessert werden. Hinzu kommt die Möglichkeit, chemische Elemente durch energie- und wellenlängendispersive Röntgenspektroskopie zu identifizieren. Mittels der Elektronenrückstreuung erhalten wir Informationen über kristallographische Orientierungen sowie Verspannungen in den Materialien. Zeit aufgelöste Photolumineszenz-Spektroskopie auf einer Zeitskala von Piko- bis Mikrosekunden vom ultravioletten (240 nm) bis zum nahinfraroten (1,3  $\mu\text{m}$ ) Spektralbereich sowie Anrege-Abtast-Spektroskopie mit einer Zeitauflösung unterhalb einer Pikosekunde werden eingesetzt, um die Ladungsträger- und Polarisationsdynamik in III-V-Schichten, -Heterostrukturen und -Nanodrähten zu untersuchen. Mittels Fouriertransform-Spektroskopie werden im ferninfraroten bzw. Terahertz-Spektralbereich die Emissionseigenschaften von Quantenkaskadenlasern und im mittleren infraroten Spektralbereich Schwingungsmoden untersucht. Die Magneto-transport-Experimente an Ferromagnet/Halbleiter-Hybrid-Bauelementen, nanoskaligen Halbleiter-Systemen und topologischen Isolatoren können in Magnetfeldern bis zu 16 T und Temperaturen bis herunter zu 20 mK durchgeführt werden.

Im Jahr 2020 wurden akustisch-erzeugte Spinresonanzen in atomar-skaligen Zentren in Siliciumcarbid bei Raumtemperatur identifiziert. In spezifischer Weise wurde ein auf akustischen Oberflächenwellen basierender Resonator verwendet, um Spinübergänge mit Änderungen der magnetischen Quantenzahl von  $\pm 1$  und  $\pm 2$  ohne externe elektromagnetische Felder im Mikrowellen-

control, enabling engineered interactions at room temperature.

Optical parametric oscillations—the non-linear coherent coupling of an optically excited, two-particle pump state with a signal and idler state correlated in energy—are relevant for optical amplification and generation of correlated photons. Optical parametric oscillations require states with well-defined symmetries and energies. The fine-tuning of material properties and structural dimensions remains a challenge for the realization of scalable optical parametric oscillations in semiconductor nanostructures. A pathway toward arrays of optical parametric oscillations has been demonstrated based on the dynamic control of microcavity exciton-polaritons confined in micrometer-sized intracavity traps by an acoustic wave. The spatially varying strain field of the wave induces state-dependent energy shifts of discrete polariton levels with the appropriate symmetry for the triggering of optical parametric oscillations. The robustness of the dynamic acoustic tuning has been shown by the synchronous excitation of an array of confined optical parametric oscillations using a single wave, which thus opens the way for the realization of scalable nonlinear on-chip systems.

Terahertz quantum-cascade lasers are based on complex semiconductor heterostructures, in which the optical gain is generated by intersubband transitions. Using the spacing of the laser modes in the emission spectra, the effective group refractive index has been determined for more than one hundred terahertz quantum-cascade lasers of the hybrid design with Fabry-Pérot resonators based on single-plasmon waveguides. The experimentally obtained values of the effective group refractive index for emission frequencies between 2.5 and 5.6 THz generally follow its trend derived from electromagnetic simulations. However, for a certain number of quantum-cascade lasers, the ex-

bereich selektiv zu adressieren. Diese Spin-akustischen Resonanzen zeigen eine nicht-triviale Abhängigkeit von der Richtung des statischen Magnetfeldes, die der intrinsischen Symmetrie der akustischen Felder verbunden mit den besonderen Eigenschaften eines halbzahligen Spinsystems zuzuschreiben ist. Ein mikroskopisches Modell der Spin-akustischen Wechselwirkung, das die experimentellen Ergebnisse ohne jegliche Anpassungsparameter beschreibt, wurde entwickelt. Weiterhin wird vorausgesagt, dass laufende Oberflächenwellen zu einer chiralen spin-akustischen Resonanz führen, die sich bei einer Inversion des Magnetfeldes ändert. Diese Ergebnisse etablieren Siliciumcarbid als eine sehr vielversprechende hybride Plattform für die *on-chip* Spin-optomechanische Quantenkontrolle, die technisch nutzbare Wechselwirkungen bei Raumtemperatur ermöglicht.

Optisch-parametrische Oszillationen – die nichtlineare Kopplung eines optisch angeregten Zweiteilchen-Pumpzustands mit einem Signal- und Leerlaufzustand, die energetisch korreliert sind – sind für die optische Verstärkung und die Erzeugung von korrelierten Photonen wichtig. Optisch-parametrische Oszillationen setzen Zustände mit wohldefinierten Symmetrien und Energien voraus. Die Feinabstimmung von Materialparametern und strukturellen Abmessungen bleibt eine Herausforderung für die Realisierung von skalierbaren optisch-parametrischen Oszillationen in Halbleiter-Nanostrukturen. Eine mögliche Realisierung von Feldern optisch-parametrischer Oszillationen wurde basierend auf der dynamischen Kontrolle von Exziton-Polaritonen, die in mikrometer-großen Fallen durch eine akustische Welle eingeschlossen wurden, aufgezeigt. Das sich räumlich ändernde Spannungsfeld der Welle verursacht Zustands-abhängige Energieverschiebungen von diskreten Polariton-Niveaus mit der geeigneten Symmetrie für die Erzeugung von skalierbaren optisch-parametrischen Oszillationen. Die Robustheit der dynamischen akustischen Abstim-

perimental values of the effective group refractive index exhibit a rather large deviation from the general trend and the simulation results. From a thorough analysis, it is concluded that differences in the optical gain/loss spectra are responsible for this deviation, which lead to a modification of the dispersion in the active region and consequently to altered values of the effective group refractive index.

Metastable  $\alpha$ -FeGe<sub>2</sub>, a layered tetragonal material, has been investigated as a spacer layer embedded in spin valve structures with ferromagnetic Fe<sub>3</sub>Si and Co<sub>2</sub>FeSi electrodes. For both types of electrodes, spin valve operation is demonstrated with a metallic transport behavior of the  $\alpha$ -FeGe<sub>2</sub> spacer layer. The spin valve signals are found to increase with both, spacer thickness and temperature, which is discussed in terms of a decreasing magnetic coupling strength between the bottom and the top ferromagnetic electrode. The temperature-dependent resistance of the spin valve structures exhibits characteristic features, which are explained by ferromagnetic phase transitions between 55 and 110 K. The metallic transport characteristics as well as the low-temperature ferromagnetism are found to be consistent with the results of first-principles calculations.

Raman spectroscopy has been utilized to study the magnetic characteristics of heteroepitaxial NiO thin films grown by plasma-assisted molecular beam epitaxy on MgO(100) substrates. For the determination of the Néel temperature, a reliable approach is demonstrated by analyzing the temperature dependence of the Raman peak originating from second-order scattering by magnons. The antiferromagnetic coupling strength is found to be strongly influenced by the growth conditions. The low-temperature magnon frequency and the Néel temperature are shown to depend on the biaxial lattice strain and the degree of structural disorder, which is dominated by point defects.

mung wurde durch die synchrone Anregung eines Feldes von eingeschlossenen optisch-parametrischen Oszillationen mittels einer einzelnen Welle nachgewiesen, wodurch die Realisierung von skalierbaren nichtlinearen *on-chip* Systemen möglich wird.

Terahertz-Quantenkaskadenlaser basieren auf komplexen Halbleiter-Heterostrukturen, in denen die optische Verstärkung durch Intersubband-Übergänge erzeugt wird. Durch die Messung der Abstände von Lasermoden in den Emissionsspektren wurde der effektive Gruppenbrechungsindex für mehr als einhundert Terahertz-Quantenkaskadenlaser des Hybrid-Designs mit Fabry-Pérot-Resonatoren basierend auf Einzel-Plasmon-Wellenleitern bestimmt. Die experimentell bestimmten Werte des effektiven Gruppenbrechungsindex für Emissionsfrequenzen zwischen 2,5 und 5,6 THz folgen allgemein dem Verlauf, der durch elektromagnetische Simulationen abgeleitet wurde. Allerdings weisen die experimentellen Werte des effektiven Gruppenbrechungsindex für eine gewisse Anzahl von Quantenkaskadenlasern eine ziemlich große Abweichung von dem allgemeinen Verlauf und den simulierten Resultaten auf. Aus einer umfassenden Analyse ergibt sich die Schlussfolgerung, dass Abweichungen in den optischen Verstärkungs- bzw. Verlustspektren, die zu einer Veränderung der Dispersion in dem aktiven Bereich und somit zu veränderten Werten des effektiven Gruppenbrechungsindex führen, für diese Unterschiede verantwortlich sind.

Metastabiles  $\alpha$ -FeGe<sub>2</sub>, ein geschichtetes tetragonales Material, wurde eingebettet als Abstandsschicht in Spinventil-Strukturen mit ferromagnetischen Fe<sub>3</sub>Si- und Co<sub>2</sub>FeSi-Elektroden untersucht. Für beide Elektrodenarten wurde der Spinventil-Betrieb mit einem metallischen Transportverhalten der  $\alpha$ -FeGe<sub>2</sub>-Abstandsschicht gezeigt. Die Spinventil-Signale steigen sowohl mit der Dicke der Abstandsschicht als auch mit der Temperatur an, was in Bezug auf eine abnehmende magnetische

The realization of integrated quantum circuits requires precise on-chip control of charge carriers. Quantum point contacts are fundamental building blocks of nanoelectronic circuits. Aiming at the coherent coupling of distant nanostructures at zero magnetic field, the ballistic electron transport has been studied through two quantum point contacts in series in a three-terminal configuration. The coupling between the quantum point contacts is enhanced by electrostatic focusing using a field effect lens. For a detailed investigation of the emission and collection properties of the quantum point contacts, the electrostatic focusing is combined with magnetic deflection. In addition, it is demonstrated how the coherent and ballistic dynamics depend on the details of the confinement potentials of the quantum point contacts. Furthermore, the one-dimensional subband spacings of various quantum point contacts has been measured as a function of their conductance. The results are compared with the results of models of a lateral parabolic versus hard-wall confinement. A gate-defined quantum point contact near pinch-off is compatible with the parabolic saddle-point scenario. However, as the number of populated subbands is increased, Coulomb screening flattens the potential bottom, and a description in terms of a finite hard-wall potential becomes more realistic.

The coupling of superconductors to a two-dimensional electron gas generates a number of magnetotransport oscillations. For instance, an Aharonov-Bohm-type oscillation at intermediate magnetic fields and an Altshuler-Aronov-Spivak-like oscillation around zero magnetic field appear when Andreev and normal reflections from the interface between the normal conductor and the superconductor coexist. The presence and the characteristics of such magnetotransport oscillations have been investigated based on fully quantum-mechanical simulations. The significant role of the quantum interference is thereby

Kopplungsstärke zwischen der unteren und der oberen ferromagnetischen Elektrode diskutiert wird. Der Temperatur-abhängige Widerstand der Spinventil-Strukturen weist charakteristische Eigenschaften auf, die durch einen ferromagnetischen Phasenübergang zwischen 55 und 110 K erklärt werden. Sowohl die metallischen Transporteigenschaften als auch der Ferromagnetismus bei tiefen Temperaturen stimmen mit Resultaten von *first-principles*-Berechnungen überein.

Die magnetischen Eigenschaften von dünnen heteroepitaktischen NiO-Schichten, die mittels Plasma-gestützter Molekularstrahlepitaxie auf MgO(100)-Substraten gewachsen wurden, wurden mit Raman-Spektroskopie untersucht. Für die Bestimmung der Néel-Temperatur wurde eine zuverlässige Methode aufgezeigt, bei der die Temperaturabhängigkeit des Maximums der Raman-Linie, die durch Streuung zweiter Ordnung an Magnonen erzeugt wird, analysiert wurde. Es zeigt sich, dass die antiferromagnetische Kopplungsstärke stark durch die Wachstumsbedingungen beeinflusst wird. Die Magnon-Frequenz bei tiefen Temperaturen und die Néel-Temperatur hängen dabei von der zweiachsigen Gitterverspannung und dem Grad der strukturellen Unordnung, die durch Punktdefekte bestimmt wird, ab.

Die Realisierung von integrierten Quantenschaltungen setzt eine präzise *on-chip* Kontrolle von Ladungsträgern voraus. Quantenpunktkontakte sind fundamentale Bausteine von nanoelektronischen Schaltungen. Für die kohärente Kopplung von räumlich getrennten Nanostrukturen bei verschwindendem Magnetfeld wurde der ballistische Elektronentransport durch zwei Quantenpunktkontakte in Serie in einer dreipoligen Konfiguration untersucht. Die Kopplung zwischen den Quantenpunktkontakten wird durch elektrostatische Fokussierung mit Hilfe einer Feldeffektlinse erhöht. Für eine detaillierte Untersuchung der Emissions- und Detektionseigenschaften der Quantenpunktkontakte wurde die

demonstrated. It is also shown how the oscillations are affected by the presence of potential disorder and a finite excitation bias. Shubnikow-de Haas oscillations of the two-dimensional electron gas are not always suppressed by the disorder under the influence of superconductivity, making their distinction from the Aharonov-Bohm-type oscillation possibly ambiguous.

elektrostatische Fokussierung mit magnetischer Ablenkung kombiniert. Außerdem wurde gezeigt, wie die kohärente und ballistische Dynamik von dem detaillierten Verlauf des Einschlusspotenzials der Quantenpunktkontakte abhängt. Weiterhin wurden die Abstände der eindimensionalen Subbandenergien für mehrere Quantenpunktkontakte in Abhängigkeit von ihrer Leitfähigkeit gemessen. Diese Resultate werden mit den Ergebnissen von Modellen eines lateralen parabolischen Einschlusses bzw. mit harten Wänden verglichen. Ein Gatterdefinierter, nahezu abgeklemmter Quantenpunktkontakt ist mit dem parabolischen Sattelpunkt-Szenario kompatibel. Allerdings flacht mit zunehmender Anzahl von besetzten Subbändern das Potenzialminimum durch Coulomb-Abschirmung ab und eine Beschreibung in Form eines endlichen Potenzials mit harten Wänden wird realistischer.

Die Kopplung von Supraleitern mit einem zweidimensionalen Elektronengas erzeugt eine Reihe von Oszillationen in Magnettransportkennlinien. Beispielsweise erscheint eine Aharonov-Bohm-artige Oszillation für mittlere Magnetfelder und eine Altshuler-Aronov-Spivak-artige Oszillation für nahezu verschwindende Magnetfelder, wenn Andreev- und konventionelle Reflektionen von der Grenzfläche zwischen dem Normalleiter und dem Supraleiter koexistieren. Das Vorhandensein und die Eigenschaften solcher Magnettransportoszillationen wurden mit Hilfe vollständig quantenmechanischer Simulationen untersucht. Die wesentliche Rolle der Quanteninterferenz wurde dadurch nachgewiesen. Weiterhin wurde gezeigt, wie die Oszillationen durch die Existenz von Potenzialunordnung und einer endlichen Anregungsspannung beeinflusst werden. Shubnikow-de-Haas-Oszillationen des zweidimensionalen Elektronengases werden nicht immer durch die Unordnung unter dem Einfluss der Supraleitfähigkeit unterdrückt, was die Unterscheidung von der Aharonov-Bohm-artigen Oszillation möglicherweise zweifelhaft macht.

# Department Microstructure

## Abteilung Mikrostruktur

Head of Department: Dr. Achim Trampert, [trampert@pdi-berlin.de](mailto:trampert@pdi-berlin.de)



The major research goal of the department Microstructure is to understand material properties on the basis of detailed knowledge of their microstructure (structure-property-relation). Here the term "microstructure" in the broadest sense includes all kinds of defects, i.e. all deviations from the regular structure, and their geometry and physical configuration — regardless of length scales. The probe volume detecting these features must therefore range from the microscopic scale to the single atom level. Consequently, advanced X-ray and electron diffraction techniques, transmission electron microscopy imaging and spectroscopy as well as scanning tunneling microscopy and spectroscopy are applied with high spatial resolution and high sensitivity to analyze quantitatively the structural, chemical and electronic properties of the wide range of material systems grown at PDI or by external collaborators. Examples are low-dimensional semiconductor heterostructures, two-dimensional layered materials, ferromagnet-semiconductor hybrid systems, and metastable materials and novel material combinations. Experimental studies are focused on hetero-phase interfaces and phase stabilities, epitaxial strain and strain relaxation processes, and the formation of extended and complex defects. The experimental results are compared with computer simulations and supported by theoretical modeling. Finite element calculations can virtually cover any non-trivial geometry and chemical composition profile of low-dimensional structures and may thereby provide a highly realistic view of elastic strain and piezoelectric polarization fields within heteroepitaxial systems.

Transmission electron microscopy (TEM) is one of the key tools for direct imaging

Das Ziel der Abteilung Mikrostruktur liegt darin, Materialeigenschaften auf der Basis einer detaillierten Kenntnis ihrer Mikrostruktur zu verstehen (Struktur-Eigenschaftsbeziehung). Hierbei werden als „Mikrostruktur“ alle Arten von Defekten in Kristallen, also alle Abweichungen von der regelmäßigen Struktur, deren Geometrie und physikalischen Konfiguration unabhängig von der Längenskala verstanden. Das Volumen, innerhalb dessen die Struktur detektiert wird, muss infolgedessen den gesamten Bereich von mikroskopischer Dimension über die Nanometerskala bis zur Ebene einzelner Atome abdecken. Dementsprechend werden Röntgen- und Elektronenbeugungstechniken, abbildende und analytische Transmissionselektronenmikroskopie sowie Rastertunnelmikroskopie jeweils mit hoher räumlicher Auflösung und Empfindlichkeit eingesetzt, um die strukturellen, elektronischen und chemischen Eigenschaften einer großen Vielfalt von Materialsystemen, die am PDI oder von externen Kooperationspartnern hergestellt werden, quantitativ zu untersuchen. Beispiele für untersuchte Materialien sind niedrigdimensionale Halbleiterheterostrukturen, zweidimensionale Schichtmaterialien, Ferromagnet-Halbleiter Hybridstrukturen sowie metastabile Materialien und neuartige Materialkombinationen. Experimentelle Ergebnisse zu Phasengrenzflächen und zur Phasenstabilität, zu Relaxationsmechanismen der Gitterfehlpassung und zur Entstehung ausgedehnter und komplexer Defekte, sowie zu künstlichen Nanostrukturen werden mit Computersimulationen verglichen und die Interpretationen durch theoretische Modelle untermauert. Aufgrund ihrer universellen Möglichkeiten bei der Simulation sehr realitätsnaher Modelle mit nicht-trivialer Geometrie und chemischer Komposition kommt der Methode der Finiten Ele-



of the local atomic structure of materials. Important supplements are the high-angle annular dark-field and (annular) bright-field detectors in a scanning (S)TEM, which are used for chemically sensitive contrast imaging with atomic resolution. Electron energy-loss spectroscopy and energy dispersive x-ray spectroscopy complete the analytical performance of our microscope tools in the field of chemical bonding and composition, and enable two-dimensional (2D) chemical mappings.

As one of our strengths high-resolution and analytical (S)TEM is used to quantitatively determine the structural roughness of semiconductor heterostructure interfaces and their chemical intermixing. In particular, we are able to analyze the chemical composition profiles of planar interfaces up to the atomic level. Moreover, there is an attempt to correlate the interface property with the physical functionality of the heterostructure. Examples are here the investigations of ultra-thin (Al,Ga)As/GaAs interface profiles in quantum cascade lasers or of III-V quantum wells in laser diodes. Another example refers to the interface study of monolithically integrated III-V layers on Si substrates. On the other hand, the atomic configurations – atom position and type – at coherent interfaces between dissimilar materials or in nanosized clusters are analyzed on the basis of (S)TEM in combination with image contrast simulations. Further examples comprise the interface character in three-dimensional (3D) core/shell or axial heterojunction nanowires and epitaxial interfaces in van der Waals heterostructures.

In parallel to our scientific research on specific materials issues, we continually refine and develop our experimental methods per se. For some years now, we have been using electron tomography, a technique that allows us to reconstruct complex structures and nanoscale materials in three dimensions. Essential prerequisites for this purpose are on the one hand a suitable imaging method fulfilling the tomographic

mente hierbei eine Schlüsselrolle zu. Als numerisches Pendant zu rein analytischen Ansätzen liefert diese quantitative, räumlich aufgelöste Deformations- und Spannungstensoren in realen Objekten, sowie für heteroepitaktische Systeme mit fehlender Inversionssymmetrie ein dreidimensionales Bild der piezoelektrischen Polarisation.

Die Transmissionselektronenmikroskopie (TEM) ist eines der zentralen Werkzeuge, um die lokale atomare Struktur von Materialien abzubilden. Wesentliche Erweiterungen im Raster-(S)TEM-Betrieb sind der ringförmige Weitwinkel-Dunkelfeld- sowie der (ringförmige) Hellfeld-Detektor, die eine chemisch sensitive Abbildung mit atomarer Auflösung ermöglichen. Dazu vervollständigen die Elektronenenergieverlustspektroskopie und die energiedispersive Röntgenspektroskopie die analytische Leistungsfähigkeit unserer Mikroskope im Bereich der Messung chemischer Bindungen und Zusammensetzungen, und ermöglichen zweidimensionale (2D) Kartierungen.

Eine unserer besonderen Stärken liegt im Einsatz von hochauflösender und analytischer TEM, um die strukturelle Grenzflächenrauigkeit und Durchmischung von Halbleiterübergängen zu bestimmen. Insbesondere das chemische Zusammensetzungsprofil über planare Grenzflächen kann bis auf die atomare Ebene quantitativ ermittelt und modelliert werden. Darüber hinaus wird versucht, die strukturelle Grenzflächeneigenschaft direkt mit der physikalischen Funktionalität der Heterostruktur zu korrelieren. Als Beispiele dienen die Untersuchungen der Profile von ultradünnen (Al,Ga)As/GaAs Grenzflächen in Quantenkaskadenlasern oder von III-V Quantentöpfen in Laserdioden. Ein weiteres aktuelles Beispiel ist die Grenzflächenuntersuchung von monolithisch integrierten III-V Schichten auf Si. Andererseits wird die atomare Konfiguration – das heißt, die Art und Position der Atome – an kohärenten Grenzflächen zwischen stark unterschiedlichen Materialien oder in nanoskopischen

projection requirement, and, on the other hand, an appropriate tomography sample preparation using the focused ion beam (FIB) technique. Currently, research is focused on tomographic studies of nanostructures such as nanowires, on the spatial distribution of dislocations in heterostructures, and on the tomography of interfaces. Thus, we have recently developed an innovative tomographic method to visualize the 3D character of buried interfaces and to quantitatively analyze their structural and chemical roughness. The ultimate goal is to determine not only the structure and morphology, but also the associated physical and chemical properties.

The tomography activities are part of our newly established "Berlin Application Laboratory Electron Tomography" (BALET). The Application Laboratory is financially supported by the European Regional Development Fund (ERDF) and by the Senate of Berlin. The reconstruction of a purpose-designed laboratory for our BALET was completed in 2019 with the successful commissioning of a new grant-funded state-of-the-art aberration-corrected (Cs) STEM microscope, Jeol ARM200F. This new Cs-corrected STEM greatly improves the performance of the tomography method. Objective of the Application Laboratory is the methodical development and extensions to promote materials research, to collaborate with external partners and to utilize the tomography method to industrial applications.

A further methodical development is related to our in-situ electron microscopy of dynamic processes. Heating experiments in the microscope serve to analyze defect formation and propagation, structural phase transitions and solid-state reactions with high spatial resolution. The ability to directly observe atoms in real time and explore their correlated motion opens new avenues to a better understanding of material properties and functionalities. Currently, the amorphous-crystalline and disorder-order

schen Clustern mit Hilfe von (Raster-) TEM in Kombination mit Bild-Kontrastsimulationen analysiert. Weitere Beispiele umfassen die Natur von Grenzflächen in Nanosäulen mit lateraler oder axialer Heterostruktur, oder in van-der-Waals-gebundenen Schichtsystemen wie Graphen auf BN oder SiC Substraten.

Parallel zu unserer Forschung zu spezifischen Materialeigenschaften, bei der ein breites Spektrum mikroskopischer Techniken als Werkzeug verwendet wird, verbessern und entwickeln wir kontinuierlich die experimentellen Methoden selbst. So haben wir die Technik der Elektronentomographie eingeführt – eine Technik, mit der man dreidimensionale (3D) Rekonstruktionen komplexer nanoskaliger Strukturen und Materialien erhalten kann. Eine wesentliche Voraussetzung dazu ist die Herstellung spezieller Tomographieproben unter Nutzung fokussierter Ionenstrahlen (FIB). Derzeit konzentriert sich die Forschung auf tomographische Untersuchungen von Nanostrukturen wie Nanodrähten, auf die räumliche Verteilung von Versetzungen in Heterostrukturen und auf die Tomographie von Grenzflächen. So haben wir kürzlich eine innovative tomographische Methode entwickelt, um den 3D-Charakter von vergrabenen Grenzflächen zu visualisieren und ihre strukturelle und chemische Rauigkeit quantitativ zu analysieren. Ziel ist hier, nicht nur die Struktur und Morphologie, sondern auch die damit verbundenen physikalischen und chemischen Eigenschaften zu studieren und miteinander in Bezug zu setzen.

Die Tomographiearbeiten sind Bestandteil des neu gegründeten „Berliner Applikationslabors Elektronentomographie“. Das Applikationslabor wird vom Berliner Senat sowie aus Mitteln des Europäischen Fonds für regionale Entwicklungen (EFRE) gefördert. Der Aufbau eines speziell entwickelten Labors ist im Jahr 2019 mit der Inbetriebnahme des aus Fördermitteln neu angeschafften und top-modernen aberrationskorrigierten Rastertransmissionselek-

phase transitions during solid state epitaxy of Ge on Fe<sub>3</sub>Si have been observed in-situ with atomic resolution. Our results showed that the crystallization occurs layer-by-layer and the growth kinetics is described by a diffusion-driven process following a square root time dependency.

The physical properties of ultimately small structures at solid-vacuum interfaces are explored by cryogenic scanning tunneling microscopy (STM) carried out in ultrahigh vacuum and at liquid-helium temperature. Our microscopes ensure state-of-the-art performance in terms of thermal and mechanical stability. This allows us to manipulate single atoms adsorbed on a semiconductor surface and build up atomically defined quantum dots and quantum-dot assemblies. The quantum properties of these artificial structures are probed by scanning tunneling spectroscopy to determine the local density of electronic states as well as elementary excitations with atomic-scale spatial resolution. Starting at a base temperature of 5 K, the sample temperature can be varied up to about 100 K at continuous STM operation in the tunneling regime. This enables to study processes such as surface diffusion at the single-atom level as well as the competition between thermally excited and current-induced dynamics of engineered nanostructures. The technical design of our microscopes makes it possible to detect current-induced light emitted from the tunnel junction, thus combining optical spectroscopy capability with the spatial resolution of STM.

X-rays, as a non-destructive probe, can penetrate fairly thick layers and therefore enables the investigation not only of surfaces but also of buried interfaces, as well as structures within the bulk crystal. As a diffraction technique, it combines sub-Ångström resolution with a large interaction volume that provides statistically reliable structural properties. Results are analyzed quantitatively on the basis of modeling and simulation of diffraction data and comple-

tronenmikroskops (Cs-STEM) abgeschlossen worden. Das Cs-STEM verbessert die Leistungsfähigkeit der Elektronentomographiemethode in erheblichem Maße. Aufgabe des Applikationslabors ist es, die Tomografiertechnik und ihre Weiterentwicklungen in der Materialforschung voranzutreiben, mit externen Partnern zu kooperieren und die Elektronentomographie für industrielle Anwendungen nutzbar zu machen.

Eine weitere methodische Entwicklung betrifft unsere in-situ Elektronenmikroskopie dynamischer Prozesse. Temperaturabhängige Experimente im Mikroskop nutzen wir dazu, Defektbildung und -propagation, strukturelle Phasenübergänge und Festkörperreaktionen an Grenzflächen mit hoher räumlicher Auflösung zu studieren. Durch die direkte Beobachtung von Atomen und deren korrelierter Bewegung in Echtzeit eröffnet sich die Möglichkeit, ein besseres Verständnis von Materialverhalten und -eigenschaften zu gewinnen. Gegenwärtig untersuchen wir den amorph-kristallinen und den Unordnungs-Ordnungs-Phasenübergang während der Festphasenepitaxie von Ge auf Fe<sub>3</sub>Si. Es konnte gezeigt werden, dass die Kristallisation Lage-für-Lage stattfindet und die Wachstumskinetik diffusionsgetrieben ist und dabei einem zeitabhängigen Quadratwurzelgesetz folgt.

Die physikalischen Eigenschaften von kleinsten Strukturen an der Grenzfläche zwischen halbleitendem Festkörper und Vakuum werden mit Tieftemperatur-Rastertunnelmikroskopie untersucht. Diese Experimente finden im Ultrahochvakuum und bei Temperaturen von flüssigem Helium statt. Der technische Aufbau unserer Mikroskope erfüllt die höchsten Anforderungen an thermische und mechanische Stabilität. Dies ermöglicht es uns, einzelne Atome auf einer Halbleiteroberfläche zu manipulieren und somit strukturell perfekte Quantenpunkte sowie definierte Anordnungen aus gekoppelten Quantenpunkten aufzubauen. Die quantenphysikalischen Eigenschaften dieser künstlichen Strukturen werden mit-

mented by electron microscopy measurements. Moreover, in the x-ray laboratory of our institute the basic parameters of many grown structures are quickly obtained in order to give immediate feedback for further growth experiments.

PDI's PHARAO end station at Berlin Synchrotron BESSYII (Helmholtz-Zentrum Berlin, HZB) facilitates in-situ x-ray diffraction during molecular beam epitaxy (MBE) in order to study the growth dynamics of epitaxial layers. A direct, surface sensitive access to crystal symmetry, elastic strain and surface reconstruction in a realistic growth environment, and, in real-time, improves our understanding of fundamental growth-related phenomena as interface formation, strain relaxation and reconstruction dynamics. Our recent work focuses on large-area heterostructures made of weakly scattering graphene and 2D ferromagnetic  $\text{Fe}_{5-x}\text{GeTe}_2$  layers. Synchrotron-based grazing incidence x-ray diffraction provides essential morphological information to establish a detailed correlation between structure and magnetism. This activity relies on active contributions of the Departments Microstructure and Epitaxy.

Addressing questions, which require very specific source characteristics as brilliance or spot size, we are regularly applying for and performing complementary x-ray diffraction measurements at dedicated third-generation synchrotron sources like PETRAIII (Hamburg, Germany), the Diamond Light Source (Didcot, UK) and the ESRF (Grenoble, France). Of particular interests are newly approaching techniques like diffraction with highly focused x-rays to study individual low-dimensional structures. Thereby, we overcome the ensemble average inherent to x-ray techniques applying millimeter-sized x-ray foci. On the other hand, investigations of ultra-thin 2D van der Waals layers, especially if consisting of weak scatterers, as B, N, and C-atoms, require extremely brilliant sources and have been performed at the external sources as well.

tels Rastertunnelspektroskopie bestimmt, so zum Beispiel die lokale elektronische Zustandsdichte oder auch Elementaranregungen bei räumlicher Auflösung auf atomarer Skala. Während der STM-Messungen kann die Proben temperatur zwischen 5 K und 100 K kontinuierlich variiert werden. Hierdurch lassen sich zum Beispiel Oberflächendiffusionsprozesse oder auch die Wechselwirkung zwischen thermisch angeregter und strominduzierter Dynamik untersuchen. Außerdem bieten unsere Mikroskope die Möglichkeit, strominduziertes Licht aus dem Tunnelkontakt zu detektieren, um so optische Spektroskopie mit ortsaufgelöster Rastertunnelmikroskopie zu kombinieren.

Die Röntgenstrahlung als zerstörungsfreie Sonde kann vergleichsweise dicke Schichten durchdringen und ermöglicht daher nicht nur die Untersuchung von Oberflächen, sondern auch von vergrabenen Grenzflächen sowie von Strukturen innerhalb des Bulk-Kristalls. Als Beugungsmethode kombiniert sie eine Sub-Ångström-Auflösung mit einem großen Wechselwirkungsvolumen, die statistisch zuverlässige Struktureigenschaften liefert. Die Ergebnisse werden auf der Basis von Modellierung und Simulation der Beugungsdaten quantitativ analysiert und durch elektronenmikroskopische Messungen ergänzt. Darüber hinaus werden im Röntgenlabor unseres Instituts die grundlegenden Parameter vieler gewachsener Strukturen schnell ermittelt, um ein unmittelbares Feedback für weitere Wachstumsexperimente zu geben.

Das PHARAO Experiment des Institutes am Berliner Synchrotron BESSYII (Helmholtz-Zentrum Berlin, HZB) ermöglicht die in-situ Röntgenbeugung während der Molekularstrahlepitaxie (MBE), um die Wachstumsdynamik von Epitaxie-Schichten zu untersuchen. Ein direkter, oberflächensensitiver Zugang zu Kristallsymmetrie, elastischer Dehnung und Oberflächenrekonstruktion in einer realistischen Wachstumsumgebung und in Echtzeit verbessert unser Verständ-

nis grundlegender wachstumsbezogener Phänomene wie Grenzflächenbildung, Spannungsrelaxation und Rekonstruktionsdynamik. Unsere jüngsten Arbeiten konzentrieren sich auf Heterostrukturen, die aus einzelnen Graphenlagen und dem Ferromagneten  $\text{Fe}_{5-x}\text{GeTe}_2$  bestehen. Hier trägt die Synchrotron-basierte Beugung unter streifendem Einfall mit Sub-Ångström Auflösung entscheidend zur Aufklärung der Realstruktur bei und liefert somit einen essentiellen Beitrag hin zu einem tieferen Verständnis des Zusammenhangs zwischen Struktur und magnetischen Eigenschaften. Diese Arbeit stützt sich auf eine aktive Zusammenarbeit der Abteilungen Mikrostruktur und Epitaxie.

Zur Adressierung von Fragestellungen, die den Einsatz höchstbrillanter Quellen erfordert, beantragen und nutzen wir regelmäßig den Zugang zu Synchrotronquellen der 3. Generation wie beispielsweise PETRAIII in Hamburg, Diamond Light Source (UK) und ESRF in Grenoble. Von besonderem Interesse sind neu angewandte Techniken wie die Beugung mit hochfokussierter Röntgenstrahlung zur Untersuchung einzelner niedrigdimensionaler Strukturen. Dabei überwinden wir die Mittelwertbildung, die den Röntgentechniken mit millimetergroßen Röntgenstrahlen innewohnt. Zur Untersuchung von ultradünnen, 2D van der Waals Schichten, die zudem oft aus leichten und daher weniger stark streuenden Elementen wie B, N und C bestehen, sind extrem brillante Quellen erforderlich, so dass die entsprechenden Experimente dazu ebenfalls an externen Quellen durchgeführt werden.

# Department Technology and Transfer

## Abteilung Technologie und Transfer

Head of Department: Dr. Carsten Hucho, hucho@pdi-berlin.de



The Department of Technology and Transfer combines all science-supporting activities of the institute. These include semiconductor technology with its scientific head Dr. Abbas Tahraoui, the building services and workshop headed by Jörg Pfeiffer, as well as personnel support in the hands of Human Resources Manager Andreas Hartung, the purchasing and finance section of Kerstin Arnhold, and the processing of third-party funds by Anja Hollmack. Intellectual Property, its screening and securing is in the hands of Mercedes Reischel, Kai Hablitzel answers all questions concerning EU research funding and coordinates the GraFOx Science Campus. The scientific special library is currently undergoing a modernization push by librarian Anne Timm. The head of department is the administrative director of the institute and coordinates the administrative necessities of the research operation with the aim of keeping non-scientific work away from researchers as far as possible. As scientific-administrative coordinator, he advises the Director on strategic research planning and develops the Institute's knowledge transfer activities.

### Utilities Management

PDI is tenant in a building administered by Humboldt-Universität (HU). While the central services are provided by HU, the special infrastructural needs of a materials science institute are coordinated within this department. This comprises the supply with technical gases (especially liquid Helium for temperature-dependent experiments and liquid Nitrogen as a coolant for MBE-systems), electricity, the data- and communication-infrastructure, the operation of clean-rooms and chemistry labs and air-conditioning as well as cooling systems of the research laboratories.

In der Abteilung Technologie und Transfer sind alle wissenschaftsunterstützenden Aktivitäten des Instituts vereint. Zu diesen zählt die Halbleitertechnologie mit ihrem wissenschaftlichen Leiter Dr. Abbas Tahraoui, die von Jörg Pfeiffer geleitete Haustechnik und feinmechanische Werkstatt, ebenso wie die Personalbetreuung in den Händen des Human Resources Managers Andreas Hartung, der Bereich Einkauf und Finanzen von Kerstin Arnhold und die Drittmittelsachbearbeitung durch Anja Hollmack. Intellectual Property, dessen Sichtung und Sicherung liegt in den Händen von Mercedes Reischel, Kai Hablitzel unterstützt bei allen Fragen im Bereich der EU Forschungsförderung und koordiniert den GraFOx Wissenschaftscampus. Die wissenschaftliche Spezialbibliothek erfährt momentan einen Modernisierungsschub durch die Bibliothekarin Anne Timm. Der Abteilungsleiter ist Verwaltungsleiter des Instituts und koordiniert die administrativen Notwendigkeiten des Forschungsbetriebes mit dem Ziel, wissenschaftsfremde Arbeiten möglichst weitgehend von Forschenden fernzuhalten. Er berät als wissenschaftlich-administrativer Koordinator den Direktor bei der strategischen Forschungsplanung und entwickelt die Wissenstransferaktivitäten des Instituts.

### Haustechnik

Das PDI ist Nutzer eines Gebäudes, das von der Humboldt-Universität verwaltet wird. Während zentrale Dienste (Strom, Heizung, Wasser) durch die HU sichergestellt werden, werden die spezielleren Infrastrukturbedürfnisse eines materialwissenschaftlichen Instituts innerhalb der Abteilung Technologie und Transfer koordiniert.

Dies umfasst neben der Versorgung mit Spezialgasen (wie Helium für temperaturabhängige Experimente und flüssigem

### Semiconductor Technology

Most materials that are grown in the epitaxy department need further processing for subsequent scientific investigations. Our technologists provide structuring on sub-micrometer scales and processes like metallization and contacting, cutting of wafers, pre patterning, cleaning and electrical characterization of processed structures. The semiconductor technology group operates clean rooms with facilities for the whole process of photolithography (mask-design, mask-writing, exposing and developing) which is employed to prepare the samples for subsequent selective metallization or overgrowth (with, e.g., piezoelectric material), wet and dry etching, sputtering and thermal evaporation. The rather limited resolution of photolithography is offset by its high flexibility and extended by electron-beam lithography. Photolithography can be used for rapid prototyping as well as for small series.

The wet chemical etching and the dry etching capabilities are optimized for the materials prepared within the epitaxy department and are constantly developed further.

### Administration

The administration of PDI relies on the backbone of the central administration of Forschungsverbund Berlin e.V. (FVB). All legally binding processes like salaries, work-contracts, purchase-orders, the administration of travel-reimbursement, etc. are administered at FVB. At the institute a small number of specially trained administrative staff provide an interface between research and administration, supervised by the scientific administrative coordinator.

All necessary paperwork related to the job is taken care of and new staff is supported in a way that makes the unavoidable bureaucracy when arriving from a different country bearable. Purchasing and finances and the administration of third-party-funded projects is supported in a way that shields scientists from the intricacies of accounting as much as possible.

Stickstoff für MBE-Systeme), Strom, die Daten- und Kommunikations-Infrastruktur, den Betrieb der Reinräume und Chemielabore und Klima und Gerätekühlung für die Labore.

### Halbleiter-Technologie

Die meisten Materialien, die in der Abteilung Epitaxie gewachsen werden, benötigen eine weitere Prozessierung für anschließende wissenschaftliche Untersuchungen – zum Beispiel Vereinzeln von Wafern, Strukturierungen, Metallisierung und das Überwachsen mit Schichten außerhalb der MBE, elektrische und strukturelle Charakterisierungen, etc. Unsere Technologie ermöglicht laterale Strukturierungen auf der sub-Mikrometer-Skala mittels konventioneller optischer Lithographie und Elektronenstrahlithographie und stellt Verfahren für die Metallisierung, Kontaktierung, das Vereinzeln, Reinigen und einfache elektrische Charakterisierungen zur Verfügung. Die Halbleiter Technologie verfügt über einen Reinraum mit einer Prozessstrecke für Foto- und Elektronenstrahlithographie (vom Maskenentwurf und –schreiben über Belichtung und Entwicklung bis zum Ätzen und Beschichten). Hierbei stehen nasschemische Ätzverfahren und Trockenätzverfahren sowie Sputteranlagen und Anlagen für das thermische Verdampfen von Metallen zur Verfügung.

Die Ätzverfahren werden auf die Materialien angepasst, die in der Abteilung Epitaxie hergestellt werden und werden ständig weiterentwickelt.

### Verwaltung

Die Verwaltung des PDI baut auf die zentrale Verwaltung des Forschungsverbund Berlin e.V. (FVB) auf, dem gemeinsamen Träger von acht Instituten. Alle rechtlich bindenden Prozesse wie die Zahlbarmachung von Gehältern, Arbeitsverträge, Beschaffungsaufträge, die Abrechnung von Dienstreisen etc. werden zentral im FVB durchgeführt. Am Institut werden alle Personalvorgänge vorbereitet und die Mitarbeiterinnen und Mitarbeiter sowie Gäste

This interfacing-approach is set up to free scientist from administrative burden as much as possible while at the same time translating their needs for the professional administration at FVB and reconciling the sometimes complex administrative needs with the reality of rapidly developing research activities, involving strategic changes, unforeseeable developments, and international staff with varying bureaucratic necessities but also the need for practical, personal support.

### **Knowledge Transfer**

The simplistic approach to ask for proof of practicability or usability of research results—especially from institutes doing 'hard' science—is recently being substituted by a deeper understanding of the necessities of transferring knowledge into society. Rather than proving short-term applicability of our research results, our understanding of transfer ranges from informing the public about nanotechnology and materials science at large (involving public relations, developing concepts for science-communication and -visualization), providing expertise to industry, education and politics, to tracing, securing and making available intellectual property—be it in the frame of open source arrangements, licensing or marketing of patents.

The engagement of our technology transfer manager has in recent years led to a considerable professionalization of the transfer activities. Besides the development of transfer-concepts and the definition of internal processes, the idea of technology transfer of PDI is being discussed within Leibniz-Gemeinschaft and in an increasing network of technology transfer professionals. The Head of the Technology and Transfer department is speaker of the workgroup Knowledge transfer of Leibniz-Gemeinschaft and member of the group initiated by the president defining the guidelines for knowledge-transfer.

werden bei allen Fragen zu Verträgen und Aufenthalt persönlich unterstützt. Diese Schnittstellenaktivitäten werden am Institut organisiert, um die Übersetzung zwischen wissenschaftlichen und Wissenschaft-unterstützenden Aktivitäten zu optimieren.

### **Wissenstransfer**

Wissenschaft zum Wohl der Gesellschaft zu betreiben, ist ein Kernpunkt des Selbstverständnisses der Einrichtungen der Leibniz-Gemeinschaft. Dies bedeutet, dass Leibniz-Einrichtungen die Verwendbarkeit ihrer Forschungsergebnisse fördern. Das PDI, dessen Forschung auf fundamentale Fragen der Materialwissenschaften zielt, die künftige Anwendungen beeinflussen, inspirieren oder gar erst ermöglichen, sieht eine wichtige Aufgabe darin, dieses Wissen zum gesellschaftlichen Nutzen zur Verfügung zu stellen.

In der Abteilung Technologie und Transfer werden Kompetenzen und Ressourcen für den Technologietransfer (im Technologietransferbüro durch die Transferbeauftragte) ebenso bereitgestellt wie für den Transfer des Wissens in die Gesellschaft. In der Leibniz-Gemeinschaft wird Transfer disziplinübergreifend verstanden. Die Disziplinspezifika werden schließlich bei der Umsetzung durch die maßgeschneiderten Transferwerkzeuge sichtbar. Das PDI stellt mit dem Leiter der Abteilung Technologie und Transfer den Sprecher des Arbeitskreises Wissenstransfer der Leibniz-Gemeinschaft – der als Mitglied der Präsidiumsgruppe auch das Leibniz Leitbild für Wissenstransfer mitformulierte

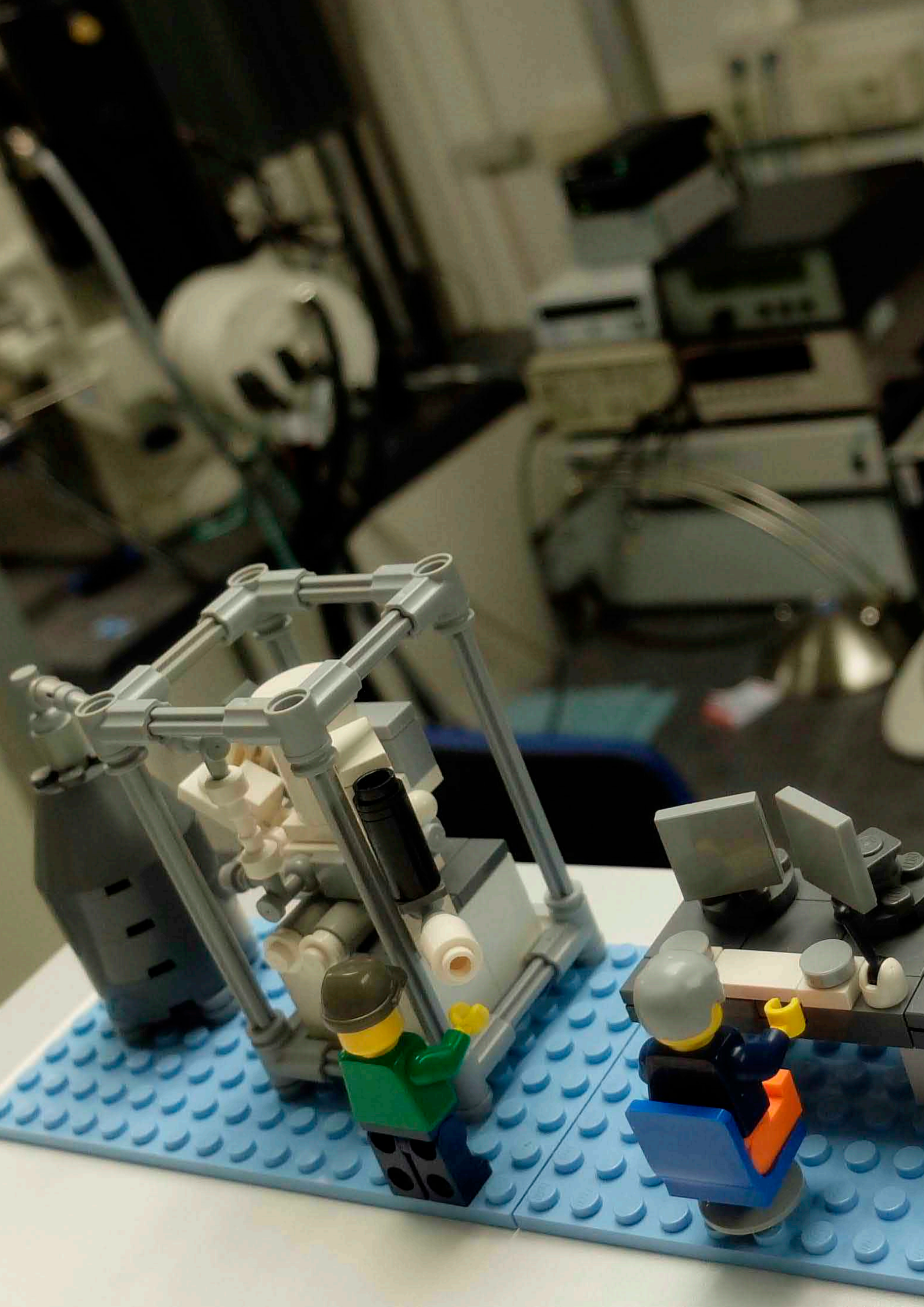


**BERLIN  
SCIENCE  
WEEK**

**1-10  
NOV  
2020**



El futuro  
es de todos



# Facts & Figures

## Zahlen und Fakten

Publications .....	156
Ph.D. Theses .....	162
Master Theses .....	162
Students Working on their Master Thesis .....	162
Seminar of Visitors .....	163
Budget Summary .....	163
Summary of External Funding .....	164
Scientific Staff .....	166
Non-Scientific Staff .....	168

## Facts &amp; Figures / Zahlen und Fakten

## Publications

Aghaeipour, M., L. Kasper, J. Herranz, L. Geelhaar, and J. Bruns,  
Efficient adjustable light couplers of integrated III-V nanowire emitters on silicon waveguides based on ring resonators,  
*Opt. Lett.* **45**, 4702–4705 (2020). DOI: 10.1364/OL.398930

Al Hassan, A., J. Lähnemann, S. Leake, H. Küpers, M. Niehle, D. Bahrami, F. Bertram, R. B. Lewis, A. Davtyan, T. U. Schüllli, L. Geelhaar, and U. Pietsch,  
Spatially-resolved luminescence and crystal structure of single core-shell nanowires measured in the as-grown geometry,  
*Nanotechnol.* **31**, 214002, 7 pages (2020). DOI: 10.1088/1361-6528/ab7590

Al Hassan, A., J. Lähnemann, A. Davtyan, M. Al-Humaidi, J. Herranz, D. Bahrami, T. Anjum, F. Bertram, A. B. Dey, L. Geelhaar, and U. Pietsch,  
Beam damage of single semiconductor nanowires during X-ray nanobeam diffraction experiments,  
*J. Synchrotron. Rad.* **27**, 1200–1208 (2020). DOI: 10.1107/S1600577520009789

Antoniazzi, I., T. Chagas, M. J. S. Matos, L. A. B. Marçal, E. A. Soares, M. S. C. Mazzoni, R. H. Miwa, J. M. J. Lopes, Â. Malachias, R. Magalhães-Paniago, and M. H. Oliveira Jr.,  
Oxygen intercalated graphene on SiC(0001): Multiphase SiO<sub>x</sub> layer formation and its influence on graphene electronic properties,  
*Carbon* **167**, 746–759 (2020). DOI: 10.1016/j.carbon.2020.05.064

Azadmand, M., T. Auzelle, J. Lähnemann, G. H. Gao, L. Nicolai, M. Ramsteiner, A. Trampert, S. Sanguinetti, O. Brandt, and L. Geelhaar,  
Self-assembly of well-separated AlN nanowires directly on sputtered metallic TiN films,  
*Phys. Status Solidi RRL* **14**, 1900615, 5 pages (2020). DOI: 10.1002/pssr.201900615

Bierwagen, O., P. Vogt, and P. Mazzolini,  
Plasma-assisted molecular beam epitaxy 2: Fundamentals of suboxide-related growth kinetics, thermodynamics, catalysis, polymorphs, and faceting,  
in *Gallium Oxide: Materials Properties, Crystal Growth, and Devices*, edited by M. Higashiwaki and S. Fujita, Springer Series in Materials Science Vol. 293, (Springer Nature Switzerland AG, Cham, 2020), pp. 95–121. DOI: 10.1007/978-3-030-37153-1\_6

Bogula, L., L. von Helden, C. Richter, M. Hanke, J. Schwarzkopf, and M. Schmidbauer,  
Ferroelectric phase transitions in multi-domain K<sub>0.9</sub>Na<sub>0.1</sub>NbO<sub>3</sub> epitaxial thin films,  
*Nano Futures* **4**, 035005, 8 pages (2020). DOI: 10.1088/2399-1984/ab9f18

Bragaglia, V., M. Ramsteiner, D. Schick, J. E. Boschker, R. Mitzner, R. Calarco, and K. Holldack,  
Phonon anharmonicities and ultrafast dynamics in epitaxial Sb<sub>2</sub>Te<sub>3</sub>,  
*Sci. Rep.* **10**, 12962, 8 pages (2020). DOI: 10.1038/s41598-020-69663-y

Budde, M., T. Remmele, C. Tschammer, J. Feldl, P. Franz, J. Lähnemann, Z. Z. Cheng, M. Hanke, M. Ramsteiner, M. Albrecht, and O. Bierwagen,  
Plasma-assisted molecular beam epitaxy of NiO on GaN(00.1),  
*J. Appl. Phys.* **127**, 015306, 9 pages (2020). DOI: 10.1063/1.5129881

Budde, M., P. Mazzolini, J. Feldl, C. Golz, T. Nagata, S. Ueda, G. Hoffmann, F. Hatami, W. T. Masselink, M. Ramsteiner, and O. Bierwagen,  
Plasma-assisted molecular beam epitaxy of SnO(001) films: Metastability, hole transport properties, Seebeck coefficient, and effective hole mass,  
*Phys. Rev. Materials* **4**, 124602, 15 pages (2020). DOI: 10.1103/PhysRevMaterials.4.124602

Budde, M., D. Splith, P. Mazzolini, A. Tahraoui, J. Feldl, M. Ramsteiner, H. von Wenckstern, M. Grundmann, and O. Bierwagen,  
SnO/ $\beta$ -Ga<sub>2</sub>O<sub>3</sub> vertical pn heterojunction diodes,  
*Appl. Phys. Lett.* **117**, 252106, 6 pages (2020). DOI: 10.1063/5.0031442

Bühler, D. D., A. Crespo-Poveda, A. Tahraoui, K. Biermann, P. V. Santos, A. Cantarero, and M. M. de Lima Jr.,  
Compact acousto-optic multimode interference device in (Al,Ga)As,  
*Opt. Express* **28**, 35833–35843 (2020). DOI: 10.1364/OE.400400

Calabrese, G., D. van Treeck, V. M. Kaganer, O. Konovalov, P. Corfdir, C. Sinito, L. Geelhaar, O. Brandt, and S. Fernández-Garrido,  
Radius-dependent homogeneous strain in uncoalesced GaN nanowires,  
*Acta Mater.* **195**, 87–97 (2020). DOI: 10.1016/j.actamat.2020.04.045

Casals, B., N. Statuto, M. Foerster, A. Hernández-Mínguez, R. Cicheler, P. Manshausen, A. Mandziak, L. Aballe, J. M. Hernández, and F. Macià,  
Generation and imaging of magnetoacoustic waves over millimeter distances,  
*Phys. Rev. Lett.* **124**, 137202, 6 pages (2020). DOI: 10.1103/PhysRevLett.124.137202

Chafatinos, D. L., A. S. Kuznetsov, S. Anguiano, A. E. Bruchhausen, A. A. Reynoso, K. Biermann, P. V. Santos, and A. Fainstein,  
Polariton-driven phonon laser,  
*Nat. Commun.* **11**, 4552, 8 pages (2020). DOI: 10.1038/s41467-020-18358-z

Czubak, D., S. Gaucher, L. Oppermann, J. Herfort, K. Zollner, J. Fabian, H. T. Grahn, and M. Ramsteiner,  
Electronic and magnetic properties of  $\alpha$ -FeGe<sub>2</sub> films embedded in vertical spin valve devices,  
*Phys. Rev. Materials* **4**, 104415, 6 pages (2020). DOI: 10.1103/PhysRevMaterials.4.104415

D'Arrigo, G., A. M. Mio, J. E. Boschker, A. Meli, S. Cecchi, E. Zallo, A. Sciuto, M. Buscema, E. Bruno, R. Calarco, and E. Rimini,  
Crystallization of nano amorphized regions in thin epitaxial layer of Ge<sub>2</sub>Sb<sub>2</sub>Te<sub>5</sub>,  
*J. Phys. D: Appl. Phys.* **53**, 194001, 8 pages (2020). DOI: 10.1088/1361-6463/ab71ae

Davtyan, A., D. Kriegner, V. Holý, A. Al Hassan, R. B. Lewis, S. McDermott, L. Geelhaar, D. Bahrami, T. Anjum, Z. Ren, C. Richter, D. Novikov, J. Müller, B. Butz, and U. Pietsch,  
X-ray diffraction reveals the amount of strain and homogeneity of extremely bent single nanowires,  
*J. Appl. Crystallogr.* **53**, 1310–1320 (2020). DOI: 10.1107/S1600576720011516

Dimkou, I., A. Harikumar, F. Donatini, J. Lähnemann, M. I. den Hertog, C. Bougerol, E. Bellet-Amalric, N. Mollard, A. Ajay, G. Ledoux, S. T. Purcell, and E. Monroy,  
Assessment of AlGaIn/AlIn superlattices on GaN nanowires as active region of electron-pumped ultraviolet sources,  
*Nanotechnol.* **31**, 204001, 15 pages (2020). DOI: 10.1088/1361-6528/ab704d

Feenstra, R. M., G. R. Frazier, Y. Pan, S. Fölsch, Y.-C. Lin, B. Jariwala, K. H. Zhang, and J. A. Robinson,  
Acquisition and analysis of scanning tunneling spectroscopy data—WSe<sub>2</sub> monolayer,  
*J. Vac. Sci. Technol. A* **39**, 011001, 14 pages (2021), published online 23 December, 2020.  
DOI: 10.1116/6.0000684

Feijó, T. O., G. Copetti, E. R. Figini Gerling, M. Hanke, J. M. J. Lopes, C. Radtke, and G. V. Soares, The role of substrate on the growth of 2D heterostructures by CVD, *Appl. Surf. Sci.* **539**, 148226, 7 pages (2021), published online 21 October, 2020. DOI: 10.1016/j.apsusc.2020.148226

Feldl, J., M. Budde, C. Tschammer, O. Bierwagen, and M. Ramsteiner, Magnetic characteristics of epitaxial NiO films studied by Raman spectroscopy, *J. Appl. Phys.* **127**, 235105, 6 pages (2020). DOI: 10.1063/5.0006085

Fernández-Garrido, S., C. Pisador, J. Lähnemann, S. Lazić, A. Ruiz, and A. Redondo-Cubero, Coalescence, crystallographic orientation and luminescence of ZnO nanowires grown on Si(001) by chemical vapour transport, *Nanotechnol.* **31**, 475603, 11 pages (2020). DOI: 10.1088/1361-6528/abadc8

Fiedler, A., M. Ramsteiner, Z. Galazka, and K. Irmscher, Raman scattering in heavily donor doped  $\beta$ -Ga<sub>2</sub>O<sub>3</sub>, *Appl. Phys. Lett.* **117**, 152107, 5 pages (2020). DOI: 10.1063/5.0024494

Flores-Rangel, G., L. F. Lastras-Martínez, R. Castro-García, O. Ruiz-Cigarrillo, R. E. Balderas-Navarro, L. D. Espinosa-Cuellar, A. Lastras-Martínez, and J. M. J. Lopes, Optical contrast in the near-field limit for structural characterization of graphene nanoribbons, *Appl. Surf. Sci.* **536**, 147710, 5 pages (2021), published online 10 September, 2020. DOI: 10.1016/j.apsusc.2020.147710

Freudenfeld, J., M. Geier, V. Umansky, P. W. Brouwer, and S. Ludwig, Coherent electron optics with ballistically coupled quantum point contacts, *Phys. Rev. Lett.* **125**, 107701, 6 pages (2020). DOI: 10.1103/PhysRevLett.125.107701

Geier, M., J. Freudenfeld, J. T. Silva, V. Umansky, D. Reuter, A. D. Wieck, P. W. Brouwer, and S. Ludwig, Electrostatic potential shape of gate-defined quantum point contacts, *Phys. Rev. B* **101**, 165429, 8 pages (2020). DOI: 10.1103/PhysRevB.101.165429

Ghalgaoui, A., K. Reimann, M. Woerner, T. Elsaesser, C. Flytzanis, and K. Biermann, Frequency upshift of the transverse optical phonon resonance in GaAs by femtosecond electron-hole excitation, *Phys. Rev. Lett.* **125**, 027401, 5 pages (2020). DOI: 10.1103/PhysRevLett.125.027401

He, Y. M., P. Y. Tang, Z. L. Hu, Q. Y. He, C. Zhu, L. Q. Wang, Q. S. Zeng, P. Golani, G. H. Gao, W. Fu, Z. Q. Huang, C. T. Gao, J. Xia, X. L. Wang, X. W. Wang, C. Zhu, Q. M. Ramasse, A. Zhang, B. X. An, Y. Z. Zhang, S. Martí-Sánchez, J. R. Morante, L. Wang, B. K. Tay, B. I. Yakobson, A. Trampert, H. Zhang, M. H. Wu, Q. J. Wang, J. Arbiol, and Z. Liu, Engineering grain boundaries at the 2D limit for the hydrogen evolution reaction, *Nat. Commun.* **11**, 57, 12 pages (2020). DOI: 10.1038/s41467-019-13631-2

Heilmann, M., A. S. Prikhodko, M. Hanke, A. Sabelfeld, N. I. Borgardt, and J. M. J. Lopes, Influence of proximity to supporting substrate on van der Waals epitaxy of atomically thin graphene/hexagonal boron nitride heterostructures, *ACS Appl. Mater. Interfaces* **12**, 8897–8907 (2020). DOI: 10.1021/acsami.9b21490

Hernández-Mínguez, A., A. V. Poshakinskiy, M. Hollenbach, P. V. Santos, and G. V. Astakhov, Anisotropic spin-acoustic resonance in silicon carbide at room temperature, *Phys. Rev. Lett.* **125**, 107702, 6 pages (2020). DOI: 10.1103/PhysRevLett.125.107702

Hernández-Mínguez, A., F. Macià, J. M. Hernández, J. Herfort, and P. V. Santos, Large non-reciprocal propagation of surface acoustic waves in epitaxial ferromagnetic/semiconductor hybrid structures, *Phys. Rev. Applied* **13**, 044018, 14 pages (2020). DOI: 10.1103/PhysRevApplied.13.044018

Hoffmann, G., M. Budde, P. Mazzolini, and O. Bierwagen,  
Efficient suboxide sources in oxide molecular beam epitaxy using mixed metal + oxide charges:  
The examples of SnO and Ga<sub>2</sub>O,  
APL Mater. **8**, 031110, 10 pages (2020). DOI: 10.1063/1.5134444

Hübers, H.-W., H. Richter, M. Wienold, X. Lü, L. Schrottke, and H. T. Grahn,  
Terahertz spectroscopy using quantum-cascade lasers,  
Photoniques **101**, 27–32 (2020). DOI: 10.1051/photon/202010127

Hubert, C., K. Cohen, A. Ghazaryan, M. Lemesko, R. Rapaport, and P. V. Santos,  
Attractive interactions, molecular complexes, and polarons in coupled dipolar exciton fluids,  
Phys. Rev. B **102**, 045307, 12 pages (2020). DOI: 10.1103/PhysRevB.102.045307

Jaloustre, L., S. Le Denmat, T. Auzelle, M. Azadmand, L. Geelhaar, F. Dahlem, and R. Songmuang,  
Toward quantitative measurements of piezoelectricity in III-N semiconductor nanowires,  
ACS Appl. Nano Mater. **4**, 43–52 (2021), published online 29 December, 2020.  
DOI: 10.1021/acsanm.0c02078

Kaganer, V. M., I. Petrov, and L. Samoylova,  
X-ray diffraction from strongly bent crystals and spectroscopy of X-ray free-electron laser pulses,  
Acta Cryst. A **76**, 55–69 (2020). DOI: 10.1107/S2053273319014347

Kamimura, J., M. Budde, P. Bogdanoff, C. Tschammer, F. F. Abdi, R. van de Krol, O. Bierwagen,  
H. Riechert, and L. Geelhaar,  
Protection mechanism against photocorrosion of GaN photoanodes provided by NiO thin layers,  
Sol. RRL **4**, 2000568, 5 pages (2020). DOI: 10.1002/solr.202000568

Karim, M., J. M. J. Lopes, and M. Ramsteiner,  
The impact of ultraviolet laser excitation during Raman spectroscopy of hexagonal boron nitride  
thin films,  
J. Raman Spectrosc. **51**, 2468–2477 (2020). DOI: 10.1002/jrs.6007

Kuşdemir, E., C. Chèze, and R. Calarco,  
Influence of Mg doping on In adsorption and In incorporation in (In,Ga)N superlattices,  
J. Appl. Phys. **128**, 085303, 9 pages (2020). DOI: 10.1063/5.0017520

Kuznetsov, A. S., K. Biermann, and P. V. Santos,  
Acoustically triggered optical memories,  
ACS Photonics **7**, 3071–3077 (2020). DOI: 10.1021/acsp Photonics.0c01143

Kuznetsov, A. S., G. Dagvadorj, K. Biermann, M. H. Szymanska, and P. V. Santos,  
Dynamically tuned arrays of polariton parametric oscillators,  
Optica **7**, 1673–1681 (2020). DOI: 10.1364/OPTICA.399747

Mazzolini, P., A. Falkenstein, C. Wouters, R. Schewski, T. Markurt, Z. Galazka, M. Martin, M. Albrecht,  
and O. Bierwagen,  
Substrate-orientation dependence of  $\beta$ -Ga<sub>2</sub>O<sub>3</sub> (100), (010), (001), and  $\bar{2}01$  homoepitaxy  
by indium-mediated metal-exchange catalyzed molecular beam epitaxy (MEXCAT-MBE),  
APL Mater. **8**, 011107, 10 pages (2020). DOI: 10.1063/1.5135772

Mazzolini, P., and O. Bierwagen,  
Towards smooth (010)  $\beta$ -Ga<sub>2</sub>O<sub>3</sub> films homoepitaxially grown by plasma assisted molecular  
beam epitaxy: The impact of substrate offset and metal-to-oxygen flux ratio,  
J. Phys. D: Appl. Phys. **53**, 354003, 9 pages (2020). DOI: 10.1088/1361-6463/ab8eda

- Mazzolini, P., A. Falkenstein, Z. Galazka, M. Martin, and O. Bierwagen, Offcut-related step-flow and growth rate enhancement during (100)  $\beta$ -Ga<sub>2</sub>O<sub>3</sub> homoepitaxy by metal-exchange catalyzed molecular beam epitaxy (MEXCAT-MBE), *Appl. Phys. Lett.* **117**, 222105, 6 pages (2020). DOI: 10.1063/5.0031300
- Mio, A. M., S. M. S. Privitera, M. Zimbone, V. Bragaglia, S. Jacobs, C. Persch, F. Arciprete, R. Calarco, M. Wuttig, and E. Rimini, Disorder process of GeSb<sub>2</sub>Te<sub>4</sub> induced by ion irradiation, *J. Phys. D: Appl. Phys.* **53**, 134001, 9 pages (2020). DOI: 10.1088/1361-6463/ab642d
- Msall, M. E., and P. V. Santos, Focusing surface-acoustic-wave microcavities on GaAs, *Phys. Rev. Applied* **13**, 014037, 6 pages (2020). DOI: 10.1103/PhysRevApplied.13.014037
- Niavol, S. S., M. Budde, A. Papadogianni, M. Heilmann, H. M. Moghaddam, C. M. Aldao, G. Ligorio, E. J. W. List-Kratochvil, J. M. J. Lopes, N. Barsan, O. Bierwagen, and F. Schipani, Conduction mechanisms in epitaxial NiO/graphene gas sensors, *Sens. Actuators B Chem.* **325**, 128797, 10 pages (2020). DOI: 10.1016/j.snb.2020.128797
- Papadogianni, A., J. Rombach, T. Berthold, V. Polyakov, S. Krischok, M. Himmerlich, and O. Bierwagen, Two-dimensional electron gas of the In<sub>2</sub>O<sub>3</sub> surface: Enhanced thermopower, electrical transport properties, and reduction by adsorbates or compensating acceptor doping, *Phys. Rev. B* **102**, 075301, 10 pages (2020). DOI: 10.1103/PhysRevB.102.075301
- Reszka, A., K. P. Korona, S. Tiagulskiy, H. Turski, U. Jahn, S. Kret, R. Bożek, M. Sobanska, Z. R. Zykiewicz, and B. J. Kowalski, Influence of growth polarity switching on the optical and electrical properties of GaN/AlGaIn nanowire LEDs, *Electronics* **10**, 45, 20 pages (2021), published online 29 December, 2020. DOI: 10.3390/electronics10010045
- Röben, B., X. Lü, K. Biermann, L. Schrottke, and H. T. Grahn, Effective group dispersion of terahertz quantum-cascade lasers, *J. Phys. D: Appl. Phys.* **54**, 025110, 10 pages (2021). DOI: 10.1088/1361-6463/abbde3
- Rogowicz, E., W. M. Linhart, M. Syperek, J. Kopaczek, O. Delorme, L. Cerutti, E. Luna, E. Tournié, J.-B. Rodriguez, and R. Kudrawiec, Optical properties and dynamics of excitons in Ga(Sb,Bi)/GaSb quantum wells: Evidence for a regular alloy behavior, *Semicond. Sci. Technol.* **35**, 025024, 6 pages (2020). DOI: 10.1088/1361-6641/ab6017
- Ruhstorfer, D., S. Mejia, M. Ramsteiner, M. Döblinger, H. Riedl, J. J. Finley, and G. Koblmüller, Demonstration of n-type behavior in catalyst-free Si-doped GaAs nanowires grown by molecular beam epitaxy, *Appl. Phys. Lett.* **116**, 052101, 5 pages (2020). DOI: 10.1063/1.5134687
- Schmidbauer, M., L. Bogula, B. Wang, M. Hanke, L. von Helden, A. Ladera, J.-J. Wang, L.-Q. Chen, and J. Schwarzkopf, Temperature dependence of three-dimensional domain wall arrangement in ferroelectric K<sub>0.9</sub>Na<sub>0.1</sub>NbO<sub>3</sub> epitaxial thin films, *J. Appl. Phys.* **128**, 184101, 9 pages (2020). DOI: 10.1063/5.0029167
- Swallow, J. E. N., C. Vorwerk, P. Mazzolini, P. Vogt, O. Bierwagen, A. Karg, M. Eickhoff, J. Schörmann, M. R. Wagner, J. W. Roberts, P. R. Chalker, M. J. Smiles, P. Murgatroyd, S. A. Razek, Z. W. Lebens-Higgins, L. F. J. Piper, L. A. H. Jones, P. K. Thakur, T.-L. Lee, J. B. Varley, J. Furthmüller, C. Draxl, T. D. Veal, and A. Regoutz, Influence of polymorphism on the electronic structure of Ga<sub>2</sub>O<sub>3</sub>, *Chem. Mater.* **32**, 8460–8470 (2020). DOI: 10.1021/acs.chemmater.0c02465



Takagaki, Y.,  
Effects of disorder on magnetotransport oscillations in a two-dimensional electron gas terminated by superconductors,  
J. Appl. Phys. **128**, 024304, 10 pages (2020). DOI: 10.1063/5.0005384

Takagaki, Y., B. Jenichen, M. Ramsteiner, and J. Herfort,  
Dependence of interfacial resistance switching on transition metal constituent M = Cu, Ag and Ni for chalcogenides Bi-M-S,  
J. Alloy Compd. **858**, 157709, 11 pages (2021), published online 27 October, 2020.  
DOI: 10.1016/j.jallcom.2020.157709

Takagaki, Y., B. Jenichen, M. Ramsteiner, and A. Trampert,  
Interfacial resistance switching characteristics in metal-chalcogenide junctions using Bi-Cu-Se, Bi-Ag-Se, and Sb-Cu-Te alloys,  
J. Alloy Compd. **824**, 153880, 12 pages (2020). DOI: 10.1016/j.jallcom.2020.153880

Tisbi, E., E. Placidi, R. Magri, P. Proposito, R. Francini, A. Zaganelli, S. Cecchi, E. Zallo, R. Calarco, E. Luna, J. Honolka, M. Vondráček, S. Colonna, and F. Arciprete,  
Increasing optical efficiency in the telecommunication bands of strain-engineered Ga(As,Bi) alloys,  
Phys. Rev. Applied **14**, 014028, 14 pages (2020). DOI: 10.1103/PhysRevApplied.14.014028

van Treeck, D., S. Fernández-Garrido, and L. Geelhaar,  
Influence of the source arrangement on shell growth around GaN nanowires in molecular beam epitaxy,  
Phys. Rev. Mater. **4**, 013404, 13 pages (2020). DOI: 10.1103/PhysRevMaterials.4.013404

von Boehn, B., M. Foerster, M. von Boehn, J. Prat, F. Macià, B. Casals, M. W. Khaliq, A. Hernández-Mínguez, L. Aballe, and R. Imbihl,  
On the promotion of catalytic reactions by surface acoustic waves,  
Angew. Chem. Int. Ed. **59**, 20224–20229 (2020). DOI: 10.1002/anie.202005883

Waters, D., Y. F. Nie, F. Lüpke, Y. Pan, S. Fölsch, Y.-C. Lin, B. Jariwala, K. H. Zhang, C. Wang, H. Y. Lv, K. J. Cho, D. Xiao, J. A. Robinson, and R. M. Feenstra,  
Flat bands and mechanical deformation effects in the Moiré superlattice of MoS<sub>2</sub>-WSe<sub>2</sub> heterobilayers,  
ACS Nano **14**, 7564–7573 (2020). DOI: 10.1021/acsnano.0c03414

Zallo, E., D. Dragoni, Y. Zaytseva, S. Cecchi, N. I. Borgardt, M. Bernasconi, and R. Calarco,  
Evolution of low-frequency vibrational modes in ultrathin GeSbTe films,  
Phys. Status Solidi RRL **15**, 2000434, 7 pages (2021), published online 19 November, 2020.  
DOI: 10.1002/pssr.202000434

Zhao, Y. K., Z. W. Xing, L. Geelhaar, J. Y. Zhang, W. X. Yang, T. Auzelle, Y. Y. Wu, L. F. Bian, and S. L. Lu,  
Detaching (In,Ga)N nanowire films for devices requiring high flexibility and transmittance,  
ACS Appl. Nano Mater. **3**, 9943–9950 (2020). DOI: 10.1021/acsnam.0c01970

### Ph. D. Theses

Ernst, Torsten  
Growth of (In, Ga)N/GaN short period superlattices using substrate strain engineering  
Humboldt-Universität zu Berlin, November 2020

Budde, Melanie  
Heteroepitaxy, surface- and bulk hole transport, and application of the p-type semiconducting oxides NiO and SnO  
Humboldt-Universität zu Berlin, December 2020

### Master Theses

Winkler, Daniel  
Effects of plasma nitridation on boron intercalated epitaxial graphene  
Technische Universität Berlin, January 2020

Nevkrytyh, Ekaterina  
Quantitative Raster-Transmissionselektronenmikroskopie und energiedispersive Röntgenspektroskopie von Halbleiter-Nanostrukturen  
Technische Universität Berlin, July 2020

Góra, Michał  
Quantitative investigation of the quantum efficiency of core/shell GaAs/(In,Ga)As nanowires for infrared light emission in the telecommunication range  
Humboldt-Universität zu Berlin, September 2020

### Bachelor Thesis

Oppermann, Lars  
Magnetische Eigenschaften von FeGe<sub>2</sub> enthaltende epitaktischen Mehrschichtsystemen  
Humboldt-Universität zu Berlin, March 2020

### Students Working on their Master Thesis

Castro Martínez, Aron Ernesto  
Humboldt-Universität zu Berlin

Graser, Karl  
Humboldt-Universität zu Berlin

Isceri, Stefania  
Politecnico di Milano

Litschauer, Maximilian  
Humboldt-Universität zu Berlin

Pudelski, Maximilian  
Humboldt-Universität zu Berlin

## Seminars of Visitors

19.02.2020

**Institute Seminar:** "More than a pretty picture – electron microscopy beyond imaging..."

Speaker: Dr. Hannah C. Nerl, Fritz Haber Institute of the Max Planck Society, Berlin

02.03.2020

**Institute Seminar:** "Picosecond acoustics in nanostructures with phase transitions"

Picosecond packets of acoustical phonons carry dynamical strain with amplitudes reaching ~1%. Such pulses are the foundational tool for developing acoustic nanoscopy, and also provide a unique mean for manipulating various properties of nanostructures at picosecond time scale. Here we report on our...

Speaker: Dr. Alexandra Kalashnikova, Ferroics Physics Laboratory, Ioffe Institute, St. Petersburg, Russia

## Budget Summary

Fiscal year	2019	2020
	k€	k€
<b>Revenues</b>		
Allocations	9,305.6	9,257.5
Earnings	21.2	42.3
<b>Sum</b>	<b>9,326.8</b>	<b>9,299.8</b>
<b>Expenditures</b>		
Staff	5,599.8	5,385.3
Administrative expenses	2,708.6	2,534.2
Equipment investment funds	1,018.4	1,380.3
<b>Sum</b>	<b>9,326.8</b>	<b>9,299.8</b>
<b>External funding through projects</b>		
Granted funds	2,643.2*	2,005.8*
Spent funds	1,599.7	862.4

\* including residual funds from the previous year

Summary of External Funding

Agency	Period	Title	Project leader
BMBF	15.04.2018 – 31.01.2021	Monolithically integrated laser made from III-V nanowires for silicon photonics (MILAS)	Dr. Lutz Geelhaar
BMBF	01.06.2018 – 31.03.2022	InterPOL - Verbundprojekt: Polariton lattices: a solid-state platform for quantum simulations of correlated and topological states - Teilvorhaben: Development of polariton lattices with correlated and topological states for quantum simulation	Dr. Paulo V. Santos
EFRE	01.08.2016– 31.07.2021	Application laboratory electron tomography	Dr. Achim Trampert
DFG	01.07.2016– 30.09.2020	Manipulation of single electrons and single excitons by surface acoustic waves	Dr. Paulo V. Santos
DFG	01.12.2015– 31.12.2023	Quantum Hall based Aharonov-Bohm spectroscopy: electron-electron interaction in non-linear magnetotransport	PD Dr. Stefan Ludwig
DFG	01.05.2017- 30.09.2021	Nonequilibrium phenomena and interactions in ultra-pure III-V nanowires	PD Dr. Stefan Ludwig
DFG	01.09.2017- 29.02.2020	Manipulation and spectroscopy of quantum structures on semiconductor surfaces by cryogenic scanning tunneling microscopy	Dr. Stefan Fölsch
DFG	01.03.2018 – 31.05.2021	Coherent acousto-optical interactions in structured polariton microcavities	Dr. Alexander Kuznetsov
DFG	01.10.2018 – 30.09.2021	Coherent acousto-optical interactions in structured polariton microcavities	Dr. Paulo V. Santos
DFG	01.11.2018 – 31.10.2021	Controlling Electron-Phonon Interaction in Nanocircuits – Strong Coupling Regime	PD Dr. Stefan Ludwig
DFG	01.04.2019 – 31.03.2022	Controlling Electron-Phonon Interaction in Nanocircuits – Strong Coupling Regime	Dr. Paulo V. Santos
DFG	01.05.2019 – 30.04.2022	Far-infrared magneto-spectroscopy of novel semiconductor materials in megagauss magnetic fields using quantum-cascade lasers	Prof. Dr. Holger T. Grahn
DFG	01.06.2020 – 31.05.2023	Artificial quantum states on semiconductor surfaces created and probed by cryogenic scanning tunneling microscopy	Dr. Stefan Fölsch
ESA/ DLR	12.02.2019 – 30.09.2021	Frequency stabilization of a Quantum Cascade Laser for Supra-THz applications	Prof. Dr. Holger T. Grahn
EU	01.01.2019 – 30.06.2022	BeforeHand – Boosting Performance of Phase Change Devices by Hetero- and Nano-Structure Material Design	Dr. Stefano Cecchi

WGL (SAW)	01.04.2018 – 31.12.2021	Barium stannate based heterostructures for electronic applications (BaSTet)	Dr. Oliver Bierwagen
WGL (SAW)	01.06.2018 – 31.12.2021	Terahertz detection of atoms in plasma processes (TERAPLAS)	Prof. Dr. Holger T. Grahn
WGL (SAS)	01.07.2016– 30.06.2020	Growth and fundamentals of oxides for electronic applications (GraFOx)	Dr. Oliver Bierwagen
WGL (SAS)	01.07.2020 – 30.06.2024	Growth and fundamentals of oxides for electronic applications (GraFOx II)	Dr. Oliver Bierwagen

## Staff

(December 31, 2020)

**Scientific Staff:**

including Ph. D. students (D) and externally funded personnel (P)

Ashurbekov, Nazim (D, P)	Radio-frequency phonon resonators for coherent electron-phonon coupling
Auzelle, Thomas	Epitaxy of group-III nitride nanowires and related applications
Ayuso Pérez, Irene (D, P)	Quantum transport in nanowires
Biermann, Klaus	Molecular beam epitaxy of GaAs-based advanced heterostructures
Bierwagen, Oliver	Molecular beam epitaxy of oxides
Brandt, Oliver	Group-III nitrides and semiconductor nanowires
Cecchi, Stefano (P)	Epitaxy of phase change materials and group-IV-Te two-dimensional materials
Crespo Poveda, Antonio (P)	Polariton lattices as a solid-state platform for quantum simulations of correlated and topological states
Czubak, Dietmar (D)	Spin transport in vertical spin valve structures based on ferromagnet-semiconductor hybrid structures
Dinh, Duc Van	Growth of h-BN thin films
Feldl, Johannes (D, P)	Optical spectroscopy of semiconducting oxides, in particular perovskites and sesquioxides
Flissikowski, Timur	Ultrafast dynamics of semiconductor structures
Fölsch, Stefan	Low-temperature scanning tunneling microscopy and spectroscopy
Geelhaar, Lutz	Molecular beam epitaxy and semiconductor nanowires
Gómez Ruiz, Mikel (D)	Cathodoluminescence spectroscopy and correlated chemical and structural analysis of core/shell nanowires
Grahn, Holger	Optical and electrical properties of semiconductor nanostructures
Hanke, Michael	Synchrotron x-ray diffraction
Hellemann, Jan (D)	Electron-phonon interaction in nanostructures
Herfort, Jens	Ferromagnet-semiconductor heterostructures
Hernández Mínguez, Alberto	Manipulation of optical and electronic properties of low-dimensional structures using surface acoustic waves
Herranz Zamorano, Jesús (P)	Devices based on group-III arsenide nanowires
Hoffmann, Georg (D, P)	Growth and doping of BaSnO <sub>3</sub> and LaInO <sub>3</sub>
Hucho, Carsten	Technology and transfer
Jordão Lopes, João Marcelo	Epitaxy of two-dimensional materials
Kaganer, Vladimir	Theories of molecular-beam-epitaxial growth and x-ray scattering
Kurlov, Sergii (P)	Terahertz quantum-cascade lasers for far-infrared magneto spectroscopy in pulsed megagauss magnetic fields

Kuznetsov, Alexander (P)	Microcavity exciton-polaritons in artificial potential landscapes
Lähnemann, Jonas	Spatially resolved optical spectroscopy and structural as well as compositional analysis of nanostructures
Lü, Xiang (P)	Terahertz quantum-cascade lasers
Ludwig, Stefan	Quantum transport in nanoelectronic systems
Luna Garcia de la Infanta, Esperanza	Transmission electron microscopy of heterointerfaces
Nevkrytyh, Ekaterina (D, P)	Multi-scale electron tomography of interfaces.
Nicolai, Lars (D, P)	Spectroscopic electron tomography and microscopy of nanomaterials
Oliva, Miriam (D)	Photoluminescence spectroscopy of ordered nanowire arrays
Papadogianni, Alexandra (D)	(In <sub>1-x</sub> Ga <sub>x</sub> ) <sub>2</sub> O <sub>3</sub> based gas sensors
Pham, Van Dong (P)	Atom manipulation on III-V semiconductors by low-temperature scanning tunneling microscopy
Ramsteiner, Manfred	Electronic, vibrational, and magnetic properties of semiconductors
Reis, Anna (D, P)	In-situ x-ray scattering study of surface and interface dynamics at growing crystalline layers
Röben, Benjamin	Terahertz quantum-cascade-lasers for spectroscopic applications
Santos, Paulo	Acoustic, optic, and magnetic properties of nanostructures
Schrottke, Lutz	Quantum-cascade lasers and optical properties of heterostructures
Sirt, Serkan (D, P)	Interplay between the quantum Hall and Aharonov-Bohm effects in mesoscopic circuits
Tahraoui, Abbas	Comprehensive semiconductor technology
Takagaki, Yukihiko	Electric properties of nanometer-scale materials
Terker, Markus (D)	In-situ transmission electron microscopy on semiconductor interfaces and defect structures
Trampert, Achim	Microstructure and electron microscopy
Yuan, Mingyun	Manipulation of single excitons by surface acoustic waves

**Non-Scientific Staff**

Anders, Walid	Technology
Arnhold, Kerstin	Finances/Purchasing
Baumann, René	Workshop
Behnke, Steffen	Technician
Bluhm, Anne-Kathrin	Technician
Ehrensack, Kerstin	Technician
Ferber, Thomas	Workshop
Hablizel, Kai (P)	European and National Grant Management and Equal Opportunities Officer
Hartung, Andreas	Human Resources and Travel Management
Heinitz, Sebastian	Electrician
Herrmann, Claudia	Technician
Holldack, Anja	Third Party Funding
Krauß, Sabine	Technician and Chairwoman Works Council
Matzeck, Christopher	Technician
Matzeck, Margarita	Technician
Meister, Sebastian	Technology
Morgenroth, Katrin	Technician
Pakulat, Bernd	Head of IT and Data Protection Officer
Pfeiffer, Astrid	Technician
Pfeiffer, Jörg	Head of Workshop
Rauwerdink, Sander	Technology
Reischel, Mercedes	Transfer Management
Riedel, Angela	Technician
Schönherr, Hans-Peter	Technician
Seidel, Werner	Technology
Sieg, Michael	Workshop
Steffen, Doreen	Technician
Stemmler, Carsten	Technician
Suchilina, Ekaterina	Office Assistant
Timm, Anne Susanne	Library
Venohr, Thomas	Workshop
Wirsig, Arno	Technology
Wirt-Brunnckow, Andreas	IT







# Contact Kontakt



## DIRECTORATE

**Dr. Lutz Geelhaar**

Acting Director  
phone: +49 30 20377-359  
fax: +49 30 20377-201  
geelhaar@pdi-berlin.de

**Dr. Carsten Hucho**

Scientific-Administrative Coordinator  
phone: +49 30 20377-234  
hucho@pdi-berlin.de

**Ekaterina Suchilina**

Office  
phone: +49 30 20377-481  
suchilina@pdi-berlin.de

## PUBLIC RELATIONS

**Dr. Carsten Hucho**

phone: +49 30 20377-234  
fax: +49 30 20377-515  
hucho@pdi-berlin.de

## GENDER EQUALITY OFFICER

**Kai Hablitzel**

phone: +49 30 20377-342  
fax: +49 30 20377-515  
hablitzel@pdi-berlin.de

## TRANSFER

**Mercedes Reischel**

Technology Transfer Manager  
phone: +49 30 20377-289  
fax: +49 30 20377-515  
reischel@pdi-berlin.de

## ADMINISTRATION

**Kerstin Arnhold**

Purchasing/Finances  
phone: +49 30 20377-358  
fax: +49 30 20377-425  
arnhold@pdi-berlin.de

**Andreas Hartung**

Human Resources  
phone: +49 30 20377-475  
hartung@pdi-berlin.de

**Anja Holldack**

Third-party funding  
phone: +49 30 20377-352  
holldack@pdi-berlin.de

## CHAIR OF WORK COUNCIL

**Sabine Krauß**

phone: +49 30 20377-258  
sabine.krauss@pdi-berlin.de

## SPEAKER OF SCIENTISTS

**Dr. Oliver Bierwagen**

phone: +49 30 20377-491  
bierwagen@pdi-berlin.de

## OMBUDSPERSON

**Dr. Oliver Brandt**

phone: +49 30 20377-332  
brandt@pdi-berlin.de

## DEPARTMENTS

**Dr. Lutz Geelhaar**

Head of Department Epitaxy  
phone: +49 30 20377-359  
fax: +49 30 20377-201  
geelhaar@pdi-berlin.de

**Dr. Achim Trampert**

Head of Department Microstructure  
phone: +49 30 20377-280  
fax: +49 30 20377-201  
trampert@pdi-berlin.de

**Prof. Dr. Holger T. Grahn**

Head of Department Semiconductor Spectroscopy  
phone: +49 30 20377-318  
fax: +49 30 20377-301  
htgrahn@pdi-berlin.de

**Dr. Carsten Hucho**

Head of Department Technology and Transfer  
phone: +49 30 20377-234  
fax: +49 30 20377-515  
hucho@pdi-berlin.de



# Imprint Impressum



LIST  
340

MIR 701

AR-P 669.04  
0.22  
0.31 / 2.000 g

# Imprint Impressum

Paul-Drude-Institut für Festkörperelektronik,  
Leibniz-Institut im Forschungsverbund Berlin e.V.

Hausvogteiplatz 5–7  
10117 Berlin  
Germany

Tel. +49 30 20377-481  
Fax +49 30 20377-515  
info@pdi-berlin.de

PUBLISHED BY / HERAUSGEGEBEN VOM  
Paul-Drude-Institut für Festkörperelektronik, 2021

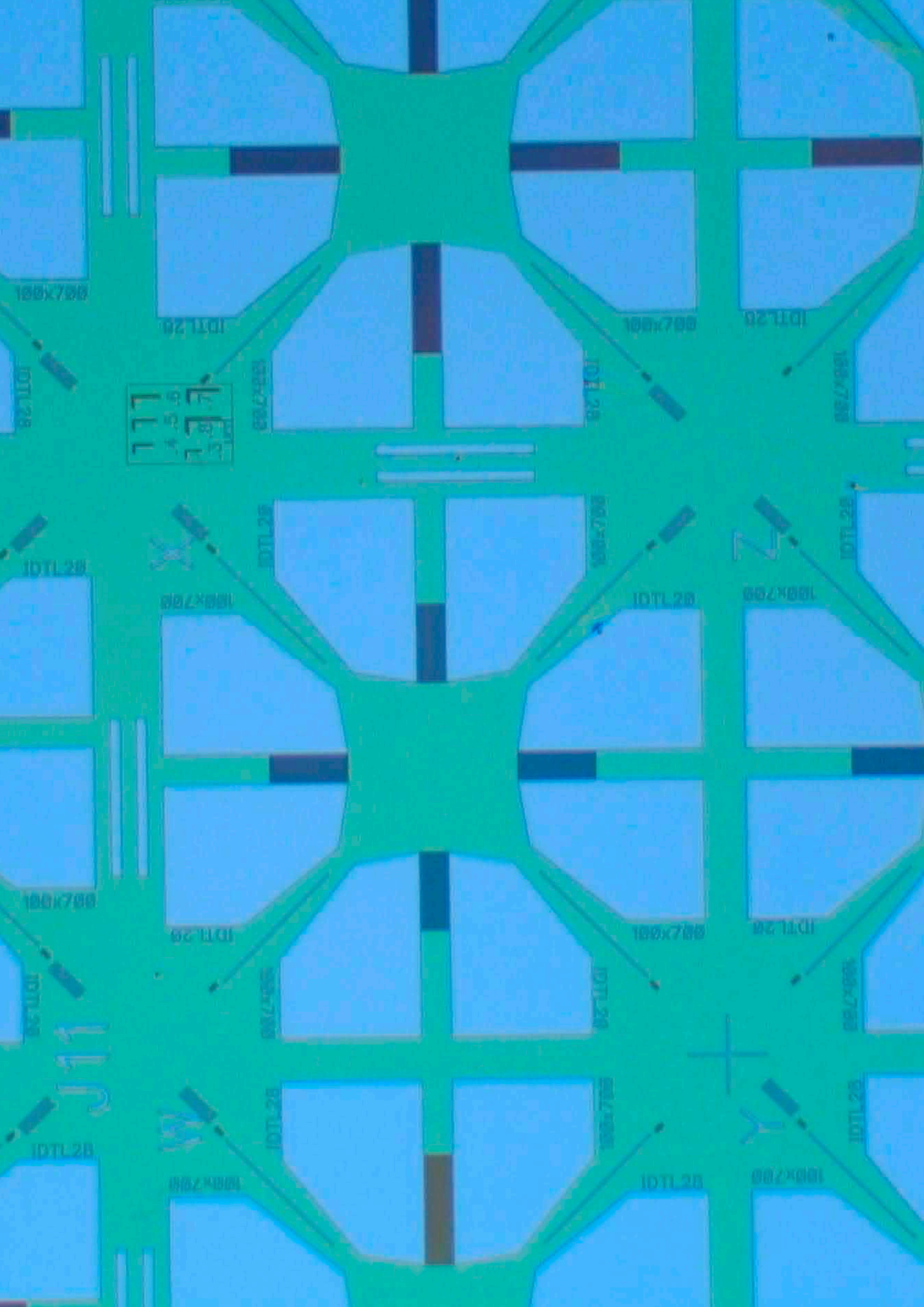
DESIGN / GESTALTUNG  
unicom-berlin.de

#### PHOTOS / FOTOS

S. 5 Ekaterina Suchilina; S. 8–9 Dr. Oliver Bierwagen; S. 10–11 Sander Rauwerdink;  
S. 19 Dr. Oliver Bierwagen; S. 27 Dr. Oliver Bierwagen; S. 35 Ekaterina Suchilina;  
S. 36–37 Sander Rauwerdink; S. 38 Ekaterina Suchilina; S. 49 Sander Rauwerdink;  
S. 64–65 Sander Rauwerdink; S. 130–131 Sander Rauwerdink;  
S. 153 Estefanía González (Botschaft von Kolumbien in Deutschland);  
S. 154–155 Dr. Jonas Lähnemann;  
S. 170–171 Estefanía González (Botschaft von Kolumbien in Deutschland) ;  
S. 174–175 Sander Rauwerdink; S. 177 Sander Rauwerdink

[www.pdi-berlin.de](http://www.pdi-berlin.de)





188x798

IDTL 28

188x798

IDTL 28

IDTL 28



887x981

IDTL 28

188x798

IDTL 28

IDTL 28

188x798

IDTL 28

188x798

IDTL 28

188x798

188x798

IDTL 29

188x798

IDTL 28

IDTL 28

188x798

IDTL 28

887x981

J11

IDTL 28

IDTL 28

188x798

IDTL 28

188x798

IDTL 28

188x798





Scientists and administrative staff experience phases of extreme stress at their workplace. The final stage of a dissertation, preparations for large conferences, or development of proposals for scholarship programs, leave little or no time for life outside the office or the lab. The employees' enormous personal engagement arises from their strong identification with the research they are involved in. While such identification can be very positive, leading to profound satisfaction with one's professional activity, it can also result in pressure and tensions in the family environment.

We at PDI place great importance on promoting work-life balance and support our employees in this respect through individual solutions. Our measures are continuously developed within an external audit process. On December 10, 2018 PDI was re-certified by berufundfamilie gGmbH for its engagement in pursuing a family-friendly human resources policy.

Alle Wissenschaftlerinnen und Wissenschaftler und die Wissenschaft unterstützenden Mitarbeiterinnen und Mitarbeiter kennen Phasen extremer zeitlicher Belastungen bei ihrer Arbeit. Während der Endphase einer Doktorarbeit, im Umfeld großer Tagungen oder in der Antragsphase für ein Stipendienprogramm ist oft kaum noch Platz für ein Leben außerhalb des Büros und Labors. Das enorme persönliche Engagement der Mitarbeiterinnen und Mitarbeiter speist sich aus der starken Identifikation mit der Forschung. Im positiven Fall bedeutet diese Identifikation große Zufriedenheit mit der beruflichen Tätigkeit – sie kann aber auch zu Belastungen und Einschränkungen im familiären Umfeld führen.

Wir legen am PDI großen Wert auf die Vereinbarkeit von Beruf und Familie und unterstützen unsere Mitarbeiterinnen und Mitarbeiter hierbei durch individuelle Maßnahmen. Im Rahmen eines externen Auditierungsprozesses werden unsere Maßnahmen weiterentwickelt. Das PDI wurde am 10. Dezember 2018 erneut für sein Engagement für eine familienbewusste Personalpolitik durch die berufundfamilie gGmbH zertifiziert.





Paul-Drude-Institut für Festkörperelektronik,  
Leibniz-Institut im Forschungsverbund Berlin e. V.

Hausvogteiplatz 5-7  
10117 Berlin  
Germany

[www.pdi-berlin.de](http://www.pdi-berlin.de)

